

The background of the entire page features a close-up of two Komondors' heads in profile, facing each other. The dog on the left is light-colored, and the one on the right is dark-colored. Both have their mouths slightly open, showing their teeth. A dense, chaotic pattern of blue lines, resembling a scribble or a complex network, is overlaid on the image, particularly concentrated in the upper half.

# The Shape of Strangeness

Transverse Sphericity and Underlying Event studies  
of  $\varphi$  and its relation to  $\Xi$  in  $\sqrt{s} = 13$  TeV pp collisions

ADRIAN FERAYDON NASSIRPOUR

DEPARTMENT OF PHYSICS | LUND UNIVERSITY | 2022



# The Shape of Strangeness

Transverse Sphericity and Underlying Event  
studies of  $\phi$  and its relation to  $\Xi$  in  $\sqrt{s} = 13$   
TeV pp collisions

by Adrian Fereydon Nassirpour



**LUND**  
UNIVERSITY

Organization <b>LUND UNIVERSITY</b>  Department of Physics Box 118 SE-221 00 LUND Sweden		Document name <b>DOCTORAL DISSERTATION</b>	
Author(s) Adrian Fereydon Nassirpour		Date of disputation 2022-12-09	
		Sponsoring organization	
Title The Shape of Strangeness: Transverse Spherocity and Underlying Event studies of $\phi$ and its relation to $\Xi$ in $\sqrt{s} = 13$ TeV pp collisions			
<p>Abstract</p> <p>Through ultrarelativistic particle collisions at the LHC, it is possible to deconfine quarks and gluons. This deconfinement gives rise to a strongly interacting medium, referred to as the Quark-Gluon Plasma (QGP). One of the earliest proposed and observed signatures of the QGP was the enhanced production of strange hadrons since the medium can thermally produce strange quarks. However, recent studies in small systems, such as proton-proton (pp) and proton-lead (pPb) collisions, have exhibited similar features. These findings are quite puzzling, as the formation of a QGP in these small collision systems challenges current theoretical frameworks.</p> <p>In this Thesis, I present two different studies on the production of <math>\phi</math> mesons, in relation to <math>\Xi</math> baryons, in pp collisions at <math>\sqrt{s} = 13</math> TeV, measured with the ALICE apparatus. Both of these studies aim to investigate the origin of strange hadron enhancement in high-multiplicity pp collisions. First, I report measurements of <math>\phi</math> production as a function of the event-shape observable Unweighted Transverse Spherocity, <math>S_O^{pT=1}</math>. With <math>S_O^{pT=1}</math>, it is possible to categorize events by their azimuthal topology. I utilize <math>S_O^{pT=1}</math> to contrast particle production in collisions dominated by many soft initial interactions, with collisions dominated by a single hard scattering. I find that strangeness enhancement is prominent in soft, isotropic topologies, whereas events with di-jet topologies showcase a clear suppression of strange particles.</p> <p>The second study presents the production of <math>\phi</math> mesons and <math>\Xi</math> hadrons as a function of the Relative Transverse Activity <math>R_T</math>. With <math>R_T</math>, one can control the size of the Underlying Event (UE). By varying <math>R_T</math>, it is therefore possible to study the interplay between particle production from hard fragmentation in jets, and soft particles produced by the UE. The reported results suggest that strange particle production is mainly a feature of the UE.</p> <p>When put together, the two studies suggest that high-multiplicity pp collisions are in general dominated by soft physics, which is also responsible for the strangeness enhancement, while high-multiplicity events dominated by hard physics are rare outliers.</p>			
Key words LHC, ALICE, quark-gluon plasma, small systems, pp collisions, underlying event, event-shape engineering, spherocity, transverse activity, strangeness enhancement, resonance production			
Classification system and/or index terms (if any)			
Supplementary bibliographical information		Language English	
ISSN and key title		ISBN 978-91-8039-454-3 (print) 978-91-8039-453-6 (pdf)	
Recipient's notes	Number of pages 269	Price	
	Security classification		

I, the undersigned, being the copyright owner of the abstract of the above-mentioned dissertation, hereby grant to all reference sources the permission to publish and disseminate the abstract of the above-mentioned dissertation.

Signature 

Date 2022-10-25



# The Shape of Strangeness

Transverse Spherocity and Underlying Event  
studies of  $\phi$  and its relation to  $\Xi$  in  $\sqrt{s} = 13$   
TeV pp collisions

by Adrian Fereydon Nassirpour



**LUND**  
UNIVERSITY

© Adrian Fereydon Nassirpour 2022

Cover images: Picture of Paddy & Eros (Dogs) by Maria Helena Nassirpour, and illustration of charged particle tracks by David Dobrigkeit Chinellato

Faculty of Science  
Department of Physics

isbn: 978-91-8039-454-3 (print)

isbn: 978-91-8039-453-6 (pdf)

Printed in Sweden by Media-Tryck, Lund University, Lund 2022



Media-Tryck is a Nordic Swan Ecolabel  
certified provider of printed material.  
Read more about our environmental  
work at [www.mediatryck.lu.se](http://www.mediatryck.lu.se)

**MADE IN SWEDEN** 

*Dedicated to my two bro's  
Sebastian and Filiph*



# Abstract

Through ultrarelativistic particle collisions at the LHC, it is possible to deconfine quarks and gluons. This deconfinement gives rise to a strongly interacting medium, referred to as the Quark-Gluon Plasma (QGP). One of the earliest proposed and observed signatures of the QGP was the enhanced production of strange hadrons since the medium can thermally produce strange quarks. However, recent studies in small systems, such as proton–proton (pp) and proton–lead (pPb) collisions, have exhibited similar features. These findings are quite puzzling, as the formation of a QGP in these small collision systems challenges current theoretical frameworks.

In this Thesis, I present two different studies on the production of  $\phi$  mesons, in relation to  $\Xi$  baryons, in pp collisions at  $\sqrt{s} = 13$  TeV, measured with the ALICE apparatus. Both of these studies aim to investigate the origin of strange hadron enhancement in high-multiplicity pp collisions. First, I report measurements of  $\phi$  production as a function of the event-shape observable Unweighted Transverse Spherocity,  $S_{\text{O}}^{p_{\text{T}}=1}$ . With  $S_{\text{O}}^{p_{\text{T}}=1}$ , it is possible to categorize events by their azimuthal topology. I utilize  $S_{\text{O}}^{p_{\text{T}}=1}$  to contrast particle production in collisions dominated by many soft initial interactions, with collisions dominated by a single hard scattering. I find that strangeness enhancement is prominent in soft, isotropic topologies, whereas events with di-jet topologies showcase a clear suppression of strange particles.

The second study presents the production of  $\phi$  mesons and  $\Xi$  hadrons as a function of the Relative Transverse Activity  $R_{\text{T}}$ . With  $R_{\text{T}}$ , one can control the size of the Underlying Event (UE). By varying  $R_{\text{T}}$ , it is therefore possible to study the interplay between particle production from hard fragmentation in jets, and soft particles produced by the UE. The reported results suggest that strange particle production is mainly a feature of the UE.

When put together, the two studies suggest that high-multiplicity pp collisions are in general dominated by soft physics, which is also responsible for the strangeness enhancement, while high-multiplicity events dominated by hard physics are rare outliers.

## Popular Science Summary

Quarks and gluons are elementary particles that constitute fundamental building blocks of matter. These particles can not normally be observed as free particles, due to the strong force, which confines both quarks and gluons into hadrons, such as neutrons and protons. However, under specific circumstances, it is possible to induce a *phase transition*; similarly to how ice melts into water, given a high enough temperature, the bindings of the strong force can “melt”, *deconfining* the quarks and gluons. This can create a new, exotic state of matter, referred to as the quark-gluon plasma (QGP). The QGP can be described as a strongly-interacting medium, which is extremely dense and driven by extremely large temperatures. Within the QGP, quarks and gluons are essentially able to roam around as free particles. Furthermore, it is hypothesized that the entire Universe once consisted of a single QGP, after the first microseconds (0.000001 seconds) of the Big Bang.

By colliding heavy ions, such as lead or gold, that are accelerated up to 99% of the speed of light, it is possible to create the experimental temperatures and pressures required to form q QGP. However, it is not possible to directly measure the properties of the strongly interacting medium, as the temperatures can not be sustained for more than an extremely short moment. The plasma quickly cools down and decays to produce hadrons that have re-confined both quarks and gluons. Instead, one has to study the interplay between different hadrons, in collisions where one thinks the QGP has been created. This is what has been done at the “The Relativistic Heavy-Ion Collider (RHIC)” in Brookhaven and at “The Large Hadron Collider” (LHC) in Geneva, which has generated a plethora of experimental evidence for the QGP. Observations suggest that the QGP acts like an almost perfect liquid, where particles exhibit movement through collective patterns, where both the transport and production of particles can be described by hydrodynamics.

However, several discoveries have been made in recent years, which suggest that several of the collective signatures are also present in proton–proton (pp) collisions. This has been a puzzling discovery, as pp collisions were not thought to be able to create the experimental conditions required for quarks and gluons to properly thermalize, to produce a QGP. One of these signatures has been the enhanced production of hadrons containing *strange* quarks. These heavier hadrons, relative to protons and neutrons which consist of lighter quarks, are not normally encountered throughout the Universe, as they are unstable and quickly decay once produced. Enhanced production of hadrons containing strange quarks was long thought to be a unique feature of heavy-ion collisions but has now also been discovered in pp collisions, published in the journal Nature



Physics [1].

The goal of the research described in this thesis is to gain further insight into what drives the enhancement of strange hadrons in extremely energetic (high-multiplicity) pp collisions. This has been done by studying strange hadrons relative to the geometry produced in each collision, which can give insight into the physical processes that drive particle production. The production of  $\phi$  mesons (pronounced “phi”, consisting of a pair of strange-antistrange quarks) has been studied relative to the production of  $\Xi$  baryons (pronounced “xi”, consisting of up quarks, and two strange quarks).

The production of  $\phi$  mesons in a QGP is described through thermal distributions, where the probability to create a  $\phi$  meson is related to its mass, which is similar to that of a proton. More traditional models in particle physics instead predict the  $\phi$  to behave more like the  $\Xi$  production, where it is instead the mass of the quarks that drives particle production. The relationship between these two particles can therefore be used to probe more information about the underlying processes of particle production in high-multiplicity pp collisions.

The results presented in this thesis suggest that the previously considered rare, “QGP-like” effects in high-multiplicity pp collisions, are not as rare as previously thought. Rather, it seems that these phenomena are the norm in high-multiplicity pp collisions. Instead, it seems that the traditional signatures in pp collisions are extremely suppressed, within the most highly energetic pp collisions.

## Populärvetenskaplig Sammanfattning

Kvarkar och gluoner, elementarpartiklar som utgör två av materians fundamentala byggblock, kan normalt sett inte observeras fritt. Detta på grund av att de hålls ihop av den starka växelverkan för att bilda hadroner, så som neutroner och protoner. Under särskilda förhållanden är det däremot möjligt att inducera en *fasövergång*; På samma sätt som is kan smälta till vatten vid tillräckligt höga temperaturer, så kan bindningarna av den starka växelverkan "smälta", och på så vis befria kvarkar och gluoner. Detta bildar ett exotiskt nytt tillstånd, som kallas *kvark-gluonplasma*. Det nya tillståndet kan beskrivas som starkt växelverkande, extremt kompakt, och drivs av enorma temperaturer, där kvarkar och gluoner i stort sätt kan röra sig som fria partiklar. Dessutom är det spekulerat att hela Universum vid en tid bestod av en singulär kvark-gluonplasma, vid de första mikrosekunderna (0,000001 sekunder) efter Big Bang.

Genom att kollidera tunga joner, så som bly eller guld, som accelererats upp till 99% av ljusets hastighet, så är det möjligt att experimentellt skapa de temperaturerna och tryck som krävs för att bilda en potentiell kvark-gluonplasma. Däremot är det inte möjligt att direkt mäta egenskaperna av det starkt växelverkande tillståndet, då de det inte går att upprätthålla temperaturerna för mer än ett otroligt kort ögonblick. Plasman kyls ner och sönderfaller, vilket producerar hadroner som återigen bundit ihop kvarkar och gluoner. För att utforska egenskaperna av kvark-gluonplasman, så måste man istället skildra hur producerade hadroner interagerar med varandra, i kollisioner där man tror plasman har bildats. På så vis har en rad av experimentella bevis av kvark-gluonplasman hittats, både från "The Relativistic Heavy-Ion Collider" (RHIC) i Brookhaven, och "The Large Hadron Collider" (LHC) i Genève. Det som observerats tyder på att kvark-gluonplasman beter sig som en perfekt vätska, där partiklar kan ses röra sig kollektivt, där transport och produktion av partiklarna kan beskrivas med vätskedynamik.

Däremot så har flera upptäckter gjorts i de senaste åren, där man kan se att många av de kollektiva signaturerna också uppträder i extremt hög-energetiska proton-proton (pp) kollisioner. Detta har varit en förbryllande upptäckt, då pp kollisioner inte troddes kunna bilda tillräckligt stora volymer, för att kvarkar och gluoner skulle kunna termalisera. En av dessa signaturer är förstärkningen av hadroner som innehåller en "*strange*" kvark (även kallat särkvark). Dessa tyngre hadroner, förhållandevis till protoner och neutroner som bara består av lättare kvarkar, är inte vanligt förekommande i universum, då de är instabila och sönderfaller snabbt. En ökad produktion av hadroner med särkvarkar som troddes vara unikt till tungjonskollisioner har nu också upptäckts i proton-proton kollisioner, vilket har publicerat i tidskriften Nature Physics [1].

Syftet med forskningen som beskrivs i denna avhandling är att bättre förstå det som driver den förstärkta produktionen av särkvarkar i extremt-högenergetiska pp kollisioner och huruvida detta är relaterat till kvark-gluonplasman. Detta har gjorts genom att studera särkvarkar i hög-energetiska pp kollisioner, förhållande till geometrin som skapas i kollisionen. Tanken är att geometrin i kollisionen som bildas kan skildra vilka typer av fysikprocesser som drivit partikelproduktionen. Produktionen av  $\phi$  mesoner (uttalas “fi”, som består av ett särkvark-antisärkvark par) har studerats i förhållande till produktionen av  $\Xi$  baryoner (uttalas “xi”, som består av en “upp” kvark, och två särkvarkar).

Produktionen av  $\phi$  mesoner i en kvark-gluonplasma beskrivs via termiska distributioner, där sannolikheten att bilda en  $\phi$  meson är relaterad till dess massa, vilket är likt protonen. Mer traditionella modeller inom partikelfysik beskriver istället  $\phi$  produktionen likt  $\Xi$  baryoner, där det är massan av särkvarkarna som driver produktionen. Förhållandet mellan dessa två partiklar kan därför ge information om hur hadronerna i sig bildas i hög-energetiska pp kollisioner.

Resultaten som presenteras i denna avhandling indikerar att de tidigare trott sällsynta, “kvar-gluonplasma-liknande” effekterna i hög-energetiska pp kollisioner, inte är lika sällsynta som förutspått. Snarare så verkar dessa fenomen beskriva normen av hög-energetiska pp kollisioner. Istället är det de traditionella proton-proton signaturerna som är extremt dämpade, inom de mest hög-energetiska pp kollisionerna.



## List of Acronyms

**ALICE:** A Large Ion Collider Experiment  
**ATLAS:** A Toroidal LHC Apparatus  
**CERN:** The European Organization for Nuclear Research  
**CMS:** Compact Muon Solenoid  
**CR:** Color Reconnection  
**EMCal:** Electromagnetic Calorimeter  
**FMD:** Forward Multiplicity Detector  
**HMPID:** High-Momentum PID  
**INEL:** Inelastic  
**ITS:** Inner Tracking System  
**LHC :** The Large Hadron Collider  
**lQCD:** Lattice QCD  
**MC:** Monte-Carlo  
**MPI:** Multiple Parton Interactions  
**MRPC:** Multiresistive plate chambers  
**MWPC:** Multi-wire proportional chambers  
**p:** Proton  
**Pb:** Lead  
**PHOS:** Photon Spectrometer  
**PHENIX:** Pioneering High Energy Nuclear Interaction experiment  
**PID:** Particle Identification  
**PMD:** Photon Multiplicity Detector  
**pQCD:** Perturbative QCD  
**PS:** Proton Synchrotron  
**PSB:** Proton Synchrotron Booster  
**QFT:** Quantum Field Theory  
**QCD:** Quantum Chromodynamics  
**QED:** Quantum Electrodynamics  
**RHIC:** Relativistic Heavy-Ion Collider  
**S/B:** Signal-to-Background Ratio  
**SPD:** Silicon Pixel Detector  
**SSD:** Silicon Strip Detector  
**SDD:** Silicon Drift Detector  
**STAR:** Solenoidal Tracker at RHIC  
**SPS:** Super Proton Synchrotron  
**TOF:** Time-of-Flight  
**TPC:** Time-Projection Chamber  
**TRD:** Transition Radiation Detector  
**UE:** Underlying Event  
**ZDC:** Zero-Degree Calorimeter

# Acknowledgements

I am writing these acknowledgments just two hours before I have to submit this very thesis for printing. Everyone listed here has, aided and supported me along the way, to be able to finally produce this thesis. If you feel that your name should've been included in these pages, and aren't, you're probably right, and I apologize. My only excuse is that these last months have induced an irreparable amount of psychic damage, brought on by two months of insane writing hours.

Anyone who has ever met me will obviously know who I have to acknowledge first; my two dogs Eros and Paddy, for being the two best dogs for which anyone could ever hope. This is followed by thanks to my two parents, Maria and Fereydon, as well as my two brothers, Sebastian and Filiph, for always believing in me, and paving the path to where I stand today.

Next up, we have my supervisor, Peter. Thank you, for not only being the best<sup>1</sup> supervisor one could ever ask for, but also for being a good friend. Your passion and curiosity for physics have always been extremely inspiring for me, which has undoubtedly left a profound impact on my view and motivations regarding science. Your skill and knowledge in both physics and programming have been extremely helpful, and you've been able to step up and lead the group during the darkest of hours.

Thanks to both of my co-supervisors, for tirelessly being able to bounce ideas about physics, coding, and life in general. Alice, thank you for your general chill attitude! Your ability to break down and describe complex concepts has been of tremendous help. Likewise, David, you have the most laid-back vibes of any physicist that I have ever met. The fact that you're available for discussion has been very helpful. Lastly, thanks to Anders, not only for the technical discussions but also for the philosophical ones (and the great stories from days past).

Next, I would like to the people that I've had to share an office with during the last couple of years. Big thanks to Oliver, Omar, and Jonatan, for being to deal with me during my crankiest days. I think we had a good dynamic during our years in the office, which made the stress of analysis more manageable, and I wish you all well in the future! Also big thanks to Anna, Lisa, and Martin, for creating a great working atmosphere, and reminding me of the good times before the pandemic. Lastly, thanks to Vytautas, for writing a super nice thesis, and also for the good times during conferences!

---

<sup>1</sup>Although it must be said, his skills in League of Legends™ leave a lot to be desired



Thanks to everyone involved in CLASH, including Leif, Christian, Torbjörn, Jarkko, and others, for providing good discussions, and willingness to stick out their necks, providing strong predictions.

Thanks to all the people and friends that I've met and interacted with throughout the years! Special thanks to Daniel, for being a great friend, and making a global pandemic feel less depressing than it otherwise would've. Big ups for Jerome, for the good times during conferences, but also for the good times while gaming. Big thanks to Sebastian, Esther, Mario, and Florian for the good times in Frankfurt. Likewise, big thanks to Oskari and Topi, for the unexpectedly wild times in central Finland.

Next up, big thanks to all of the people that have been around in the division! This includes Sumit, Eleni, Katja, Eva, Trine, Katja, Caterina<sup>2</sup>, Eric, Nathan, Alexander, Einar, Ruth, Hannah, Will, Lennart, and Else. Special thanks to Oxana, and Geoffrey for the engaging lunch discussions! Huge thanks to Florido, for helping me to set up and maintain BEAST! Also, thanks to Bozena, for being able to stay cool while trying to decipher my travel reports.

Lastly, an extra thanks to everyone that has read through, and given good feedback for the thesis. This includes Peter, David, Alice, Anders, Jarkko, Topi, Christian, Daniel, Roman, Hannah, and Adam. Without you all, this thesis would have been almost impossible to produce.

Alright, that should be it! I am now done rambling, and off to catch some sleep.

# Contents

<b>1</b>	<b>Introduction</b>	<b>1</b>
1.1	Thesis outline . . . . .	4
1.2	Summary of my contributions . . . . .	6
<b>2</b>	<b>The Standard Model of Particle Physics</b>	<b>11</b>
2.1	The Standard Model . . . . .	11
2.2	Feynman Diagrams and Quantum Electrodynamics (QED) . . .	14
2.3	Quantum Chromodynamics . . . . .	18
<b>3</b>	<b>Observables, Heavy-Ion Physics and the Quark-Gluon Plasma</b>	<b>23</b>
3.1	Basic observables and quantities . . . . .	24
3.2	QCD Phase Transitions & The Quark-Gluon Plasma . . . . .	30
3.3	Signatures of the Quark-Gluon Plasma . . . . .	37
3.4	The New Paradigm: High-Multiplicity Proton-Proton Collisions . . . . .	49
<b>4</b>	<b>Monte-Carlo Models, and Phenomenology of Particle Production</b>	<b>57</b>
4.1	The Lund String Model . . . . .	59
4.2	Cluster Hadronization with Herwig 7 . . . . .	67
4.3	Hydrodynamical & Thermal Hadronization . . . . .	68
4.4	Phenomenological Understanding of the $\phi$ Meson in Experiments	70
<b>5</b>	<b>The Large Hadron Collider &amp; The ALICE Detector</b>	<b>75</b>
5.1	The Large Hadron Collider . . . . .	75
5.2	The ALICE Detector . . . . .	79
<b>6</b>	<b><math>\phi</math> Meson and <math>\Xi</math> Baryon Reconstruction</b>	<b>97</b>
6.1	Common Event Selection . . . . .	97
6.2	Reconstruction & Identification of $\phi$ (1020) Mesons . . . . .	99
6.3	Reconstruction and Identification of $\Xi^- + \bar{\Xi}^+$ (1322) Baryons . .	116
<b>7</b>	<b><math>\phi</math> and <math>\Xi</math> Yields as Functions of Unweighted Transverse Sphericity <math>S_{\text{O}}^{p_{\text{T}}=1}</math></b>	<b>127</b>
7.1	Charged particle production as a function of the azimuthal topology	127

7.2	Unweighted Transverse Sphericity $S_{\text{O}}^{p_{\text{T}}=1}$ . . . . .	132
7.3	Definition of “High-Multiplicity” . . . . .	143
7.4	Systematic uncertainties for the $S_{\text{O}}^{p_{\text{T}}=1}$ analysis . . . . .	147
7.5	Results . . . . .	153
7.6	Summary And conclusions . . . . .	171
<b>8</b>	<b><math>\phi</math> and <math>\Xi</math> yields as Functions of Relative Transverse Activity <math>R_{\text{T}}</math></b>	<b>173</b>
8.1	Definition of Relative Transverse Activity $R_{\text{T}}$ . . . . .	173
8.2	Track Selection and Bias Estimation . . . . .	178
8.3	Investigation of Experimental Bias . . . . .	180
8.4	Systematic Uncertainties . . . . .	183
8.5	Results & Discussion . . . . .	187
8.6	Interpretation of Ratios, and Outlook . . . . .	193
<b>9</b>	<b>Conclusions</b>	<b>195</b>
<b>10</b>	<b>Appendix A: Invariant Mass Distributions and Fits for the <math>S_{\text{O}}^{p_{\text{T}}=1}</math> Analysis.</b>	<b>199</b>
10.1	Invariant Mass Distributions . . . . .	200
10.2	Invariant Mass Peak Fits . . . . .	212
<b>11</b>	<b>Appendix B: Geometrical Cut for the <math>R_{\text{T}}</math> Analysis</b>	<b>225</b>
<b>12</b>	<b>Appendix C: Systematic Uncertainties and Roger-Barlow Checks for <math>\phi</math> Meson Analysis</b>	<b>229</b>
12.1	V0M: 0-10% . . . . .	230
12.2	Jetty Events (V0M:0-10%, $S_{\text{O}}^{p_{\text{T}}=1}$ 0-10%) . . . . .	235
12.3	Isotropic Events (V0M:0-10%, $S_{\text{O}}^{p_{\text{T}}=1}$ 90-100%) . . . . .	240
<b>13</b>	<b>References</b>	<b>245</b>
13.1	References . . . . .	245



# Chapter 1

## Introduction

The main purpose of this thesis, and much of the entire heavy-ion research field, is to gain further insight into the properties and dynamics of the quark-gluon plasma (QGP). At the energy scales at which we exist, quarks and gluons are normally bound together as hadrons, such as protons and neutrons, by the strong force, and cannot be observed as independent particles. However, given extreme energy densities and pressure, quarks and gluons have been observed to *deconfine*, to form a semi-coherent, strongly interacting medium. This medium is referred to as the QGP, where partons can roam for distances longer than the size of a nucleon [2]<sup>1</sup>. Furthermore, it is hypothesized that during the first microseconds after the Big Bang, the entire known Universe consisted of a single, large QGP [3]. This expansion of the Universe is illustrated in Fig. 1.1. Moreover, it is theorized that QGP naturally composes the core of supermassive neutron stars [4].

The possibility of producing man-made QGP in ultra-relativistic heavy-ion collisions has been hypothesized since the mid-1970's [5], due to the large temperatures and pressures created in the collisions. These collisions consequently produce an enormous entropy, with up to as many as 30,000 particles [6]. This can be seen in Fig. 1.2, showing a typical central Pb–Pb collision measured by the A Large Ion Collider Experiment (ALICE). However, the particle collisions can not sustain the temperature of the QGP, giving it an extremely short lifetime (approximately  $\approx 10\text{ fm}/c \approx 10^{-23}\text{ s}$ ), making direct observations of the QGP impossible. Instead, signatures of the QGP have to be inferred by the behavior and dynamics of the produced final-state particles, which can be measured experimentally.

---

<sup>1</sup>The size of a nucleon is about one *fermi*, where  $1\text{ fm} = 10^{-15}\text{ m}$

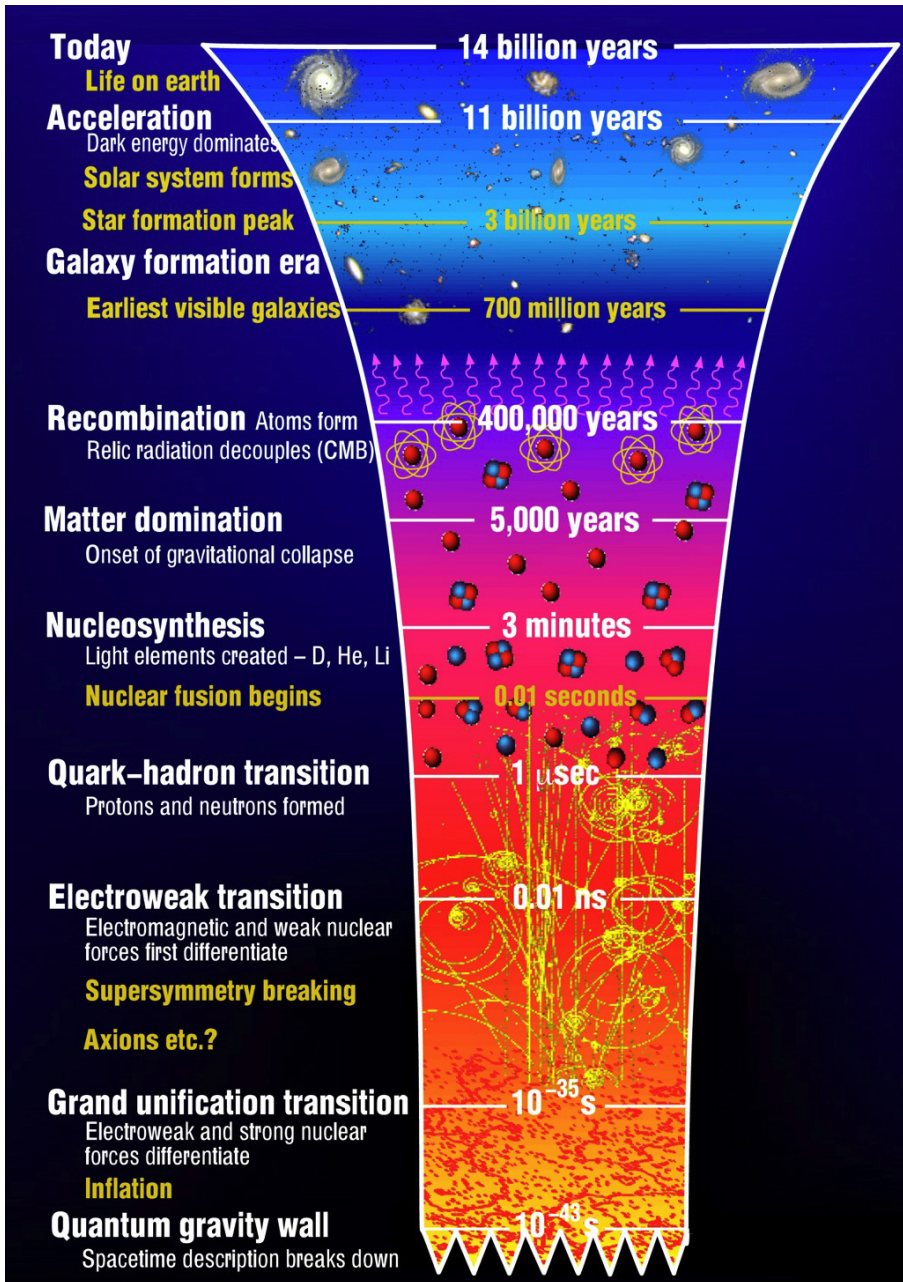


Figure 1.1: Sketch of the formation of the Universe, from the Big Bang until today. The figure is borrowed from Ref. [7].



Circumstantial observations of the QGP were first made at the CERN Super Proton Synchrotron (SPS) [8][9]. This was followed up by more confident observations with measurements from the heavy-ion program at the Relativistic Heavy-Ion Collider (RHIC) [10][11][12][13], which suggested that the QGP has properties similar to that of a perfect liquid<sup>2</sup>. The observations from RHIC were supplemented with additional evidence from the heavy-ion program from the Large Hadron Collider (LHC); the largest man-made apparatus ever constructed, which opened for operation in 2010, allowing for Pb–Pb collisions at center-of-mass energies 10 times larger than those of RHIC (200 GeV and 2760 GeV per nucleon pair, respectively). Experimental measurements in Pb–Pb collisions at a center-of-mass energy ( $\sqrt{s_{NN}}$ ) equivalent to 2.76 TeV (approximately  $4.422 \times 10^{-7}$  J) have suggested that the temperatures of a QGP are of the order of 300 MeV [14] (approximately  $3.481 \times 10^{12}$  K)<sup>3</sup>.

However, during recent years, a large collection of studies of high-multiplicity proton–proton (pp) and proton–lead (p–Pb) collisions have revealed that small collision systems<sup>4</sup> exhibit signatures that were previously considered to be unique features of the QGP [15][1][16]. The formation of a QGP in these small collision systems challenges current theoretical frameworks, as the initial small volumes imply lifetimes too short for the produced systems to fully equilibrate. Moreover, the results in small systems also challenge the idea that the aforementioned observations are necessarily signs of the QGP, which is the widely accepted interpretation of measurements in experiments from both RHIC and LHC. This has created a sub-community within the traditional heavy-ion community, probing the universality of a potential QGP in different collision systems.

One of the first proposed signatures of the QGP has been the enhanced production of strange ( $s$ ) quarks, relative to lighter up ( $u$ ) and down ( $d$ ) quarks [18]. This quite abundant strange quark has appeared to be a very powerful probe for QGP-like effects, in small and large collision systems alike (described in detail in Sec. 3.3.1). Results on strangeness production in small systems can facilitate progress in both QCD dynamics, in addition to putting constraints on phenomenological, non-perturbative descriptions of hadronization. The ALICE collaboration has previously reported that strangeness enhancement does not depend on the collision system, nor the center-of-mass energy, but has a universal scaling, depending on the charged particle density produced at midrapidity [1].

This thesis will provide new tools and measurements to further study the en-

---

<sup>2</sup>“Perfect”, in this sense, implying a shear viscosity to entropy density of nearly 0

<sup>3</sup>For more relatable references, the temperature of volcanic lava is approximately 1500 K. The core of the sun is estimated to be  $15.7 \times 10^7$  K

<sup>4</sup>Relative to larger, nucleon–nucleon collisions, e.g., lead–lead collisions (Pb–Pb)

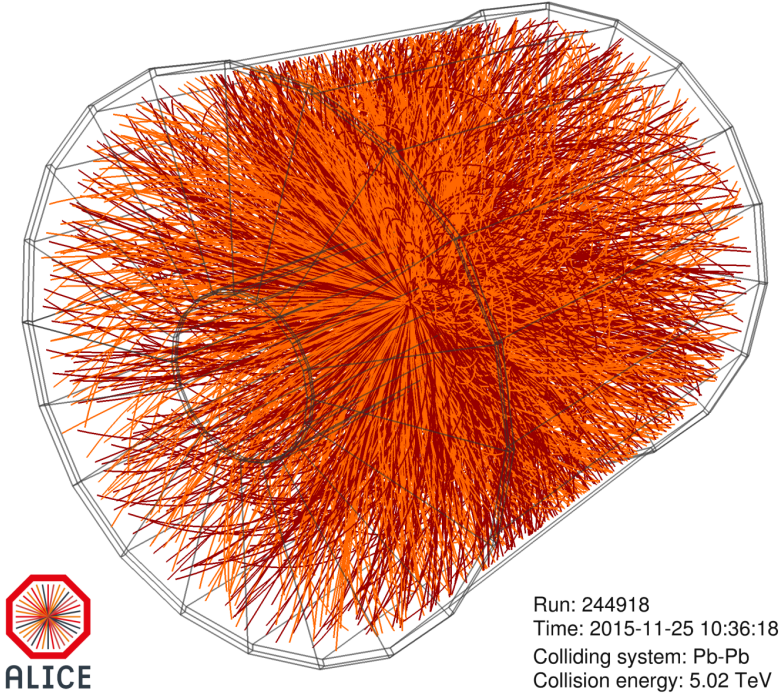


**Figure 1.2:** Event display of a single Pb-Pb collisions, at  $\sqrt{s_{NN}} = 5.02$  TeV, measured by the ALICE collaboration. Each individual line represents a charged particle track. The figure is taken from Ref. [17].

hancement of strange hadrons, in particular, the  $\phi$  and  $\Xi$  hadrons, relative to different properties measured in the collision, through multi-differential analyses to probe pp collisions in the regime where QGP-like features are prevalent. This thesis will report on new measurements of particle production in high-multiplicity pp collisions at  $\sqrt{s} = 13$  TeV, as functions of azimuthal event topology, estimated through the unweighted transverse spherocity  $S_O^{p_T=1}$ . This is followed by a measurement of  $\phi$  and  $\Xi$  production as functions of the relative transverse activity  $R_T$ .

## 1.1 Thesis outline

This thesis is divided into three parts; 9 chapters in total. The first part consists of three chapters covering elementary theory and phenomenological concepts, which puts the research presented in this thesis into context with broader heavy-ion research. Chapter 2 introduces the Standard Model, the basic theory of QED and QCD, lattice QCD and Feynman diagrams. This is followed by an overview

of the QGP and the signatures and properties of the QGP in chapter 3. Chapter 4 covers different phenomenological frameworks to describe the hadronization processes of  $\phi$  and  $\Xi$  hadron production.

Chapter 5 comprises the second part, which covers a brief overview of the LHC, followed by a detailed description of the ALICE apparatus. Experimental techniques used for charged particle track reconstruction, as well as particle identification (PID) techniques utilized by ALICE, are covered in this chapter.

The last part details the two major studies that I have primarily contributed to during my time as a Ph.D. student; particle production as functions of the unweighted transverse sphericity  $S_O^{p_T=1}$ , and the relative transverse activity  $R_T$ .

I detail the  $\phi$  and  $\Xi$  reconstruction procedures in Chapter 6. I was the primary analyzer for the  $\phi$  yield extraction for both studies, spanning a kinematic range of  $(1 \leq p_T \leq 5)$  GeV/ $c$  at midrapidity ( $|\eta| < 0.8$ ). I describe the procedure of identifying oppositely charged kaon pairs, through different particle identification techniques, which I then used to reconstruct the  $\phi$  meson. I performed the full analysis, from optimizing the track configuration, and fitting and calibrating the combined peak parameterization, to obtaining the final, fully corrected yields. Furthermore, I developed a new method to estimate the combinatorial background, which allowed for a yield extraction with better precision. I made rigorous cross-examinations to ensure that my analysis technique was robust and that the obtained yields were consistent with results from prior ALICE publications.

The first study is presented In Chapter 7. Here, I measure the production of  $\phi$  yields with respect to the azimuthal topology. The azimuthal topology is estimated through the unweighted transverse sphericity  $S_O^{p_T=1}$ . I report that the traditional transverse sphericity observable  $S_O$  contained a large bias when measuring the production of particles that are not reconstructed as primary charged particles. Based on my investigation of the  $S_O$  estimator and the findings of its shortcomings, I developed the modified  $S_O^{p_T=1}$  observable. Furthermore, I report a robust series of cross-checks, not only for the  $\phi$  meson, but a large range of light-flavor particles ( $\pi, K, p, K_S^0, \Lambda, \Xi, K^{*0}$ ), to ensure that selecting events based on  $S_O^{p_T=1}$  would produce results directly comparable to MC generator predictions, for all light-flavor particle species. Moreover, I produced the MC predictions for all ALICE light-flavor  $S_O^{p_T=1}$  studies. I present  $S_O^{p_T=1}$ -differential measurements of  $\phi$ , including a large range of  $\phi$   $p_T$ -differential spectra, in different multiplicity intervals. I compare the  $\phi$  measurements to equivalent  $\Xi$  results, followed by a comprehensive discussion of the results.

For the second study, presented in Chapter 8, I measure the production of  $\phi$  yields as a function of the underlying event (UE). The size of the UE is estimated through the relative transverse activity,  $R_T$ . I show that there is a large experimental bias when measuring the  $p_T$ -differential  $\phi$  spectrum as a function of  $R_T$ . This is attributed to the smearing by the detector, and I demonstrate how this bias is effectively canceled when comparing particle species. I present the  $p_T$ -differential production of both  $\phi$  and  $\Xi$ , relative to the production of  $\pi$  mesons.

Chapter 9 summarizes the results obtained from the analyses presented in Chapters 7 and 8. Furthermore, it contains a comprehensive discussion where the role of  $\phi$  is contrasted between  $S_O^{p_T=1}$  and  $R_T$ , and how this relates to the equivalent observations of  $\Xi$  production.

## 1.2 Summary of my contributions

A large proportion of my time as a Ph.D. has been dedicated to rigorously testing and developing new event observables, suitable for high-multiplicity proton–proton collisions, where several experimental biases were uncovered and accounted for during development. Consequently, I have worked on my major research project in parallel, culminating in three papers that are at different (two of them mostly finalized) stages in the internal ALICE publication procedure. I played a major role in the development of both event observables discussed in this thesis: Unweighted Transverse Spherocity  $S_O^{p_T=1}$  and the Relative Transverse Activity  $R_T$ . Additionally, I was the main analyzer for  $\phi$  yield extraction, and have given a large contribution for the  $\Lambda$ ,  $K_S^0$  and  $\Xi$  analyses, w.r.t. to both aforementioned event observables. However, one should keep in mind that I was not the primary analyzer for the  $\Xi$  reconstruction. Therefore, some of the decisions taken for the  $\Xi$  analysis, especially in regard to the evaluation of the systematic uncertainty, differ compared to the  $\phi$  meson analysis.

I have also contributed to the data taking and managing of the ALICE apparatus in several detector shifts, both during the LHC Run 2 and Run 3 periods. Moreover, during my ALICE service task, I contributed to the Run 3 upgrade of the ALICE detector, by decommissioning and recommissioning the ALICE Time-Projection Chamber (TPC), between Run 2 and Run3.

### 1.2.1 Papers

Here I list ongoing papers which include major contributions from my side. These papers are not yet published and are in internal ALICE review. The papers are listed in order of completeness, where the two first papers are quite mature and will be published in the near future. Additionally, I list a published write-up from a workshop that I was involved with.

- Production of pions, kaons, and protons as a function of the transverse event activity in pp collisions at  $\sqrt{s}=13$  TeV. *I am in the paper committee for this paper, and I had a large part in R&D of  $R_T$  observable, to understand experimental biases in the yield extraction of the  $p_T$ -differential spectra. It was decided to break up this analysis into two publications, the first one to mainly publish the unfolding technique for the  $N_T$  spectra, as well as physics results for primary  $\pi, K, p$  production. This paper is spearheaded by my colleague O. Vázquez [19]*
- Light-flavor particle production in pp collisions at  $\sqrt{s} = 13$  TeV as a function of transverse sphericity. *A comprehensive paper of light-flavor particle production as a function of unweighted transverse sphericity  $S_O^{p_T=1}$ . This paper is primarily chaired, written, and driven by myself, along with several colleagues of primary analyzers for different particle species.*
- Production of  $\Lambda$ ,  $K_S^0$ ,  $K^{*0}$ ,  $\phi$ , and  $\Xi$  as a function of the transverse event activity in pp collisions at  $\sqrt{s}=13$  TeV. *Continuation of the  $R_T$  analysis. I will be part of the paper committee for this paper, which is primarily driven by my colleague O. Matonoha*
- J. Adolfsson et al. *QCD challenges from pp to A–A collisions*. Eur.Phys. J.A 56 (2020) 11, 288. <https://doi.org/10.1140/epja/s10050-020-00270-1>. *This is a published write-up from the workshop “3rd International Workshop on QCD Challenges from pp to AA”, which took place 19 - 23 Aug 2019.*

### 1.2.2 Proceedings

I have given several talks during my time as a Ph.D. student, totaling 15 presentations. These presentations do not include internal ALICE talks or analysis reviews. Some of these talks included an opportunity to write and publish proceedings. All of these proceedings were for centrally approved ALICE talks,

except my first presentation, where I showcased results from simulated data. The listings are presented in reverse-chronological order:

- A. Nassirpour, on behalf of the ALICE collaboration (2022). *Light-flavor hadron production in small collision systems with ALICE*. Will be published on EPJ Web of Conference. The proceeding is under review by journal editors.
- A. Nassirpour, on behalf of the ALICE collaboration (2022). *Event-shape studies of strangeness production in 13 TeV proton–proton collisions with ALICE*. *EPJ Web Conf.* **259**, 13005. <https://doi.org/10.1051/epjconf/202225913005>
- A. Nassirpour, on behalf of the ALICE collaboration (2020). *Probing strangeness production in small systems through new, multi-differential measurements with ALICE at the LHC*. *Journal of Physics: Conference Series*, **1602**(1), 012007. <https://doi.org/10.1088/1742-6596/1602/1/012007>
- A. Nassirpour (2019). *Improved Event Mixing for Resonance Yield Extraction*. *MDPI*, **10**, 1, 26. <https://doi.org/10.3390/proceedings2019010026>



# Part I

## Elementary Theory & Heavy-Ion Phenomenology



## Chapter 2

# The Standard Model of Particle Physics

This chapter will cover the basics of the Standard Model; a theory that describes all fundamental particles of matter (quarks and leptons), and the fundamental interactions between them (the gauge bosons). This is not a comprehensive review of the Standard Model, but rather a cursory overview of the theory and concepts needed to discuss upcoming chapters in this thesis. The chapter will mainly focus on the theory describing the electromagnetic interaction between quarks, leptons, and photons, Quantum Electrodynamics (QED), and the theory describing the interaction between quarks and gluons, Quantum Chromodynamics (QCD).

### 2.1 The Standard Model

The Standard Model contains three types of different elementary particles: quarks, leptons, and force mediators (bosons). In addition to the particles listed in Fig. 2.1, all particles have corresponding anti-particles; particles that share the same mass, but with opposite electric charges.

The Standard Model mainly describes the interactions between three out of the four fundamental forces: the Electromagnetic, Weak, and Strong nuclear forces. The fourth fundamental force, Gravity, proposed to be mediated via the Graviton, interacts too weakly to be detected on a microscopic level [21, p. 9], and can not currently be formulated into a gauge theory, and is therefore

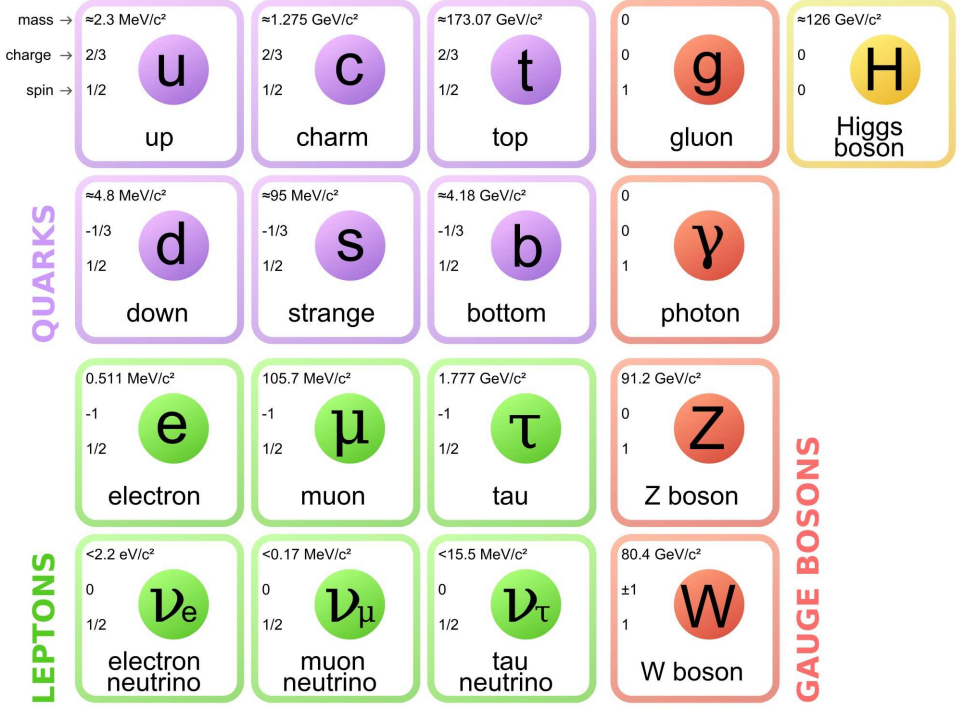


**Figure 2.1:** Overview of the different particles included in the Standard Model. The different colors distinguish the different types of particles; quarks, leptons, and bosons. The listed numbers are the mass (top), electrical charge (middle), and spin (bottom). The figure is taken from Ref. [20].

not incorporated into the standard model. The electromagnetic force acts on electrically charged particles, while the strong force acts on particles that carry color charges (quarks and gluons). Lastly, the weak force (weak, due to the large mass of the force mediators,  $W^\pm/Z^0$ ), acts on quarks, leptons, and electroweak bosons [21, p. 6].

The quarks constitute the building blocks of hadrons. Quarks are fermions that obey the Pauli exclusion principle, have spin  $\frac{1}{2}$ , are massive, carry the color charge of QCD, and electric charges in fractions of either  $\frac{2}{3}e$  or  $-\frac{1}{3}e$ . The color charges are split into three different values, red ( $r$ ), green ( $g$ ), and blue ( $b$ ). These colors are not “colors” in a traditional sense, but rather represent different quantized charges, each one similar to the electric charge.

All hadrons consist of two different types of quarks; sea quarks and valance quarks. The valence quarks determine the quantum numbers of hadrons and ensure that hadrons are color neutral, i.e, they consist of partons that form a color-neutral singlet. This is done either by combining a triplet of different color charges ( $rgb$  or  $\bar{r}\bar{g}\bar{b}$ ) which are called Baryons, or a quark-antiquark pair

with opposite charges (for example,  $r\bar{r}$ ), called Mesons<sup>1</sup>. Conversely, sea quarks are quark-antiquark pairs that form due to quantum fluctuations inside the hadron [21, p. 208].

There are 6 known quarks, divided into three generations with ascending masses. The different quarks are often referred to as different “flavors”. The two lightest quarks, the “up” ( $u$ ) and “down” ( $d$ ) quarks, are the most abundant ones, which are the building blocks for protons ( $uud$ ) and neutrons ( $udd$ ). The heavier quarks do not comprise any stable hadrons but can be produced in ultra-relativistic particle collisions.

Leptons are massive fermions, and unlike quarks, do not carry any color charge, and can therefore only interact through weak and electromagnetic interactions. The electron, muon, and tau leptons carry an electric charge, and all have their corresponding neutrino particles, which carry no electric charge and can only interact through the weak force.

The bosons mediate the different forces. Unlike the leptons and quarks, they do not follow the Pauli exclusion principle, as they have an integral spin of 1 (except for the Higgs Boson, which has an integral spin of 0). Furthermore, since the bosons can be derived through the framework of gauge theories, they are also referred to as “gauge bosons”. The photons transmit the electromagnetic force. They are massless mediators and do not carry any inherent electromagnetic charge. In contrast, the massless gluons, which mediate the strong force, carry an inherent color charge as well; leading to several unique properties of the interactions between quarks and gluons, further discussed in Sec. 2.3. The  $W^\pm$  and  $Z^0$  bosons, which mediate the weak interaction, are both massive, where the  $W^\pm$  boson also carries either positive or negative electrical charge, while the  $Z^0$  boson is electrically neutral.

It is possible to formalize quantum mechanical frameworks to describe the interactions between matter and forces, referred to as *Quantum Field Theories* (QFT). The QFT for interactions between electrically charged particles is referred to as Quantum Electrodynamics (QED), whereas the QFT for strong interactions is referred to as Quantum Chromodynamics (QCD). The QFTs based on different symmetry groups within the SM. The different symmetry groups for the SM can be expressed as:

$$SU(3) \times SU(2)_L \times U(1). \quad (2.1)$$

The  $U(1) \times SU(2)_L$  term describes the electroweak forces. The  $L$  in  $SU(2)_L$

---

<sup>1</sup>LHCb has discovered other types of hadrons, e.g., pentaquarks [22]. However, these hadrons are rare, and not relevant to the work presented in this thesis.

signifies that massless fermions can only interact weakly if their spin is anti-aligned (left-handed). Finally, the non-abelian  $SU(3)$  group describes the strong gluon-quark color interactions.

The Higgs Boson is the last boson of the Standard Model. It is related to the Higgs mechanism, which gives mass to the  $W^\pm$  and  $Z^0$  boson (and all SM fermions except for neutrinos) through electroweak symmetry breaking. The Higgs boson is an excitation of the Higgs field described by the Higgs mechanism.

## 2.2 Feynman Diagrams and Quantum Electrodynamics (QED)

The different interactions between hadrons, leptons, and bosons can be depicted through *Feynman diagrams*, introduced by Feynman during the early 1940s [23, p. 9]. The Feynman diagram allows one to intuitively illustrate complex QFT interactions, and also carries a mathematical description embedded into each diagram. A simple photon exchange for an electron-electron scattering of the lowest order is illustrated in Fig. 2.2, where the strength of the interaction is assigned as  $\sqrt{\alpha}$ , and the probability amplitude of the process is directly proportional to the scattering amplitude  $\mathcal{M}$ , with momentum  $\mathbf{q}$  and potential  $V(\mathbf{r})$ :

$$\mathcal{M}(\mathbf{q}) = \int V(\mathbf{r}) e^{(i\mathbf{q}\cdot\mathbf{r}/\hbar)} d^3\mathbf{r} \quad (2.2)$$

By substituting in the Yukawa potential<sup>2</sup>  $V_Y(r)$  [23, p. 17]:

$$V_Y(r) = -\frac{g^2}{4\pi} \frac{e^{-r/R}}{r}, \quad (2.3)$$

into Eq. 2.2, we obtain the following expression for  $\mathcal{M}$  (by integrating over polar coordinates) [23, p. 18]:

$$\mathcal{M}(\mathbf{q}) = \frac{g^2 \hbar^2}{|\mathbf{q}|^2 - M_X^2 c^2} \quad (2.4)$$

where  $M_X$  is the mass of the exchanged particle in the interaction. However, Eq. 2.4 is only valid for low energies, where it is assumed that the initial scattering occurs from a static source. The lowest-order perturbation theory calculation

---

<sup>2</sup>The Yukawa potential is an electrostatic Coulomb potential in the limit for massive particles

of a fully relativistic treatment instead yields [23, p. 18]:

$$\mathcal{M}(q^2) = \frac{g^2 \hbar^2}{q^2 - M_X^2 c^2} \quad (2.5)$$

where  $q^2$  is the squared four-momentum transfer,  $g$  the coupling strength of the interaction. In general, the momentum exchange contribution (also known as the *propagator*), for a mediator particle of mass  $m$ , is proportional to

$$\frac{1}{q^2 - m^2}. \quad (2.6)$$

The coupling strength is used to define the coupling constant  $\alpha_X$ , which is a dimensionless quantity, generalized to the coupling of an interaction of strength  $g$ :

$$\alpha_X = \frac{1}{4\pi} \frac{g^2}{\hbar c}. \quad (2.7)$$

For electromagnetic interactions, the coupling strength for each interaction vertex is related to the fine-structure constant [23, p. 11]:

$$\alpha_{EM} \equiv \frac{1}{4\pi\epsilon_0} \frac{e^2}{\hbar c} \approx \frac{1}{137}, \quad (2.8)$$

where  $e$  is the elementary charge,  $\epsilon_0$  the permittivity in vacuum,  $c$  the speed of light, and  $\hbar$  Planck's constant. With the coupling constant of the electromagnetic interaction, it is possible to describe the scattering amplitude of the direct photon exchange presented in Fig. 2.2. Letting  $g = e$  for  $\alpha_X$ , and  $m = 0$  for the propagator (photons are massless) the scattering amplitude  $|A|$  can be expressed as:

$$|A| = \bar{\psi}_1(p_1 - q)(-ie\gamma^\nu)\psi_1(p) \frac{-ig_{\mu\nu}}{q^2} \psi_2(p_2 + q)(-ie\gamma^\mu)\psi_2(p_2), \quad (2.9)$$

where  $\psi_{1,2}$  represents the wave function for each electron, (photon emitted from  $\psi_1$ ),  $p_1$  and  $p_2$  the initial momentum for each electron, and  $q$  the momentum transfer of the photon.

Furthermore, the coupling strength can be estimated by measuring the decay rate of  $W^{+-}$  decays into  $e^\pm\nu$ :

$$\Gamma(W \rightarrow e^\pm\nu) \approx 0.223 \pm 0.007 \text{ GeV} \quad (2.10)$$

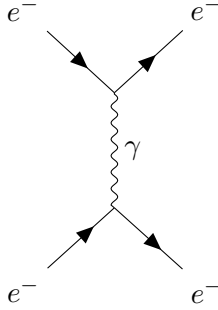


**Figure 2.2:** Simple Feynman diagram of photon exchange in an electron-electron scattering.

This can be related to the weak interaction coupling constant  $\alpha_W$  and the  $W$ -boson mass  $M_W$  (the full derivation can be found in Ref. [23, p. 253]):

$$\Gamma(W \rightarrow e\nu) = 2\alpha_W M_W/3 \quad \rightarrow \alpha_W \approx 0.0042 \approx \frac{1}{236} \quad (2.11)$$

Compared to Eq. 2.8, the electromagnetic interaction is only roughly 1.7x the strength of the weak interaction. The main reason why the weak interaction remains “weak” is due to the massive properties of the propagators; the photon is massless, whereas the mass of  $W^\pm$  is  $80.4 \text{ GeV}/c^2 \pm 0.012$  and the mass of  $Z^0$  is  $91.2 \text{ GeV}/c^2 \pm 0.0021$  [24]. This results in weakly decaying particles being more long-lived, with roughly  $10^7$  longer lifetimes than particles undergoing electrodynamical decays.

### 2.2.1 Screening & Running Coupling Constant $\alpha_{EM}$

In Eq. 2.8, the fine-structure constant is presented as a constant number. However, this is only consistent within a classical picture of the scattering. In QFT, corrections have to be introduced to also accommodate for virtual fermion pair creation-annihilation. In Feynman diagrams, the creation/annihilation of the virtual pairs manifests as loops, illustrated in Fig. 2.3. This means that the coupling constant  $\alpha_{EM}$  is dependent on the momentum transfer  $q^2$ , and one has to account for any and all possible virtual fluctuations to recover the  $1/137$  value of  $\alpha_{EM}$ .

The full derivation of this procedure can be found in Ref. [23, p. 235]. If we measure  $\alpha = 1/137$  for  $q^2 = -k^2$ , and we let each vertex (including the loop



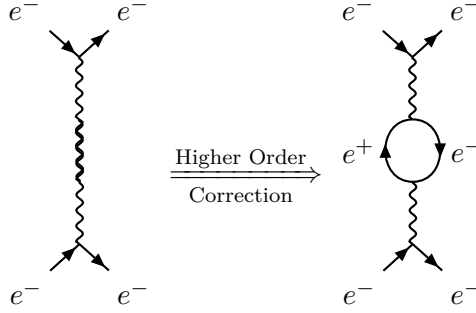


**Figure 2.3:** Illustration of two different Feynman diagrams, where the right figure has created a virtual pair of electrons. The physical amplitude is given by a total sum of all necessary higher-order corrections.

vertices) carry a bare coupling of  $\alpha_0 = e_0^2/4\pi$ , then

$$\alpha_{EM}(k^2) = \frac{\alpha_0}{1 + \frac{\alpha_0}{3\pi} \ln \frac{\Lambda^2}{k^2}} \quad (2.12)$$

which can be solved into a generalized form for  $\alpha_{EM}(q^2)$ , at some given scale  $q^2 = -\mu^2$ :

$$\alpha_{EM}(q^2) = \frac{\alpha(k^2)}{1 + \frac{\alpha(k^2)}{3\pi} \ln \frac{k^2}{q^2}}. \quad (2.13)$$

Due to its momentum dependence,  $\alpha_{EM}(q^2)$  is commonly referred to as a *running coupling constant*. The fact that the strength of the expression in Eq. 2.13 is correlated to  $q^2$ , i.e. increases in  $|q^2|$  lead to increases in  $\alpha_{EM}$ , is quite remarkable. This consequently leads to a screening effect between electrical charges; to illustrate this, imagine a single-loop virtual electron is created in the vacuum. The virtual electron will instantly attract positive charges around it, polarizing the vacuum, illustrated in Fig. 2.4. This vacuum polarization will then screen a passing probe, reducing the electric field of the bare electron charge. So a probe at some distance with a small  $|q^2|$  will be screened by the vacuum polarization, while probes closer to the origin with larger  $|q^2|$  will detect a stronger effective charge, leading to a larger value of  $\alpha_{EM}(q^2)$ . As is discussed in detail in Ref. [21, p. 236], this effect is not negligible. If  $\alpha_{EM}(4M_e^2) = 1/137$ , where  $M_e$  is the electron mass, the corresponding coupling strength for a  $W^\pm$  exchange with mass  $M_W$  is approximately  $1/127$ .

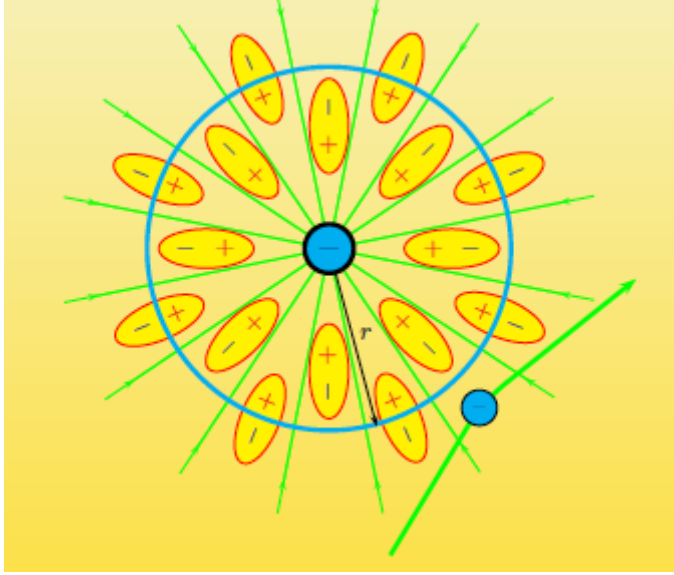


**Figure 2.4:** Illustration of the QED screening effect. A probe far from the origin is screened by the vacuum polarization, while a probe close to the origin will be able to see the original charge. Figure is obtained from Ref. [25].

## 2.3 Quantum Chromodynamics

*Quantum Chromodynamics*, or QCD, is a theory that describes the strong interaction between gluons and quarks. “Chromo” in this case refers to the color charges exchanged between the quarks and gluons. Color in this sense is not an actual transfer of color; similar to electrical charges being characterized by a single integer, positive or negative, color charges are characterized by three such numbers. The quarks carry *red*, *green* or *blue* charges ( $rgb$ ), and the anti-quarks *anti-red*, *anti-green* and *anti-blue* anti-charges ( $\bar{r}\bar{g}\bar{b}$ ). These color charges were originally introduced to satisfy the Pauli exclusion principle for hadron formation, otherwise, the quarks would, in some hadrons, occupy the same quantum state.

Gluons not only mediate the interaction between quarks, but unlike photons, also carry an intrinsic color charge (the photon in this case propagates the electric charge, but does itself not interact electrically). Quarks carry a single color charge, anti-quarks carry anti-color, and gluons always carry both a color and a different anti-color charge simultaneously. This difference leads to some unique interactions for the strong force, which partially explains why it is considered “strong” in the first place.

### 2.3.1 Antiscreening

Analogous to the QED case, to find the coupling constant of the strong interaction  $\alpha_S$  (also referred to in the literature as  $\alpha_3$ ), one has to account for all possible virtual fluctuations and loop corrections that arise from perturbation theory. However, since gluons also carry color charge, they can self-interact when undergoing these virtual fluctuations! This phenomenon is illustrated in Fig. 2.5, in particular in the third diagram, highlighting the gluon self-interaction. Since gluons carry more color charge than quarks, the third diagram contributes more to the coupling strength than the second diagram, which will also contribute to  $\alpha_S$  as screening. Far away from the origin, with a small momentum transfer, a blue color charge is seen concentrated in the quark  $q_b$ . With increasing  $|q^2|$ , one can probe closer to  $q_b$ , although larger  $|q^2|$  introduces larger probabilities for the quark to disassociate, for example through  $q_b \rightarrow q_r + g_{b\bar{r}}$ . For a probe with larger  $|q^2|$ , one would see the blue color charge from the gluon instead of the original quark. As  $|q^2|$  increases, the virtual fluctuations start to dominate. So close to the origin, all the color charge would be concentrated in the gluon, which in turn would make original  $q_b$  behave like a free particle. Analogous to the QED case, this effect is called *antiscreening*, and property of the anti-correlation between  $\alpha_S$  and  $|q^2|$  (higher  $|q^2| \rightarrow$  smaller  $\alpha_S$ ) is referred to as *asymptotic freedom*. The running coupling constant is derived in full in Ref. [21, p. 238], resulting in:

$$\alpha_S(q^2) = \frac{\alpha_S(k^2)}{1 + \frac{\alpha_S(k^2)}{12\pi}(33 - 2n_f)(\ln(-q^2/k^2))} \quad (2.14)$$

where we see that for very large  $|q^2|$ ,  $\alpha_S$  becomes very small.  $\alpha_S(q^2)$  is shown in Fig. 2.6, together with experimental constraints, highlighting the asymptotic feature of the strong interaction.

To properly quantify the strength of the strong interaction, the energy scale  $\Lambda_{\text{QCD}}$  is introduced.  $\Lambda_{\text{QCD}}$  is defined where the denominator of Eq. 2.14 approaches zero, i.e, when  $q = -\Lambda_{\text{QCD}}$ . At this scale, the coupling strength is incredibly strong. Given  $k = 10$  GeV, and  $\alpha_S = 0.2$ ,  $\Lambda_{\text{QCD}}$  turns out to be  $\approx 166$  MeV. At the scale of a few  $\Lambda_{\text{QCD}}$ , the strong force is expected to be strong enough to bind together quarks and gluons to form hadrons [21, p. 239]. This phenomenon is called *confinement*, where at small  $|q^2|$ , the quarks and gluons are confined in hadrons as a color singlet (on a scale of roughly  $k < 1.0$  GeV), but will behave like free particles at larger  $|q^2|$  (small distances inside the hadrons). For proton-proton collisions, this consequently means that at higher energies, the constituent quarks in the protons become more opaque to each

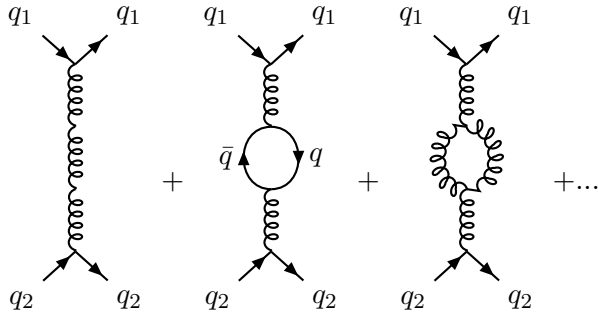


**Figure 2.5:** Illustration of how gluon self-interaction affects the higher order corrections in  $qq \rightarrow qq$  scatterings.

other during the collision.

The QCD interactions can be described through Feynman diagrams at large  $|q^2|$  through a perturbation theory called  $pQCD$ , where higher-order contributions from perturbative calculations are renormalized. The same cannot be said for the confinement region at small  $|q^2|$ . In this regime, non-perturbative techniques have to be applied, as highly non-linear contributions to interactions from several gluons can not be neglected. The strong force at low  $|q^2|$  is approximately  $10^{15}$  GeV/m  $\approx 2 \cdot 10^4$  N<sup>3</sup>.

### 2.3.2 Lattice QCD

Since perturbation theory cannot be applied to calculate the interaction strength of QCD at small  $|q^2|$ , other approaches and techniques have been developed to study and directly calculate the non-perturbative part of QCD. One of the most prolific solutions to this problem is to analyze QCD through lattice gauge theory, also known as *lattice QCD*. Here, the theory is cut-off in momentum transfer, by calculating QCD processes numerically over a lattice with a minimum distance scale. The calculations are extremely computationally demanding, and since the solutions have to be extrapolated to the limit where the distance scale reaches zero. Performing these calculations within a reasonable timeframe requires complex statistical solutions and techniques.

While computationally demanding and non-analytic, lattice QCD has many advantages, as it is not constrained by phenomenological assumptions, but is instead based on first-principle calculations. This has led to a lot of promising results, allowing for a non-perturbative calculation for the equation of state

<sup>3</sup>For a reliable reference, the gravitational force acting on a 1500 kg car is approximately  $\approx 1.5 \cdot 10^4$  N

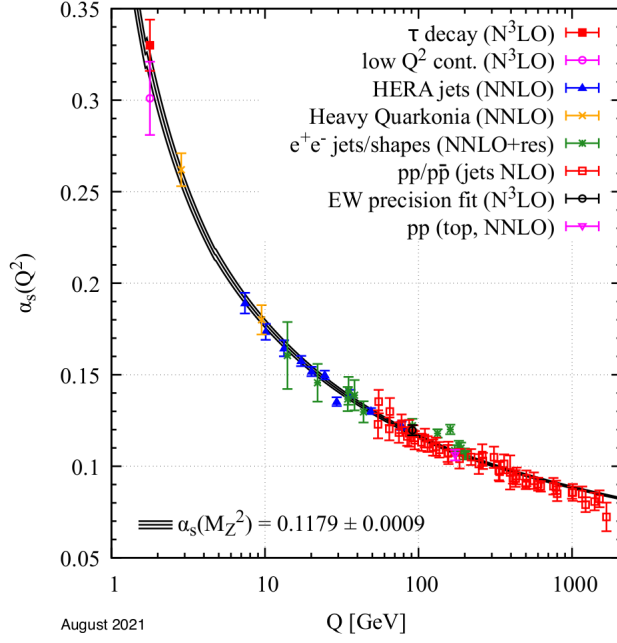


**Figure 2.6:** A diagram of  $\alpha_s$  as a function of  $q^2$ , highlighting the asymptotic freedom of the strong interaction. Points are from different experimental measurements, used to constrain  $\Lambda_{\text{QCD}}$ . Figure is taken from Ref. [26]

(this will be more thoroughly discussed in Sec. 3.2.2), specifying the phases and transitions between different states of quark-gluon matter.



## Chapter 3

# Observables, Heavy-Ion Physics and the Quark-Gluon Plasma

This chapter will cover some basic high-energy physics (HEP) observables and definitions, which are needed to interpret the results contained in this thesis, such as the transverse momentum  $p_T$ , center-of-mass energy  $\sqrt{s}$ , and pseudorapidity  $\eta$ . This will be followed by an introduction to what drives the study of high-energy nucleus–nucleus collisions; The Quark-Gluon Plasma (QGP), as well as the definition and results of observables that are both currently and historically believed to be signatures of the QGP.

While the results in this thesis are from data produced in proton-proton collisions, I think it is important to understand the context of how these results relate to the overall understanding of the QGP. As such, some observables and ideas discussed in this chapter are **not** explicitly required in order to understand the work presented later in this thesis. Such sections are marked with an \*.

## 3.1 Basic observables and quantities

### 3.1.1 Center-of-mass energy $\sqrt{s}$

In a collision, between two particles with masses  $m_A$  and  $m_B$  and momenta  $p_A$  and  $p_B$ , the center-of-mass frame (CM) is defined such that the momenta cancel:  $\vec{p}_A + \vec{p}_B = 0$ . The center-of-mass energy  $s$  in such a frame is Lorentz invariant, and the  $s$  for two colliding beams is expressed as:

$$s \equiv (p_a + p_b)^2 = m_A^2 + m_B^2 + 2(E_A E_B - |\vec{p}_A| |\vec{p}_B|) = (E_A + E_B)^2, \quad (3.1)$$

where  $E_A$  and  $E_B$  are the total energies of the particles  $A$  and  $B$ . For a fixed-target experiment ( $B$  is fixed):

$$s \approx m_A^2 + m_B^2 + 2m_B E_A \quad (3.2)$$

This means that, for two colliding beams (given  $E_A = E_B$ ),  $\sqrt{s} = 2E$ , while  $\sqrt{s} \approx \sqrt{2m_B E_A}$  for a fixed target collisions. Thus, one would require extremely large beam energies in a fixed target experiment to attain the equivalent center-of-mass energy produced in collider experiments.

For pp collisions, the center-of-mass energy is simply defined as  $\sqrt{s}$ , but for heavy-ion collisions it is customary to add a subscript  $\sqrt{s_{NN}}$ , to indicate the center-of-mass energy per nucleus–nucleus pair.

### 3.1.2 Transverse Momentum $p_T$ and Azimuthal angle $\phi$

The *transverse momentum*  $p_T$  is one of the most important observables in HEP. It is defined as the momentum transverse to the beam axis (along the  $z$ -direction). Hence:

$$p_T = \sqrt{p_x^2 + p_y^2}. \quad (3.3)$$

If  $p_T$  is known, the  $x$  and  $y$  components can be found through the *azimuthal angle*, which is the angle that spans over the  $x - y$  plane (illustrated with an  $x - y$  cross-section of the beam in Fig. 3.1).

$$\begin{aligned} p_x &= p_T \cos \phi \\ p_y &= p_T \sin \phi. \end{aligned} \quad (3.4)$$



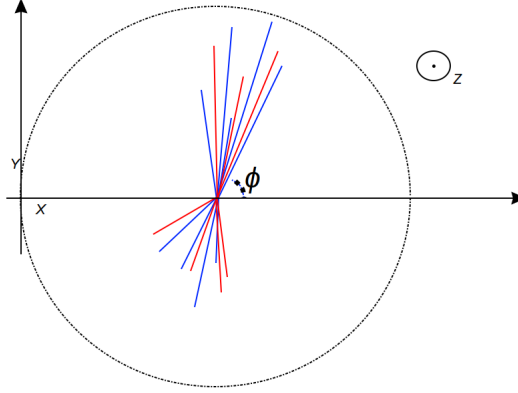


**Figure 3.1:** Illustration of the azimuthal angle  $\phi$ , relative to the beam-axis  $z$ .

Measuring observables and yields as a function of  $p_T$  is prolific within the field, mainly due to the following (non-exclusive) reasons:

- $p_T$  is Lorentz invariant for boosts along the beam direction. This means that the measurement is consistent between different frames, moving along the beam direction.
- Since the partons before the collision will have  $\vec{p} \approx (0, 0, p_z)$ , and  $p_T \approx 0$  before the collision, a non-zero  $p_T$  implies that an interaction occurred, which can give us information about the kinematics of the collision.
- The measurement is a good probe of the virtuality of the partons within the colliding hadrons; a larger  $p_T$  implies a larger momentum transfer  $|q^2|$  on average.

### 3.1.3 Rapidity $y$ and Pseudorapidity $\eta$

The *rapidity*  $y$  is used as a measure instead of the longitudinal velocity since the collisions occur at relativistic energies.  $y$  is additive under Lorentz boosts along the  $z$ -direction (still assuming that  $z$  is along the beam-axis), and is defined as [27, p. 27]:

$$y = \frac{1}{2} \ln \frac{E + p_z}{E - p_z} = \operatorname{arctanh} \frac{p_z}{E} \quad (3.5)$$

where  $E$  is the energy of the particle, and  $p_z$  the momentum along the beam-axis. One can easily see that this quantity is additive in Eq. 3.6, by boosting

along  $z$  axis, by an amount  $b$ , such that  $E_{boost} = E \cosh b - p_z \sinh b$  and  $p_{z_{boost}} = p_z \cosh b - E \sinh b$ , then:

$$\begin{aligned} y_{boost} &= \frac{1}{2} \ln \frac{E_{boost} + p_{z_{boost}}}{E_{boost} - p_{z_{boost}}} \\ &= \frac{1}{2} \frac{(E + p_z)(\cosh b - \sinh b)}{(E - p_z)(\cosh b + \sinh b)} \\ &= y + \frac{1}{2} \ln \frac{e^{-b}}{e^b} = y - b. \end{aligned} \quad (3.6)$$

Since it can be experimentally challenging to measure  $E$  for any given particle track (since it is dependent on particle mass, and therefore requires the particle to be identified), it is more practical to define the quantity *pseudorapidity*:

$$\eta = \frac{1}{2} \ln \frac{|\mathbf{p}| + p_z}{|\mathbf{p}| - p_z} = -\ln \tan \frac{\theta}{2}, \quad (3.7)$$

where  $\theta$  is the *scattering angle*; the angle to the beam-axis  $z$ . An illustration of how  $\eta$  evolves with  $\theta$  is shown in Fig. 3.2.

For the massless limit,  $E = |\mathbf{p}| = p$ , so rapidity and pseudorapidity become identical. In the massive limit, the relationship between  $\eta$  and  $y$  is more complex: [27, p. 28]:

$$y = \frac{1}{2} \ln \left( \frac{\sqrt{m_T^2 \cosh^2 \eta + m^2} + p_T \sinh \eta}{\sqrt{m_T^2 \cosh^2 \eta + m^2} - p_T \sinh \eta} \right) \quad (3.8)$$

Together with Eq. 3.8, it is possible to construct a relationship (the Jacobian transformation) between the  $y$  and the  $\eta$  distributions of charged particles:

$$\frac{d^2 N}{d\eta dp_T} = \frac{|\bar{\mathbf{p}}|}{E} \frac{d^2 N}{dy dp_T} \quad (3.9)$$

At *midrapidity*, where  $y \approx \eta \approx 0$ , particle production is mainly dominated by particles produced in the collision. In the context of this thesis, and ALICE publications in general, midrapidity will refer to  $|\eta| < 0.8$  (this will be discussed in further detail in Sec. 5.2.3).

At midrapidity, Eq. 3.9 can be simplified into the following expression:

$$\left. \frac{d^2 N}{d\eta dp_T} \right|_{\eta=0} = \frac{p_T}{m_T} \left. \frac{d^2 N}{dy dp_T} \right|_{y=0} \quad (3.10)$$

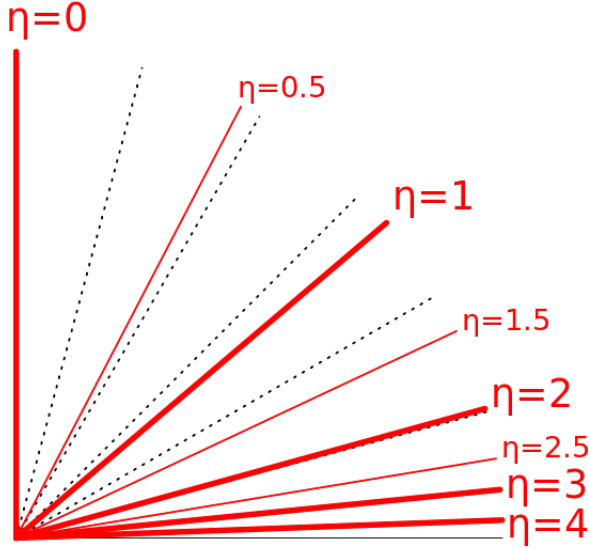


**Figure 3.2:** Illustration of the relationship between the pseudorapidity  $\eta$  and the scattering angle  $\theta$ . Dashed curves represent the scattering angle in integers of  $15^\circ$ . Figure is taken from Ref. [28].

Experimentally, for identified particles, event selection is imposed by either constraining rapidity or pseudorapidity. The Jacobian transformation highlighted in Eq. 3.10 is then used to carry over particle spectra between the two different phase spaces.

### 3.1.4 Centrality and Multiplicity

The *centrality* of an event refers to the geometric overlap between two colliding nuclei. If the beam direction is along the  $z$ -axis, the overlap is characterized by the impact parameter  $b$ , the transverse distance between the two ion centers in the  $x - z$  plane (also known as the *reaction plane*). The impact parameter can be utilized in simulations to estimate the number of *participants*  $N_{\text{part}}$ , nucleons that partake in the collision, and the number of *spectators*  $N_{\text{spec}}$ , nucleons that will not interact. A visualization of these quantities can be seen in Fig. 3.3.

It is important to note that, even though the nuclei selected for nucleus–nucleus collisions can be spherical (which is the case for lead nuclei)<sup>1</sup>, they are not spher-

---

<sup>1</sup>This is determined by the nuclear electric quadrupole moment  $Q$ , where a zero value of  $Q$  implies that the outermost shell of the nucleus is closed.

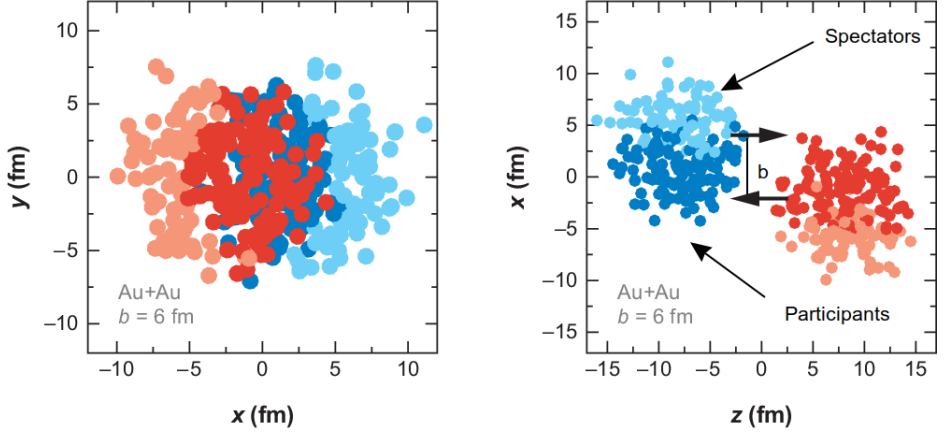


**Figure 3.3:** Illustration of the reaction plane in the  $x - y$  (left panel) and  $x - z$  (right panel) planes, with the impact parameter  $b$ , showing the shape of two gold nuclei right before the collision. The original figure is taken from Ref. [29] and then modified by me.

ical along the beam-axis. This is due to Lorentz contraction, which compresses the spherical nuclei into flat disks along the beam axis.

In pp collisions, it is difficult to formalize a robust definition for centrality. Instead, charged particle *multiplicity* is used to estimate the activity of a collision, which is simply a measurement of the amount of primary charged particles that are produced in the event.

## Glauber Modelling

Due to the small distances (in the order of several fm), it is impossible to directly measure  $N_{\text{part}}$  and  $N_{\text{part}}$  in each event. Experimentally, centrality is defined based on the multiplicity and is given in percentiles, e.g., 0-10% (90-100%) means the 10% of events with the largest (smallest) multiplicity. The number of participants is then estimated by a *Glauber* parameterization to the spectra of produced charged particles. The Glauber model is a geometrical model that describes the collision processes between different nuclei in a nucleus–nucleus collision. The model is implemented through a Monte-Carlo (MC) framework, to compute collisions and nuclei interactions event by event. The Glauber formalism relies on two important assumptions:

- The Glauber model is based on the *eikonal* approximation [30] assuming

that the different nuclei travel in straight lines before the collision, where  $\vec{p} \approx (0, 0, p_z)$ , with negligible interchange of transverse momenta.

- Following the eikonal approximation, and the Lorentz contraction due to the nuclei traveling at relativistic speeds, it is assumed that each nucleon-nucleon collision is independent. Therefore, the entire nucleus-nucleus collision can be treated as a superposition of several nucleon-nucleon sub-collisions.

The Monte-Carlo implementation<sup>2</sup> of the Glauber model simulates two nuclei by stochastically populating the nucleon density in each nucleus [32]. The position of each nucleon is estimated through a functional form of the nuclear Woods-Saxon distribution  $\rho(r)$ :

$$\rho(r) = \rho_0 \left( \frac{1 + w(r/R)^2}{1 + \exp(\frac{r-R}{a})} \right), \quad (3.11)$$

where  $\rho_0$  is the nucleon density,  $R$  the radius of the nucleus (estimated for spherical nuclei by the number of nucleons  $A^{1/3}$ ,  $w$  a parameter which accounts for asymmetrical nuclei, where the maximum density is reached at  $r > 0$ , and  $a$  the nucleon skin thickness, describing how quickly the density falls off towards the edge of the nucleus radii. The Woods-Saxon distribution in Eq. 3.11 can only describe the population density of large, spherical nuclei.

Once the two nuclei are populated, nucleons are assumed to collide if the distance  $d$  between the transverse centers is smaller than the distance of the corresponding, inelastic nucleon–nucleon cross-section<sup>3</sup>  $\sigma_{\text{NN}}^{\text{inel}}$  [32]:

$$d = \sqrt{\sigma_{\text{NN}}^{\text{inel}}/\pi} \quad (3.12)$$

Finally,  $N_{\text{coll}}$  is estimated by counting the number of binary nucleon collisions, and  $N_{\text{part}}$  is determined by counting the number of nucleons that experience one or more collisions.

Once the Glauber modeling is complete, it is coupled to a negative binomial distribution (NBD)  $P_{\mu,k}(N_{\text{ch}})$  to parameterize the amount of produced charged particles  $N_{\text{ch}}$ . The usage of an NBD is motivated through the assumption that

---

<sup>2</sup>This is slightly different from the analytical expression from the total inelastic cross-section derived for the optical limit, see Ref. [31] for details.

<sup>3</sup>This value is extracted from interpolations of pp collisions at different  $\sqrt{s}$  [33].

the initial state of a nucleus–nucleus collision can be treated as a sum of individual minimum bias<sup>4</sup> pp collisions. The NBD is defined as:

$$P_{\mu,k}(N_{\text{ch}}) = \frac{\Gamma(N_{\text{ch}} + k)}{\Gamma(N_{\text{ch}} + 1)\Gamma(k)} \frac{(\mu/k)^{N_{\text{ch}}}}{(\mu/k + 1)^{(N_{\text{ch}}+k)}} \quad (3.13)$$

The charged particle distribution is then assumed to be:

$$P_{\mu,k}(N_{\text{ch}}) \times (fN_{\text{part}} + (1 - f)N_{\text{coll}}), \quad (3.14)$$

where  $f$  is a free fit parameter, used to control the fractional contribution from processes that scale with  $N_{\text{part}}$  and  $N_{\text{part}}$ , respectively. The entire NBD-folded Glauber distribution is then fitted to experimental data. Figure 3.4 shows the comparison between the amplitude of energy deposited by charged particles at forward-rapidities<sup>5</sup> and a combined MC Glauber-NBD fit. A good agreement is found between the measured data and the combined Glauber-NBD parametrization, which allows  $N_{\text{part}}$  to be extracted from the Glauber simulation for the percentiles, represented by the sectioned areas in Fig. 3.4.

## 3.2 QCD Phase Transitions & The Quark-Gluon Plasma

As discussed previously in Sec. 2.3, quarks and gluons are confined within hadrons, due to the large value of  $\alpha_S$  at small  $|q^2|$ . However, by increasing the energy density and pressure around the hadrons,  $\alpha_S$  could hypothetically decrease, allowing the quarks and gluons inside to be deconfined. This would then cause a *phase transition*, from confined hadrons into a coherent, strongly interacting medium. This medium is commonly referred to as the *quark-gluon plasma*<sup>6</sup> (QGP) [34].

Either a sufficiently high temperature or particle density (often expressed through the baryon chemical potential,  $\mu_B$ ) is required to induce the phase transition from confinement into a QGP. A sketch of the QCD phase diagram is illustrated in Fig. 3.5, showcasing the different phase transitions from the confinement to a QGP. The first-order transition is analogous to a thermodynamic transition of water to steam; at first, the temperature of the water will increase proportionally to the energy deposited into the system. However, if the temperature reaches the boiling point, the water will phase transition into steam. At this

---

<sup>4</sup>These are collisions recorded by the detector with the minimal possible trigger bias.

<sup>5</sup>Refer to Sec. 5.2.1 for more information regarding the V0 detectors.

<sup>6</sup>A “Plasma” refers to a gas of free, charged particles.

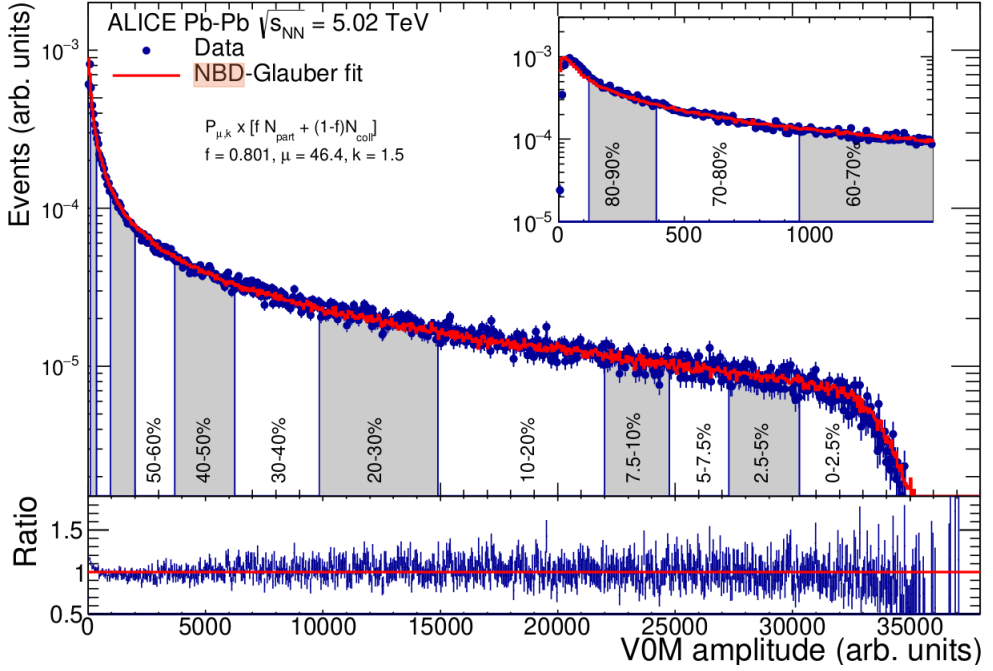


**Figure 3.4:** A measurement of the VOM amplitude (charged particle density at forward rapidities), in Pb-Pb collisions at  $\sqrt{s_{NN}} = 5.02$  TeV. The data is compared to a combined NBD-Glauber fit, where the marked percentiles represent the equivalent centrality limits. Results are taken from Ref. [32]

point, energy is required to convert the water into steam, and thus the temperature of the steam will plateau as a function of energy until all the available water has transitioned into steam. The temperature of the steam will only rise once the full phase transition has taken place.

From lattice QCD calculations, one can predict a transition between a gas of hadrons at  $\mu_B = 0$ , into a QGP. However, this transition does not behave like a thermodynamic singularity [35], but instead has a smooth transition, through a crossover between the phases. In the water/steam analogy, this transition would allow the temperature of the medium to increase simultaneously as the phase transition occurs.

The two aforementioned phase transitions are sketched in Fig. 3.5, where the dotted line represents the boundary for the crossover transition, and the solid line the thermodynamic singularity. Consequently, there has to be a point in the phase diagram where the two competing phase transitions switch (“a transition in the order of the phase transitions”). This point is referred to as the *critical point*. The precise value of the critical point is a hotly debated topic within the field. Around the critical point, it is currently hypothesized that there is a

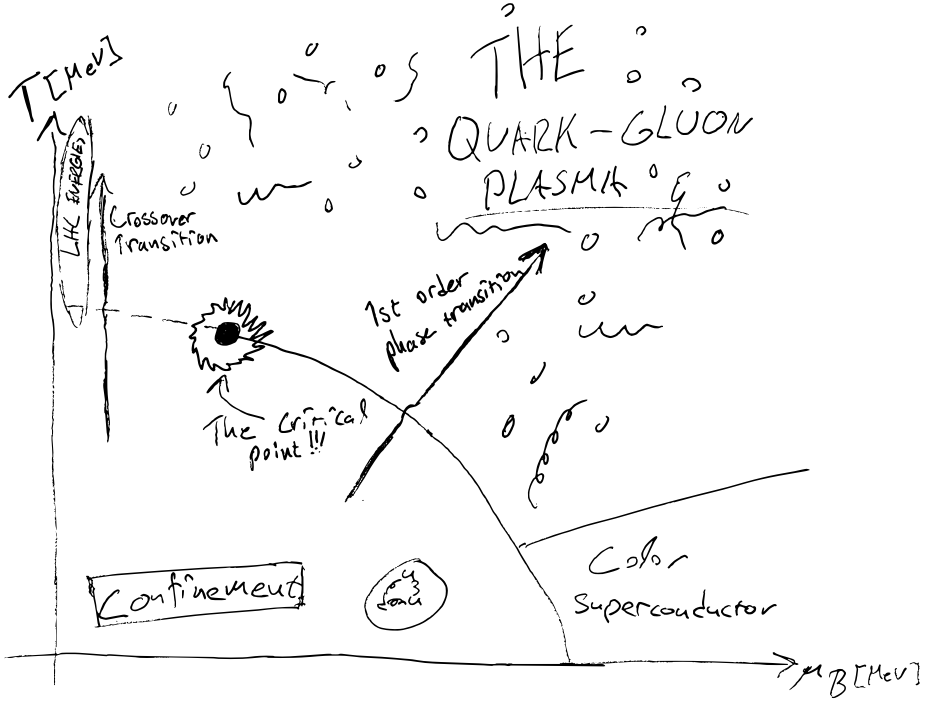


**Figure 3.5:** Artistic rendition of the QCD phase diagram, showcasing the different states of QCD matter, and the different phase transitions.

2nd order phase transition before criticality is reached, and the crossover occurs. The characteristic behavior of the three different phase transitions mentioned can be seen sketched out in Fig. 3.6.

### 3.2.1 \*Non-Zero Baryon Chemical Potential $\mu_B$

The baryon chemical potential  $\mu_B$  gives a measure of the balance between baryons and anti-baryons produced in a collision.  $\mu_B = 0$  means that there is an equal amount of baryons and anti-baryons, while  $\mu_B > 0$  indicates an overabundance of baryons.

Due to collision kinematics,  $\mu_B$  can be rapidity dependent; baryons and anti-baryons produced in the collision will be created in balance (the baryon number is conserved), and the main particle production will occur at midrapidity



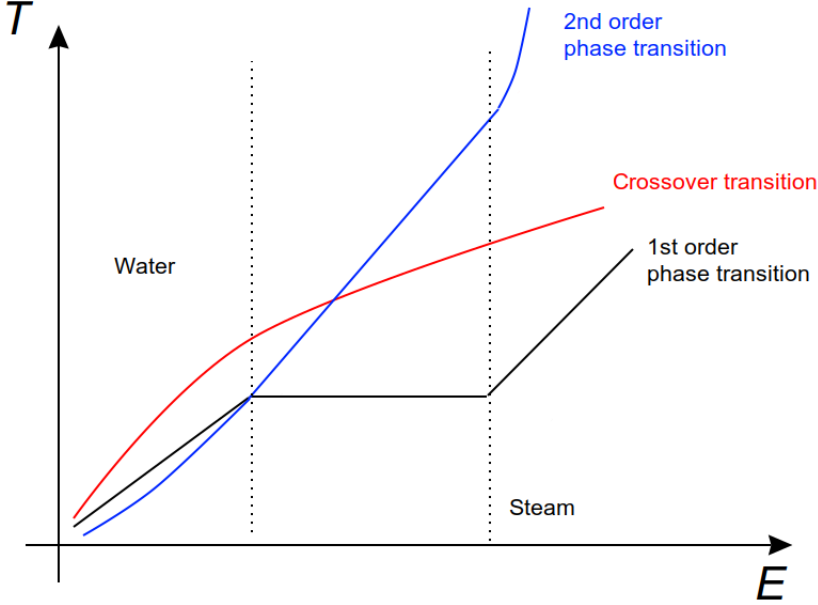


**Figure 3.6:** Sketch illustrating the characteristic behaviors of the different phase transitions between solid and gaseous states.

( $y \approx 0$ ). However, the stopped<sup>7</sup> *primordial baryons* (protons and neutrons from the original ions) will also contribute to  $\mu_B$ , leading to a net-positive  $\mu_B$ . The produced particles contribute mainly to  $\mu_B$  at midrapidity but would taper off at increasing rapidities, where contributions to  $\mu_B$  are dominated by primordial baryons. This feature can be seen in Fig. 3.7, where the net-proton yield (i.e., antiproton-to-proton difference) is plotted as functions of rapidity for Au+Au collisions at  $\sqrt{s_{NN}}$  200 GeV measured by the BRAHMS collaboration at RHIC [36]. There is a clear rapidity dependence for the ratio, as expected from the above discussion.

The rapidity dependence of  $\mu_B$  goes hand-in-hand with a center-of-mass energy dependence of the colliding beams. At SPS energies, the energy is low enough to make the colliding particles almost reach a full stop. However, at top RHIC and LHC energies, particles (either protons or ions) are colliding at such high energies that they penetrate each other. Therefore, the primordial baryons will end up at large rapidities, while the particles at midrapidity will all have been produced in the collision, and therefore  $\mu_B \approx 0$ . This is sketched out in Fig. 3.8, where the high-energy (red) protons will pierce through and leave an open rapidity gap solely dominated by newly produced particles, while the

<sup>7</sup>Baryons with rapidity near beam rapidity

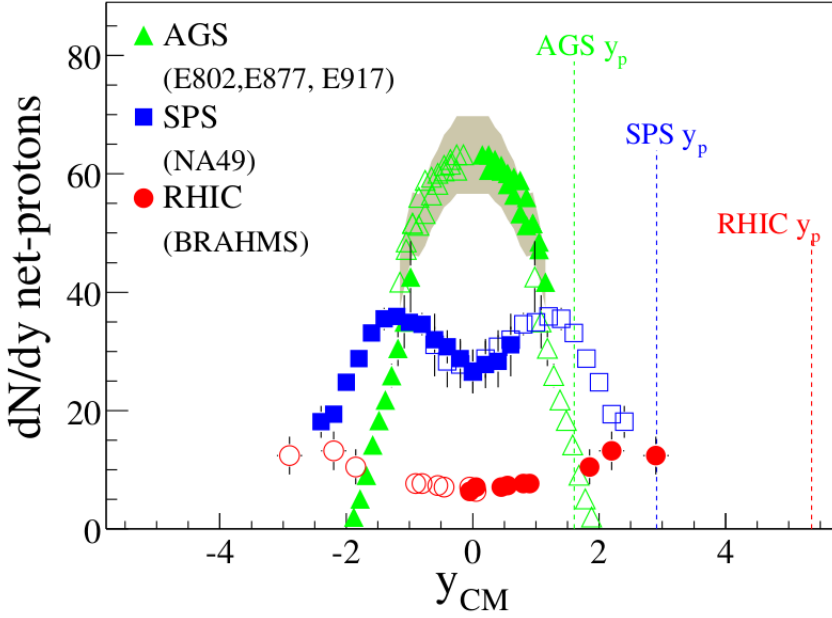


**Figure 3.7:** The net-proton yield plotted as a function of rapidity, for top-5% central Au+Au collisions at  $\sqrt{s_{NN}}$  200 GeV measured at the BRAHMS experiment, Pb+Pb collisions at  $\sqrt{s_{NN}}$  17 GeV measured at the SPS, and Au+Au collisions at  $\sqrt{s_{NN}}$  5 GeV measured at the AGS. Results are taken from Ref. [36]

low-energy (blue) packets will come to a stop, contaminating the mid-rapidity region with primordial baryons.

### 3.2.2 Quark-Gluon Plasma Characteristics

Even though the confining part of the QCD potential within a QGP is weak enough to allow for quarks and gluons to separate, the QGP itself is strongly interacting. This means that there will be partonic interactions within the QGP. In this sense, the quarks and gluons are not “free”, but instead *deconfined*.

Lattice QCD is able to provide strong predictions concerning the properties of deconfinement and the QGP. By calculating the energy density and pressure, relative to the temperature of a hadronic gas, one can see a clear transition in the equation of state, between confined matter into a deconfined QGP. This is presented in the left panel for Fig. 3.9, highlighting that the critical temperature  $T_c$ , which is the temperature required for the phase transition to occur, is predicted to be  $T_c \approx 145 - 150$  MeV. Figure 3.9 also presents the entropy density, which is obtained by combining the results for pressure and energy density, also

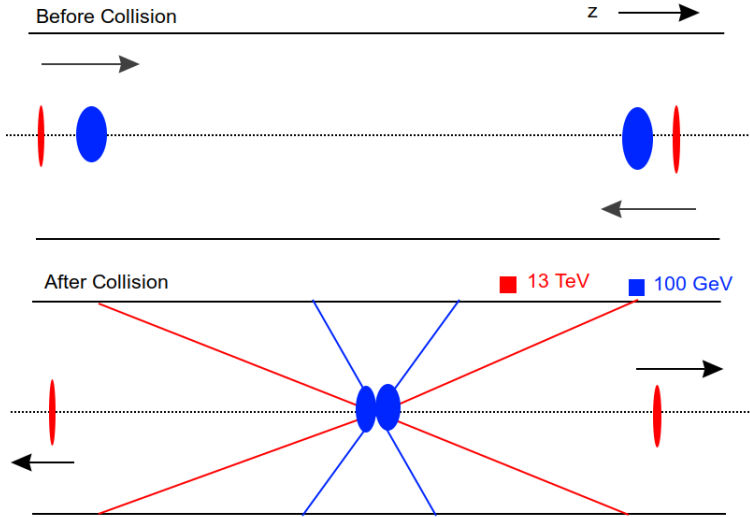


**Figure 3.8:** A rough sketch of why  $\mu_b$  is both rapidity and center-of-mass energy-dependent.

consistent with a change in the equation of state between  $T_c \approx 145 - 150 \text{ MeV}$ .

Furthermore, lattice QCD calculations can predict the QCD color screening (see Sec. 2.3.1 for details), highlighting that the strong interaction range (consequently, the level of deconfinement) is inversely proportional to the temperature of the system [37]. This is demonstrated in Fig. 3.10, which presents the free potential energy of static, heavy quark-antiquark pairs, as a function of the temperature, which is measured in fractions of the critical temperature  $T_c$ . The interaction range is suppressed for higher temperatures, with a drastic change in range when crossing the boundary of  $T_c$ , suggesting that the spatial quark-antiquark correlations are more diluted [37].

As the QGP is a very complex system, it is easier to build up an understanding of the QGP by categorizing the interactions into different *length scales*. The different length scales are illustrated in Fig. 3.11, where  $1/T$  corresponds to the average distance between two partons in the medium, and  $g$  proportional to the coupling strength<sup>8</sup>. Perturbative QCD calculations can describe interactions at extremely small length scales of  $l < 1/T$ . QCD calculations at finite temperature can be used to estimate particle dynamics at  $\approx 1/gT$ , the non-perturbative processes will dominate around  $\approx 1/g^2T$ , which are estimated through lattice QCD calculations. At scales of  $l \approx 1/g^2T$ , the partons will have soft collisions with small  $|q^2|$ , and at length scales of  $l \approx 1/g^4T$ , one has to account for hard col-

<sup>8</sup>As defined in Sec. 2.3,  $g = \sqrt{\alpha 4\pi}$ , where  $\alpha$  is the coupling constant.

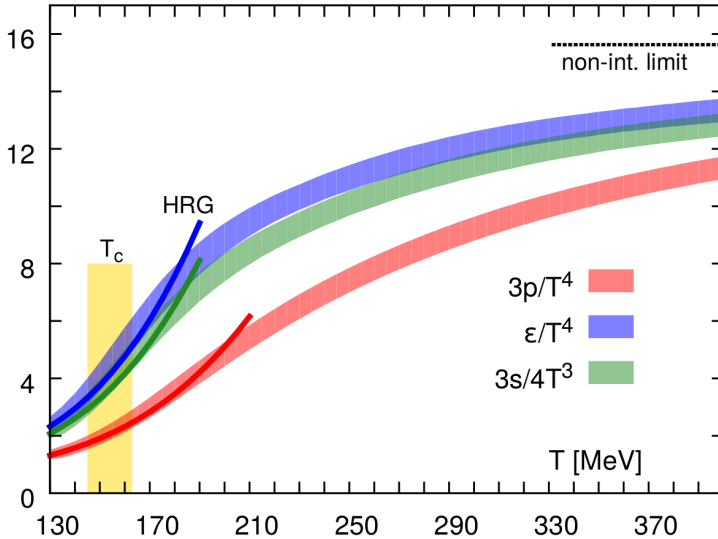


**Figure 3.9:** (Left panel): Lattice QCD calculations of the energy density (blue curve), three times pressure (red curve), and the entropy density (green curve). All three measurements are compared with an equivalent hadron-resonance gas (HRG), represented by the thinner curves. All three curves are consistent with a phase transition between  $T_c \approx 145 - 150 \text{ MeV}$ . Results are obtained from Ref. [38]

lisions with large momentum transfer through the Boltzmann equation. Lastly, a hydrodynamic description is required to gain a meaningful understanding of the QGP dynamics at large length-scales of  $l \gg g^4 T$  [40].

At the hydrodynamic length scales, it is possible to estimate the shear viscosity of the medium itself. This is done through a conjecture called Anti-de-Sitter/Conformal Field Theory (AdS/CFT). The theory is a rough approximation, as it assumes a scale-free theory (which is not the case for QCD, as it requires a  $\Lambda_{\text{QCD}}$ ), and large coupling strengths. While the underlying workings of this theory are very complicated and well outside the bounds of this thesis (more in-depth information can be found in Ref. [41]), it has led to some remarkable “postdictions” regarding transport properties of the QGP. Through the conjecture, the QGP is predicted to behave like an almost-ideal fluid (incompressible, with close to zero viscosity), where the relative shear viscosity  $\eta$  to volume entropy density  $s$  can be estimated as [42]:

$$\frac{\eta}{s} \geq \frac{\hbar}{4\pi k_B} \approx 6.11 \times 10^{-13} \text{ s K} \quad (3.15)$$

To highlight how small the estimated  $\eta/s$  for the QGP is, the  $\eta/s$  in water, at

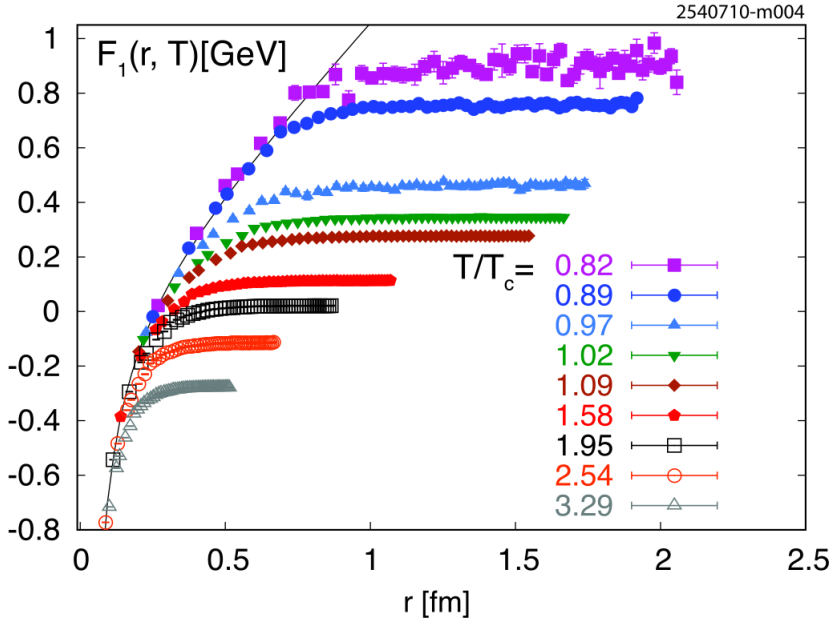


**Figure 3.10:** Lattice QCD calculation of the energy potential of heavy quark-antiquark pairs, highlighting how the interaction range of QCD is inversely proportional to the temperature. Figure taken from Ref. [39]

300K of the order of 10s K. Hence, the QGP appears to be “the most perfect liquid” in the known Universe [43].

### 3.3 Signatures of the Quark-Gluon Plasma

As discussed in Sec 3.2, the QGP is an extremely hot and dense medium that is very short-lived. Therefore, secondary probes and signatures are required to access information about the QGP, deconfinement, and the initial stages of the collision. This section will present a non-exhaustive list of different measurements, both historically and contemporary, that are used to demonstrate the formation of a QGP.

#### 3.3.1 Strangeness Enhancement

The increased production of hadrons containing strange quarks was one of the first proposed signatures of the QGP [18]. The idea proposed was that strangeness abundance would saturate for a sufficiently excited QGP. The soft produc-

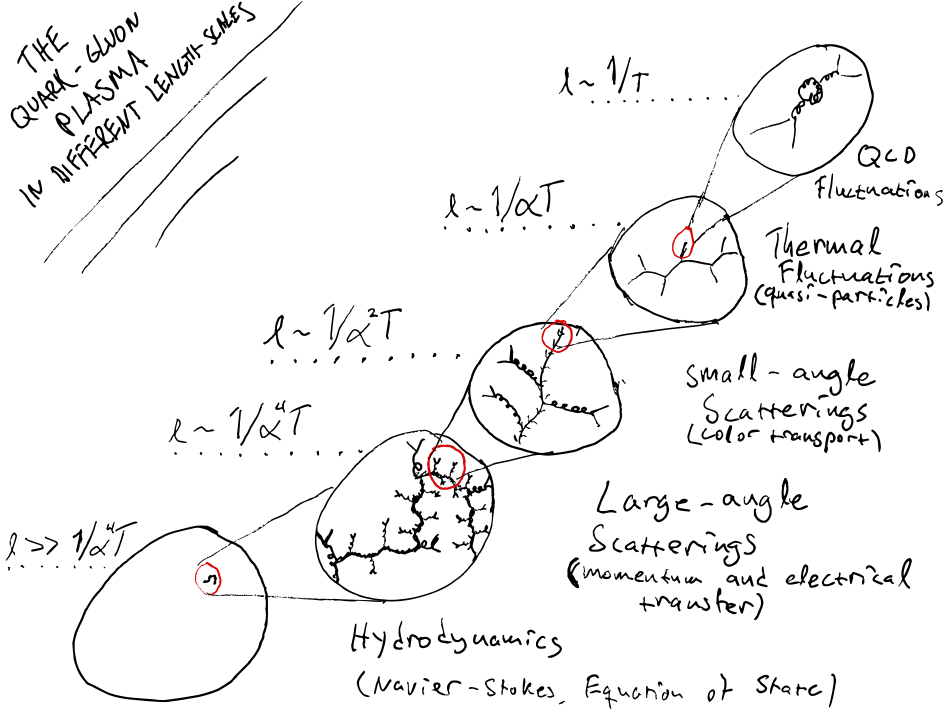


**Figure 3.11:** Rendition of QGP interactions broken down into different length-scales.  $1/T$  represents the typical distance between two partons, where  $\alpha$  is the interaction strength.

tion of strange (and heavier) particles in a hadron gas is suppressed, as QCD requires large confinement energies to bind the heavier quarks<sup>9</sup>. This is not of importance in a QGP, given that quarks and gluons are deconfined, where the production is only dictated by the masses of the constituent quarks. Furthermore, as is shown in Ref. [44], given the conditions of a QGP, the production rate of  $q\bar{q} \rightarrow s\bar{s}$  is expected to increase at a much faster rate as a function of temperature, compared to the lighter quarks produced through gluon splittings  $g\bar{g} \rightarrow q\bar{q}$ . This would in turn increase the production of rare, multi-strange hadrons, which could be used as indicators for the formation of a QGP.

One could also consider strangeness enhancement through the thermal production of hadrons from the QGP. If a QGP were to be formed in a collision,

<sup>9</sup>This can be illustrated with the  $\phi$  meson, where the sum of the constituent strange quarks is  $\approx 200 \text{ MeV}/c^2$ , whereas the mass of a  $\phi$  meson is in the order of  $\approx 1 \text{ GeV}/c^2$ .

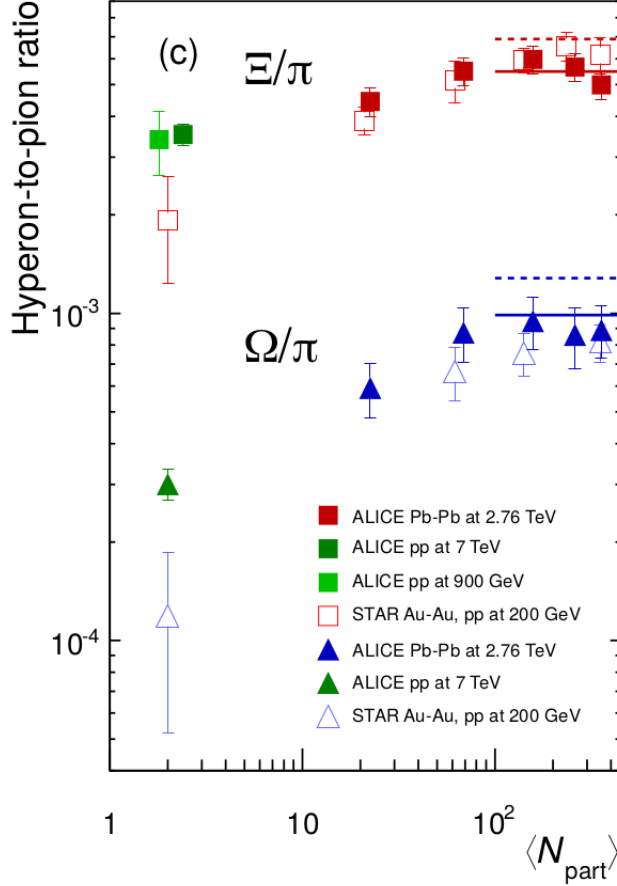


**Figure 3.12:**  $\Xi/\pi$  and  $\Omega/\pi$  ratios presented as a function of  $\langle N_{part} \rangle$  for Pb-Pb collisions at  $\sqrt{s_{NN}} = 2.76$  TeV and Au-Au collisions at  $\sqrt{s_{NN}} = 0.2$  TeV for ALICE and STAR respectively. Results are obtained from Ref. [45].

one would expect hadrons to follow a statistical thermal distribution. The thermal yields would not be suppressed by the quark mass but rather dictated by the hadron mass, implying a comparable production rate of non-strange and multistrange particles with similar masses. This is in contrast to most QCD-inspired models of hadronization, where strangeness production is exponentially suppressed (by the quark mass). Consequently, measuring the relative strange-to-nonstrange hadron yields becomes a good experimental probe of the QGP. These two different paradigms are explored in further detail in Chapter 4.

Experimentally, the yields of strange hadrons are normally compared to the amount of produced pions ( $\pi^+ + \pi^-$ ). A potential abundance of strange particles is referred to as *strangeness enhancement*. Both LHC and RHIC have observed

strangeness enhancement in heavy-ion collisions. Fig. 3.12 highlights that the relative yields of multistrange<sup>10</sup> hadrons  $\Xi$  and  $\Omega$  are larger in heavy-ion collisions, compared to a minimum bias pp baseline. The enhancement also grows as a function of centrality, estimated by the average number of  $N_{part}$ . This effect seems to be largely independent of collision energies and is observed by both the STAR and ALICE collaborations. In both instances, the enhancement increases with the strange quark content of the baryons. The centrality dependence of the enhancement is in agreement with (but does not necessarily prove) the potential formation of an equilibrated QGP. Since more central collisions would have larger temperatures, they would also have better conditions for forming a QGP.

### 3.3.2 \*Quarkonium Suppression

Quarkonia (mesons that are flavor neutral) suppression is one of the most convincing signatures of deconfinement, which I will describe in the following. Let us first consider the production of an upsilon  $\Upsilon$  meson, which consists of a pair of  $b\bar{b}$  quarks. Given the mass of a  $b$  quark, the probability to produce a  $b\bar{b}$  pair in the initial hard scattering is extremely rare, ideally having zero or one  $b\bar{b}$  pair produced per nucleus–nucleus collision [6]. Furthermore, the  $\Upsilon$  can be produced in three different spin states (1S, 2S, 3S), each with different binding energies. The  $\Upsilon$  (1S) state is the most tightly bound of the three states, which has a size smaller than an ordinary hadron. Even if immersed in a QGP, the confining part of the QCD potential for  $\Upsilon$  (1S) is strong enough for it to potentially remain bound as a  $b\bar{b}$  pair [6]<sup>11</sup>. However, this does not hold for the  $\Upsilon$  (2S, 3S) states, due to anti-screening, and the melting of the QCD potential for heavy quarks shown in Fig. 3.10. For these weakly bound states, the screening from the QGP is strong enough to prevent the  $b\bar{b}$  pair from attracting each other, which consequently leads to the quarks drifting apart, dissolving the hadron. This is especially true for the  $\Upsilon$  (3S), which is comparable to the size of an ordinary hadron [6].

This effect is demonstrated when comparing the production of  $\Upsilon$  (1S, 2S, 3S) between nucleus–nucleus and pp collisions. Figure 3.13 presents results of  $\Upsilon$  production, by reconstructing the invariant mass of muon-pairs, from Pb–Pb and pp collisions at  $\sqrt{s_{NN}} = 5.02$  TeV and  $\sqrt{s} = 13$  TeV, respectively. Here, one can see that the production rates of  $\Upsilon$  (1S), which is the largest

---

<sup>10</sup>“Multistrange” refers to consisting of multiple strange quarks.

<sup>11</sup>While more resilient than the weaker  $\Upsilon$  (2S,3S) spin states, experimental observations have shown that  $\Upsilon$  (1S) production is suppressed in Pb–Pb collisions, see Ref. [46] for details



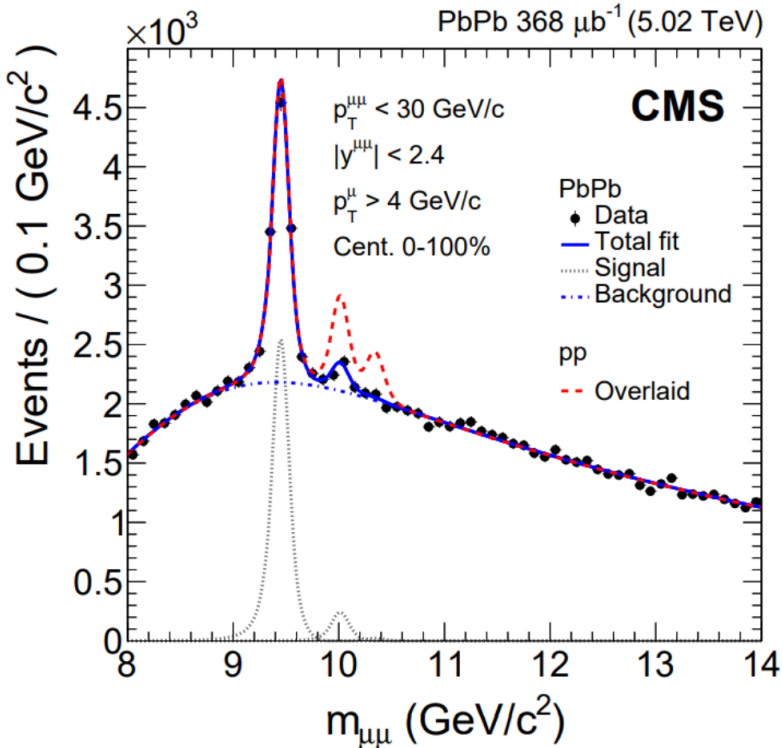


**Figure 3.13:** The invariant mass of muon pairs, which reconstruct the yields of the  $\Upsilon$  (1S, 2S, 3S) states, measured by CMS in Pb–Pb collisions at  $\sqrt{s_{NN}} = 5.02$  TeV. One can note that the more weakly bound  $\Upsilon$  (2S, 3S) states are suppressed, with respect to the equivalent pp yield. See text for more details. Results are obtained from Ref. [47].

peak shown in the figure<sup>12</sup>, for both pp and Pb–Pb collisions. However, the productions of  $\Upsilon$  (2S, 3S) are clearly suppressed, with the (3S) state completely vanishing, in Pb–Pb collisions, with respect to pp collisions. This is interpreted as the formation of a QGP in central Pb–Pb collisions, which melts and diffuses the weakly bound  $\Upsilon$  states.

### 3.3.3 Flow

So far, the discussion of the QGP has been in the context of a stationary thermal source. However, this is most likely an oversimplified view of the QGP. Evidence suggests that the medium itself is expanding during its evolution. Massive

<sup>12</sup>This figure can be misleading; The production of  $\Upsilon$  1(S) is suppressed in heavy-ion collisions. In Fig. 3.13, the pp data is normalized to the Pb–Pb peak, to highlight the relative suppression between different  $\Upsilon$  states in the two systems

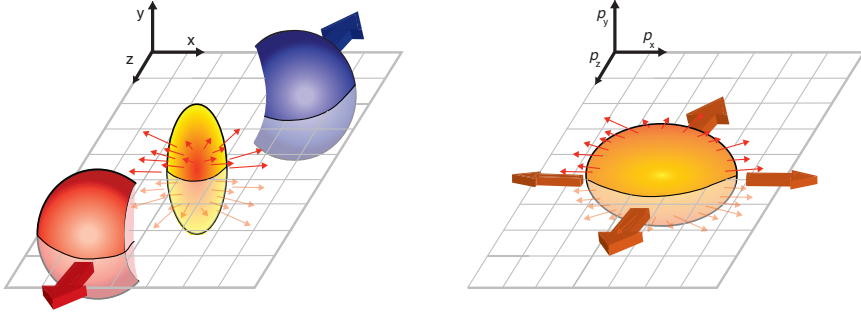


**Figure 3.14:** Illustration of the coordinate and momentum anisotropy that creates elliptic flow. The figure is obtained from Ref. [48].

hadrons that interact with the QGP will be collectively affected by the expansion, generating what is referred to as *flow*. This section will discuss how the expansion of the medium can be studied through both anisotropic and radial flow.

### \*Anisotropic Flow

Anisotropic flow is a natural consequence of a hydrodynamical expansion developing from a non-uniform geometry. This is best described by a characteristic oval ellipsoid (often referred to as an “almond shape”) collision geometry along the reaction plane, illustrated in Fig. 3.14. At initial times, the almond-shaped reaction zone will have asymmetric pressure gradients; anisotropy in coordinate space leads to anisotropy in momentum space. The gradients along the  $z - x$  plane will be much stronger than along the  $y$  direction. This will start to drive an expansion in the  $z - x$  plane. This process is self-attenuating; once the pressure gradients along  $z - x$  are weakened, the expansion is already well underway. Therefore, the spatial anisotropy will be converted into a momentum anisotropy. This phenomenon is referred to as *anisotropic flow*.

Anisotropic flow can be generalized by Fourier decomposition along the event plane  $\Psi_n$ , utilizing the total particle distribution:

$$\frac{E d^3 N}{d p^3} = \frac{1}{2 \pi p_T} \frac{d^2}{d p_T d \eta} \left( 1 + \sum_{n=1}^{\infty} 2 v_n \cos(n(\phi - \Psi_n)) \right) \quad (3.16)$$

$v_n$  in Eq. 3.16 is the coefficient for the different *flow harmonics*. The harmonics

represent types of different anisotropic flow, each sensitive to fluctuations in different ways. The elliptic flow discussed previously is characterized by the 2nd harmonic,  $v_2$ , and shapes up to the fifth harmonic are illustrated in Fig. 3.15.

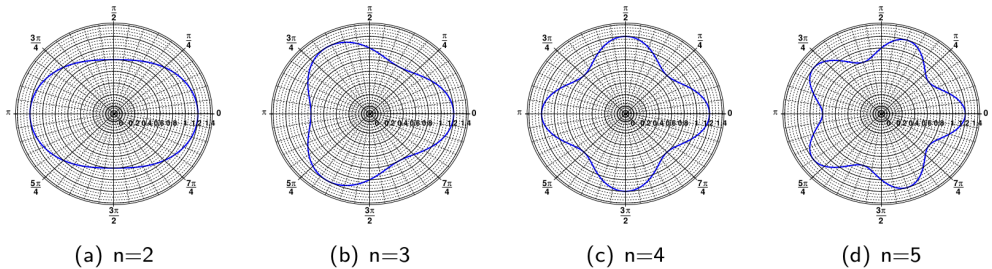


**Figure 3.15:** Illustration of different anisotropic flow harmonics, starting from elliptic flow at  $v_2$ , up to  $v_5$ . Figure is obtained from Ref. [49]

A robust way of determining the harmonic coefficients is to use *two-particle cumulants*. The expression for two-particle cumulants can be derived by expanding  $\phi \rightarrow \Delta\phi = \phi_1 - \phi_2$ , where  $\phi_1$  and  $\phi_2$  are azimuthal angles from the two correlated particles:

$$\frac{dN^{\text{pairs}}}{d\Delta\phi} \propto \left( 1 + \sum_{n=1}^{\infty} 2v_{n\Delta} \cos(n(\phi - \Psi_n)) \right) \quad (3.17)$$

By expanding the flow harmonic for the two-particle correlation  $v_{n\Delta}$ , one can decompose the individual, single-particle contributions. By decomposing the contribution, it becomes clear in Eq. 3.18 that the flow coefficient for the two-particle correlation is equivalent to the product of the corresponding single-particle coefficients. Experimentally, this is an incredibly strong tool, as the coefficients can now be calculated by simply averaging over all charged particle pairs.

$$\begin{aligned} v_{n\Delta} &= \langle \cos(n\Delta\phi) \rangle \\ &= \langle \cos(n(\phi_1 - \psi_n)) \cos(n(\phi_2 - \psi_n)) \rangle \\ &\approx \langle \cos(n(\phi_1 - \psi_n)) \rangle \langle \cos(n(\phi_2 - \psi_n)) \rangle \\ &= v_{n,\phi_1} \cdot v_{n,\phi_2} = v_n^2 \end{aligned} \quad (3.18)$$

One should keep in mind that there can be positive contributions to the flow coefficients, without a collective origin. This is referred to as *non-flow* and arises from azimuthal correlations not linked to the symmetry plane, mainly

driven by resonance decays and jet fragmentation. Experimental measurements of anisotropic flow implement sophisticated techniques to remove the non-flow contribution for the flow harmonics. These techniques will not be discussed further here, as it falls outside the purview of this thesis. Additional reading on this subject can be found in Ref. [50].

ALICE measurements of different flow harmonics, with different orders of cumulants, are presented in Fig.3.16 in Pb-Pb collisions at both  $\sqrt{s_{\text{NN}}} = 2.76$  and 5.02 TeV as a function of centrality. The results highlight the measured final-state particles exhibit a positive  $v_2$ , which increases as a function of centrality. As centrality increases, so does the anisotropy in coordinate space (the event geometry becomes increasingly “almond-shaped”), suggesting that there is elliptic flow driven by anisotropy in the initial state. Furthermore, one can note that the elliptic flow is well described by hydrodynamical calculations, suggesting the presence of a strongly interacting medium.

## Long-range angular correlations

Early measurements of long-range angular correlations, in central nucleus–nucleus collisions, have suggested that the produced particles exhibit longitudinal collective behavior. Figure 3.17 reports the STAR measurement of two-track angular correlations in  $\Delta\eta$  and  $\Delta\phi$ , obtained from central Au–Au collisions at  $\sqrt{s_{\text{NN}}} = 200$  GeV. The peak centered around  $\Delta\phi \approx \Delta\eta \approx 0$  arises from correlations between the large number of particles produced in particle jets. An away-side ridge can be observed at  $\Delta\phi \approx \pi$ , across the entire  $\Delta\eta$  range. This is interpreted as a measurement of the sub-leading jet, which is suppressed due to the presence of a QGP (discussed in Sec. 3.3.4). The sub-leading jet is smeared across the entire  $\eta$  range since di-jets are not necessarily produced back-to-back in  $\eta$  (due to asymmetric fractional momentum carried by the partons in the initial hard scattering). Remarkably, there is also a long, and pronounced ridge around  $\Delta\phi \approx 0$ , over the full  $\Delta\eta$  range. This indicates that even particles that are produced in close  $\Delta\phi$  have a strong, longitudinal correlation, which can be interpreted as flow (and an indication of the geometry produced at early stages of the collision) due to the presence of a QGP medium.

## Radial Flow

Another manifestation of flow is through a radial expansion of the system, arising from extremely strong internal pressure released when deconfined from hadronic

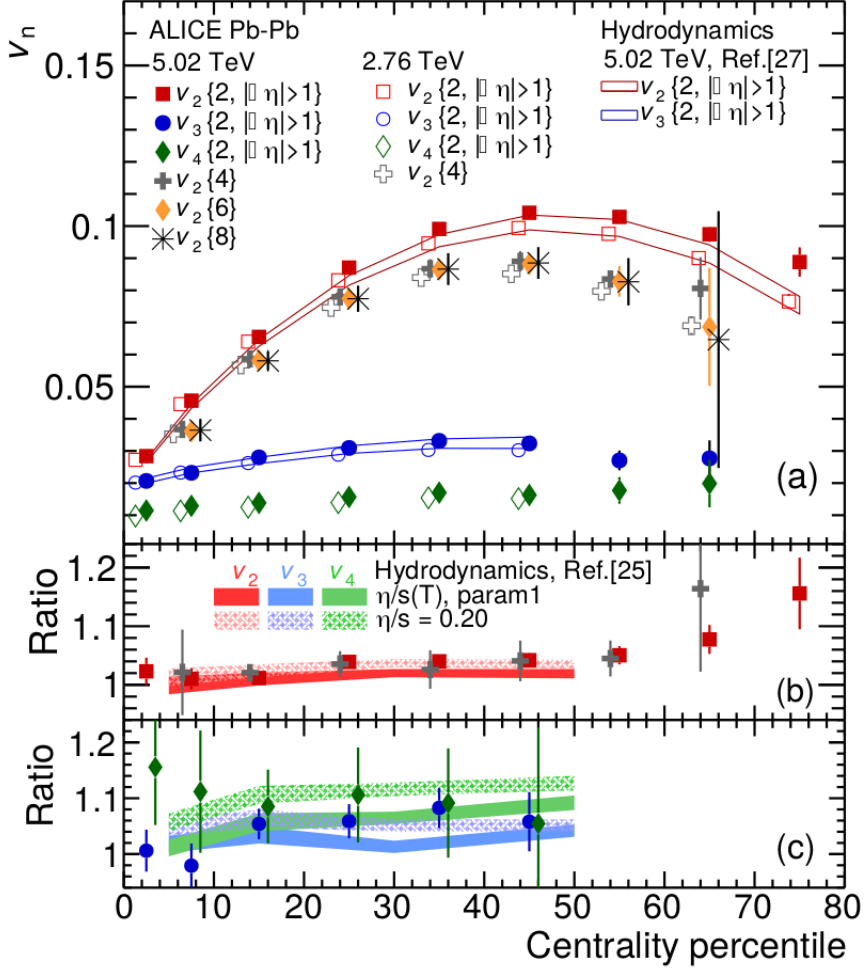


**Figure 3.16:** ALICE measurements of different flow harmonics in Pb-Pb collisions both at  $\sqrt{s_{NN}} = 2.76$  and 5.02 TeV, plotted as a function of centrality. The results are compared with hydrodynamical calculations for both  $v_2$  and  $v_3$  [50].

matter. This creates a velocity field of expanding matter, which can be parameterized by the *Blast-Wave model*, where the transverse velocity distribution of thermalized matter  $\beta_T(r)$  can be expressed as [37]:

$$\beta_T(r) = \beta_S \left( \frac{r}{R} \right)^k, \quad (3.19)$$

where  $\beta_S$  is the velocity at surface  $R$ , and  $k$  is a free parameter, which is determined by fits to data. During the expansion, the velocity field will push out heavier particles toward larger momenta. This behavior can be described by an analogy of a river. Assume that the river applies a constant velocity field. If two

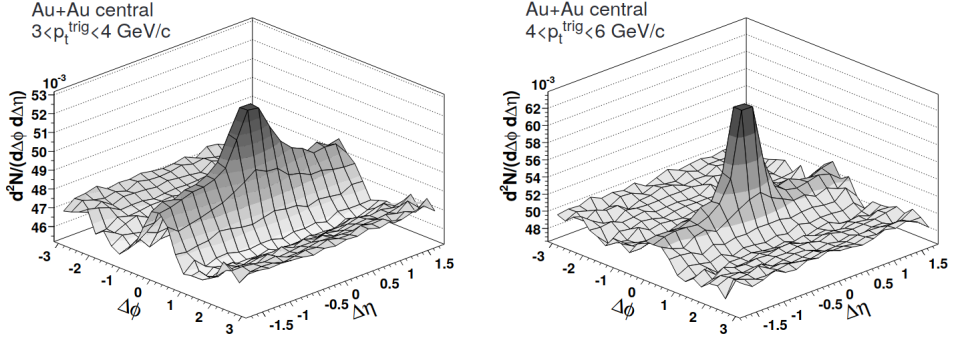


**Figure 3.17:** Two-particle correlations measured in  $\Delta\eta$  and  $\Delta\phi$ , for two different  $p_T$  intervals, measured in Au–Au collisions at  $\sqrt{s_{NN}} = 200$  GeV. The results indicate a strong, near-side ridge around  $\Delta\phi \approx 0$ , across the entire  $\Delta\eta$  range. Results are taken from Ref. [51].

rocks of different weights are tossed into the river, they will pick up the same speed due to the velocity boost. However, the heavier rock requires more effort to push, leading to a larger momentum. While simplified, this analogy would lead us to believe that this also applies to particles with relativistic momenta.

Experimentally, this can be studied by measuring the  $p/\pi$  ratio as a function of  $p_T$ . If an expanding velocity field is produced, the protons would be pushed towards larger  $p_T$ . Fig. 3.18 shows the centrality differential  $p/\pi$  as a function of  $p_T$ , clearly demonstrating that  $\langle p_T \rangle$  gets pushed towards higher values, with increasing centrality. One should keep in mind that there is no enhancement of protons at higher centralities; rather, the integrated  $p/\pi$  ratio is in fact suppressed as a function of centrality. The overall peak-shape changes and becomes taller due to that a majority of the yield is located at low- $p_T$ . Furthermore, all curves saturate toward the same values at high- $p_T$ . This is due to hard (perturbative) processes being dominant at such large  $p_T$  values. This is also suggested by the fact that the pp curves align with the Pb-Pb curves.

### 3.3.4 \*Jet Quenching and Energy Loss

Jet production can provide valuable insight into the dynamics of the QGP since they are produced from hard scatterings, which occur at very early stages of the collision. If a QGP is formed, jets have to propagate through the medium. Figure 3.19 shows the azimuthal angular correlation between unidentified hadrons for different collision systems. All presented systems have a clear peak around  $\Delta\phi \approx 0$ . This is interpreted as the particles from the leading jet, which are produced in a tight cone with a high density of tracks. Consequently, A

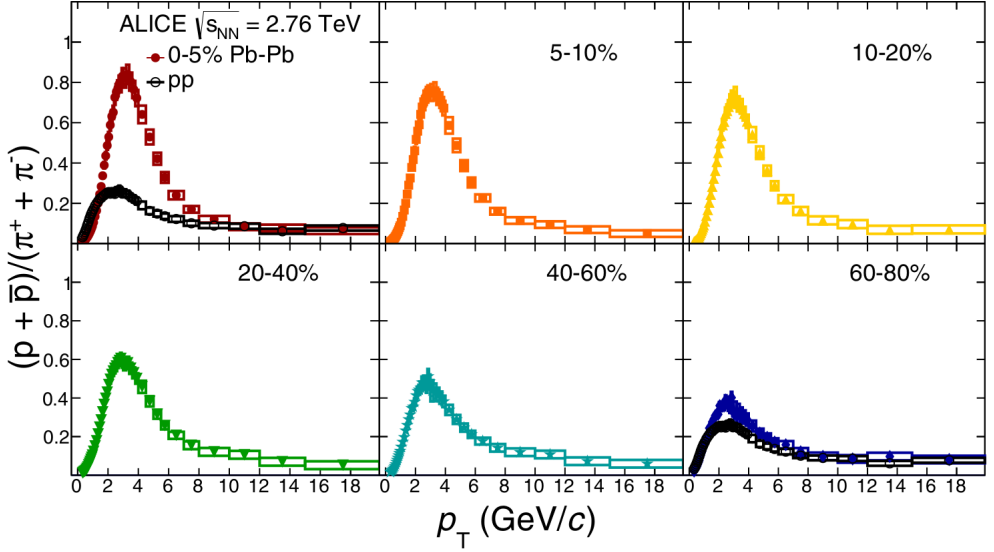


**Figure 3.18:** ALICE measurement of the proton-to- $\pi$  ratio as a function of  $p_T$ , in different centrality bins, for Pb-Pb collisions at  $\sqrt{s_{NN}}$  2.76 TeV. The results are obtained from Ref. [52].

jet is produced in the opposite direction (away-side) of the leading jet, which balances the momentum conservation. This peak can be seen at  $\Delta\phi \approx \pi$  for the smaller collision systems. However, the away-side peak is not present for the Au–Au collisions. This is interpreted as the away-side jet being absorbed by a QGP, where the initial high-momentum is deposited and “lost” in the medium, instead ending up as many soft particles (e.g., through gluon bremsstrahlung), which are diffused over broader angles relative to the original jet direction. This phenomenon is referred to as *jet quenching*, which supports the idea that strong interactions still occur after the initial hard scattering [6].

The energy lost due to jet quenching can be quantified by the *nuclear modification factor*  $R_{AA}$ , which measures the energy loss in heavy-ion collisions, defined as

$$R_{AA} = \frac{dN^{AA}/d\eta dp_T}{\langle N_{coll} \rangle dN^{pp}/d\eta dp_T}. \quad (3.20)$$

The  $R_{AA}$  measures the modification of a given observable between a nucleus–nucleus collision, with respect to a pp collision, which is upscaled with the number of binary collisions that occur during the nucleus–nucleus collision.  $R_{AA} \approx 1$  would indicate that the hard production in a heavy-ion collision can simply be

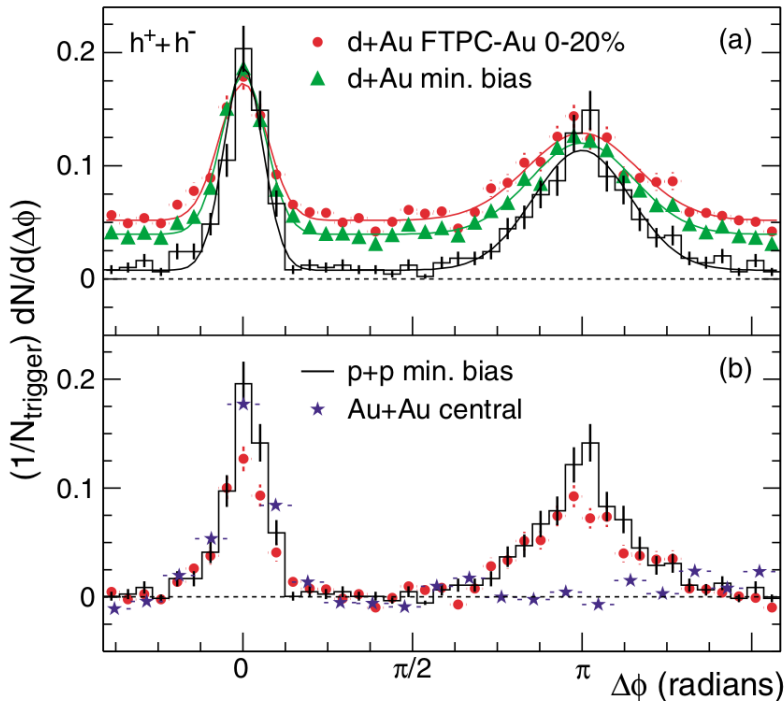


**Figure 3.19:** STAR measurements of two-particle azimuthal angular correlations, for different collision systems. See text for details. Results are taken from Ref. [53].

modeled by a superposition of several pp collisions, whereas  $R_{AA} \neq 1$  would imply a nontrivial modification created nucleus–nucleus collisions, often interpreted as the formation of a QGP medium. Figure 3.20 presents the  $R_{AA}$  as a function of the jet  $p_T$  (the combined  $p_T$  of particles within a jet cone), for Pb–Pb collisions of different centralities at  $\sqrt{s_{NN}} = 5.02$  TeV, measured by ATLAS. The results report a significant suppression of the jet  $p_T$  as a function of centrality, suggesting that a significant portion of the jet momentum is absorbed by the medium formed in more central Pb–Pb collisions.

Moreover, Fig. 3.21 presents the  $R_{AA}$  for different particle species, from PHENIX measurements in Au–Au collisions at  $\sqrt{s_{NN}} = 200$  GeV, for the 0–10% most central events. One can see suppression of all particle species which interact strongly, with proton production being slightly boosted at intermediate  $p_T$ , most likely as a result of radial flow. However, the direct photon measurement is consistent with  $R_{AA} \approx 1$ , implying that the unique dynamics that arise in nucleon–nucleon collisions are not sensitive to electroweak interactions, which suggests the formation of a strongly interacting medium.



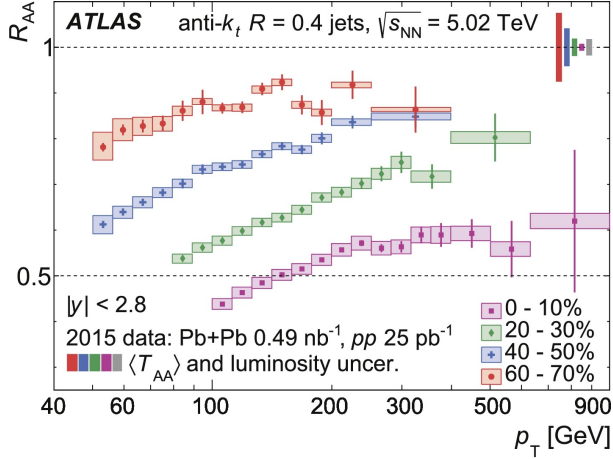


**Figure 3.20:** ATLAS measurement of the  $R_{AA}$  as a function of jet- $p_T$ , for Pb–Pb collisions with different centralities. There is a clear suppression of the overall jet- $p_T$  for higher centralities. Results are obtained from Ref. [54]

### 3.4 The New Paradigm: High-Multiplicity Proton-Proton Collisions

Several results were presented in Sec. 3.3, which all could be understood as final-state effects resulting from the formation of a strongly interacting medium. Historically, these signatures were believed to be unique features of heavy-ion collisions, and robust probes for investigating the properties of the QGP.

However, several results from high-multiplicity pp and p-Pb collisions in recent years have revealed that these signatures are also present in smaller collision systems. This creates a difficult challenge for current theoretical frameworks, as smaller collision systems produce a very small volume. Consequently, these small volumes will have too short lifetimes for the system to fully equilibrate. This has generated a lot of confusion, as previously non-controversial interpretations of past measurements have to be re-examined in this new context, leading to several potential outcomes:

1. Either there is enough lifetime to equilibrate in small volumes, to create QGP droplets, or the QGP does not need to fully equilibrate to form. This implies that previous measurements are signs of a QGP forming, for small and large systems alike.
2. QCD-inspired models being able to describe “QGP features” in smaller collision systems opens up the possibility that heavy-ion measurements

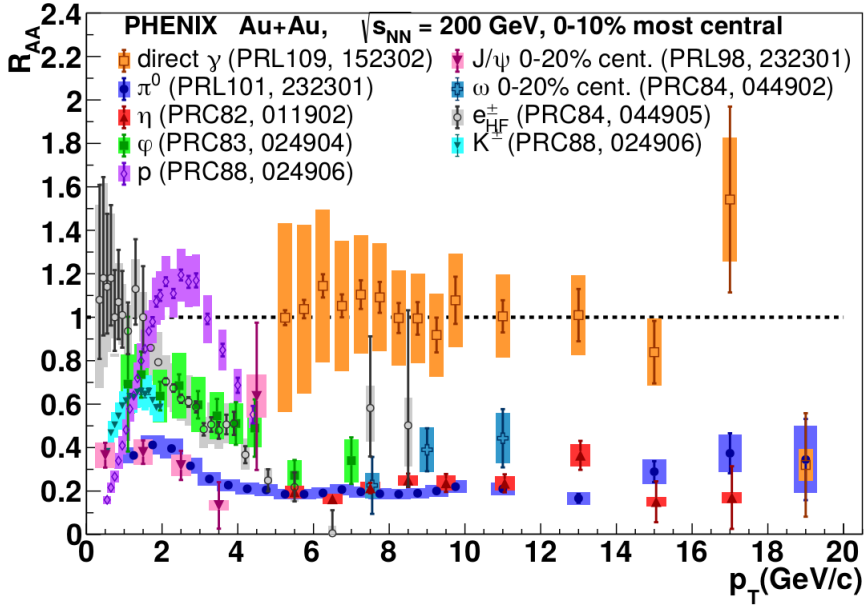


**Figure 3.21:** PHENIX measurement of  $R_{AA}$  for different particle species, obtained from the 0-10% most central Au–Au collisions at  $\sqrt{s_{NN}} = 200$  GeV. Results are taken from Ref. [55]

are not measurements of the QGP at all. Instead, these features could be described by different phenomenological adaptations of QCD.

3. While the signatures are qualitatively similar, the collective effects (strangeness enhancement, anisotropic flow, nuclear modification) in small and large systems could originate from different phenomena.

These findings come with severe implications; for QCD-inspired models, this means that pp collisions can no longer be thought of as incoherent sums of parton-parton interactions. This violates the concept of “Jet Universality”, a longstanding QCD principle that assumes that color fields and hadronization processes are universal. Consequently, a high-multiplicity pp collision cannot be described by a scaled-up minimum bias pp-collision. Conversely, hydrodynamical descriptions have to incorporate a relative fraction of “QGP-like” and “ $e^+e^-$ -like” processes to describe the features found in small systems.

This sets the context for the overall motivation and work performed in this thesis, as new observables are required to gain further insight into high-multiplicity pp collisions, and their relation to the QGP. These new multi-differential observables are developed to be sensitive to the QGP-like effects observed in the

high-multiplicity pp collisions, which can put constraints on different phenomenological descriptions.

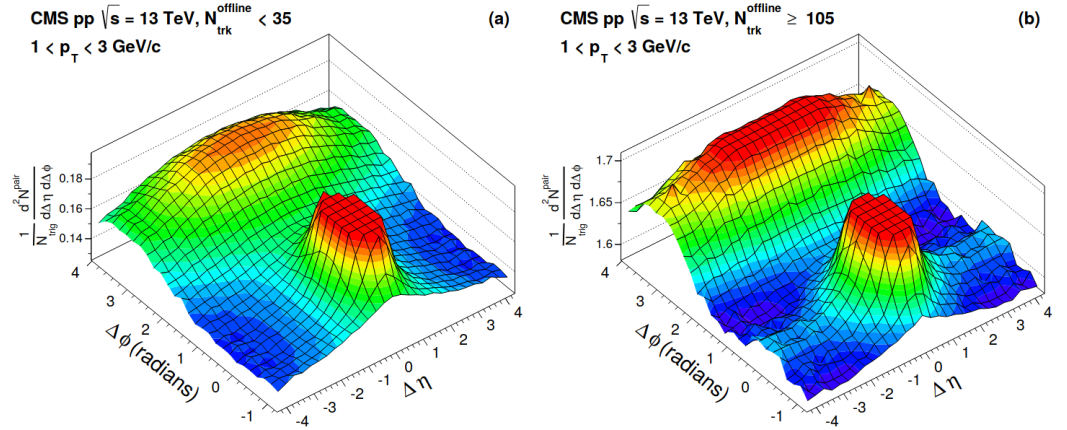


**Figure 3.22:** Two-particle correlations measured in  $\Delta\eta$  and  $\Delta\phi$ , measured in pp collisions at  $\sqrt{s} = 13$  TeV for low (high)-multiplicity events in the left (right) panel. The results indicate a near-side ridge around  $\Delta\phi \approx 0$ , across the entire  $\Delta\eta$  range. Results are taken from Ref. [56]

In 2013, the CMS experiment reported that long-range angular, near-side correlations are produced in central p-Pb collisions [16]. This was followed up in a similar study of pp collisions at  $\sqrt{s} = 13$  TeV, presented in Fig. 3.22. The left panel reports the two-particle correlation for low-multiplicity events, which reflects what would be expected from a hard di-jet; a leading jet with strong correlation at  $\Delta\phi \approx \Delta\eta \approx 0$ , followed by a ridge from the sub-leading jet at  $\Delta\phi \approx \pi$  along the entire  $\Delta\eta$  range. Remarkably, the same measurement at high multiplicity presents a significant ridge along the near-side jet, at  $\Delta\phi \approx 0$ , along the entire  $\Delta\eta$  range. The strength of this correlation is suggested to increase linearly with multiplicity and indicates that longitudinal collective behavior is also present in smaller collision systems.

ALICE has shown that the strangeness enhancement observed in Pb-Pb collisions is also found in high-multiplicity pp and p-Pb collisions, presented in Fig. 3.23. Here, the hadron-to- $\pi$  ratios are listed, for several hadrons containing strange quarks, as a function of midrapidity multiplicity. It can be seen that the smaller collision systems fall into the same, universal curve as the Pb-Pb curves. Both pp and p-Pb exhibit strangeness enhancement, seeing large relative increases at higher multiplicities. Furthermore, similar to the observation in Pb-Pb, the enhancement grows stronger with increased strangeness content.

Furthermore, ALICE has also presented observations of both radial flow and anisotropic flow in high-multiplicity pp systems [57]. Proton-to- $\pi$  ratios, for pp

collisions at  $\sqrt{s} = 13$  TeV, as a function of  $p_T$  are displayed in Fig. 3.24 for different multiplicities (third line of panels). Here, one can see the same  $\langle p_T \rangle$  hardening of the  $p/\pi$  ratio as for Pb-Pb collisions (third row). This effect is not as strong for the  $K/\pi$  ratios, suggesting a mass dependence. This implies that the protons are pushed to higher momentum by a constant velocity field in all three collision systems.

Figure 3.25 shows measurements of different flow harmonics measured in pp, p-Pb, Xe-Xe, and Pb-Pb collisions for different  $\sqrt{s_{NN}}$  energies measured by ALICE. Even after subtracting non-flow, there are positive contributions to  $v_2$  in both pp and p-Pb collisions. However, the contributions are not as strong as they are in larger collision systems. Hydrodynamical models have difficulties describing the flow harmonics for pp systems, while PYTHIA 8, a general-purpose QCD-inspired event generator (with no implementation of hydrodynamics), can qualitatively describe both  $v_2$  and  $v_4$ .

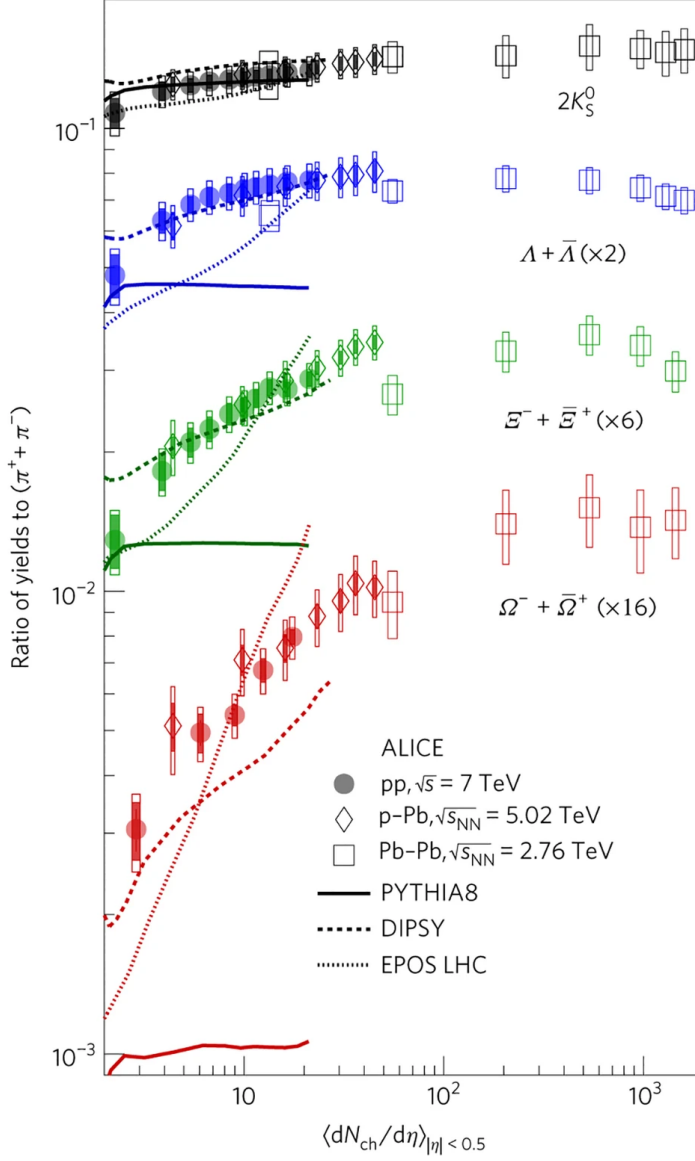


**Figure 3.23:** ALICE measurements of hadron-to- $\pi$  ratios for different collision systems and energies, as a function of multiplicity. The measured data points are compared to different phenomenological models. Results are obtained from Ref. [1].

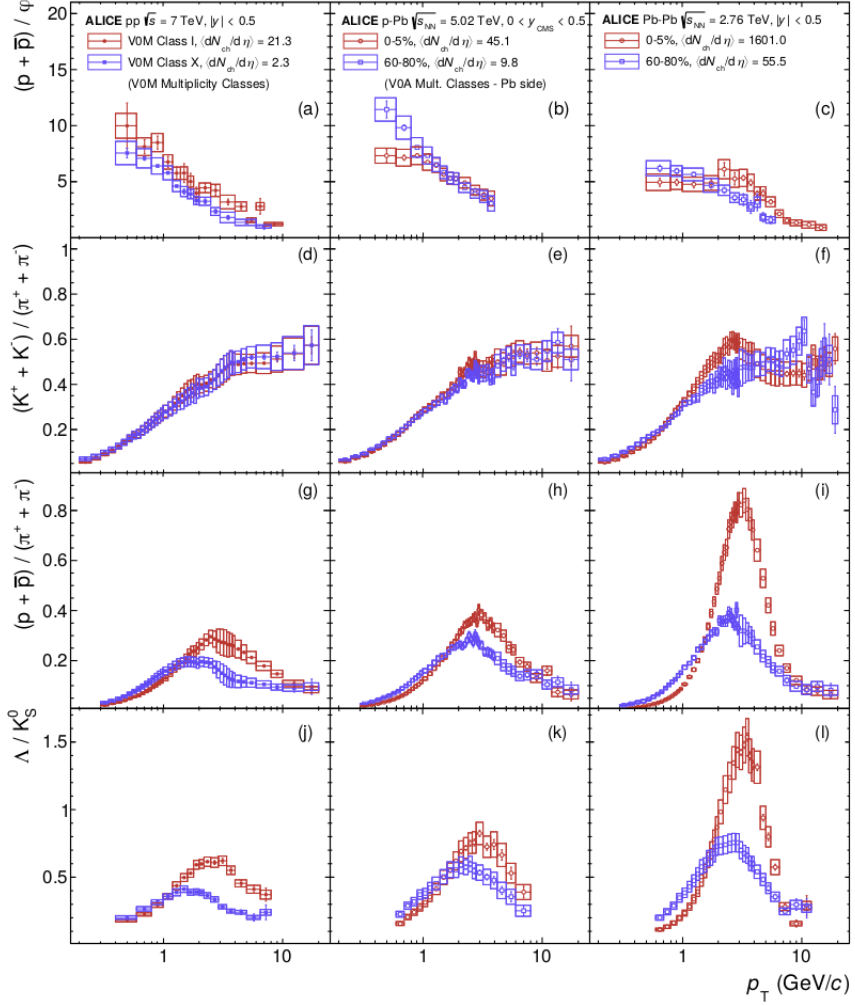


**Figure 3.24:** Different identified hadron-to- $\pi$  ratios as a function of  $p_T$  for pp, p-Pb, and Pb-Pb collisions at different  $\sqrt{s_{NN}}$  energies. Results are obtained from Ref. [57].

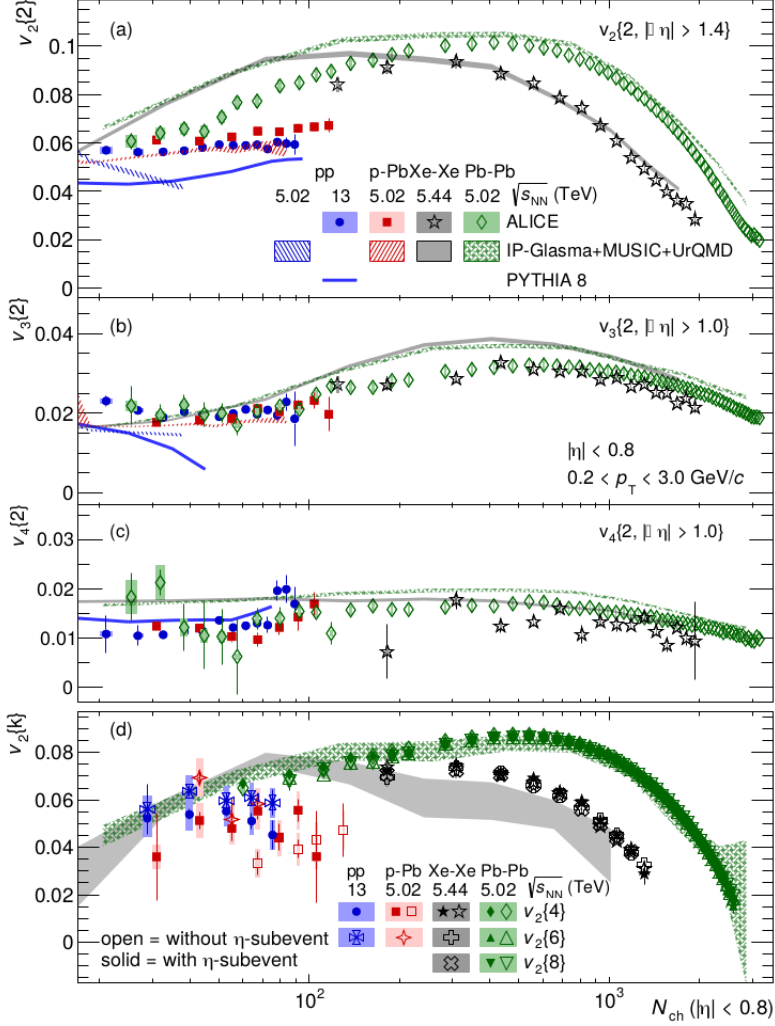


**Figure 3.25:** ALICE measurements of different flow harmonics for pp, p-Pb, Xe-Xe, and Pb-Pb collisions at different  $\sqrt{s_{NN}}$  energies. Data are compared with predictions from PYTHIA 8 and a hydrodynamical description (IP-Glasma+MUSIC+UrQMD). Results are obtained from Ref. [58].





## Chapter 4

# Monte-Carlo Models, and Phenomenology of Particle Production

This chapter will detail the different phenomenological descriptions of particle production. The actual mechanisms of hadronization in QCD can not currently be calculated and have to be described through phenomenological adaptations. The general picture of how hadronization occurs is different from a proton–proton and nucleus–nucleus standpoint. This is illustrated in Fig. 4.1, where traditional pp collisions are modeled to produce particles through fragmentation of gluon strings. For heavy-ion models, the QGP is developed in different stages, affecting the final state of produced particles. Once the QGP cools down, partons within the QGP will either coalesce or fragment. This will create a hadron gas, which will eventually freeze out, both chemically (quark flavor) and kinetically (momentum), to produce free hadrons. A main distinction between the two paradigms is that, for proton–proton models, hadronization is often described on a microscopic level, where quantum numbers between parton–parton interactions are conserved close in phase-space. For heavy-ion models, quantum numbers are usually conserved globally.

Due to the onset of collective behavior in high-multiplicity pp systems, the two paradigms clash. QCD-inspired models have to include new phenomenological concepts to describe how high-multiplicity pp collisions transition into a similar QGP-like picture seen in Fig. 4.1, or introduce new features which can reproduce collective effects without the presence of a QGP. Likewise, heavy-ion-inspired pp event generators have to model the onset of QGP formation in a pp collision,

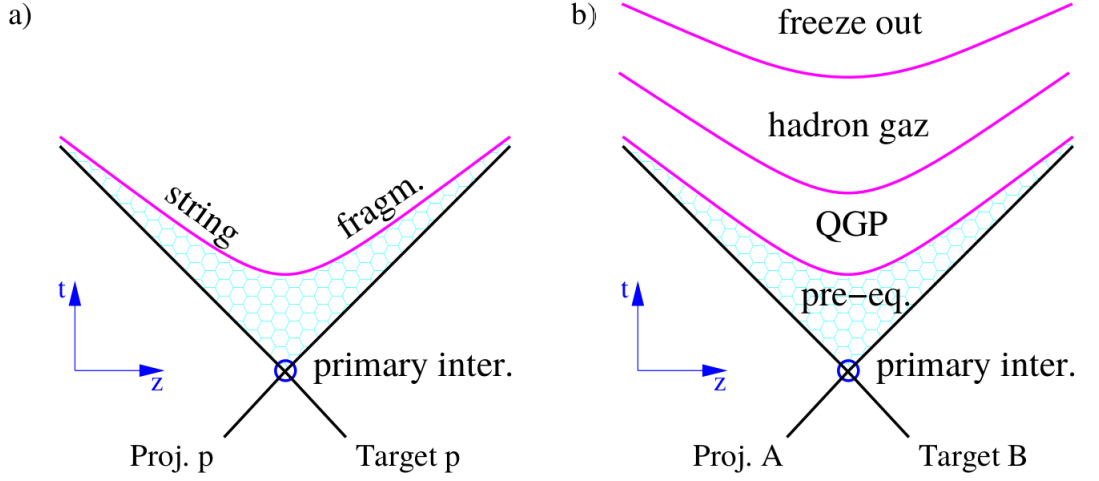


**Figure 4.1:** An illustration of the two different paradigms for hadronization. a) depicts the traditional hadronization picture for  $pp$  collisions, where partons are created through string fragmentation. b) depicts the process of the creation of a QGP in a nucleus-nucleus collision, which eventually freezes out to produce hadrons. The figure is taken from Ref. [59].

most often through a two-component model.

In this context, a comparison between the  $\phi$  meson and the  $\Xi$  baryon carries a large discriminatory power. The  $\phi$  meson consists of a strange-antistrange quark pair ( $s\bar{s}$ ), carrying zero net strangeness, while the  $\Xi$  baryon consists of a  $dss$  triplet. In the context of a traditional  $pp$  picture, the  $\phi$  meson has to conserve strangeness on a microscopic level, implying an associative strangeness production close in phase space. This is not the case in a hydrodynamical picture, where the  $\phi$  meson is formed inherently with zero net strangeness. Consequently, the  $\phi$  meson is expected to behave like a proton in heavy-ion-inspired models (due to their similar masses), and like a multistrange particle in QCD-inspired models. Both of these different paradigms will be discussed in the following Chapter, where I will detail three event generators; PYTHIA 8, and Herwig 7, QCD-inspired event generators based on the Lund string model and cluster hadronization, respectively, and EPOS-LHC, a semi-hydrodynamical, core-corona model.

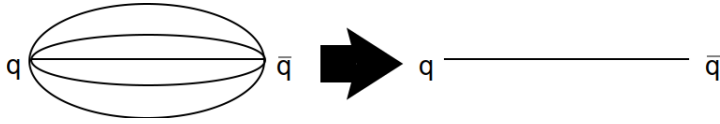


**Figure 4.2:** Sketch of the 1-dimensional simplification of the gluon field between a quark-antiquark pair, used in the Lund String Model.

## 4.1 The Lund String Model

In the Lund string model, (1+1)-dimensional<sup>1</sup>, massless, relativistic strings are used to model the QCD-color fields that arise from quark confinement [60]. The simplification of the topology is illustrated in Fig. 4.2. The strength of the QCD-potential  $V_{QCD}(r)$ , between a quark and antiquark (for a color singlet) of distance  $r$ , can be approximated as [61]:

$$V_{QCD}(r) \approx -\frac{4}{3} \frac{\alpha_s}{r} + \kappa r \quad (4.1)$$

The linear term,  $\kappa r$ , will dominate at large  $r$ , where a large amount of energy has been deposited into the gluon color fields. The motivation for a linear component of confinement has been confirmed through lattice QCD calculations [62], represented by the solid curve previously seen in Fig. 3.10. Consequently, field lines between the quark-antiquark pairs, which are formed from parton-parton interactions during the collision, are compressed into tube-like regions, which can be approximated as *strings*. The quark-antiquark pair, now traveling in opposite directions as a result of the collision, are confined by the string, with a string tension of approximately  $\kappa \approx 1\text{GeV/fm}$ , with no transverse excitations.

The color field between the quark-antiquark pair will oscillate through space-time, forcing the string to expand and contract, bringing the quarks further and closer apart. This is referred to as a *yo-yo* motion between the two quarks, where the momentum-energy for the quark-antiquark  $p_{q\bar{q}}$  as a function of time can be expressed as:

$$p_{q\bar{q}} = \frac{\sqrt{s}}{2} - \kappa t \quad (4.2)$$

From Eq. 4.2, it becomes clear that all the energy from the quark-antiquark pair has been deposited into the gluon field at  $t = \sqrt{s}/2\kappa$ , where none of the momenta is carried by the quarks. At this point, the string is expanded to its maximum length, and will thereafter start to contract. After a full oscillation, the two quarks will meet at the origin and now travel in opposite directions toward the

---

<sup>1</sup>Only one spatial dimension, i.e, space + time

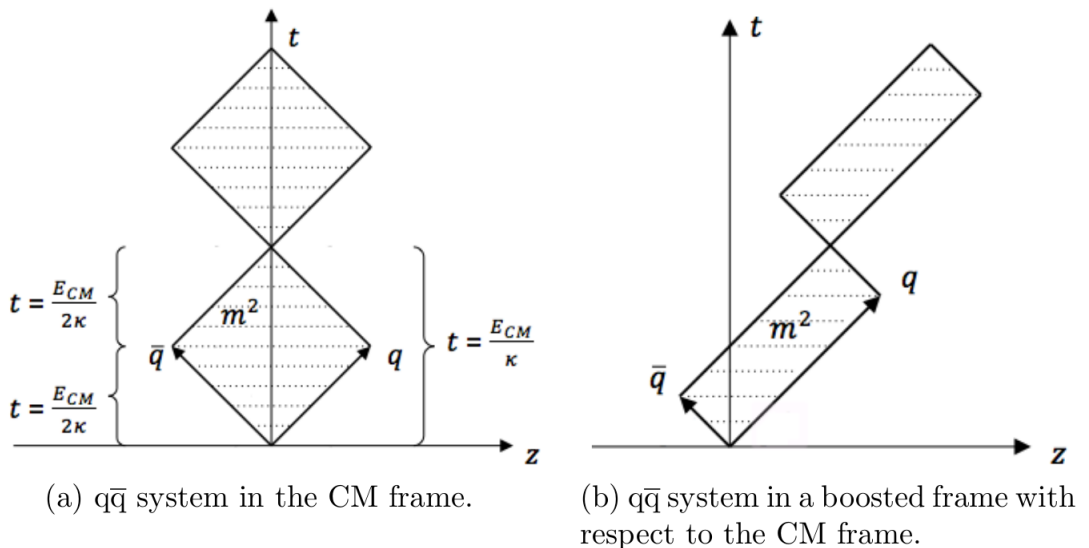


**Figure 4.3:** Illustration of the “yo-yo” motion for a quark-antiquark pair, connected with a Lund string, with string tension  $\kappa \approx 1\text{GeV/fm}$ .  $E_{CM}$  refers to the center-of-mass energy, and is denoted as  $\sqrt{s}$  in the text of this thesis. The figure is taken from Ref. [61]

origin. This motion is illustrated in Fig. 4.3, both in the center-of-mass frame and a Lorentz-boosted frame w.r.t. the center-of-mass frame [61].

While the quark-antiquark pair “yo-yo’s” through space-time, the string can break up and form new quark-antiquark pairs. This process is analogous to the production of  $e^+e^-$  pairs in a homogenous electric field [63], produced with a rate per unit time/volume  $Y_{e^+e^-}$  proportional to

$$Y_{e^+e^-} \propto (qE(r))^2 \exp\left(-\frac{\pi m_e^2}{qE(r)}\right), \quad (4.3)$$

where  $m_e$  is the electron mass, with an electric charge  $q$ , and  $E(r)$  is the strength of the electric field. New, massive pairs cannot be produced in a point through classical means, and have to be separated by a minimal distance  $l_{ee} = 2m_e/qE(r)$ . However, it is possible to produce massive  $e^+e^-$  pairs, in the context of a quantum tunneling process. Virtual electrons are then produced, which can tunnel through the classically forbidden region  $l_{ee}$ , to be produced in a point.

It is possible to apply this interpretation to the creation of new quark-antiquark pairs, exchanging the electric field strength, with the color field strength approximated through Lund color strings. If the Lund string is carrying energy

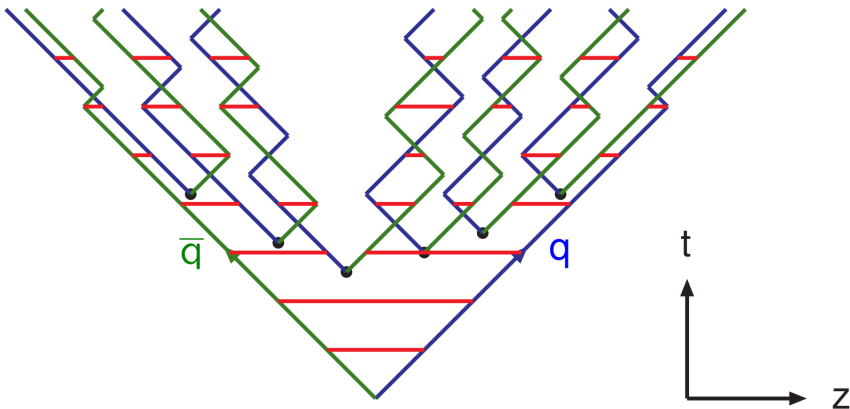


**Figure 4.4:** An example of the fragmentation process in the Lund Model, illustrating how new quark-antiquark pairs are formed by fragmenting Lund strings. Figure taken from Ref. [65]

equivalent to an on-shell hadron mass, the gluon field can deposit the energy to produce a new quark-antiquark pair. However, if the quarks produced in a string-breaking are massive, or carry transverse momentum  $p_T$ , they have to be produced as virtual particles and tunnel out at a distance  $l_{qq}$  to be produced as massive particles, similar to the process described for the creation of  $e^+e^-$  pairs. The distance  $l_{qq}$  is proportional to the transverse mass  $M_T = \sqrt{m_q^2 + p_T^2}$ , where  $l_{qq} = M_T/\kappa$ . The new quark-antiquark would then be produced with opposite  $p_T$  to the longitudinal expansion of the string, with a quark-antiquark pair production rate  $Y_{q\bar{q}}$ , expressed as [64]:

$$Y_{q\bar{q}} \propto \kappa \exp\left(-\frac{\pi}{\kappa} M_T^2\right). \quad (4.4)$$

The *fragmentation process*, describing how Lund strings are transformed into new  $q\bar{q}$  pairs, is illustrated in Fig. 4.4, where the distance between the initial quark-antiquark pair is plotted as a function of time. The quark-antiquark pairs are confined during the entire process, connected through Lund strings, which can momentarily break to form new  $q\bar{q}$  pairs. The probability for each string to fragment, with a momentum fraction of  $z$  taken away in the string-breaking, is defined by the fragmentation function  $f(z)$ :

$$f(z) \propto (1/z)(1-z)^a \exp(-bM_T^2/z), \quad (4.5)$$

where  $a$  and  $b$  are free parameters related to the number of hadrons [64]. Equations 4.4 and 4.5 highlight a fundamental property of the Lund strings; the production of a new quark-antiquark pair is exponentially suppressed with growing

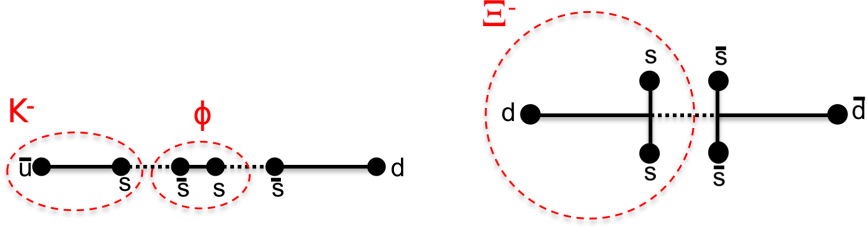


**Figure 4.5:** Illustration of the production of a  $\phi$  meson (left panel) and a  $\Xi$  baryon (right panel), in the context of a Lund string model. The figure is taken from Ref. [66].

$p_T$  and quark masses  $m_q$ , implying that the production rate of heavier quarks is suppressed in the Lund model. The effective strange masses are tuned to LEP data, giving a strange-to-up quark production rate  $s/u$  of  $\approx 0.2^2$ . The relative production of  $\phi$  mesons, in the context of a Lund string, would be doubly-suppressed, requiring a simultaneous string-breaking to form an  $s\bar{s}$  pair, illustrated in Fig. 4.5. This aspect is crucial to keep in mind for the interpretation of the results presented in this thesis.

In the Lund model, baryon production is accommodated by introducing a probability for a diquark-antidiquark breaking to form at any given string fragmentation. This occurs through a vacuum fluctuation along the string, forming a  $q\bar{q}$  pair momentarily before the string fragments. An example of a  $\Xi$  hadron and anti-hadron production, in a string-like picture, is illustrated in Fig. 4.5. The probability to produce a baryon is exponentially suppressed by the effective mass of the diquark. This means that strange baryons will be doubly suppressed, both from a decreased rate in  $s/u$ , but also from a decreased probability to form a strange diquark-antidiquark breaking. Therefore, in the context of a Lund string model, multistrange baryons have a lower relative production of strange particles, compared to lighter flavors.

**One of the key takeaways** is that the production of a  $\phi$  or a  $\Xi$  hadron, in a Lund string-like context, would necessarily imply the formation of other strange hadrons, close in phase space. This is well summarized in Fig. 4.5, where one can see that the string-fragments that *do not* contribute to either the  $\phi$  or  $\Xi$  production, have to carry strange quarks to conserve quantum numbers along the string. Therefore, even though the net strangeness between  $\phi$  and  $\Xi$  is very different ( $|s| = 0$  and  $|s| = 2$ , respectively), the kinematics and hadrochemistry for particles produced alongside both the  $\phi$  and  $\Xi$  would be very similar, in the context of Lund strings.

<sup>2</sup>Given that the mass of a charm quark is in the order of  $\approx 12x$  times heavier than a strange quark, producing  $c, b, t$  quarks in a Lund string is extremely improbable.

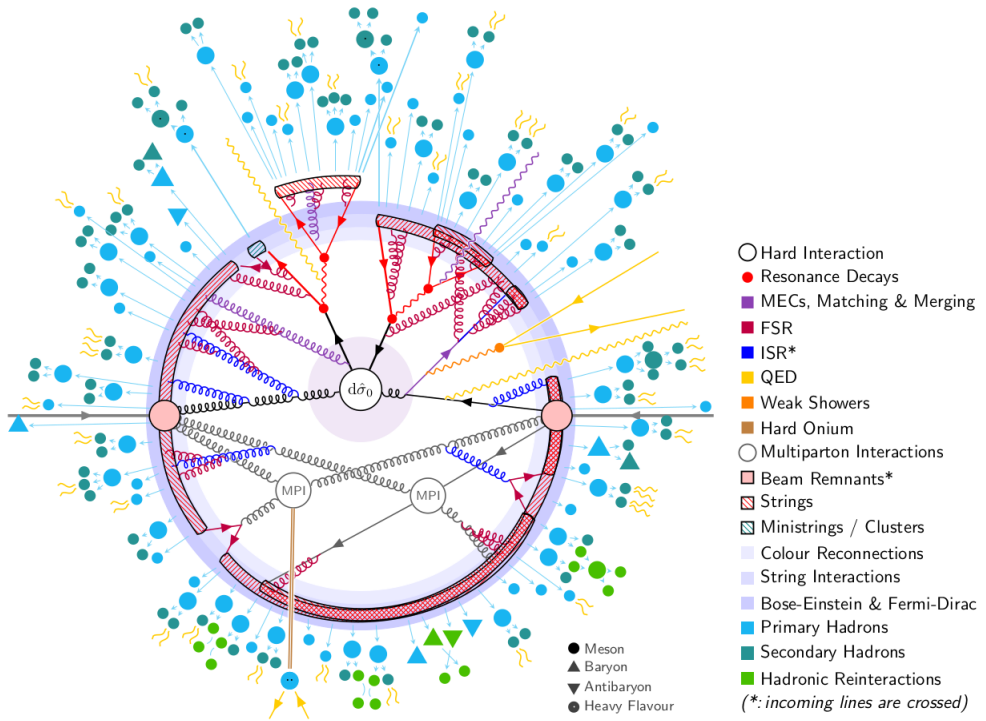


Figure 4.6: Illustration of a fully modeled proton-proton collision in PYTHIA 8. Figure is taken from Ref. [64]

#### 4.1.1 PYTHIA 8

PYTHIA 8 is a general-purpose Monte-Carlo (MC) event generator, which implements the Lund hadronization model to simulate the full dynamics of a  $pp$  collision. Figure 4.6 illustrates the different processes that occur in a  $pp$  collision, illustrating the complexity of PYTHIA 8. The full details of PYTHIA 8 are outside the scope of this thesis, please refer to Ref. [64] for further details. In the following, I will summarize the physics processes in PYTHIA that are relevant for interpreting the results in this thesis.

1. **The initial hard scattering.** A hard scattering occurs between two partons, one from each colliding proton, calculated through pQCD at Leading Order (LO). The common process is a  $2 \rightarrow 2$  scattering of either light quarks or gluons. The scattering produces new partons and gluons, usually carrying a large  $p_T$ .
2. **Parton Showers.** Radiative processes arise from the partons in the hard scattering. The radiation occurs before the scattering through initial state

radiation (ISR), and for the particles produced after the scattering through final state radiation (FSR). The radiative processes produce a large number of partons, and are commonly referred to as “parton showers” [64]. Both ISR and FSR are directly tied to the strength of the initial hard scattering, where a larger momentum transfer produces larger parton showers, carrying a larger  $p_T$ .

3. **Multiple-Parton Interactions.** Protons are composite objects, consisting of sea quarks and gluons, in addition to the valence quarks. When accelerated to relativistic energies, sea quarks can scatter against each other, in addition to the initial hard scattering. Hence, a single pp collision can consist of several parton-parton collisions. These are referred to as multiple-parton interactions (MPIs). Partons produced from MPIs *are not* associated with the strength of the initial hard scattering. Moreover, particles originating from sources outside the initial hard scattering, are referred to as the *underlying event* (UE).
4. **Color reconnection.** Produced partons will form gluon color strings, which stretch out through phase space. However, the color fields between the scattered partons can reconnect with partons from the beam remnant, merging gluon dipoles from softer MPIs to harder MPIs<sup>3</sup>. Consequently, the average string length is reduced, producing fewer particles from softer MPIs, and more particles from harder MPIs. This process is called *color reconnection* (CR). The introduction of this feature allowed PYTHIA 8 to give accurate predictions of how the  $\langle p_T \rangle$  evolves as a function of multiplicity.
5. **Hadronization.** Hadrons are produced from the gluon fragmentation processes described in Sec. 4.1. Produced hadrons are allowed to re-scatter, and will eventually decay down to stable hadrons. For results presented in this thesis, PYTHIA 8 simulated events are required to meet the same definition of “primary particles” used by ALICE collaboration [67].

## Color Ropes

As described in Sec. 4.1, relative strangeness production is not only suppressed in each string fragmentation but doubly so for multistrange baryons, requiring strange diquark-antidiquarks to form. Furthermore, the probability of producing a strange quark scales linearly with the number of produced strings, where the production rate  $s/u$  is independent of the size of the produced system.

---

<sup>3</sup>“softness” and “hardness” in this context refers  $p_T$  of the MPI.



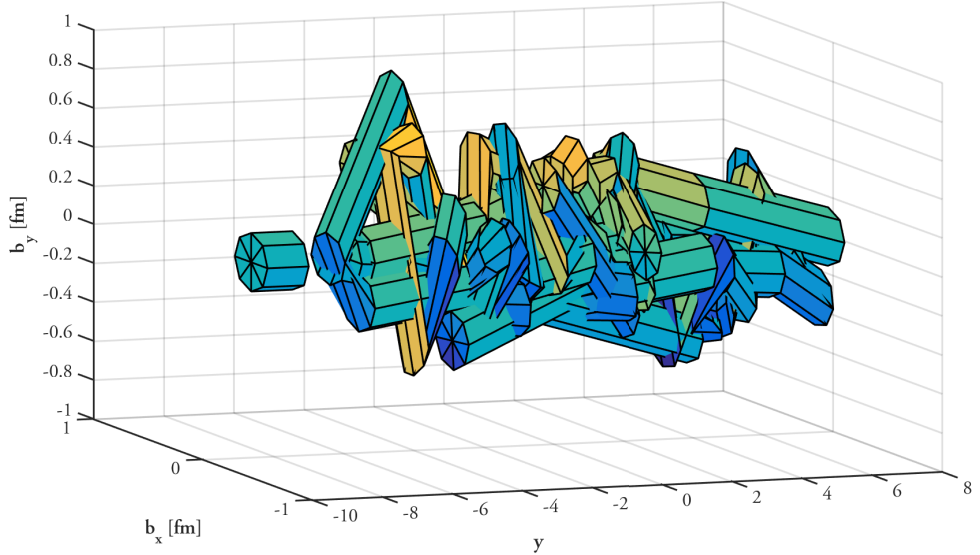


**Figure 4.7:** An illustration of a coherent color rope formed from several Lund strings, simulated for a pp collision at  $\sqrt{s}$  7 TeV. Figure is taken from Ref. [68]

This is incongruent with observations seen in data, where ALICE results have demonstrated that strange particles are produced at higher rates, for larger multiplicities, in pp collisions at both 7 and 13 TeV.

PYTHIA has introduced a new phenomenological feature, where color strings in densely populated regions of phase space act coherently. This coherent structure is referred to as a *color rope*. [63][64]. An illustration of the field lines in a color rope is presented in Fig. 4.7. The color rope acts as a stronger field than individual strings and thereby carries a larger string tension. The *effective string tension* for each strand in the color rope can be expressed as [69]:

$$\kappa_{\text{Eff}} = \frac{2p + q + 4}{4} \kappa, \quad (4.6)$$

where  $p, q$  represents the coherent number of color multiplets forming the rope. When the rope breaks, it does so one string at a time, with a decaying effective string tension in each splitting. I.e., a rope formed with two color strings would imply that for the first string fragmentation  $p = 5/4$ , where  $\kappa_{\text{Eff}} = (5/2 - 1)\kappa$ , where the following string fragmentation would only consist of a single string, and therefore  $\kappa_{\text{Eff}} = \kappa$ .

An increased effective string tension modifies the expressions in both Eq. 4.4 and Eq. 4.5. Since Eq. 4.4 is tuned to LEP data to extract the  $s/u$  fraction for each

produced string fragmentation, an increase of effective string tension increases the relative probability to form both strange quarks, and strange diquarks, proportional to a power of  $x^{\kappa_{\text{eff}}/\kappa}$ . By introducing color ropes, PYTHIA is able to qualitatively describe the enhancement of multistrange baryons observed at high-multiplicity pp collisions. This is presented in Fig. 4.8, where the relative yields of multistrange hadron-to-pion ratios are measured as functions of multiplicity, in different collision systems measured by ALICE, and are qualitatively predicted by PYTHIA 8 with color ropes.

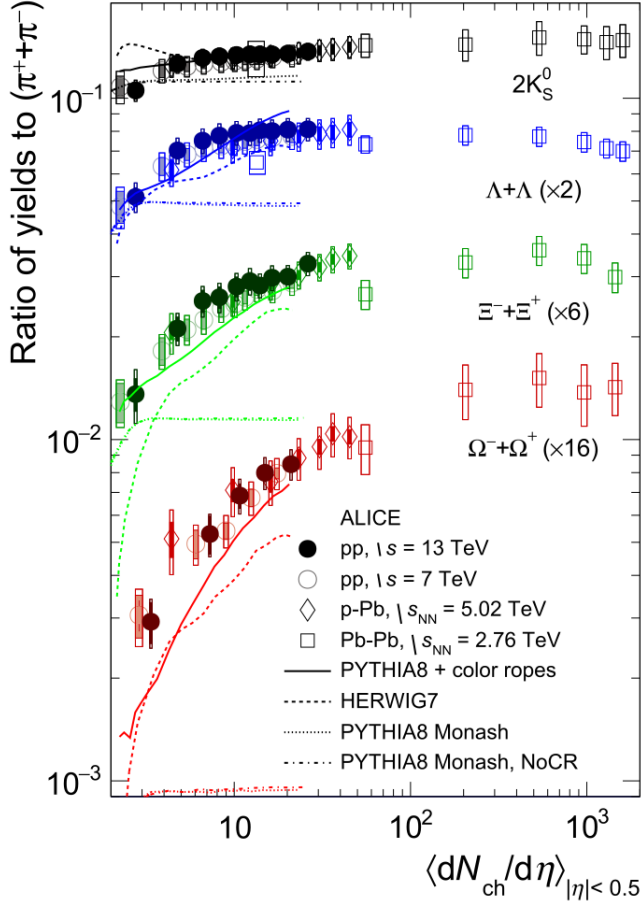


**Figure 4.8:** ALICE measurements of hadron-to- $\pi$  ratios for different collision systems and energies, as a function of multiplicity. The measured data points are compared to different phenomenological models, including PYTHIA 8 with color ropes, which manages to qualitatively predict the trends observed in data. Results are obtained from Ref. [70]

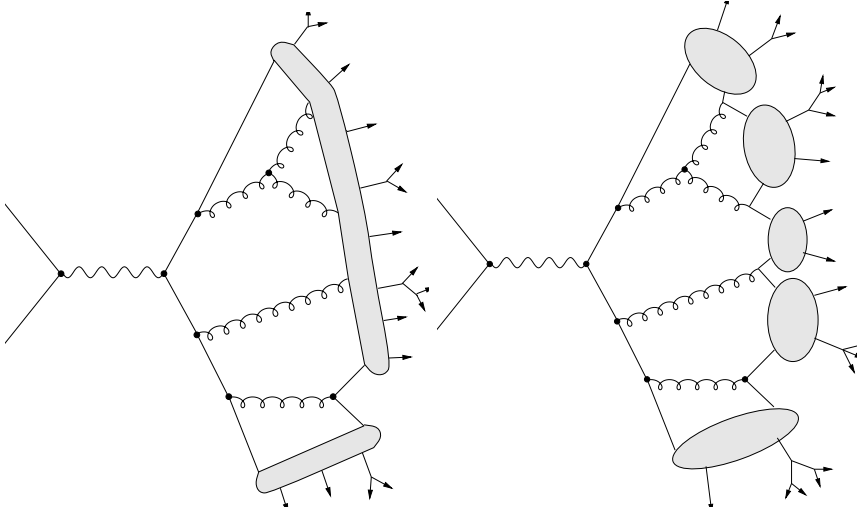


**Figure 4.9:** An illustration of the difference between two QCD-inspired hadronization approaches, with a string model (left panel) and a cluster model (right panel). Both figures are obtained from Ref. [73].

## 4.2 Cluster Hadronization with Herwig 7

*Herwig 7* [71] is a general purpose, QCD-inspired event generator, that unlike PYTHIA does not rely on Lund strings, but rather implements a cluster approach to describe hadronization [72]. The cluster model relies on the concept of *preconfinement*, i.e, the idea that pairs of color-connected partons, nearby in phase-space, have asymptotic mass distributions, that fall rapidly with higher masses [73, p. 189]. Similar to the Lund string model, clusters are formed through the splitting of gluons into  $q\bar{q}$  pairs. However, instead of one-dimensional strings, the energy from the gluon fields are stored in clusters, with an average mass of each cluster of roughly  $1 - 5 \text{ GeV}/c^2$ . Figure 4.9 presents a sketch of the hadronization process in a string versus several clusters, clearly illustrating the difference between the two approaches. The clusters can generally be treated as a superposition of meson resonances, and new hadrons are produced by clusters isotropically radiating particles, with branching ratios determined by the density of states, until the cluster mass is depleted.

Herwig 7 has recently implemented baryonic ropes; a reconnection scheme which, similarly to the ropes in PYTHIA 8, can enhance the probability of multistrange baryons forming. As is shown in Fig. 4.8, Herwig 7 gives a qualitatively good description of the relative enhancement of multistrange baryons, as a function of the charged particle density at midrapidity.

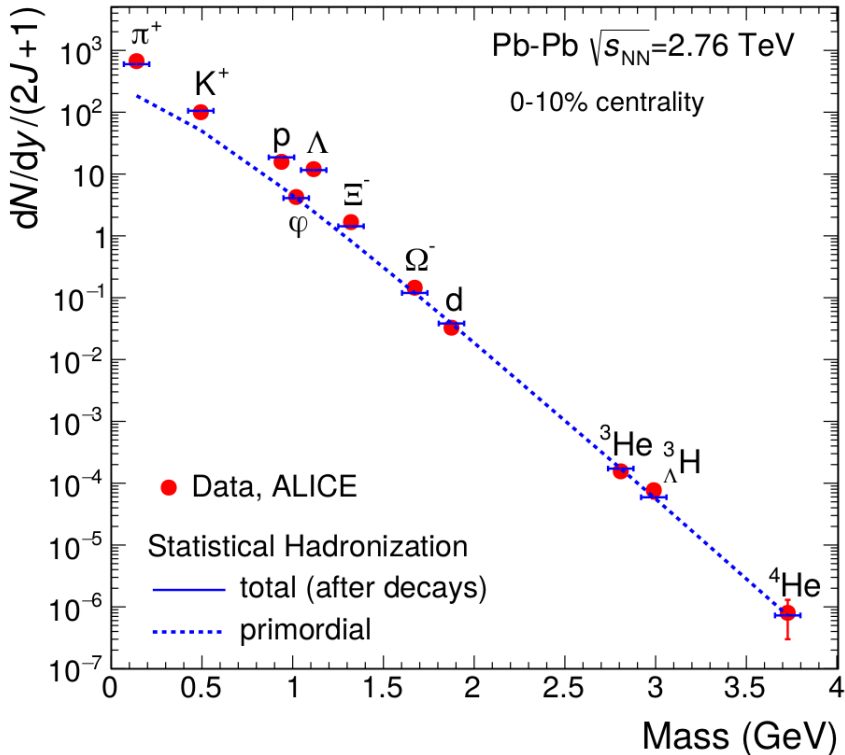


**Figure 4.10:** ALICE data of hadron yield, as a function of hadron mass, from Pb-Pb collisions  $\sqrt{s_{NN}} = 2.76$  TeV/ $c$  measured by ALICE. The ALICE data are compared with calculations from thermal-statistical hadronization, both from total decays (including resonance), and primary particles (here referred to as “primordial”). Results are from, and presented in Ref. [76]

### 4.3 Hydrodynamical & Thermal Hadronization

The production of hadrons in the context of a QGP is often modeled through thermal [74]. While individual nucleon-nucleon scatterings still produce hard interactions, forming parton showers and jets, the main bulk of hadron production is expected to be driven by the thermal production from the QGP. Heavier, less energetic hadrons form quicker, relative to lighter, more energetic quarks. The details of how hadrons are decoupled from the QGP to final-state hadrons are model-specific. Simpler models abruptly truncate the hydrodynamic phase (Cooper-Frye hadronization [75]), while more ambitious models try to regulate the transition from the hydrodynamic phase into a hadron gas (transport models, allowing for hadron-hadron interactions to occur within the QGP).

Thermal production of hadrons is “democratic” w.r.t. the quark content, in the sense that the probability to produce a hadron is directly proportional to

the hadron mass. Figure 4.10, highlights the thermal production of different hadrons, compared to hadron yield in Pb–Pb collisions at  $\sqrt{s_{\text{NN}}} = 2.76 \text{ TeV}/c$  from ALICE. There is a good agreement between the thermal calculations and data, suggesting a Poisson distribution of particles relative to the hadron mass. This is in remarkable contrast to the QCD-inspired Lund model, revealing that hadronization, in a statistical-thermal context, is not suppressed by the quark mass, but rather the hadron mass. Since  $\mu_B \approx 0$  at midrapidity for ultra-relativistic, high-energy nucleon–nucleon collisions, so will strangeness chemical potential  $\mu_S \approx 0$ . This implies that the strange quark content plays no role in particle production [76], and thermal production is solely governed by the effective hadron mass.

**One of the key takeaways** is that  $\phi$  meson, which is doubly suppressed in the Lund model, is produced to have similar dynamics to protons in the context of a thermal model, given that the effective  $\phi$  mass is approximately the same as the proton mass, which is also observed in Fig. 4.10. Therefore, the dynamics and characteristics of particle production between  $\phi$  and  $\Xi$  are expected to be very different in the context of thermal hadronization, due to the large difference in particle mass.

### 4.3.1 EPOS-LHC

EPOS-LHC is a MC, general purpose pp event-generator, based on a two-component, *core-corona* description. Hadronization in EPOS-LHC simultaneously combines QCD and QGP-inspired features. Nucleus-nucleus scatterings are simulated on a partonic level, where gluon strings form a “parton ladder” (illustrated in Fig. 4.11) between the interacting partons.

The string density in phase-space is then compared at a proper time  $\tau_0$ , well before hadronization occurs. A *core* is formed for large string densities, where the mass of the core is proportional to the center-of-mass energy of the strings in given  $\eta$ -differential regions [59]. Each core produces hadrons through a thermal-statistical process, where the probability to radiate a given hadron is linked directly to the effective hadron mass, as previously discussed in Sec. 4.3. In competition with hadron production from the core, strings located in regions with a low string density will fragment, to produce mesons through hard scattering processes, similar to strings in the Lund model. The production of hadrons from less dense string segments is referred to as the *corona*. An illustration of the corona relative to the fraction of core, for different collision systems, is presented in Fig. 4.12.

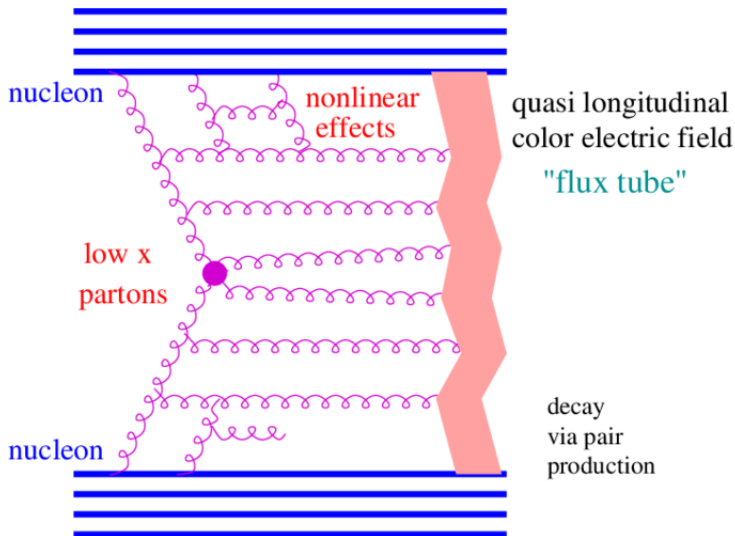


**Figure 4.11:** Illustration of the elementary interaction in the EPOS model, featuring the “parton ladder” which forms together into a coherent color-field flux tube. The figure is taken from Ref. [59].

Hadrons are produced from both the core and corona in each EPOS-LHC event, where the average size of the core grows with the total number of produced charged particles. QGP-like features are modeled by the core, with an overall higher strangeness production (due to the thermal production), and relative hardening of protons-to-pions with increasing multiplicities, attributed to radial flow. In contrast, hard, perturbative QCD-inspired particle production is controlled by the corona. Combining both paradigms, EPOS-LHC can qualitatively describe the enhancement of strange particles as a function of multiplicity in pp collisions, which can be seen in Fig. 3.23.

## 4.4 Phenomenological Understanding of the $\phi$ Meson in Experiments

I will give a brief review of the current experimental findings of the properties of  $\phi$  mesons, and how they relate to  $\Xi$  baryons. The  $\phi$ -to- $\pi$ , and  $\Xi$ -to- $\phi$  ratios are presented in Fig. 4.13, measured by ALICE for different collision systems, as a function of multiplicity. One can see a clear enhancement of the  $\phi$  production as a function of the midrapidity charged particle density, where the different collision systems scale as a single curve. This is in line with the ob-

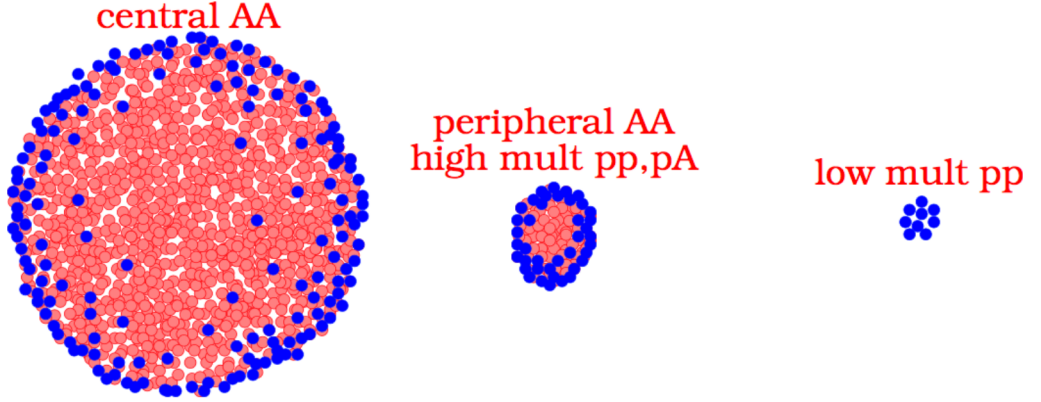
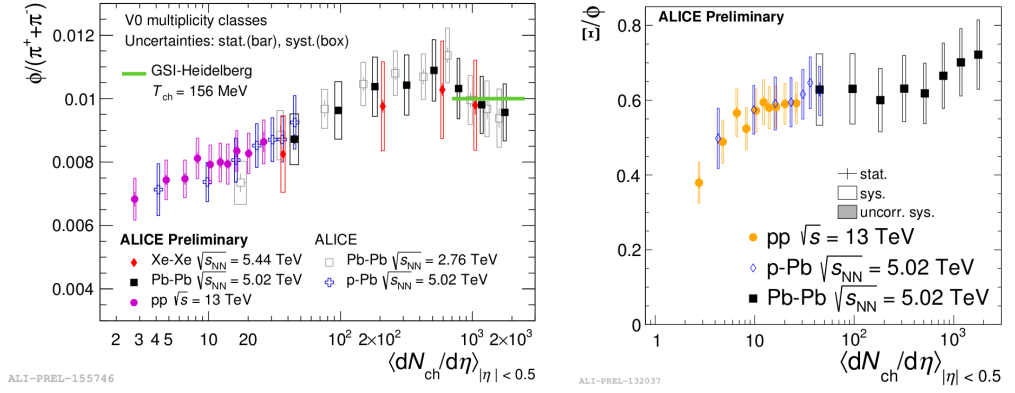


**Figure 4.12:** Illustration of the relative fraction of core (orange dots) and corona (blue dots), for different collision systems. Particle production from the core is modeled from a statistical thermal source, whereas hadronization in the core is modeled through string fragmentation. Figure is taken from Ref. [77]

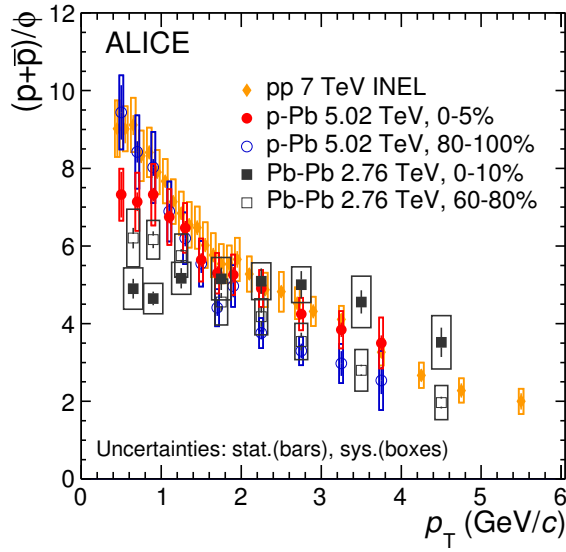
served strangeness enhancement as a function of multiplicity, earlier presented in Fig. 3.23, although the effect is not as pronounced. The  $\Xi$ -to- $\phi$  ratio suggests a flat modification between  $\phi$  and  $\Xi$  yields for large systems, but highlights a pronounced enhancement at lower multiplicities, for smaller collision systems.

Figure 4.14 reports the proton-to- $\phi$  as a function of  $p_T$ , for different collision systems and centralities measured by ALICE. Here one can see a large modification going from central, heavy-ion collisions, to smaller and more peripheral systems. The 0-10% most central Pb-Pb collisions suggest a flat  $p_T$ -dependence, whereas the smaller systems (and peripheral Pb-Pb collisions) align on a seemingly universal trend, showcasing a relative suppression of proton production (or an enhancement of  $\phi$  production) at high- $p_T$ .

Lastly, Fig. 4.15 presents  $v_2$  for identified particles as a function of  $p_T$ , measured in Pb-Pb collisions at  $\sqrt{s_{NN}} = 5.02$  TeV, in different centrality bins. The trends observed for the  $\phi$  meson points to two different hierarchies; at low- $p_T$  (approximately  $p_T < 2.0 \text{ GeV}/c$ ), the  $v_2$  between  $\phi$  mesons and protons are similar, suggesting that the  $\phi$  particle dynamics are mainly driven by the mass. However, at higher  $p_T$ , the  $v_2$  of  $\phi$  mesons diverge w.r.t. the  $v_2$  of protons, to align with the kaons (both charged and neutral). This implies that, at high- $p_T$ , the dynamics of the  $\phi$  meson follow the other mesons (scales with the number of valance quarks). Given that high- $p_T$  production is normally associated with hard, pQCD physics, the results indicate that there are two parallel production mechanisms; thermal, soft production at low- $p_T$  (where  $\phi$  dynamics scale with



**Figure 4.13:** Multiplicity dependence of  $\phi$ -to- $\pi$  (left) and  $\Xi$ -to- $\phi$  (right), measured by ALICE for difference collision systems. See text for more details. Results are obtained from Ref. [78]



**Figure 4.14:** Proton-to- $\phi$  ratio as a function of  $p_T$ , for different collision systems. See text for details. Results are obtained from Ref. [79]

particle mass), and recombination at high- $p_T$ .



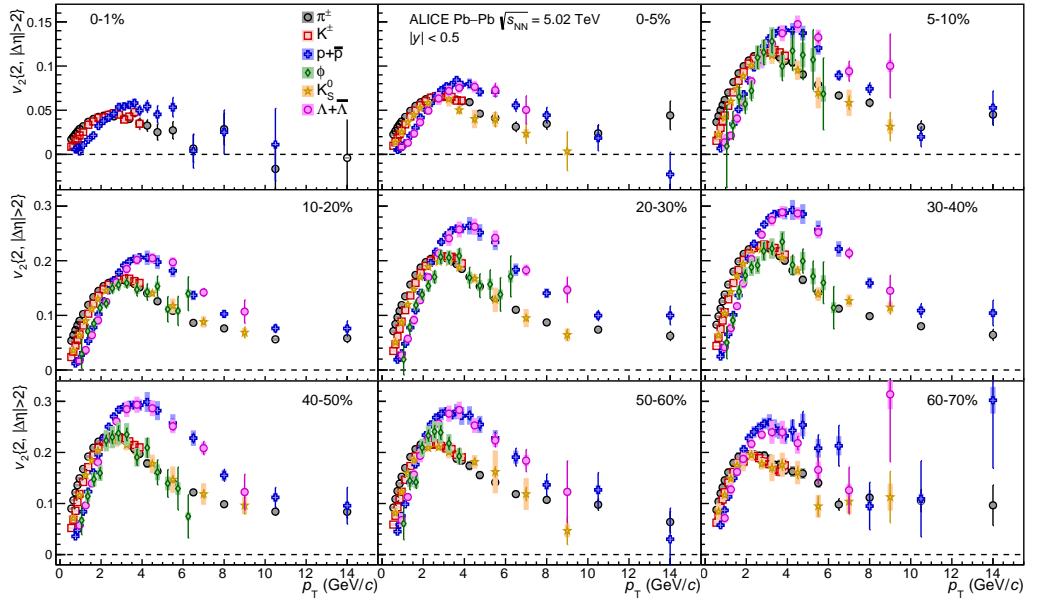


**Figure 4.15:** Measurements of elliptic flow ( $v_2$ ) as a function of  $p_T$ , for identified particles in different centrality bins, measured in Pb–Pb collisions at  $\sqrt{s_{NN}}=5.02$  TeV by ALICE. Results are obtained from Ref. [80].

# Part II

## The ALICE Experiment

## Chapter 5

# The Large Hadron Collider & The ALICE Detector

This chapter will detail the experimental setup of ALICE, one of the four main experiments at the Large Hadron Collider (LHC). This includes a brief overview of the LHC, but will mainly focus on describing the different sub-detectors of ALICE, in particular the sub-detectors used for charged particle track reconstruction, and centrality/multiplicity estimations. Refer to Ref. [81] for a comprehensive review of the ALICE detector. One should keep in mind that the description that I will give of ALICE is the Run 2 configuration, which was used to record the results presented in this thesis. During Run 3 and onward, ALICE has undergone upgrades, which will improve aspects of (and completely rebuild) some detector systems.

### 5.1 The Large Hadron Collider

The Large Hadron Collider (LHC) is a synchrotron/storage ring accelerator system, operated & constructed by the European Organization of Nuclear Research (CERN<sup>1</sup>), located near Geneva on the border between Switzerland and France. The LHC is located 100 m underground, and spans a circumference of 27 km, with 1232 superconducting dipole magnets, which can bend a beam of protons and ions in two separate beam-lines, to collide pp, p-Pb, and Pb-Pb nuclei at peak, center-of-mass energies of 13.7, 8.16 and 5.02 TeV, respectively.

---

<sup>1</sup>The name acronym is derived from the French translation: Conseil européen pour la recherché nucléaire (European council of nuclear research)

# The CERN accelerator complex Complexe des accélérateurs du CERN

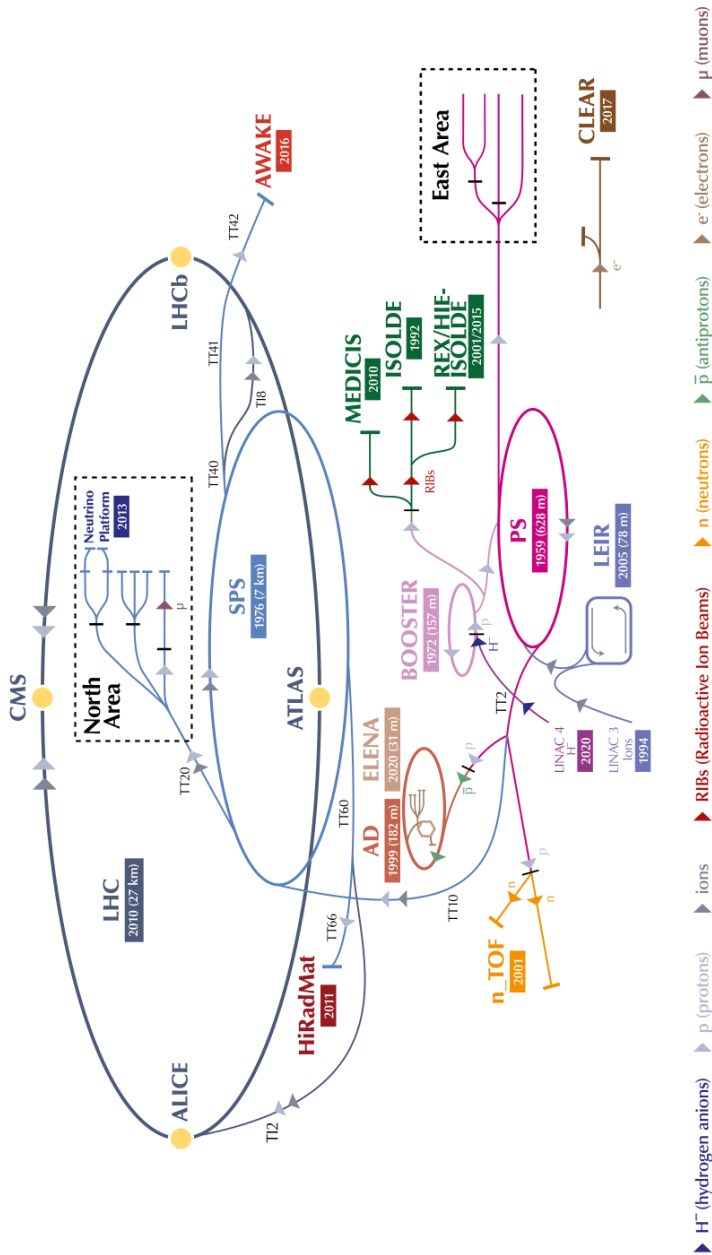
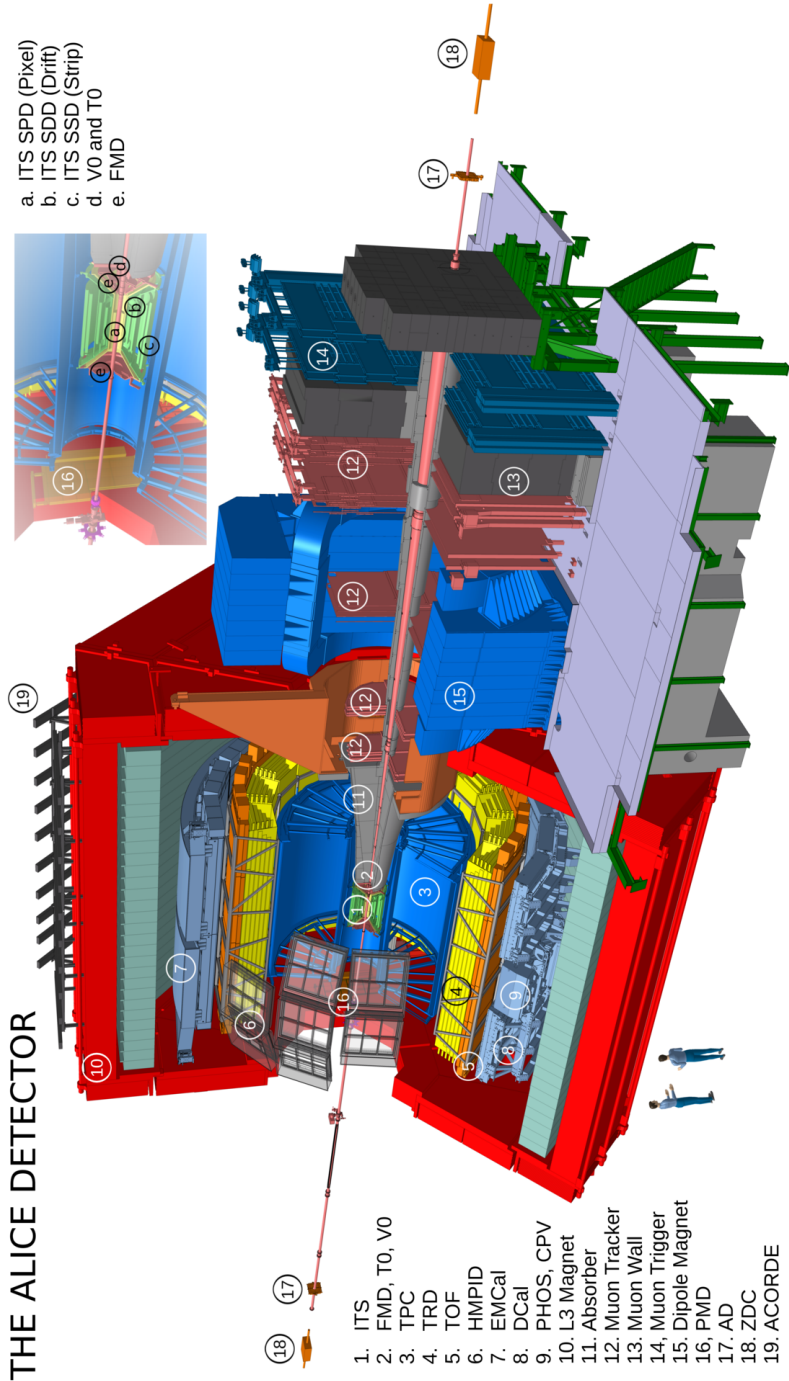


Figure 5.1: Schematic of the entire LHC accelerator complex, highlighting the 4 main LHC experiments. Figure is taken from Ref. [82]

The beams at the LHC are accelerated in several steps to reach the peak collision energy. This is achieved through a complex system of several accelerators, illustrated in Fig. 5.1. After being stripped from electrons, the protons and ions are accelerated up to 2 GeV in Proton Synchrotron Booster (PSB), which are then ramped up to 26 and 450 GeV through the Proton Synchrotron (PS) and Super Proton Synchrotron (SPS) respectively. The protons and ions are then finally injected into the LHC, where they are accelerated to their final peak collision energies.

The LHC physics program currently includes 4 major experiments. A Toroidal LHC Apparatus (ATLAS) and the Compact Muon Solenoid (CMS), are two general-purpose pp experiments, which are primarily focused on the study of rare physics processes. These two experiments are currently focused on the search for dark matter and other physics beyond the standard model. The two remaining experiments are specialized detectors; The LHCb experiment is designed to study flavor physics, in particular  $b\bar{b}$  physics, while A Large Ion Collider Experiment (ALICE) is the only experiment optimized for heavy-ion collisions in the LHC physics program. The majority of each run year is dedicated to proton–proton collisions, where each year has a short period of heavy-ion data taking, from either p–Pb, Pb–Pb, or Xe–Xe collisions (and Oxygen–Oxygen collisions in the upcoming Run 3).

While all 4 major LHC experiments have their own heavy-ion physics programs, ALICE is the only detector that is designed to study ultra-relativistic heavy-ion collisions. The pp experiments, which search for rare phenomena and decay modes, are designed to operate at maximum collision rates (luminosity). However, luminosities for heavy ion collisions are relatively low. Here, the experimental challenge is primarily to design a detector that is capable of measuring the extremely large charged particle densities produced in central collisions, particularly in the low- $p_T$  regime. ALICE is designed with this challenge in mind. When used for pp collisions, ALICE does not reach the sensitivity to rare probes of the dedicated pp experiments but instead complements them with low- $p_T$  measurements, and excellent PID performance. The studies presented in this thesis benefit strongly from both of these two factors, as the data analyzed in this thesis is recorded by the ALICE apparatus, which will be described in more detail in the following.



**Figure 5.2:** An illustration of the entire ALICE apparatus, highlighting different subdetectors in both the central barrel (encapsulated by the large dipole magnet) and the forward regions. The figure is taken from Ref. [83].

## 5.2 The ALICE Detector

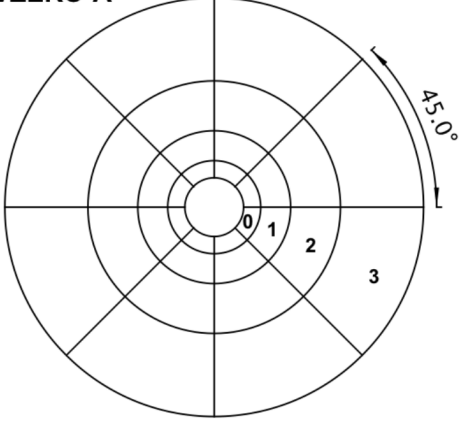
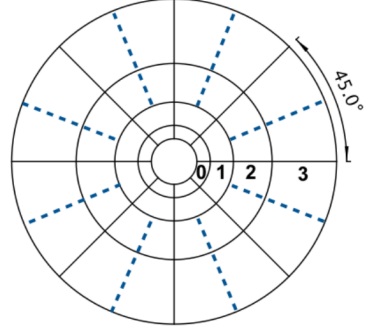
*A Large Ion Collider Experiment* (ALICE) is one of the four main experiments at the LHC. ALICE is an experiment that is primarily intended to study nucleus–nucleus collision, which is reflected in the overall design of the detector. ALICE is capable of capturing the full dynamics, at midrapidity, of Pb–Pb nuclei colliding at relativistic energies. Unlike a pp collision, with charged particle densities at midrapidity of  $\langle dN_{\text{ch}}/d\eta \rangle \approx 7$  at  $\sqrt{s} = 13$  TeV [84], a Pb–Pb collision at  $\sqrt{s_{\text{NN}}} = 5.02$  TeV produces  $\langle dN_{\text{ch}}/d\eta \rangle \approx 1950$  for the top-5% most central collisions [85]. Superb spatial resolution is required to reconstruct each individual particle trajectory. However, this precision comes at a cost of a slow recording rate; during LHC Run 2, ALICE was only able to operate at a rate of 0.2 kHz for Pb–Pb collisions, and 350 kHz for pp collisions [81], out of the 8 kHz and 40 MHz collisions rate provided by the LHC for Pb–Pb and pp collisions, respectively.

An overview of the detector is presented in Fig. 5.2. The entire detector can be categorized into two different sections, based on their pseudorapidity coverage:

- **The central barrel** is enclosed inside the large L3 solenoid magnet (the red structure illustrated in Fig. 5.2), weighing 7800 tons, with a nominal magnetic flux density of 0.5 T<sup>2</sup>. The central barrel houses the main tracking detectors, the Inner Tracking System (ITS), the TPC, and the Transition Radiation Detector (TRD). It also includes detectors designed for particle identification, such as the Time-of-Flight Detector (TOF), the High-Momentum Particle Identification Detector (HMPID), and the Photon Spectrometer (PHOS). Moreover, the central barrel also contains an Electromagnetic Calorimeter (EMCal), which is primarily designed and utilized to measure jet physics and to reconstruct particles decaying to electrons and photons.
- **The forward detectors** refer to the detectors located outside the central barrel. The forward detectors are divided into two “sides”, with respect to the central barrel; The “C”-side, which points toward the CMS experiment (right-direction w.r.t Fig. 5.2), and the “A”-side, facing the ATLAS experiment (left-direction w.r.t Fig. 5.2). Certain forward detectors cover pseudorapidity intervals on both sides. This includes the V0 minimum bias trigger and multiplicity detectors and the T0 detector, which generates a start time for central barrel detectors. The Zero Degree Calorimeter

---

<sup>2</sup>The applied magnetic field will bend the particle trajectory of charged particles produced at midrapidity, where the momentum of each particle can be obtained from the radii of the curvature as projected onto a plane, perpendicular to the beam axis

**VZERO-A****VZERO-C**

**Figure 5.3:** Front view (along the beam-axis) of the two V0 disks, V0A in the left panel, and V0C in the right panel. Figure taken from Ref. [87]

(ZDC), used to estimate the effective energy transferred from the beam particle to the collision, and Forward Multiplicity Detector (FMD) are also situated on both sides. Additionally, the C-side contains the Muon spectrometer, including a dipole magnet (with a magnetic field strength of 0.666 T).

For the remainder of this chapter, I will provide details for the detector subsystems relevant to the analyses presented in this thesis. Refer to Ref. [81] for a full description of the ALICE detector, with additional information on subdetectors not utilized for analyses presented in this paper.

### 5.2.1 The V0 System

The V0 detector (also referred to as VZERO) consists of two disk-shaped arrays on either side of the interaction point, each segmented into 4 rings, consisting of 32 individual plastic scintillator detectors, illustrated in Fig. 5.3, placed at forward rapidities: V0A at  $2.8 < \eta < 5.1$ , and V0C at  $-3.7 < \eta < -1.7$ . The radial size of the V0A is larger, with a radius of 41.2 cm, compared to the radius of 32.0 cm for the V0C [81]. The detector material consists of Bicron-404, which is a plastic scintillator with a decay time of 1.8 ns, and a fast rise time of 0.7 ns [86].

The V0 detectors are primarily designed for two purposes. First, the V0 contributes to the *minimum bias* (MB) trigger, to select and measure inelastic pp, p-Pb,



and Pb-Pb collisions. Secondly, the V0 detectors can estimate the charged multiplicity produced in a given collision, due to the monotone dependence between the signal amplitude in the V0 detectors and the number of charged primary particles. The material will scintillate (and produce a pulse) whenever a charged particle interacts with the material. The scintillation photon pulse is amplified by a photomultiplier tube and then digitized. The measured response correlates to the total amount of charged particles produced in the V0 pseudorapidity interval. The charged particle multiplicity is then estimated through percentiles of the V0M distribution, which is the mean between the raw (corrected independently for respective gain) V0A and V0C signals<sup>3</sup>. The self-normalized V0M distribution for pp collisions at  $\sqrt{s}=13$  TeV is presented in Fig. 5.4. A comparison to the equivalent V0M distribution for Pb-Pb collisions, presented previously in Fig. 3.4, highlights that the overall multiplicity distribution is much broader in Pb-Pb collisions. In pp collisions, even though the V0A covers a broader rapidity interval, the signal detected in the V0C is usually dominant for the multiplicity estimation, since it is located closer to the interaction point (and thereby absorbs a larger charged particle density).

By estimating the multiplicity in the V0 detectors, one can estimate multiplicity and measure physics observables in two independent pseudorapidity regions. The benefit of this approach is that one avoids possible auto-correlations, which could otherwise bias observables toward unphysical results. If the particle extraction and multiplicity estimation occur in the same pseudorapidity region, one risks biasing the event selection toward local fluctuations that produce an abundance of charged particles. This can alter the overall perception of the hadrochemistry, which is demonstrated in the multiplicity dependence between neutral and charged kaons, presented in Fig. 5.5<sup>4</sup>.

## 5.2.2 The Inner Tracking System

The inner tracking system is, as the name suggests, the innermost tracker, closest to the interaction point. The ITS is primarily designed to track and identify particles with low momenta and to localize and reconstruct the primary (and potentially secondary) vertex for each collision. The ITS consists of 6 cylindrical

---

<sup>3</sup>One should keep in mind that the V0M signals are presented in arbitrary units, and not in units of the elementary charge. The gain is equalized between the two detectors, therefore ensuring that the distribution is directly proportional, within percentiles, to the produced charge particles.

<sup>4</sup>To avoid potential confusion, I will state here that the analyses presented in Chapter 7 utilize a midrapidity multiplicity estimation (through *tracklets*, defined in Sec. 5.2.2), where this “bias” is used as an advantage. This will be discussed in more detail in Sec. 7.3

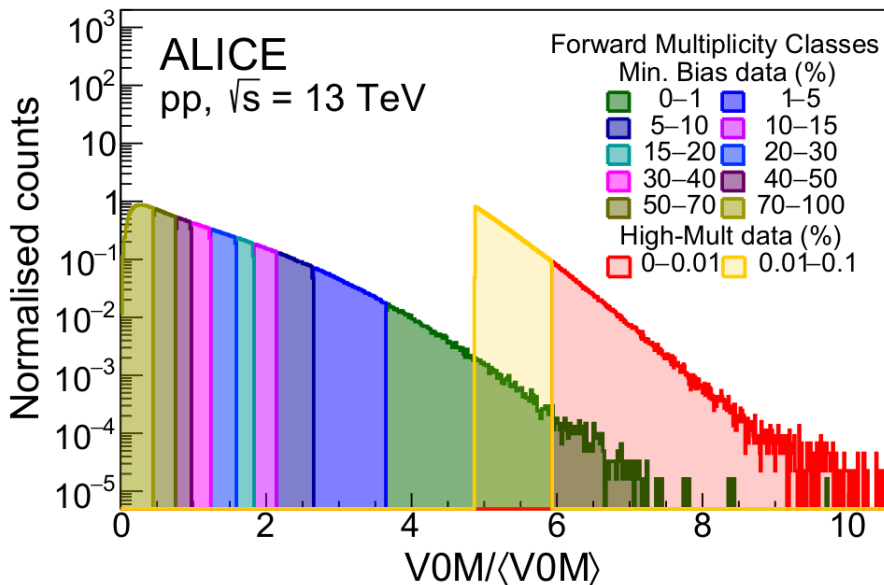


**Figure 5.4:** Self-normalized distribution of VOM signals for pp collisions at 13 TeV. The High-Multiplicity trigger is not used for the analyses presented in this thesis, but instead only utilizes the normal VOM Forward Multiplicity Classes. The figure is taken from Ref. [88].

layers of silicon detectors, which surround the beam pipe. The 6 layers are separated into three different groups, for two layers each. Each group uses different techniques to reconstruct the track coordinates. The SPD covers the two first layers (layers 0 and 1), followed by the SDD (layers 2 and 3), ending with the SSD (layers 4 and 5). The layout for the ITS is illustrated in Fig. 5.6.

The design parameters of the different silicon layers vary based on their proximity to the beamline. The SPD, closest to the beamline, at an innermost radius of  $\approx 3.9$  cm, has to operate at extremely large track densities and high radiation levels [81]. Therefore, the SPD is constructed to have high granularity, based on reverse-biased silicon detector diodes that are bonded onto a two-dimensional, flat matrix, with a thickness of  $200 \mu\text{m}$ . Each matrix consists of  $256 \times 156$  cells, measuring  $50 \mu\text{m}$  in the x-y plane perpendicular to the beam-axis, and  $425 \mu\text{m}$  in the z-direction, along the beam-axis. The two-dimensional array covers 12.8 mm in the x-y plane and 70.7 mm in z. The geometry of the SPD consists of staves, built from 4, two-dimensional silicon matrices, which are then assembled into a sector consisting of two layers; two staves in the inner layer, and four in the outer layer. By combining 10 sectors, one gets full azimuthal coverage around the beam pipe, with two layers of silicon pixel detectors, covering the pseudorapidity region  $|\eta| < 1.4$ .

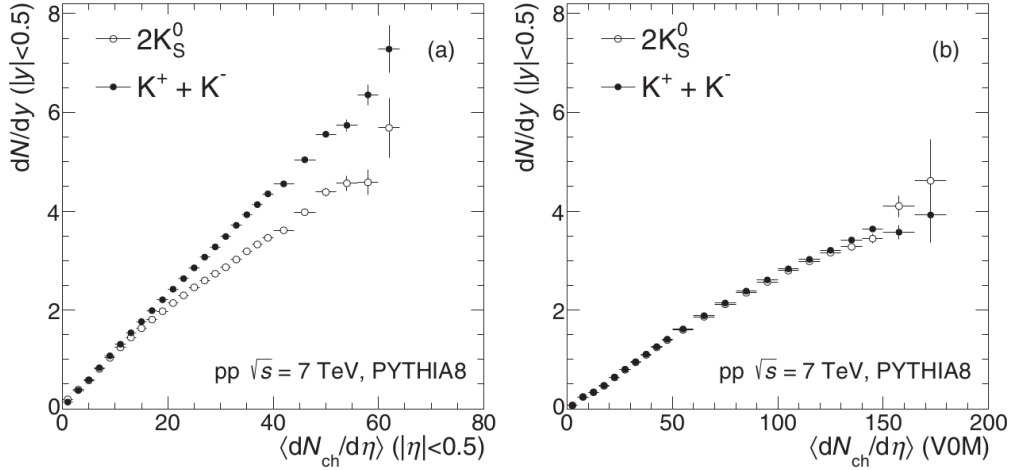


**Figure 5.5:** Comparison of neutral-to-charged kaon production for multiplicities measured at midrapidity (left) and forward rapidities (right), for simulated pp collisions at  $\sqrt{s} = 7$  TeV. Results are taken from Fig. [89]

Each pixel diode generates a pulse when a charged particle deposits sufficient energy into the silicon. This pulse is then read out to form coordinates for two-point track segments, referred to as *tracklets*. Tracklets have a good spatial resolution and are used for both efficient vertex determination, and as an estimate of the charged-particle multiplicity at midrapidity. Most ALICE analyses at midrapidity utilize the V0 for multiplicity estimations, to avoid biasing the multiplicity selection toward fluctuations from jets and parton showers, which can occur if the physics observable and multiplicity estimate are measured in the same pseudorapidity region. However, for the analysis presented in Chapter 7, this bias can be fully exploited, discussed more in detail in Sec. 7.3.

Tracklets are also used to find the primary vertex for each collision. The  $z$ -coordinate, of the primary vertex is initially estimated by a linear extrapolation of the  $z$ -coordinate for tracklet pairs which are close in azimuthal angle (transverse to the beam-axis). Since the two SPD layers are close to the interaction point, track bending due to the magnetic field can be neglected for the initial estimation. The primary vertex is used as an input for the full track reconstruction, where the full tracks are then used to recalculate the primary vertex with better precision.

The SDD consists of two layers of Neutron Transmutation Doped (NTD) silicon detectors. The silicon detectors are positioned as segmented, semicircular ladders, at a radius of 150 mm and 239 mm from the interaction point, for the 3rd and 4th ITS layer, respectively. Since the two SDD layers are located further away from the beam axis, each cell will have a lower track density, and therefore

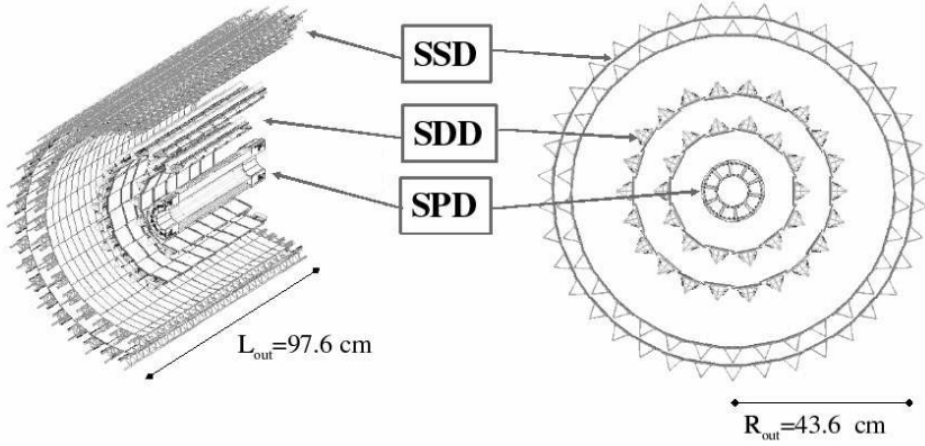


**Figure 5.6:** An illustration of the layout of the ITS, and its corresponding layers, from two different angles; an isometric view of the ITS cylindrical geometry (left), and a view of the different layers along the beam-axis (right). The Figure is taken from Ref. [81]

requires less granularity than the SPD. Each NTD silicon cell has an active area of  $70.17 \text{ mm}(x-y) \times 75.26 \text{ mm}(z)$ . Each cell is divided into two drift regions of approximately 35 mm, which are separated by a -2.4 kV potential. Once a charged particle track interacts in the drift region, it will ionize the substrate, and produce charge carriers that drift through the active volume, illustrated in Fig. 5.7. Because of the coordinate-dependent drift time, signals will be spread out in time. This gives a good multihit capability, and readout can be handled with a minimum number of electrical channels. The spatial coordinates of a particle track are then determined by measuring the drift time, compared to the drift-velocity ( $8.1\mu\text{s}$  over 35 mm, at -2.4kV), which is monitored by MOS injectors.

The two outermost layers consist of double-layered silicon strip detectors, which form the SSD. Each strip has a sensor area of  $75 \times 42 \text{ mm}^2$ . The double-faced layers of silicon are positioned back-to-back on square modules. Strips on one face have a relative pitch of 30 mrad, w.r.t. the strips on the opposite face. Spatial coordinates are determined where strips that generate a signal intersect. The SSD rows are organized in the same way as for the SSD, with radii of 378(384) mm and 428(434) mm for the inward (outward) pointing silicon face, for the two layers, respectively.

Only the SPD is utilized to estimate the midrapidity multiplicity and vertex locations. The remaining layers of the ITS are only used for track reconstruction in the analyses presented in this thesis. In total, the ITS can provide 6 spatial

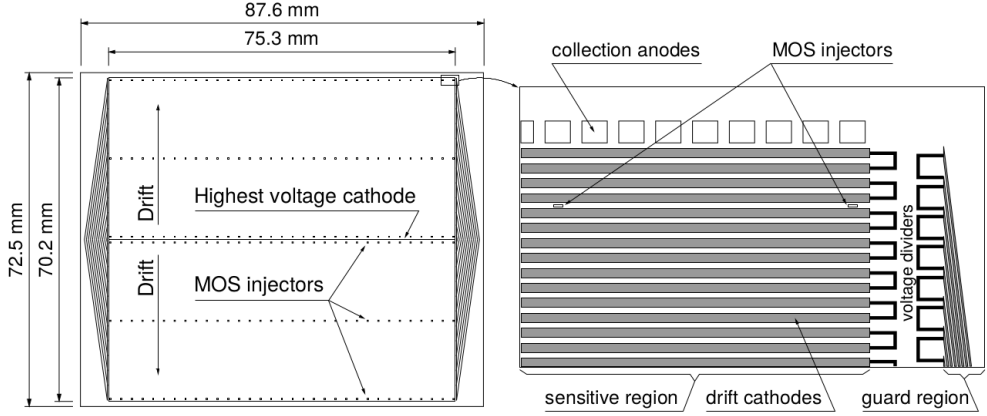


**Figure 5.7:** A schematic of the ALICE SDD cells. There are 33 MOS injectors in each row and a total of 256 collection anodes. The Figure is taken from Ref. [81]

points for each track, where 4 points in the SDD and SSD can be used to measure energy loss, which can be used for PID measurements (discussed in Sec. 5.2.6).

### 5.2.3 The Time-Projection Chamber (TPC)

The TPC is the main tracking detector of ALICE, located in the central barrel, with a cylindrical geometry across full azimuthal acceptance, and covering  $|\eta| < 0.8^5$  for full track lengths, with an outer radius of 2.5 m. As is illustrated in Fig. 5.8, the TPC has a cylindrical cut-out through the center, with a radius of 85 cm, to accommodate both the beamline and the ITS.

The TPC consists of a field cage, divided into two symmetric 250 cm halves covering the interaction point, separated by a central high-voltage electrode. The field cage is filled with about a 90 m<sup>3</sup> Ne/CO<sub>2</sub>/N<sub>2</sub> gas mixture, in relative parts of (18:2:1)<sup>6</sup>. Neon is used as the main ionizing agent, allowing for operations at a very low drift velocity, with low diffusion and low radiation length coefficients. A negative voltage of 100 kV is applied to the central electrode, which will create an axial electric field of 400V/cm along the beam-axis, resulting in a drift velocity of 2.7 cm/ $\mu$ s, with a maximum drift time (from an electron having to traverse the full 250 cm) of 92 $\mu$ s.

<sup>5</sup>The TPC covers up to  $|\eta| < 0.9$ , however, the particle reconstruction efficiency drops sharply around  $0.8 < |\eta| < 0.9$ . Therefore, outside technical tests, the TPC is only used to reconstruct charged particles up to  $|\eta| < 0.8$ .

<sup>6</sup>In official ALICE documentation this is often written as (90/10/5). One should keep in mind that these are relative parts, and note relative fractions of the total gas volume

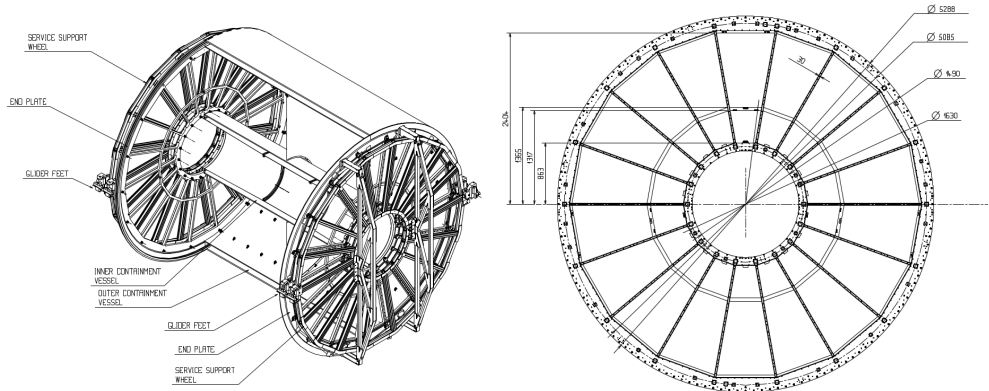


**Figure 5.8:** Schematics of the ALICE TPC from two different perspectives; an isometric view of the cylindrical field cage (left), and a view of the read-out chambers along the beam-axis (right). The Figure is taken from Ref. [81]

Readout chambers are positioned at the opposite end of the central electrode, divided into two radially segmented sections, an inner readout chamber (IROC) covering  $84.8 \text{ cm} < r < 132.1 \text{ cm}$  and an outer readout chamber (OROC), covering  $134.6 \text{ cm} < r < 244.6 \text{ cm}$ . In the azimuth, there are 18 IROC and OROC chambers, composing one of the two readout planes of the TPC. Each readout chamber consists of an array of multi-wire proportional chambers (MWPC). The geometry of each MWPC is illustrated in Fig. 5.9, consisting of three wire planes (gating grid, cathode, and anode wires) facing the drift volume. A 1.5 kV potential is applied to the anode wire, creating a strong electric field near the anode wire. Circuit boards are placed near the anode wire, with etched-out pads for signal readout. The readout pads are organized in rows along each cathode wire, to read out the charge produced from the electron avalanches. The size of each pad in the IROC is  $4 \times 7.5 \text{ mm} (\phi \times r)$ , while the OROC has two different pad sizes<sup>7</sup>:  $6 \times 10 \text{ mm}$  and  $6 \times 15 \text{ mm}$ . The IROC holds 63 pad rows, whereas the OROC holds 96 pad rows. This totals into 159 pad rows (maximum spatial points for track reconstruction<sup>8</sup>). Each IROC and OROC hold 5504 and 9984 readout pads, respectively, which totals approximately 560 000 readout pads for the entire detector. The detector is non-sensitive in the regions where the different readout chambers meet, corresponding to 10% of the total azimuthal acceptance. This creates narrow azimuthal regions with poor reconstruction efficiency for intermediate-to-high  $p_T$  (mostly radial) tracks, which is discussed in more detail in Sec. 8.2.

<sup>7</sup>Each pad covers multiple cathode wires, given that the spacing between wires (on average 2 mm) is smaller than each pad.

<sup>8</sup>In Chapter 6, these pad rows are sometimes referred to as the “number of crossed TPC rows”.

The basic operating principle of a TPC is that of a gaseous detector used to measure ionizing radiation. A charged particle traversing the gas volume creates electron-ion pairs through ionization. By applying an external electric field over the gas, the electron-ion pairs will drift apart, instead of recombining[p. 204] [90]. The electrons will drift toward the readout chambers, whereas the ions will drift toward the central electrode. An electron avalanche will occur once the drifting electrons approach the anode inside the MWPCs, which will amplify the signal. The amplification is read out by the readout pads, resulting in an  $x - y$  coordinate. Since the charge is smeared over several pads in a single pad row (referred to as a *cluster*), one gets a resolution of approximately 1 mm [91]. The electron avalanche is eventually quenched by the CO<sub>2</sub> component in the gas mixture, which is also included to prevent secondary ionization from ultraviolet photon emission. CO<sub>2</sub> was selected over other typical quenching gasses, such as CH<sub>4</sub> and CF<sub>4</sub>, due to CO<sub>2</sub> having better aging properties<sup>9</sup>. The quenching, as well as the overall stability of the gas, is improved by adding N<sub>2</sub> into the gas mixture.

The electron avalanche from the MWPC will produce a large number of positive ions that drift back toward the negative potential of the central cathode. This is not an issue on an event-by-event basis, since electrons produced from the particle track drift faster than the ions produced during the amplification (due to their difference in mass). However, this could potentially create space-charge distortions for consecutive events, as newly ionized electrons would have to drift against ions that were produced in an earlier event. To maintain good spatial accuracy, each MWPC is equipped with a gating grid of wires. Once an L1 trigger signal is received<sup>10</sup>, the gating grid will open for the duration of one electron drift interval (approximately 92 $\mu$ s). At this stage, the gating wires in each readout chamber are given the same potential, making the gating transparent to electrons and ions alike (same electric field as the external drift field), which allows for electrons in the drift volume to pass into the amplification region. The gating grid will then close by applying an alternating potential between the wires in the grid, creating an electric field transverse to the drift field, and thus catching both electrons and ions. This is crucial for the ions, as the gate prevents them from entering the long drift region of the TPC, which would take the ions many milliseconds to traverse. The gating grid must not be opened until all ions have been captured, which consequently limits the interaction rate of the ALICE TPC to about 3 kHz.

The charges collected by the 560 000 pads are further amplified and digitized into

---

<sup>9</sup>Perhaps most importantly, to avoid 90 cubic meters of flammable gas in the experiment.

<sup>10</sup>The L1 signal is sent from the ZDC, approximately 6.5  $\mu$ s after the collision.

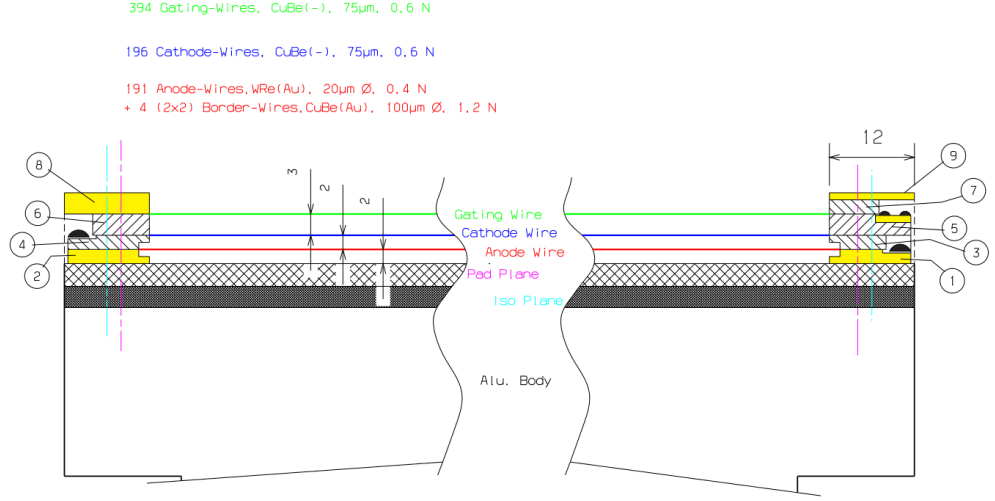


**Figure 5.9:** A schematic of the MWPC configuration in the ALICE TPC, including the wire used for the gating grid. The Figure is taken from Ref. [81]

signals by the front-end readout electronics. While the spatial  $x$ - $y$  coordinates are determined by the clusters that have read out an electric impulse from the MWPC, the  $z$ -coordinate is determined by measuring the drift time between the L0 trigger, to when the charge is detected in the readout pads. More information about the digitization of the readout signal and data acquisition can be found in Ref. [81].

## 5.2.4 Time-of-Flight Detector

The TOF detector consists of a cylindrical array, with full azimuthal coverage, consisting of  $18(\phi) \times 5(z)$  individual sectors. Each sector houses 15-19 multi-gap resistive-plate chambers (MRPC), which are gaseous detectors used to measure the time-of-flight arrival time for charged particles, for a total of 1593 [81] MRPC strips. The main design purpose of the TOF detector is to provide particle identification of massive particles, by measuring the time-of-flight relative to the momentum of each reconstructed track.

An MRPC consists of a stack of resistive plates (in the case of ALICE, two rows of 5 glass plates surrounded, by anode and cathode plates, illustrated in Fig. 5.10). The resistive glass plates are spaced with nylon fishing lines to create gas gaps, filled with a mixture of  $\text{SF}_6$  and  $\text{C}_2\text{F}_4\text{H}_2$ . A 6.5 kV potential is applied symmetrically w.r.t. the middle plate in each MRPC stack. The potential is only applied between the outer-to-middle stack, while the in-between stacks are



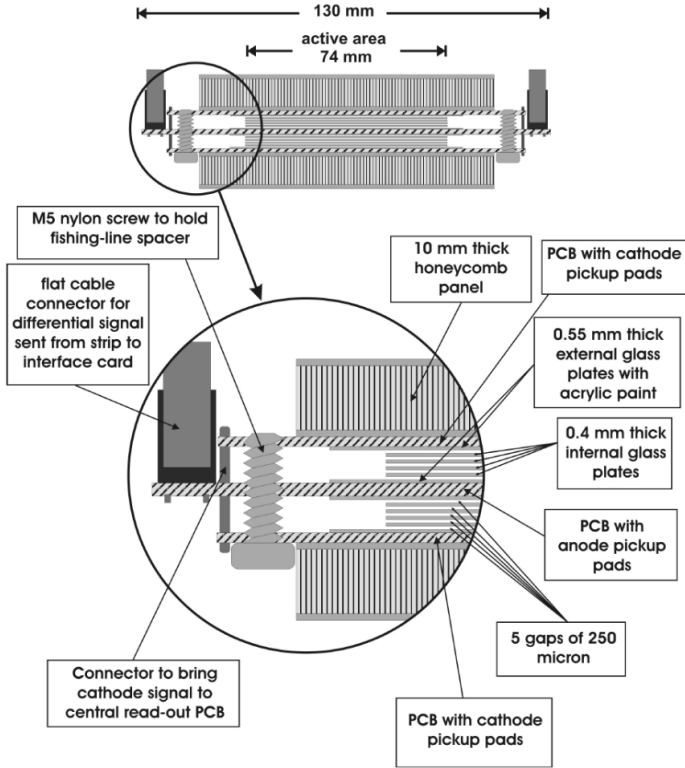


**Figure 5.10:** Illustration of the cross-section in a single MRPC module, used in the TOF sub-detector in ALICE. Schematic is taken from Ref. [81]

left electrically floating. When a particle traverses the MRPC stack, an electron avalanche is produced in each gas gap. The resistive plates themselves are transparent to the electromagnetic signal generated by the electron avalanches, thereby allowing one to retrieve the full signal deposited on the external electrodes, by integrating the signal produced in each gas gap. The narrow gaps allow for more precise time measurements, as the time jitter scales with the propagation distance (from plate to plate) through the gas. This allows for a very precise measurement of the arrival time of each particle, with a time resolution of less than 50 ps [92].

### 5.2.5 Charged Particle Track Reconstruction

The reconstructed charged particle tracks in this thesis will utilize spatial coordinates from both the TPC and ITS. The trajectory fit is based on a Kalman

filter [81][93], which can iteratively estimate a trajectory that is perturbed by noise and stochastic losses. The Kalman filter requires a *seed* to start the fitting procedure, and a stable fitting procedure relies on establishing a “good” seed [91]. The seed is estimated in the TPC but requires a primary vertex to be found by the ITS. A parameterized helix is fitted by finding pairs of points, one in the outer rims of the TPC, and the second point 20 pad rows inwards, both pointing toward the primary vertex. The helix parameterization is taken as an estimate of the full trajectory, and a Kalman filter is started, limited to the 20 points between the initial pair that point toward the primary vertex. If the majority of the points between the initial pair are successfully associated with the track candidate derived from the helix parameterization, the seed is considered good<sup>11</sup>.

When a seed has been established, a full Kalman filter procedure is started, propagating from the outermost point of the TPC, inwards to the ITS. The track information is updated for each space point compatible with a track prolongation through the Kalman filter. Once the Kalman filter has swept through all available data points in the TPC, a new Kalman filter is started in the ITS, using the track parameterization from the TPC. The inward track propagation is done twice, first with the primary vertex as a fixed constraint, and then without this condition. This is done to identify if particle tracks are associated with the primary vertex, or come from secondary decays (kinked tracks, or weakly-decaying particles, described in detail in Sec. 6.2.1).

Once the Kalman filter has created a track parameterization in both the TPC and ITS, a new Kalman filter is started in the opposite direction, from the ITS and outwards. The track parameterization from the inwards propagation is used as an initial seed for outwards propagation, allowing for a more precise fit, rejecting points that were outliers in the inward propagation. Particularly, the outward extrapolation is performed out to the TOF detector, where momentum from the TPC is matched with TOF hits. Finally, the track can potentially be fitted a third time, by re-fitting the original track parameterization, going inward from the rim of the TPC, down to the ITS, where information from the outwards fit is used as the initial seed. This third *refit* is referred to as the TPCRefit and ITSRefit, for each respective detector, and can be used as an additional requirement for track reconstruction quality assurance. A figure illustrating the entire procedure, from initial fit, to outwards fit, to refit, is illustrated in Fig. 5.11.

---

<sup>11</sup>To avoid biases, a second seed-finding procedure is started, which looks for track pairs shifted inwards by 10 rows

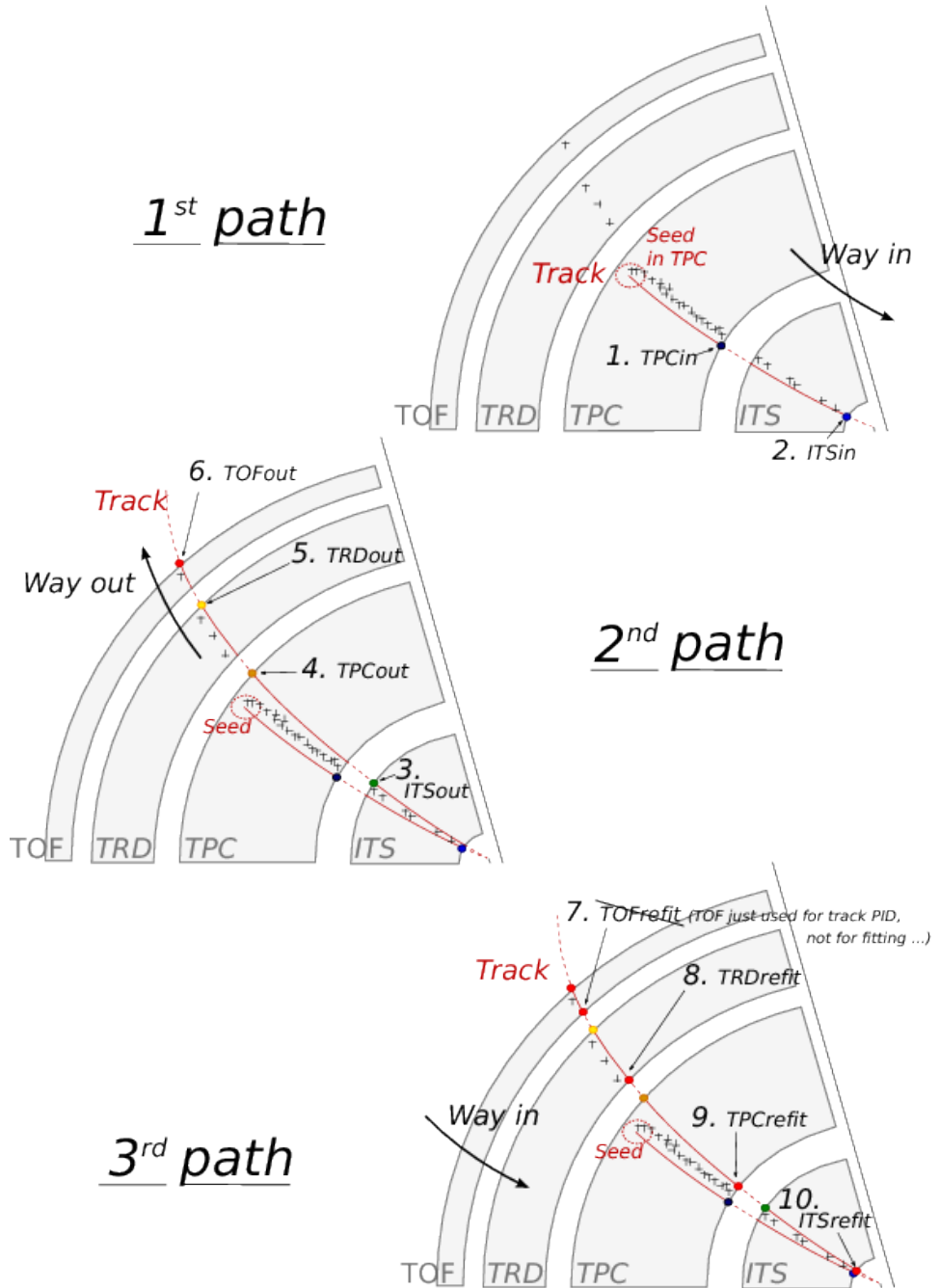


**Figure 5.11:** An illustration of the three Kalman filters used for the full reconstruction of charged particle tracks in ALICE. See text for details. Figure is taken from Ref. [94]

## 5.2.6 Particle Identification

### Particle identification through energy loss

Particles traversing material will lose energy with respect to the length the particles travel. In a gaseous detector, such as the TPC, the deposited energy in the readout chambers is directly proportional to the number of initial ionizations that were collected from the detected particle track<sup>12</sup>, which in turn is proportional to the energy deposited into the gas itself. The average energy loss per unit length  $\langle dE/dx \rangle$  (also referred to as “stopping power”) for a quantum mechanical description of a collision process can be obtained through the Bethe-Bloch formula:

$$\langle dE/dx \rangle = \frac{4\pi\alpha^2 h^2 Z^2 n_e}{m_e \beta^2} \left[ \ln \left( \frac{2m_e c^2 \beta^2 \gamma^2}{I} \right) - \beta^2 - \frac{\delta(\gamma)}{2} \right], \quad (5.1)$$

where  $I$  the ionization potential,  $m_e$  the electron mass, of  $n_e$  electrons,  $Z$  the atomic number, and  $\alpha$  the fine-structure constant. The Lorentz factor  $\gamma$  and the absolute velocity  $\beta$ , are defined in terms of momenta, expressed as:

$$\begin{aligned} \beta &= \frac{p}{\sqrt{p^2 + m^2}} \\ \gamma &= \sqrt{1 + \left(\frac{p}{m}\right)^2}. \end{aligned} \quad (5.2)$$

In the ALICE TPC, the momentum of particles is estimated by measuring the *larmor radius*  $\rho$ , which is a measurement of a particle’s track curvature with charge  $q$ , due to the external magnetic field  $B$ :

$$B \cdot \rho = p_T/q \rightarrow p_T = B \cdot \rho \cdot q. \quad (5.3)$$

Furthermore, the energy-loss measurement in ALICE relies on a different parameterization compared to the theoretical Bethe-Bloche formula. This is because the Bethe-Bloch formula presented in Eq. 5.1 includes all sources of energy loss, while ALICE only measures the ionization energy loss (and no  $\Delta$  electrons). This modified parameterization is expressed as [91]:

$$dE/dx = \frac{P_1}{\beta^{P_4}} \left( P_2 - \beta^{P_4} - \ln \left[ P_3 + \frac{1}{(\beta \cdot \gamma)^{P_5}} \right] \right). \quad (5.4)$$

---

<sup>12</sup>This is only valid if the external voltage is within the *proportional region*. Detectors that operate at higher voltages, such as the Geiger-Muller tube, will not have a direct proportional response between incoming-and-outgoing charge.

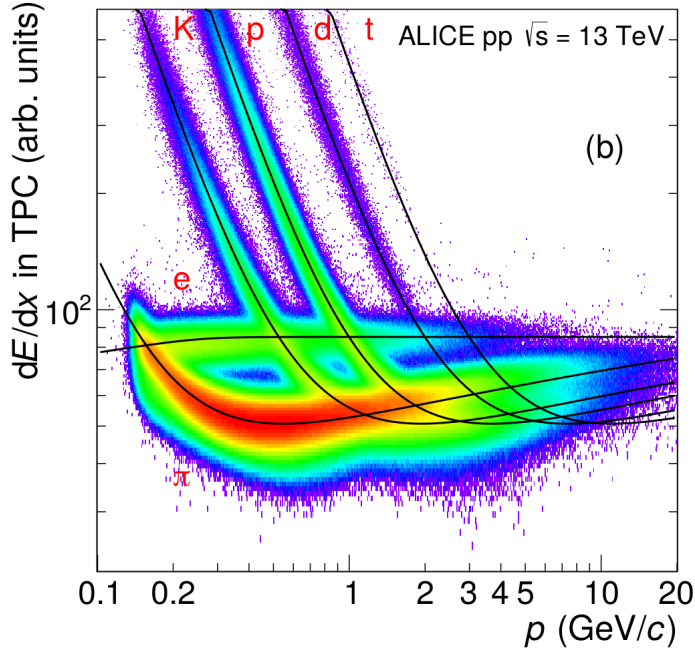


**Figure 5.12:** ALICE performance measurement of  $dE/dx$  for pp collisions at  $\sqrt{s} = 13$  TeV. Black lines are fits from the parameterized Bethe-Bloch formula in Eq. 5.4. See text for details. Figure is taken from Ref. [95]

Parameters  $P_1$  through  $P_5$  are free parameters that are calibrated by fitting the energy-loss measurements in a gas mixture for a known particle mass.

The  $dE/dx$  as a function of momentum for pp collisions at  $\sqrt{s} = 13$  TeV measured in ALICE, for different particle masses, is presented in Fig. 5.13. The figure highlights clear, identifiable bands for primary  $\pi, K, p$  particles (as well as deuterons) at low-to-intermediate momenta. The overall  $dE/dx$  resolution depends on the charged-particle density, with an approximate 5.5% smearing of the resolution in pp collisions [81]. At larger momenta, where  $\beta \rightarrow 1$ , distinguishable particle bands start to mix, which makes it difficult to accurately identify particles on a track-by-track basis. Information from the TOF is used for PID (which is described in the following) at intermediate momenta. For higher momenta, one has to utilize statistical methods to extract the yield of different particles. For the analyses presented in this thesis, primary  $\pi, K, p$  are identified through  $n\sigma$  distributions. The  $n\sigma$  information is available from the central processing of ALICE data. The reconstructed detector  $dE/dx$  response is compared to the expected detector response for each particle mass. The reconstructed distribution includes contamination from other particles at higher- $p_T$ . Since the energy-loss distribution has very broad tails toward higher momenta, the truncated mean of the energy-loss is measured for each particle

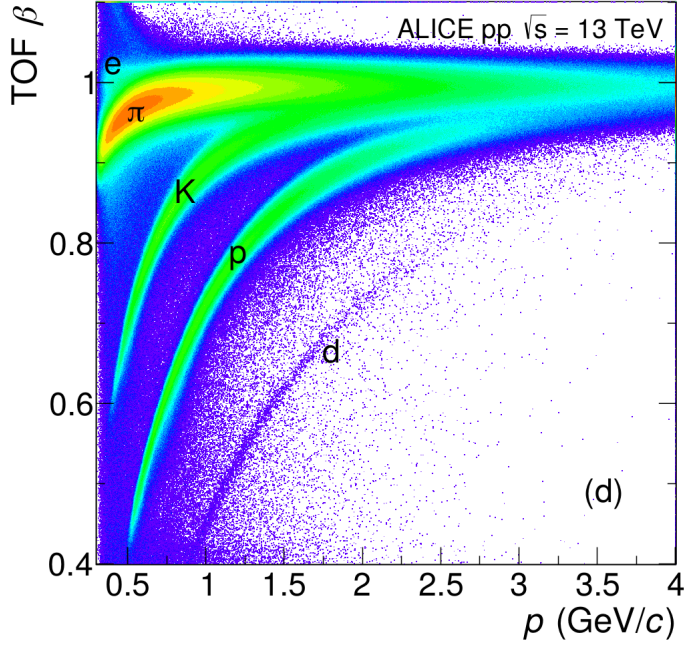


**Figure 5.13:** ALICE performance measurement of  $\beta$  for pp collisions at  $\sqrt{s} = 13$  TeV. See text for details. Figure is taken from Ref. [95]

track instead of the average energy-loss, resulting in an approximately Gaussian response. A clean sample (at low momentum, c.f. Fig. 5.13) is used to produce clean curves, which are extrapolated to higher momentum. The TPC response for each particle mass can be estimated through Gaussian distributions, where the deviation between the reconstructed and expected distributions are quantified in terms of the expected resolution,  $n\sigma$ , defined as:

$$n\sigma = \frac{dE/dx_{\text{measured}} - \langle dE/dx_{\text{expected}} \rangle}{\sigma}. \quad (5.5)$$

Through this technique, it is possible to identify particles on a track-by-track in the clean regions (low- $p_T$ ), where the probability to be of an identified particle mass is proportional to  $n\sigma$ , and via statistical methods in regions where the bands overlap (high- $p_T$ ). A smaller  $n\sigma$  allows for higher purity, at the cost of reduced efficiency and limiting statistics.

## Particle identification through time-of-flight

Similarly to energy loss, particles can be identified by measuring the velocity  $\beta$ , which can be obtained through the time-of-flight measurement in the TOF detector, together with the momentum from the TPC. This requires an extrapolation of the tracks in the TPC to match the TOF detector. The time-of-flight for a distance of  $L$  can be expressed as:

$$\begin{aligned}\Delta t_{\text{TOF}} &= \frac{L}{\beta c} = \frac{L}{c} \sqrt{\frac{p^2 + m^2}{p^2}} \longrightarrow \\ \beta &= \frac{L}{\Delta t_{\text{TOF}} c}\end{aligned}\tag{5.6}$$

Since the time-of-flight in Eq. 5.6 depends on mass, each massive particle will have a distinct curve in absolute velocity, as a function of momentum. The  $\beta$  measured by ALICE for pp collisions at  $\sqrt{s} = 13$  TeV is presented in Fig. 5.10. Compared to the TPC PID in Fig. 5.13, the TOF PID allows for a cleaner separation between particle species toward larger momenta. Similarly to the  $dE/dx$  measurement, primary  $\pi, K, p$  for the analyses presented in this thesis are obtained from  $n\sigma$  distributions. One of the main caveats for the TOF  $n\sigma$  measurement is that, unlike the  $dE/dx$ ,  $\beta$  is not well-described by a Gaussian distribution, and has a much broader tail (decaying as  $e^{-\beta}$ ), which has to be incorporated in the modeling between measured-and-expected value. Utilizing PID information from both the TPC and the TOF leads to a precise, track-by-track identification of particles at low-to-intermediate  $p_T$ .

# Part III

## Main Analyses



# Chapter 6

## $\phi$ Meson and $\Xi$ Baryon Reconstruction

This chapter will detail the procedure for identifying and reconstructing  $\phi(1020)$  mesons and  $\Xi^\pm(1322)$  baryons as functions of  $p_T$ .  $\Xi^\pm$  will simply be denoted as  $\Xi$  in the following, describing the reconstruction procedure for particle and antiparticle alike. The extraction techniques described in this Chapter will apply to the analyses presented in Chapter 7 and Chapter 8 unless otherwise stated. Minor caveats apply, which are discussed in the respective chapters.

### 6.1 Common Event Selection

The results presented in this thesis are obtained from collisions measured during the LHC Run 2 pp program, running from 2016-2018. The dataset corresponds to roughly 1.2 billion events. Rigorous cross-examinations for both  $\Xi$  and  $\phi$  analyses were performed to ensure consistency of the extracted yield between each run year. The measurement of pions, which in this thesis is used as a baseline for both  $\phi$  and  $\Xi$ , excluded data gathered from 2017. This was done due to a change of gas mixture used in the TPC, which negatively affected the  $dE/dx$  performance for primary  $\pi, K, p$  analyses [19]. Excluding the 2017 dataset, the combined dataset measured during the years 2016 and 2018 yields approximately 820M events.

Each run period (a period with a consistent ALICE configuration) of data recording also has a corresponding Monte Carlo (MC) production. The MC

datasets were produced by generating PYTHIA 8 events and propagating them through a full simulation of the ALICE detector. The detector simulation is constructed using the GEANT3 framework; software which is designed to simulate particle transport and interaction properties with matter [96]. The generated events are propagated through a virtual version of the ALICE detector, where GEANT3 signals are digitized to look like real data, and then reconstructed according to the standard reconstruction procedure. The efficiency and resolution of the ALICE detector can be estimated by comparing the original, generated event, to the corresponding event after reconstruction. The datasets are “anchored” to the run periods, in a sense that the GEANT3 digitization matches the ALICE configuration used for data taking during each run period. This includes, but is not limited to, matching the gas mixture in the TPC, the detector status (high-voltage and magnetic field strengths, etc.), and calibration procedures. Each anchored simulation contains approximately 25% of the events measured for each corresponding period, yielding  $\approx 190\text{M}$  and  $\approx 300\text{M}$  events for the 2016+2018 and 2016+2017+2018 datasets, respectively.

A standard event selection is applied to the entire Run 2 dataset, to ensure that events with incomplete detector information, or events without a precisely defined primary vertex, are rejected. This selection is required in addition to the analysis-specific event selections discussed in Chapter 7 and Chapter 8. The event selection must be applied consistently between all measured particles for a given observable for all analyses. This allows for an “apples-to-apples” comparison between the measured yields of each particle. Events are required to pass the following criteria:

- Standard ALICE physics selection, with a minimum bias trigger threshold. For the run periods analyzed in this thesis, the minimum bias trigger requires a hit in both V0A and V0C detectors. Furthermore, considered events have to be inelastic ( $\text{INEL} > 0$ ), requiring at least one charged track reconstructed at  $|\eta| < 0.8$ .
- Events with incomplete information from the data acquisition are rejected. This includes events where sub-detectors fail mid-run, and full event information is not retained.
- Events are required to have a primary vertex reconstructed by the SPD. This vertex is required to have a resolution in the  $z$  plane within 0.25 cm and with a dispersion no greater than 0.04 cm. This is to ensure that there is a primary vertex produced in the bunch-crossing. Broader vertices are likely to include multiple vertices, either from overlapping bunch-crossings or secondary decays.

- The primary vertex z-position  $|v_z|$  is required to be within  $|v_z| < 10$  cm of the ALICE midpoint. This requirement is implemented such that the primary vertex is within the luminous region of ALICE, and ensures consistent kinematic properties between different events.
- Multiple constraints are implemented to reject *pile-up* events. There are two different forms of detector pile-up; *in-bunch pile-up* and *out-of-bunch pile-up* (OOB pile-up). The former arises from overlapping or broad vertices formed during the same bunch-crossing, whereas the latter arises from vertices produced from different bunch-crossings. OOB pile-up is mainly produced due to the TPC being a slow detector. To reject these events, a hit in the SPD has to be connected to the primary vertex. The SPD is a fast detector, ensuring that tracks<sup>1</sup> in the event are associated to a reconstructed primary vertex. The V0 minimum bias triggers are required to synchronize with tracks detected in the SPD, which removes in-bunch pile-up. OOB pile-up is rejected if a particle track cannot be associated with either of the faster SPD or TOF detectors.

Approximately 15% of events from the entire 2016+2017+2018 pp dataset are rejected according to the above criteria. The largest source of rejected events is due to vertices outside of  $|v_z| < 10$  cm, followed by events with no/mismatched reconstructed vertices.

## 6.2 Reconstruction & Identification of $\phi$ (1020) Mesons

The  $\phi$  meson is a neutral, strongly-decaying hadron. The  $\phi$  meson is a resonance particle, with a lifetime of  $10^{-23}$  s. While this is relatively long-lived for a resonance particle, it is too short to detect directly. Instead, we have to detect it statistically, by reconstructing the *invariant mass*  $M_{inv}$  of the constituent decay daughters. If  $m_{1,2}$  and  $p_{1,2}$  are defined as the total mass and momentum for each respective daughter, the  $M_{inv}$  is calculated as:

$$M_{inv}^2 = (p_1 + p_2)^2 = m_1^2 + m_2^2 + 2p_1 p_2 \quad (6.1)$$

The three largest branching ratios of  $\phi$  meson decay are listed in Table. 6.1 [97]. The 2nd and 3rd decay modes pose considerable experimental challenges, as  $K_S^0$ ,  $K_L^0$  and  $\rho$  are neutral particles, which cannot be detected directly by the TPC, and have complex, three-body decays. Therefore, for the work presented here,

---

<sup>1</sup>These are not fully-reconstructed tracks, but *tracklets*, defined in Sec. 5.2.2.

the  $\phi$  meson yield is reconstructed through the decay mode with the largest branching ratio:  $\phi \rightarrow K^+ + K^-$ .

**Table 6.1:** The three most common decay modes for  $\phi$  meson resonances. Data is taken from the Ref. [97].

Decay Mode	Branching Ratio
$\phi \rightarrow K^+ K^-$	$48.9 \pm 0.5\%$
$\phi \rightarrow K_L^0 K_S^0$	$34.2 \pm 0.4\%$
$\phi \rightarrow \rho\pi + \pi^+ \pi^- \pi^0$	$15.32 \pm 0.32\%$

Due to the short lifetime of the resonance, the kaon decay daughters created from the  $\phi$  meson are experimentally impossible to distinguish from primary, charged kaons. Consequently, this means that ALL charged particle tracks, which are associated with the primary vertex and identified as kaons, have to be considered as potential  $\phi$  decay daughters. The  $M_{\text{inv}}^2$  distribution will therefore contain a lot of background, as kaons are quite abundant (being the 2nd lightest hadron).

### 6.2.1 Reconstruction of $\phi$ Decay Daughters

Particle tracks are reconstructed using combined information from both the ITS and TPC, to achieve high precision in both spatial and momentum resolution. To maintain high precision on a track-by-track basis, the reconstructed tracks are required to pass a set of quality assurance criteria. Tracks that pass the following criteria are referred to as “global tracks” throughout this thesis:

1. Reconstructed tracks require a signal from at least 70 crossed pad rows in the TPC:  $N_{cr,TPC} > 70$
2. Requires the ratio between crossed rows and findable clusters<sup>2</sup> to be less than 0.8:  $R_{TPC} = N_{cr,TPC}/N_{clstr,TPC} < 0.8$
3. The reconstruction fit requires a maximum  $\chi^2$  per cluster in TPC:  $\chi_{TPC}^2 < 4$ .
4. The reconstruction fit requires a maximum  $\chi^2$  per cluster in ITS:  $\chi_{ITS}^2 < 36$ .
5. Requires a maximum  $\chi^2$  globally in the TPC across all findable clusters:  $\chi_{G,TPC}^2 < 36$ .

---

<sup>2</sup>A cluster is a segment of a pad row, which has measured current from the electron avalanches. See Sec. 5.2.3 for details.

6. Requires a converging TPCRefit
7. Requires a converging ITSRefit
8. The transverse momentum is required to be larger than  $p_T > 0.15 \text{ GeV}/c$
9. The pseudorapidity is required to be less than  $\eta < |0.8|$
10. Requires a hit in any SPD cluster
11. Requires a cut on the Distance-of-closest-approach (DCA) in the  $x - y$  plane, between the primary vertex and the reconstructed track:  $|DCA_{xy}| < 0.0105 + \frac{0.350}{p_T^{1.1}}$
12. Requires a maximum DCA from track to primary vertex in the  $z$  plane:  $DCA_z < 2.0$ .
13. Rejects secondary particles that decay through kinks (aka “kink daughters”).

The numerical values for all the above parameters have been calibrated centrally by ALICE, to optimize tracking precision relative to reconstruction efficiency. Conditions 1-7 are required to maintain good tracking precision for the reconstructed tracks. A larger number of crossed rows in the TPC results in more spatial points to fit the particle trajectory, leading to a more precise momentum resolution for each reconstructed track. The average fit quality is further improved by constraints on the maximum  $\chi^2$ , both per cluster, and globally, for each track. The tracks are also required to be “re-fitted” down towards the primary vertex, both from the ITS and TPC (discussed in further detail in Sec. 5.2.5). Furthermore, conditions 8-9 implement constraints on  $\eta$  and  $p_T$  near the boundary of the TPC acceptances, to reduce inefficiencies from fringe effects.<sup>3</sup>

Conditions 10-13 are required to ensure that there is a primary vertex in the event and that the tracks are associated with that vertex. This is done to avoid contamination from secondary particles that decay from weakly-interacting particles. “Kink daughters” are defined as secondary particles that originate from charged pions and kaons that weakly decay within the TPC volume. The decay will produce a change in curvature for the propagated track, producing a distinct kink. The kinks are identified by extrapolating tangents to reconstructed track trajectories.

---

<sup>3</sup>Both  $\eta$  and  $p_T$  are steeply falling distributions around the cut boundaries, resulting in poor reconstruction efficiencies.

If a track passes the quality criteria and is ensured to originate from the primary vertex, it must then pass additional criteria to be identified as a Kaon. This is done through central ALICE calibrations with  $n\sigma$  distributions, both from the TPC ( $dE/dx$ ) and TOF ( $1/\beta$ ). This procedure is explained in further detail in Sec. 5.2.6. One should keep in mind that this identification technique has constraints at larger momenta, where both  $dE/dx$  and  $1/\beta$  merge into a single distribution. This is referred to as the *relativistic rise*, where tracks cannot be identified on a track-by-track basis. This does not pose a significant problem for the  $\phi$  analysis, for the following reasons: First, misidentification on a track-by-track basis does not contaminate the measurement of the raw  $\phi$  meson yield. There is a second layer of identification through the  $M_{\text{inv}}$  spectra, which the raw yields are extracted from. Secondly, the combinatorial background grows with the square number of particles. The  $p_T$  distribution of charged particles is steeply falling at higher  $p_T$ . The *signal-to-background* (S/B) ratio at high- $p_T$  is therefore quite large, resulting in a low combinatorial probability for the available charged particle tracks to randomly sum to have the same  $M_{\text{inv}}$  as a  $\phi$  meson. This effect is illustrated in Fig. 6.1.

### 6.2.2 Identification of $\phi$ Mesons and Background Reduction

The  $M_{\text{inv}}$  is calculated for oppositely charged pairs of identified kaons, (passing the requirements in Sec. 6.2.1), in narrow  $p_T$ -intervals. Examples of raw  $M_{\text{inv}}$  distributions are presented in Fig. 6.1. The relative fraction of (S/B) is quite large, with  $(S/B) \approx 0.5$  around low (1-2 GeV/c)  $p_T$ .

The  $\phi$  meson mass of 1.019 GeV/c<sup>2</sup> is quite close to the combined mass of two kaons  $2M_{K^\pm} = 0.987354$  GeV/c<sup>2</sup>. Since kaon masses are assumed when calculating the  $M_{\text{inv}}$ , it is kinematically impossible for the  $M_{\text{inv}}$  of two combined tracks to be lower than  $2M_{K^\pm}$ . For this reason, the background is asymmetric around the central peak (seen in Fig. 6.2), and cannot be evaluated using the *sideband method*<sup>4</sup>

In the work presented here, four different  $M_{\text{inv}}$  spectra are constructed, to create three different estimates of the combinatorial background for  $\phi \rightarrow K^+K^-$ . An example containing all three different methods can be found in Fig. 6.2. In all

---

<sup>4</sup>This method utilizes the regions around the peak (sidebands) to estimate the combinatorial background. The sidebands are normally estimated at  $3\text{-}6\sigma$  from the central peak region. Due to the asymmetry and limited range of the left sideband, the combined sidebands will give a bad description of the combinatorial background under the peak (and also contain a non-trivial portion of the yield), therefore making this method unviable

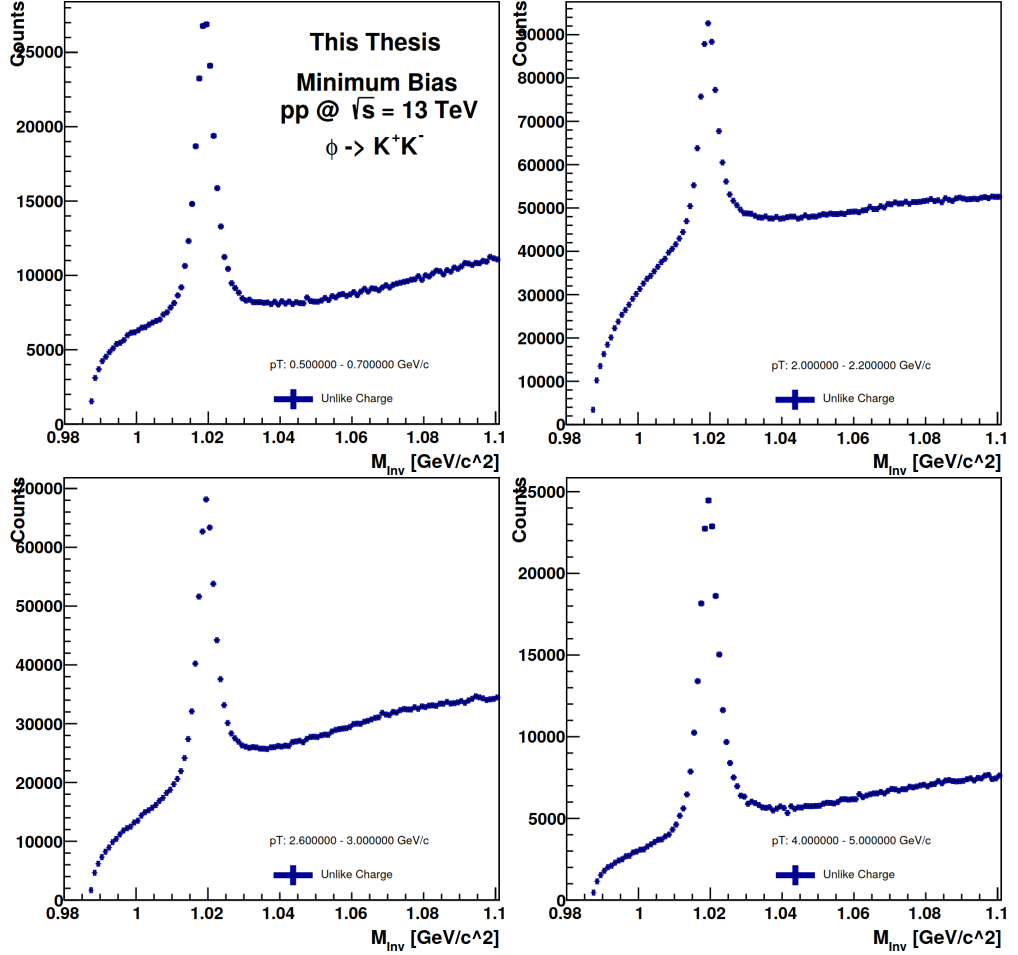


**Figure 6.1:** Invariant mass distributions of  $\phi \rightarrow K^+ + K^-$ , for minimum bias pp collisions at  $\sqrt{s} = 13$  TeV, measured by ALICE. The  $p_T$  intervals range from 0.5 - 5.0 GeV, with the lower (upper) limit presented in the top (bottom) left panels, whereas the right panels represent two intermediate  $p_T$  intervals.

cases, the background spectra are normalized to the right of the peak, far away from the central peak region (quantified in Sec. 6.2.5):

1. Like-Charge, Same-Event (**LSS**)

Invariant mass distributions are created with kaon pairs that have the same charge. The entries in the invariant mass distribution consist of the geometric mean of  $K^+K^+$  and  $K^-K^-$  pairs.

2. Unlike-Charge, Mixed-Event (**USM**)

Invariant mass distributions are created with kaon pairs with opposite

charges, originating from different events. Each event is mixed with 9 other events.

### 3. Like-Charge, Mixed-Event (**LSM**)

Invariant mass distributions are created with kaon pairs with the same charge, originating from different events. Each event is mixed with 9 other events. This is not used directly to estimate the combinatorial background but is used as a tool for the following  $M_{\text{inv}}$  spectrum.

### 4. Reweighed Unlike-Charge, Mixed-Event (**Rew. USM**)

The  $\Delta R = \sqrt{\Delta\phi^2 + \Delta\eta^2}$  is calculated for the LSS and LSM distributions. A ratio of  $\Delta R_{LSS}/\Delta R_{LSM}$  is then used as a weight to correct for the difference in topology (loss of di-jet structure, which will be discussed in the following) between same-event and mixed-events. The event-mixed distribution is then reweighed accordingly.

Under ideal conditions, the LSS  $M_{\text{inv}}$  distribution should give a good description of the combinatorial background. However, utilizing the track requirements listed in Sec. 6.2.1 results in a non-uniform azimuthal acceptance. This is partially due to non-active regions in the SPD. Consequently, the azimuthal charge acceptance is also not symmetric. Furthermore, in the context of the Lund model, production of  $\phi$  ( $s\bar{s}$ ) creates a large amount of associated strangeness, creating a kaon background that is correlated. A sum of like-sign kaon pairs is therefore not able to adequately describe the combinatorial background in the oppositely-charged channel, which can be seen in Fig. 6.2.

One can avoid the charged bias by using a technique called *event-mixing*. Here, tracks are collected from 10 different events. The  $M_{\text{inv}}$  is then constructed with individual kaons from regular events paired up with kaons from different events. This ensures, by definition, that the kaon pairs used to construct the  $M_{\text{inv}}$  spectra are uncorrelated, and can be used to estimate the combinatorial background. To ensure that the mixed events have similar detector acceptances, the largest deviation to the collision vertex in the  $z$ -plane is required to be within  $\Delta v_z < 1\text{cm}$ .

Unfortunately, the implementation of the event-mixing technique introduces a new bias. As mentioned previously, the mixed pairs are by definition uncorrelated. This also means that any information regarding the topology of the signal events is lost. For example, mixing 10 events with *di-jet topologies*, events where the majority of tracks are produced along a 180-degree jet-axis, will produce a mixed event with an isotropic topology. This effect is illustrated in Fig. 6.3. A change in angular topology will consequently lead to a change in average



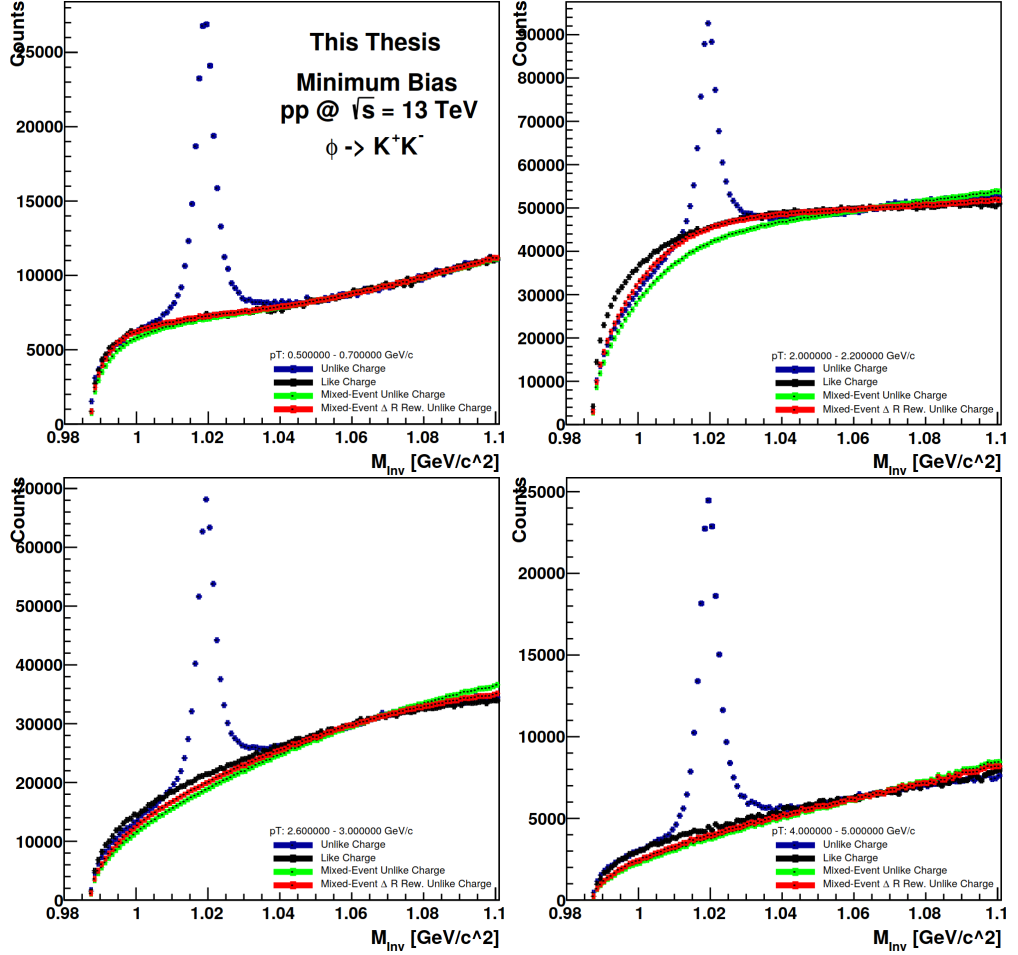


**Figure 6.2:** Invariant mass distributions of  $\phi \rightarrow K^+ + K^-$ , for minimum bias pp collisions at  $\sqrt{s} = 13$  TeV, measured by ALICE. The signal distribution is compared with three different  $M_{\text{inv}}$  spectra that are used to estimate the combinatorial background. The  $p_T$  intervals range from 0.5 - 5.0 GeV, with the lower (upper) limit presented in the top (bottom) left panels, whereas the right panels include two intermediate  $p_T$  intervals.

$M_{\text{inv}}$ , given that  $p_x$  and  $p_y$  enter into the  $M_{\text{inv}}$  calculation. Contributions to the combinatorial background originating from events with strong di-jet structures cannot be described by event-mixing alone. This will be of particular importance later when extreme di-jet topologies are studied in Chap. 7.

A technique that attempts to circumvent both of these biases has been pioneered in this thesis. Like-sign, same-event, and mixed-event  $M_{\text{inv}}$  spectra, are measured to quantify the “loss” of the correlated topology. The difference between these two spectra should be independent of any bias in charge acceptance. The difference in topology between the two like-sign spectra is estimated by measur-

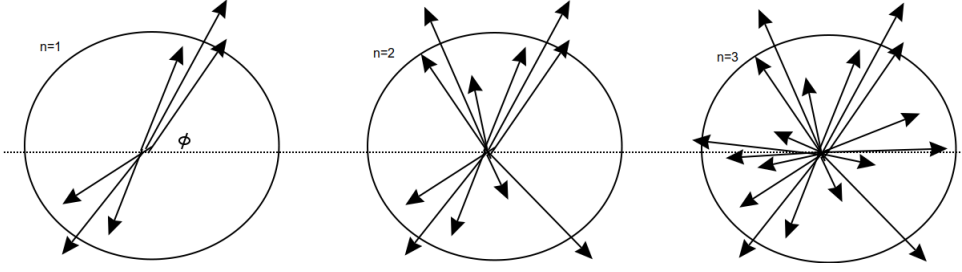


**Figure 6.3:** Illustration of how an azimuthal di-jet topology can be lost when utilizing event-mixing.  $n=1,2,3\dots$  represents the number of events mixed.

ing the *jet cone*  $\Delta R = \sqrt{\Delta\phi^2 + \Delta\eta^2}$ , as functions of both  $M_{\text{inv}}$  and  $p_T$ . Weights are constructed by taking the ratio of  $\Delta R_{LSS}/\Delta R_{LSM}$ . These weights are used to re-weigh the oppositely charged, mixed-event  $M_{\text{inv}}$  spectra, thereby creating an  $M_{\text{inv}}$  spectra of uncorrelated, oppositely charged kaon pairs, corrected for the difference in topology. The improvement of the background description is limited for minimum bias collisions but gives a more precise description of the background when measured in contrast to variables sensitive to the event topology, c.f., Appendix A. Further details on the reweighing procedure can be found in Ref. [98].

### 6.2.3 Extracting The $\phi$ Yield

Figure 6.4 highlights the  $M_{\text{inv}}$  spectra of oppositely charged kaon pairs, after subtraction of the combinatorial background by standard event-mixing (referred to as “reduced  $M_{\text{inv}}$  spectra” in the following). However, the background estimation is not perfect, therefore residual background remains after subtraction. To extract the yield, the reduced  $M_{\text{inv}}$  spectra are fitted with a combined peak function<sup>5</sup>. The combined peak function incorporates a residual background function, as well as a Voigtian function. The Voigtian function, expressed in Eq. 6.2, is defined as the convolution of a parameterized relativistic Breit-Wigner distribution, together with a Gaussian. Under ideal circumstances, a Breit-Wigner distribution should perfectly describe the peak shape, given that  $\phi$  is a resonance particle. However, the detector resolution is not constant as a function  $p_T$ , which will broaden the peak at larger momenta. A Gaussian is therefore convoluted with the relativistic Breit-Wigner distribution to account for this

<sup>5</sup>Keep in mind that Fig. 6.4 is included here for illustrative purposes. The fit functions have been calibrated for the event selection presented in Chap. 7 and Chap. 8, and therefore are not optimized for fits to minimum bias data. These fits can be found in Appendix A, highlighting a much more precise  $\chi^2/\text{ndf}$ .

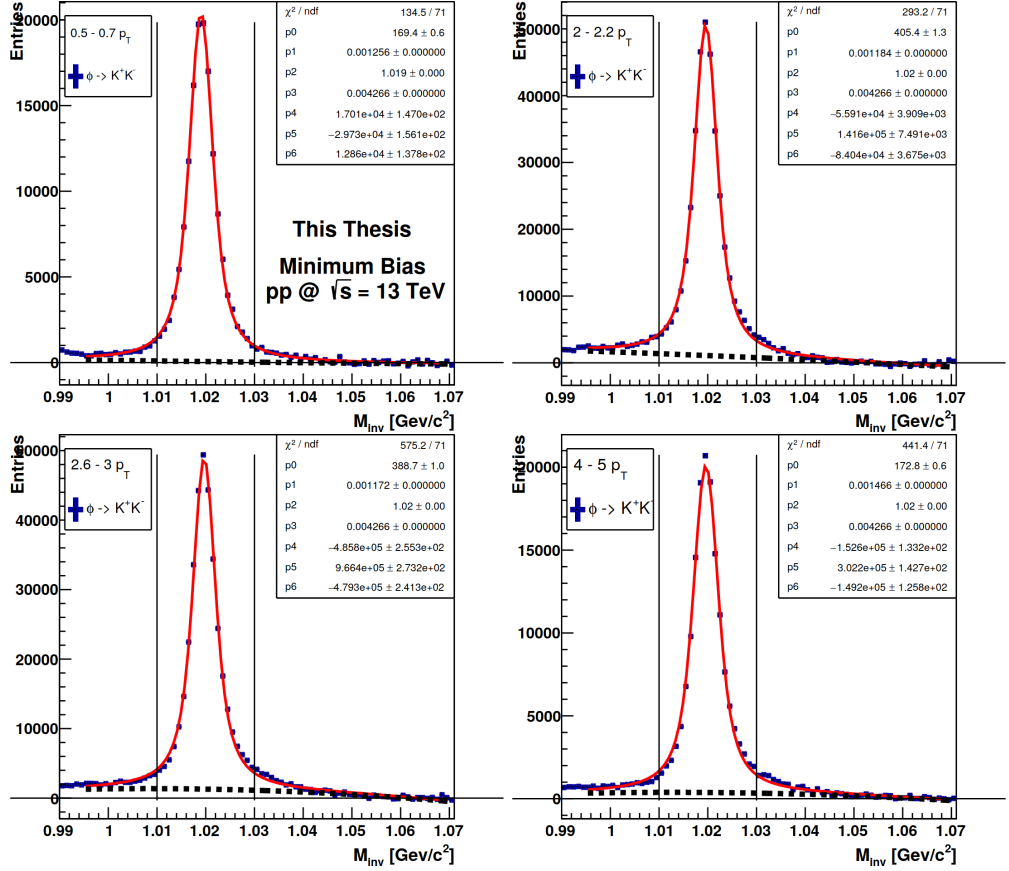


Figure 6.4: Fits to the reduced  $M_{inv}$  spectra for  $\phi \rightarrow K^+K^-$ , for the same  $p_T$  interval as shown previously. The spectra are fitted by a combined peak function, where the solid line is described by a Voigtian function and the dashed line a 2nd-degree polynomial function. The  $p_T$  intervals range from 0.5 - 5.0 GeV, with the lower (upper) limit presented in the top (bottom) left panels, whereas the right panels include two intermediate  $p_T$  intervals.

effect.

$$\text{Voig}(M_{inv}) = \frac{dN}{dM_{inv}} = \frac{p_0}{\Gamma(2\pi)^{3/2}} \int_{-\infty}^{\infty} \left( \frac{(M_{inv} - M')^2}{2\sigma^2} \right) \frac{1}{(M' - M_\phi)^2 + \Gamma^2/4} dM'. \quad (6.2)$$

$\Gamma$  and  $\sigma$  are the Breit-Wigner and Gaussian widths respectively,  $M_\phi$  is the ideal  $\phi$  meson mass (1019.455 MeV/c<sup>2</sup>), and  $p_0$  the integrated yield.

One of the most important criteria for the parameter configuration is to optimize the number of degrees of freedom to describe the peak shape, but not to the degree such that statistical fluctuations of the peak shape are also fitted. This

is particularly the case for the analyses described in this thesis, where different event classes, which have different shapes of combinatorial backgrounds, are directly compared to each other. Therefore, the same parameter configuration is used between all different event classes, to allow for differences in yield to be driven by the different event characteristics, rather than trivial differences in peak shapes. The optimized parameter configuration, which allowed for the most robust fits across different event selections and  $p_T$  bins, are as follows:

- The Gaussian  $\sigma$  was first calibrated as a free parameter on high-statistics event samples<sup>6</sup>. The same Gaussian smearing was fixed and used across the different event samples.
- The resonance width  $\Gamma$  was fixed to the vacuum expectation value (4.266 MeV/c<sup>2</sup>).
- The mean mass calibrated to the mean value of 100M simulated PYTHIA  $\phi$  mesons, seen in Fig. 6.5.
- All background parameters were left as free parameters.

Finally, the yield is extracted in two steps:

1. In the integration region around the peak  $1.01\text{GeV}/c^2 < M_{\text{inv}} < 1.03\text{GeV}/c^2$ , the polynomial background function is evaluated in the bin-center of each bin, and the raw yield  $N_{\phi}^{\text{Hist}}$  is estimated by subtracting the background from the raw entries in each bin. This difference is then summed up for each bin within the integration region:

$$N_{\phi}^{\text{Hist}} = \sum_{\text{bin}=1.01}^{1.03} (\text{USS} - \text{USM}_{\text{rew}})_{\text{bin}} - \text{B}(\mathbf{x})_{\text{bin}} \quad (6.3)$$

2. 10-15%<sup>7</sup> of the total  $\phi$  yield sit in the tails outside the central peak region. The yield in the tails are estimated by evaluating the integral of the combined peak fit, bounded outside the integration region. The upper bound integrates from 1.03 GeV/c<sup>2</sup> to infinity, while the lower bound starts from the kinematically forbidden limit  $2M_{K^{\pm}}$  up to 1.01 GeV/c<sup>2</sup>.

$$N_{\phi}^{\text{Tails}} = \int_{2M_{K^{\pm}}}^{I_{\text{min}}} \text{Voig}(M_{\text{inv}})dM_{\text{inv}} + \int_{I_{\text{max}}}^{\infty} \text{Voig}(M_{\text{inv}})dM_{\text{inv}} \quad (6.4)$$

---

<sup>6</sup>High-multiplicity reference for the  $S_{\text{O}}^{p_T=1}$  analysis described in Chap. 7, and events with a 5.0 GeV trigger for the  $R_T$  analysis described in Sec. 8

<sup>7</sup>This number is obtained from PYTHIA simulations.

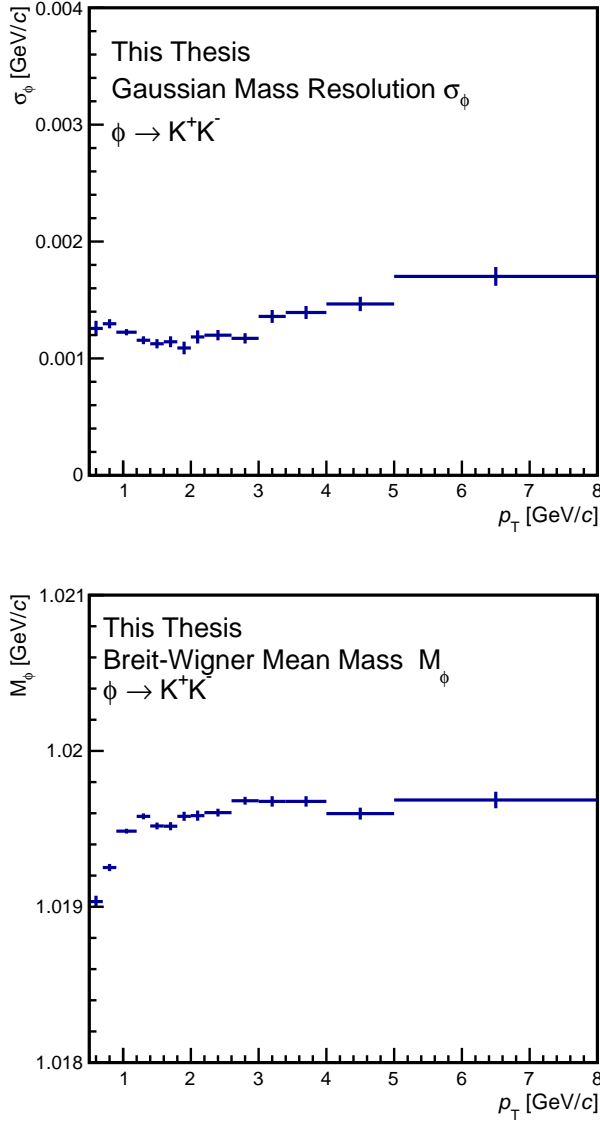


**Figure 6.5:** The Gaussian resolution  $\sigma$  (top panel), and the mean mass  $M_\phi$  (lower panel) presented as functions of  $p_T$ . The same values are applied across different event selections, to ensure that the yields are not trivially modified by changing the peak parameterization. The values are calibrated on clean peaks from PYTHIA 8 simulations.

By combining both methods, the majority of the yield is extracted directly from the  $M_{\text{inv}}$  spectra (avoiding irregularities of the peak shape due to binning effects), while retaining a good estimation of the signal present in the broad

tails. The total estimated raw yield  $N_{\phi}^{Raw}$  in each  $p_T$  interval:

$$\frac{dN_{Raw}^2}{d\eta dp_T} = \frac{1}{d\eta dp_T} \left( N_{\phi}^{Hist} + N_{\phi}^{Tails} \right). \quad (6.5)$$

#### 6.2.4 Fully Corrected $\phi$ Yields as a Function of $p_T$

The fully corrected,  $p_T$ -differential  $\phi$  spectrum is obtained as:

$$\frac{dN_{\phi}^2}{dy dp_T} = \frac{1}{N_{norm}} \frac{dN_{Raw}^2}{dy dp_T} \frac{1}{\epsilon_{corr}}. \quad (6.6)$$

The analyses performed throughout this thesis are constructed to be sensitive to the event shape, leading to a potential bias if the raw rapidity spectra were measured. Instead, the raw spectrum is measured differential to  $\eta$  and is transformed into rapidity space by using the relationship between rapidity and pseudorapidity<sup>8</sup> (also illustrated in Fig. 6.6).

$$\frac{dN_{Raw}^2}{dy dp_T} = \frac{m_T}{p_T} \frac{dN_{Raw}^2}{d\eta dp_T} \quad (6.7)$$

This approximation works well at midrapidity  $y = \eta = 0$ , and is transformed over the entire TPC acceptance for each  $\eta$  interval :  $(y(\eta = 0.8) - y(\eta = -0.8))/1.6$ .

The spectrum is corrected for both detector efficiency, and branching ratio<sup>9</sup>. As described in Sec. 6.1, the efficiency  $\epsilon_{corr}$  is estimated using simulated PYTHIA events. The efficiency  $\epsilon_{corr}$ , is calculated as a ratio:

**Numerator:** The total amount of generated  $\phi$  mesons that pass all event selection criteria, as well as the rapidity criteria  $|\eta| < 0.8$ .

**Denominator:** The total amount of reconstructed  $\phi$  mesons within  $|\eta| < 0.8$ , originating solely from the decay mode  $\phi \rightarrow K^+ K^-$ , passing all event and track selection criteria.

The  $p_T$ -differential efficiency is presented in Fig. 6.7, for different PID configurations.

---

<sup>8</sup>This relation is described in further detail in Sec. 3.1.3.

<sup>9</sup>A slight caveat applies for the analysis in Chap. 7, where the branching ratio is not corrected for. Refer to Sec. 7.2 for details

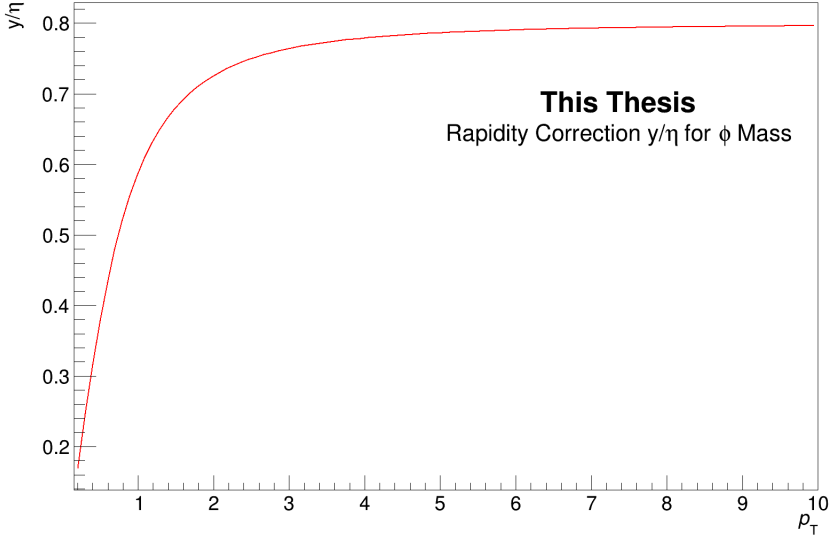


**Figure 6.6:** Conversion between  $\eta \rightarrow y$ , as a function of  $p_T$  for the specific  $\phi$  mass.

The fully corrected  $\phi$  spectrum is normalized by  $N_{\text{norm}}$ . This includes the total number of analyzed events that pass the event selection, with a correction factor for vertex loss. If the number of events with a good vertex,  $|v_z| < 10$  cm, is defined as  $N_{|vtx < 10|}$ , the number of events with a good vertex independent of position in the  $z$ -plane as  $N_{|vtx|}$ , and the number of events with a bad vertex as  $N_{\text{no vtx}}$ , the normalization factor is defined as:

$$N_{\text{norm}} = N_{|vtx < 10|} + \frac{N_{\text{no vtx}} \cdot N_{|vtx < 10|}}{N_{|vtx|}}. \quad (6.8)$$

One should keep in mind that the probability of vertex loss is larger in low-multiplicity events (too few tracks to propagate down to the vertex). This effect is negligible for high-multiplicity events, where  $N_{\text{norm}} \approx N_{|vtx < 10|}$ .

Furthermore, a signal-loss correction is normally applied to fully corrected, minimum bias  $\phi$  spectra. However, for higher multiplicities, the signal correction gives a sub-1% contribution. The signal loss is negligible for the work presented in this thesis, and therefore no correction was applied.

The corrected  $\phi$  meson yield obtained from my analysis is compared to the published ALICE results in Fig 6.8. Both the published yields and the yields obtained in this thesis are extracted from events included in the top-10% quantile

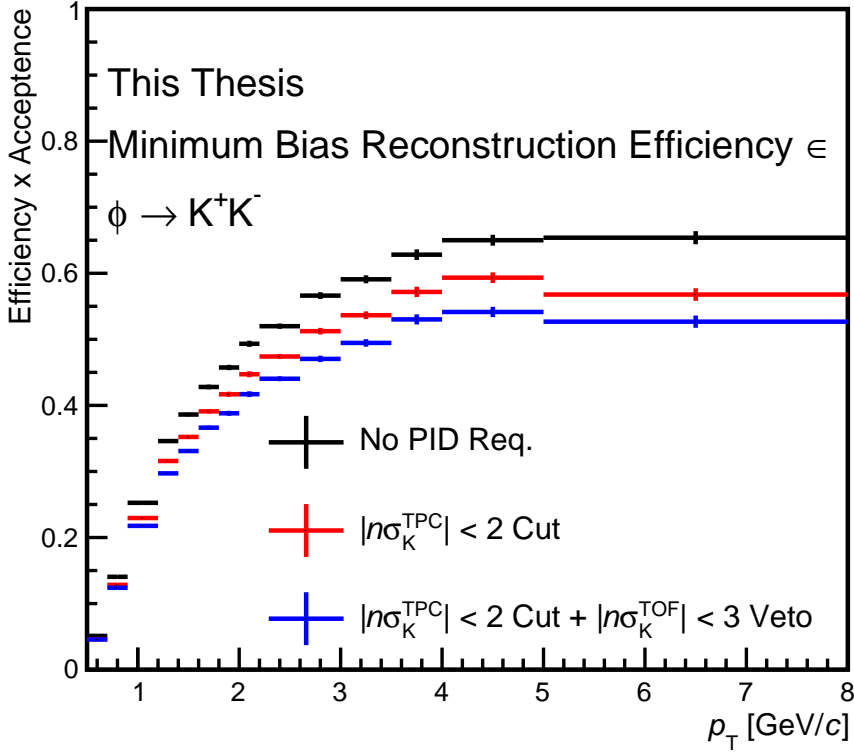


**Figure 6.7:** The detector reconstruction efficiency of  $\phi$  mesons, as a function of  $p_T$ . The efficiency is calculated by taking the ratio of generated and reconstructed  $\phi$  mesons, from PYTHIA 8 simulations propagated through a GEANT 3 simulation of ALICE. The efficiency is presented for three different PID configurations. The blue markers (bottom trend) represent the nominal PID configuration.

of the multiplicity distribution. One can see that the yield extraction presented in this thesis is consistent with prior ALICE results.

### 6.2.5 Variations considered for the systematic uncertainty in the $\phi$ analysis

Sections 6.2.1 - 6.2.4 detail the nominal configuration of parameters and techniques utilized for the full  $\phi$  yield extraction. These parameters were optimized by systematically altering the values, both through isolated and simultaneous variations. The performance of the variations was evaluated using PYTHIA simulations, where the total amount of available yield is known. In this way, one can define a robust extraction method.



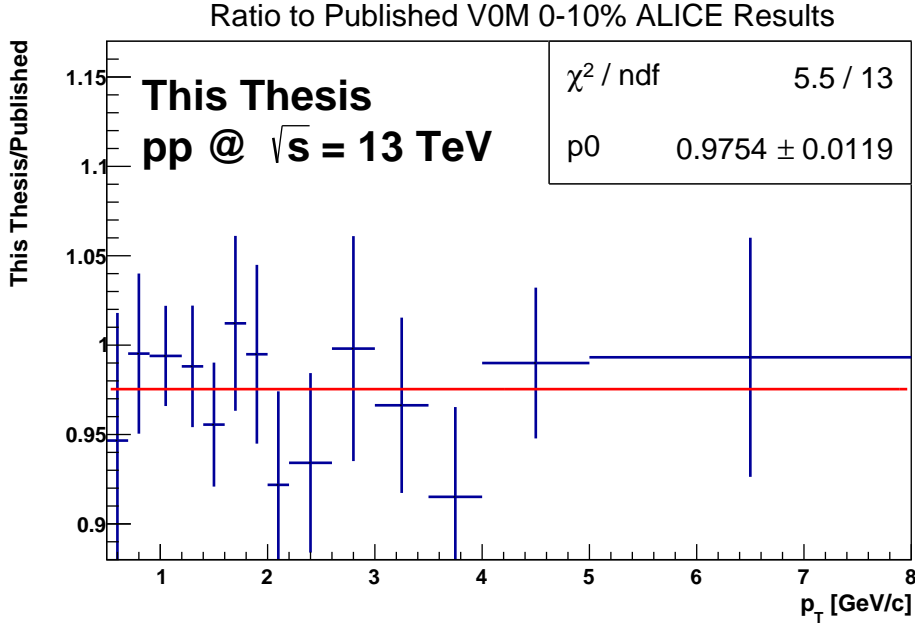


**Figure 6.8:** A comparison between the corrected  $\phi$  yield presented in this thesis, and the published ALICE data for the top 0-10% quantile (left) forward multiplicity [99]. The red line represents a 0th-degree polynomial fit. Errors are purely statistical. See text for details.

Therefore, parameter variations were used to assess the systematic uncertainty. This section will list the variations of each parameter included in evaluating the systematic uncertainty, where the variation enumerated by **1** represents the nominal configuration. The variations are then tested against the Roger-Barlow criteria, to evaluate whether the variations can be ascribed to a statistical fluctuation. This procedure is described in detail in Sec. 7.4.1. One should keep in mind that the variations described in this section were only *considered* for systematic uncertainty, and do not necessarily enter into the estimation of the systematic uncertainty. Refer to Sec. 7.4 for more details.

### Overall track quality

The overall quality requirements for global tracks were varied, where loose (tight) track criteria were tested to confirm that the analysis was robust when the efficiency (purity) is increased. The different configurations used are listed in Tab. 6.2. The different track criteria were tightened/loosened simultaneously. due to the parameters being strongly correlated with each other.

### PID configuration

The PID criteria are varied to have both looser (higher efficiency) and stricter (higher purity) variations. In ALICE, a variation without a TOF veto is some-

**Table 6.2:** The variations of parameters used to define a well-reconstructed, global track.

Cuts on Global Tracks	Nominal	Loose	Tight
Minimum Crossed Rows in TPC $N_{\text{cr}}$ :	70	50	80
Maximum $\chi^2$ for TPC Kalman fit per Cluster:	4	5	N/A
Maximum distance to vertex in $z$ - plane $DCA_z$ :	3 cm	N/A	2 cm
Cut on impact parameter in $x - y$ :	$0.0105 + \frac{0.0350}{p_T^{1.1}}/$	N/A	$0.0182 + \frac{0.0350}{p_T^{1.01}}$

times included for minimum bias analyses. However, the differential analyses presented in this thesis are constrained by low statistics. Consequently, the combinatorial background becomes so large that the yield extraction was unstable. For this reason, the variation without a TOF has not been included, as it is considered too extreme, e.g, in the  $p_T$  interval of 1-2 GeV/ $c$ , there is approximately a 10% gain in efficiency (seen in Fig. 6.7), but roughly a 50% lower S/B.

**Table 6.3:** A table showcasing the different PID configurations used for the  $\phi$  meson analysis

PID Configurations	TPC Cut	TOF Veto
<b>PID Config. 0</b>	$ n\sigma_K^{\text{TPC}}  < 2$	$ n\sigma_K^{\text{TOF}}  < 2$
<b>PID Config. 1</b>	$ n\sigma_K^{\text{TPC}}  < 2$	$ n\sigma_K^{\text{TOF}}  < 3$
<b>PID Config. 2</b>	$ n\sigma_K^{\text{TPC}}  < 4$	$ n\sigma_K^{\text{TOF}}  < 4$

## Background subtraction technique

The combinatorial background is estimated using the three techniques described in Sec. 6.2.2. Different descriptions of the combinatorial background results in varying qualities of the combined peak fit of the residual background. The performance of the three techniques varies as a function of  $p_T$ , and the difference in yield from each method is used to study the systematic uncertainty of the combinatorial background reduction.

- **Background Estimation 0:** Event-mixed  $K^+ + K^-$  pairs.
- **Background Estimation 1:**  $\Delta R$  Reweighed, Event-Mixed  $K^+ + K^-$  pairs.
- **Background Estimation 2:** Same-event, like-sign kaon pairs.

## Background normalization regions

The  $M_{\text{inv}}$  spectra used to evaluate the combinatorial background are normalized such that the integral between signal and background spectra are equal, for different regions around the central peak.

- **Normalization Region 0:**  $1.04\text{GeV}/c^2 < M_{inv} < 1.06\text{GeV}/c^2$
- **Normalization Region 1:**  $1.05\text{GeV}/c^2 < M_{inv} < 1.10\text{GeV}/c^2$
- **Normalization Region 2:**  $1.10\text{GeV}/c^2 < M_{inv} < 1.15\text{GeV}/c^2$
- **Normalization Region 3:**  $1.20\text{GeV}/c^2 < M_{inv} < 1.25\text{GeV}/c^2$

### Residual background fit function

Both 1st and 2nd order polynomials are used to estimate the residual background that remains after the background subtraction. This is correlated with how well the combinatorial background is estimated; a good estimate will yield reduced  $M_{inv}$  spectra that contain almost no residual background.

- **Fit Polynomial 0:** Linear polynomial,  $B(x) = p_0 + xp_1$
- **Fit Polynomial 1:** Quadratic polynomial,  $B(x) = p_0 + xp_1 + x^2p_2$

### Fitting ranges

The fitting ranges for the combined peak shape are varied both simultaneously and asynchronously, with tighter and looser cuts relative to the central peak. This is done to test how well the parameterization of the combined peak fit is with looser/tighter constraints.

- **Fitting Range 0:**  $0.990\text{--}1.07 \text{ GeV}/c^2$
- **Fitting Range 1:**  $0.995\text{--}1.07 \text{ GeV}/c^2$
- **Fitting Range 2:**  $0.995\text{--}1.09 \text{ GeV}/c^2$
- **Fitting Range 3:**  $0.990\text{--}1.09 \text{ GeV}/c^2$

### Central integration region

The regions where the yield is evaluated by either fit or raw histogram counting are varied around the mean of the central peak region. This is done to test the largely arbitrary thresholds for when the two different yield-extraction techniques are applied (Eq. 6.3 and Eq. 6.4).

- **Integration Region 0:**  $1.005 \leq I \leq 1.025$
- **Integration Region 1:**  $1.01 \leq I \leq 1.03$
- **Integration Region 2:**  $1.015 \leq I \leq 1.035$

**Primary vertex position relative to ALICE center in the  $z$ -plane,  $|v_z|$**   
Finally, the vertex cut along the  $z$ -plane is varied, which is used to estimate the compromise between statistics and event homogeneity.

- **Vertex Cut 0:**  $|v_z| < 5\text{cm}$
- **Vertex Cut 1:**  $|v_z| < 10\text{cm}$
- **Vertex Cut 2:**  $|v_z| < 15\text{cm}$

## 6.3 Reconstruction and Identification of $\Xi^- + \bar{\Xi}^+$ (1322) Baryons

The  $\Xi^-$  baryon and respective anti-baryon  $\bar{\Xi}^+$ , are charged, weakly-decaying particles. Both  $\Xi^-$  and  $\bar{\Xi}^+$  have to be reconstructed through the invariant mass  $M_{\text{inv}}$  of its decay constituents. The decay has a characteristic topology, seen in Fig. 6.9, which is easily resolved by the TPC, as both decays are weak. For the work presented here,  $\Xi$  baryons are reconstructed through the following decay mode

$$\begin{aligned}\Xi^- (\bar{\Xi}^+) &\longrightarrow \Lambda(\bar{\Lambda}) + \pi^-(\pi^+), & 99.887 \pm 0.035\% [100] \\ \Lambda(\bar{\Lambda}) &\rightarrow \pi^-(\pi^+) + p(\bar{p}), & 63.9 \pm 0.5\% [101] \end{aligned} \quad (6.9)$$

The decay topology illustrated in Fig.6.9 is referred to as a *cascade*. The topology of the  $\Lambda$  decay is commonly referred to as a  $V^0$ , due to the characteristic shape formed by the decay daughters. The  $\Xi$  baryons are identified through this decay topology, where the decays are long-lived enough to produce a set of three distinct vertices. The invariant masses are then reconstructed for each step of the decay, to eventually identify if it is a valid  $\Xi$  candidate. Exploiting the cascade topology yields a signal with low combinatorial background.

### 6.3.1 Cascade Reconstruction

Potential cascades are first identified through the internal, central ALICE data processing stage. Only secondary tracks are used as candidates for the cascade decay daughters (tracks outside the impact parameter cut specified in Sec. 6.2.1). The identification process involves three different steps:

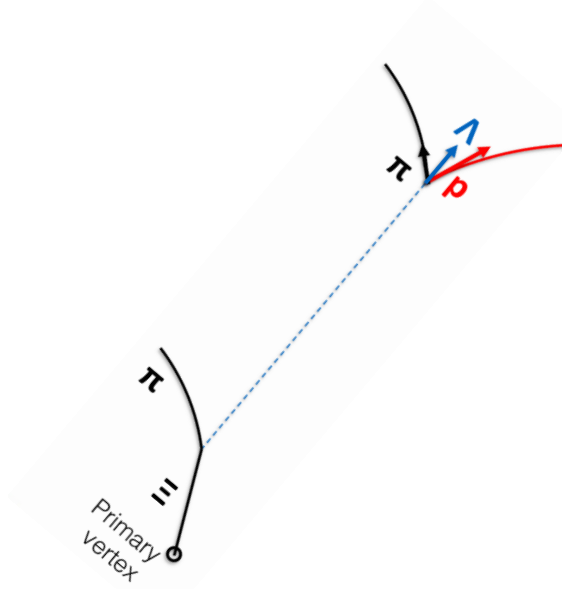


**Figure 6.9:** Illustration of the characteristic cascade decay topology. The figure is obtained from Ref. [102].

### 1. $V^0$ daughter DCA determination

First, the  $V^0$  (decay product from  $\Xi$ ) is reconstructed by identifying the decay daughters, referred to as  $\text{PID}_{\text{daughters}}$ , to reconstruct the  $M_{\text{inv}}$  of the  $V^0$ . In the case of a  $\Lambda$ ,  $\text{PID}_{\text{daughters}}$  consists of a proton and a  $\pi$  meson. The  $\text{PID}_{\text{daughters}}$  are identified by measuring the *distance-of-closest approach* (DCA) between oppositely charged particle tracks, that do not point toward the primary vertex. Potential  $\text{PID}_{\text{daughters}}$  are considered if they can be propagated to a tertiary vertex, with a DCA of less than 2 cm in the  $x - y$  plane ( $\text{DCA}_{xy}$ ). There is a possibility for two minima, depending on the curvature of the tracks. To separate these, most often false  $V^0$  signals, the radii of the curvature are compared to a hypothetical circle of the trajectory. If the two minima are identified, the DCA is determined from where the three-dimensional  $\text{DCA}_{3D}$  is minimized. This is illustrated in Fig. 6.10.

### 2. Cascade daughter DCA determination

Once a  $V^0$  is reconstructed, the algorithm identifies whether the  $V^0$  itself is produced as a secondary particle. This is done by finding a charged particle track which represents the  $\pi$  decay from the initial  $\Xi$  decay (left-most pion in Fig. 6.9), referred to as *bachelor* track, and denoted as  $\text{PID}_{\text{bachelor}}$ . If a  $\text{PID}_{\text{bachelor}}$  intersects with the extrapolated trajectory of the  $V^0$  candidate,

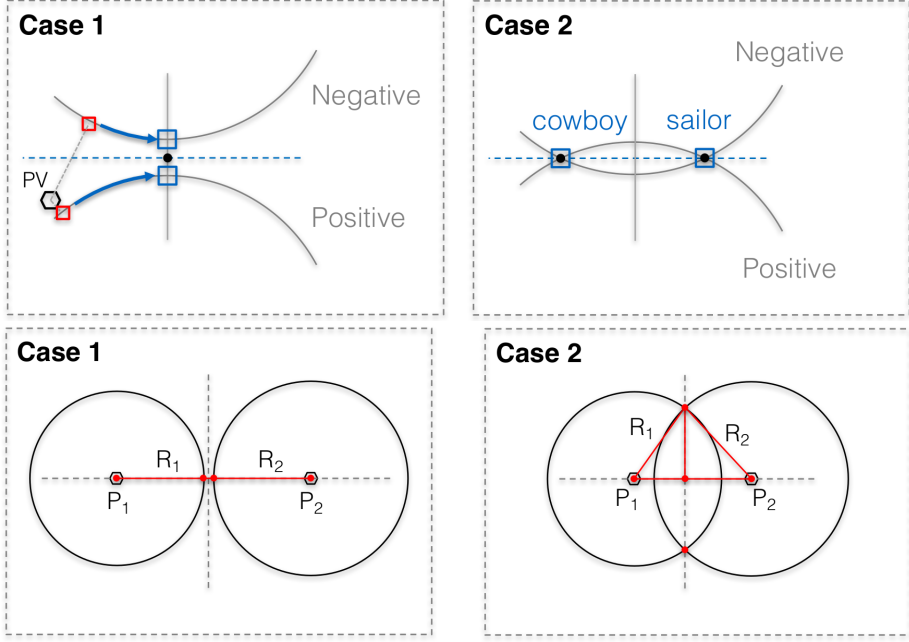


**Figure 6.10:** (Top panel): Illustration of the DCA estimation of  $V^0$  candidates with one (left) and two (right) minima. The case of two minima is often referred to as “cowboy/sailor” minima. (Bottom panel): Illustration of how the two different examples above are distinguished, by extrapolating circles from the particle trajectories. Figure is taken from Ref. [102]

both the  $\text{PID}_{\text{bachelor}}$  and the  $V^0$  are considered as cascade candidates. The bachelor track is propagated through a curve from the primary vertex. The distance between the curved propagation to the secondary vertex in the  $x-y$  plane is defined as the  $\text{DCA}_{xy}$  for the cascade and is limited to 2 cm.

### 3. Cascade decay point estimation

Lastly, the decay point of the original  $\Xi$  baryon is determined by utilizing the reconstruction probabilities from the  $V^0$  and bachelor decay points. Covariance matrices  $C_{\text{bach}}$  and  $C_{V^0}$  are extracted from the position of the bachelor ( $r_{\text{bach}}$ ) and  $V^0$  ( $r_{V^0}$ ), in-line with the original decay vertex. Based on the weights from the covariance matrices, the  $\Xi$  decay vertex is then extrapolated back to the  $V^0$  DCA point, seen in Eq. 6.10. The decay point is reconstructed somewhere in between these two points, as illustrated in Fig. 6.11. Valid cascade candidates also require a decay radius  $r_{\Xi}$  of more than 3 cm.

$$r_{\Xi} = [C_{\text{bach}}^{-1} + C_{V^0}^{-1}] \times [C_{\text{bach}}^{-1} r_{\text{bach}} + C_{V^0}^{-1} r_{V^0}] \quad (6.10)$$

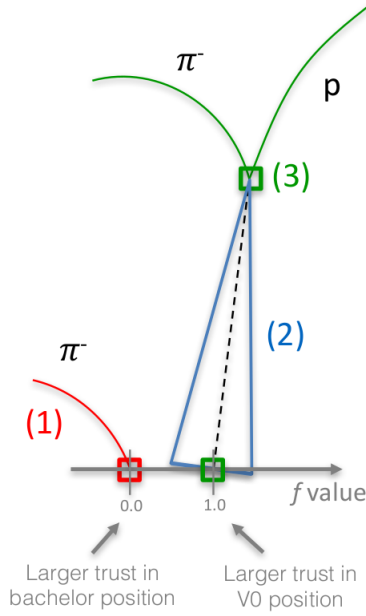


**Figure 6.11:** Illustration of the procedure performed to find the decay point of the original cascade. Figure taken from Ref. [102]

### 6.3.2 Identification of $\Xi^- + \bar{\Xi}^+$ Baryons

Once a cascade candidate is found, further selection criteria are applied to reduce the background of misidentified cascades. An illustration of these parameters can be found in Fig. 6.12. The parameters are defined as follows:

- PV: Primary vertex
- $DCA_{\text{Bachelor}} - PV$ : The impact parameter between bachelor track and primary vertex.
- $DCA_{PV} - V_0$ : The impact parameter between primary vertex and  $V_0$ .
- SV: Secondary Vertex, where  $\Xi$  decays.
- $DCA_{\text{Bachelor}} - V_0$ : The DCA between bachelor and  $V^0$
- PA: Pointing angle between cascade momentum vector, and a vector from the primary vertex to the secondary vertex.
- TV: Tertiary Vertex, where the  $V_0$  decays.

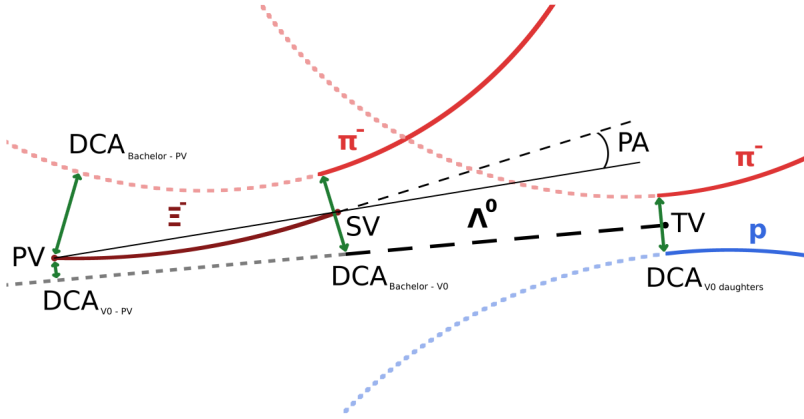


**Figure 6.12:** An illustration of the cascade decay topology, including experimental parameters that are tuned to select identified  $\Xi$  baryons. A full description of the different parameters can be found in the text. The illustration is borrowed from Ref. [103]

- $DCA_{V^0 \text{ daughters}}$ : The DCA between the two  $V^0$  daughters at the TV

Table. 6.4 presents the parameters selected for  $\Xi$  identification in this thesis. These values, as well as the final yield extraction, were calibrated and refined by Peter Christiansen, based on the existing, published ALICE  $\Xi$  results [15].

**Table 6.4:** Summary of the topological cut values used for the  $\Xi$  candidate selection. All impact parameter cuts on tracks are 2D ( $xy$ ).

Cut Variable	Cut Value
Topology of $\Xi$	
$DCA_{\text{Bachelor} - V^0}$	$< 1.6 \text{ cm}$
$DCA_{\text{Bachelor} - PV}$ (Impact Parameter)	$> 0.05 \text{ cm}$
Pointing Angle $\cos PA$	$> 0.97$
Cascade transverse decay radius	$> 0.8 \text{ cm}$
Topology of Secondary $\Lambda$	
Window around $\Lambda$ mass	$< 0.006 \text{ (GeV}/c^2\text{)}$
$DCA_{V^0 \text{ daughters}}$	$< 1.6 \text{ cm}$
$DCA_{PV - V^0}$ (Impact Parameter)	$> 0.07 \text{ cm}$
$DCA_{V^0 \text{ daughters} - PV}$	$> 0.04 \text{ cm}$
$V^0$ transverse decay radius	$> 1.4 \text{ cm}$
Daughter Track Selection	
Pseudorapidity	$ \eta  < 0.8$
TPC clusters	$> 70$
TPC PID of daughters	$< 5\sigma$

In addition to the requirements listed in Tab. 6.4, at least one of the three de-



cay daughters (bachelor, or one of the two V0 daughters) is required to have a matching ITS track (reconstructed with good quality), or a hit in the TOF detector. This additional constraint made it possible to reject background originating from OOB pile-up at high- $p_T$ .

### 6.3.3 $\Xi^- + \bar{\Xi}^+$ Signal Extraction

Once a valid  $\Xi$  candidate is identified, the invariant mass distribution is measured in narrow  $p_T$  intervals. Figure 6.13 presents an example of the difference between the measured  $M_{\text{inv}}$ , to the  $\Xi$  vacuum expectation value, for select  $p_T$  intervals. While the topological selection allows for a much cleaner signal than the  $\phi$  meson, the signal is still contaminated by significant amounts of background. This effect is especially pronounced at low  $p_T$ . The background sources are mainly V0's (either fake or real) that get mismatched with random  $\pi$  mesons produced at low  $p_T$ , or  $\pi^-\pi^-p$  triplets where the bachelor pion gets mistaken for a V0 decay daughter (thus reconstructing a “V0” with the *wrong* pion).

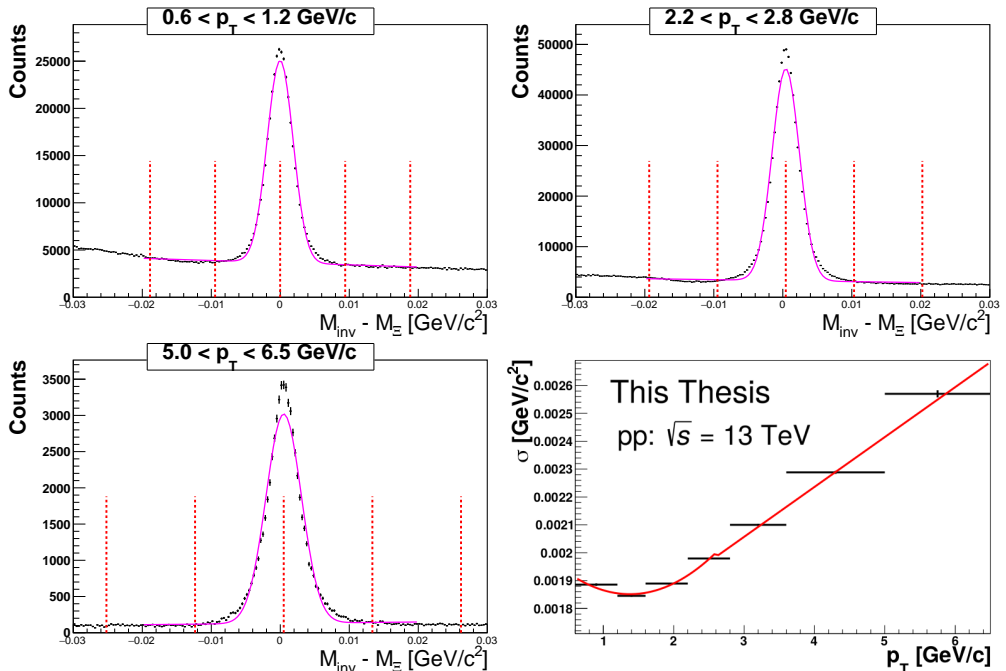


**Figure 6.13:** Invariant mass distributions for  $\Xi \rightarrow \Lambda \pi$ , for the central (top-right panel) and two most extreme  $p_T$  bins (left panels). The magenta line (Gauss+pol1) is a fit to the distribution used to extract  $\mu$  and  $\sigma$ . The red dashed lines are drawn at  $\mu - 10\sigma$ ,  $\mu - 5\sigma$ ,  $\mu$ ,  $\mu + 5\sigma$ , and  $\mu + 10\sigma$ , to indicate the Background,  $B$ , and Peak,  $P$ , regions. 4th panel (bottom-right) presents the extracted Gaussian variance as a function of  $p_T$ .

The signal is extracted by evaluating the background in the regions outside the central peak. This technique is referred to as the *sideband* subtraction method. First, a combined peak fit (Gaussian + 1st order polynomial) is applied to each  $p_T$ -differential  $M_{\text{inv}}$  spectra. The Gaussian mean  $\mu$  and variance  $\sigma$  parameters are then extracted from the fit. The  $M_{\text{inv}}$  spectra are then segmented into different regions, as shown in Fig. 6.13, based on the number of deviations away from the mean. The regions  $5 - 10\sigma$  away from the peak regions are selected as sidebands, which are used to estimate the combinatorial background under the central peak region.

The underlying assumption of this method is that the sidebands contain essentially zero contribution to the overall  $\Xi$  production. If the shapes of the sidebands are flat (or linear relative to the peak), the raw  $\Xi$  yield produced in the central peak region,  $N_{\Xi}^{\text{Raw}}$ , can be estimated as the difference between the integrals (counted by summing bins) of the central peak region  $N_{\text{Peak}}^{\text{Raw}}$  and the sidebands  $N_{\text{Background}}^{\text{Raw}}$ :

$$\begin{aligned}
N_{\text{Peak}}^{\text{Raw}} &= \sum_{\text{bin}=\mu-5\sigma}^{\mu+5\sigma} (M_{\text{inv}})_{\text{bin}} \\
N_{\text{Background}}^{\text{Raw}} &= \sum_{\text{bin}=\mu-10\sigma}^{\mu-5\sigma} (M_{\text{inv}})_{\text{bin}} + \sum_{\text{bin}=\mu+5\sigma}^{\mu+10\sigma} (M_{\text{inv}})_{\text{bin}} \\
N_{\Xi}^{\text{Raw}} &= N_{\text{Peak}}^{\text{Raw}} - N_{\text{Background}}^{\text{Raw}} \\
\sigma(N_{\Xi}^{\text{Raw}}) &= \sqrt{N_{\text{Peak}}^{\text{Raw}} + N_{\text{Background}}^{\text{Raw}}}
\end{aligned} \tag{6.11}$$

### 6.3.4 Fully Corrected $\Xi^- + \Xi^+$ Yields As a Function of $p_T$

The final yields are obtained by correcting the raw yields extracted from the  $M_{\text{inv}}$  spectra for detector efficiency  $\epsilon_{\text{eff}}$ , and a rapidity correction to transform the measurement from  $\eta$  to  $y$ , similar to the  $\phi$  meson analysis (refer to Sec. 6.2.4 for details). The extraction procedure utilizing the reconstructed, simulated tracks is identical to the procedure performed in the data analysis. The fully corrected  $\Xi$  spectrum is then expressed as:

$$\frac{dN_{\Xi}^2}{dy dp_T} = \frac{dN_{\Xi^-}^2}{dy dp_T} + \frac{dN_{\Xi^+}^2}{dy dp_T} = \frac{1}{N_{\text{norm}}} \frac{dN_{\text{Raw}}^2(\Xi^- + \Xi^+)}{dy dp_T} \frac{1}{\epsilon_{\text{corr}}} \tag{6.12}$$

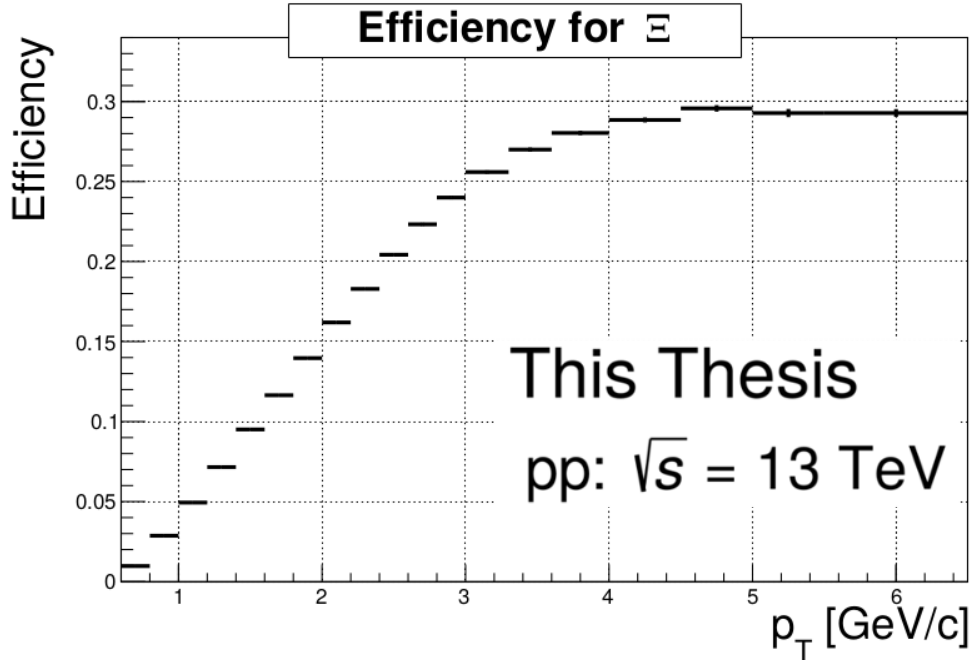


**Figure 6.14:** Minimum bias reconstruction efficiency  $\times$  acceptance for  $\Xi^- + \Xi^+$  as a function of  $p_T$ . Efficiency is estimated by comparing the  $\Xi$  yield in PYTHIA 8 events before/after propagated through a simulation of ALICE.

$N_{\text{norm}}$  contains a vertex correction, and is defined in Eq. 6.8 (see Sec. 6.2.4 for details).

### 6.3.5 Systematic Variations for the $\Xi^- + \Xi^+$ analysis

Similar to the  $\phi$  meson analysis, the nominal parameters utilized for the  $\Xi$  baryon extraction were calibrated to find a good compromise between reconstruction efficiency and signal purity. Variations enumerated by **1** represent the nominal variation used in the final extraction.

#### Variations to cascade identification

The cascade identification cuts were varied as a group, in “looser” and “tighter” configurations relative to the nominal selection, as presented in Tab. 6.5.

#### Estimation of out-of-bunch (OOB) pile-up

The OOB pile-up rejection is varied to require at least two of the three decay tracks (bachelor and  $V^0$  daughters) to have a fast detector signal. It was not possible to reproduce published ALICE data without the OOB pile-up rejection, and therefore the parameter was never “loosened”. This variation tests to what

**Table 6.5:** The variations done to study the systematic uncertainties associated with the topological PID selection of  $\Xi$  baryons.

Cuts on $\Xi$	Nominal	Loose	Tight
Max DCA between daughters (cm)	1.6	1.9	1.5
Min bachelor impact parameter (cm)	0.05	0.03	0.05
Min cos of cascade PA	0.97	0.95	0.98
Cuts on $V^0$ daughter			
Window around $\Lambda$ mass ( $\text{GeV}/c^2$ )	0.006	0.006	0.005
Min cos of cascade PA	0.97	0.92	0.97
Min $V^0$ impact parameter (cm)	0.07	0.07	0.08
Min impact parameter for daughters (cm)	0.04	0.02	0.05

degree the MC can correct for this additional requirement.

- **OOB variation 1:** One of three daughters are required to have a hit in either the ITS or TOF.
- **OOB variation 2:** Two of three daughters are required to have a hit in either the ITS or TOF.

### TPC PID $n\sigma$ requirement for decay daughters

The systematic uncertainty due to the TPC PID is usually tested by varying the amount of  $n\sigma$  for the identified protons and pions that decay from  $\Lambda$ . However, extensive testing found that a stricter cut does not improve the background in any meaningful way. Implementing a looser,  $5\sigma$ , was found to only incorporate more background. A  $4\sigma$  TPC PID selection, therefore, does not reject any signal.

### Track requirement for crossed-rows in the TPC

The  $\Xi$  analysis does not utilize global tracks, and instead, uses tracks that are connected to the overall  $\Xi$  topology. The systematic uncertainty introduced by using looser track criteria was tested by varying the number of required crossed-rows in the TPC,  $N_{\text{cr}}$

- **TPC configuration 1:**  $N_{\text{cr}} \geq 70$
- **TPC configuration 2:**  $N_{\text{cr}} \geq 80$

### Variations of sidebands in $M_{\text{inv}}$ signal extraction

Uncertainties related to the consistency of the sideband method are tested by also performing the sideband subtraction in arbitrary, fixed regions around the central peak region.

- **Sideband configuration 1:**  $5\sigma$  intervals around fitted peak mean  $\mu$
- **Sideband configuration 2:** Fixed sidebands, for  $M_{\text{inv}} - M_{\Xi}$  at  $[-0.2; -0.1)$  and  $(0.1; 0.2]$   $\text{GeV}/c^2$ .



## Chapter 7

# $\phi$ and $\Xi$ Yields as Functions of Unweighted Transverse Spherocity $S_O^{p_T=1}$

The first analysis presented in this thesis will focus on particle production relative to different azimuthal topologies. The azimuthal topologies are characterized by the event-shape observable Transverse Spherocity. The experimental definition of the observable itself has gone through several iterations of optimization, to reduce the experimental bias. The optimization process is described in the following, detailing the necessity to slightly alter the definition of Transverse Spherocity  $S_O$ , into the Unweighted Transverse Spherocity  $S_O^{p_T=1}$ .

Consequently, the measured spectra can be directly compared to MC generator predictions, without requiring unfolding. I will report on preliminary results from ALICE, presenting  $p_T$ -differential spectra and particle ratios, along with integrated quantities, for both  $\phi$  and  $\Xi$  as functions of  $S_O^{p_T=1}$ .

### 7.1 Charged particle production as a function of the azimuthal topology

This section will detail the original definition, as well as the track requirements used to calculate the Transverse Spherocity  $S_O$ , event-by-event. A comparison between charged and neutral particles will be used to evaluate any potential

bias introduced by defining the event topology w.r.t. the distribution of charged particles.

### 7.1.1 Transverse Sphericity $S_O$

The Transverse Sphericity  $S_O$ , which was originally proposed in Ref. [104], can be used to quantify the topology of the event plane [105][106]. It is defined in the transverse plane, for the unit vector  $\hat{n}$  that minimizes the ratio:

$$S_O = \frac{\pi^2}{4} \min_{\hat{n}} \left( \frac{\sum_i |p_{T,i} \times \hat{n}|}{\sum_i p_{T,i}} \right)^2. \quad (7.1)$$

The sums in Eq. 7.1 are calculated over all *primary* charged particles, with a requirement of  $p_T > 0.15 \text{ GeV}/c$ . The value of  $S_O$  is, by construction, constrained between the limits 0 and 1. Events with  $S_O \approx 0$  implies that  $|p_T \times \hat{n}| \approx 0$  for all charged particle tracks. To satisfy this condition, all  $p_T$  vectors from the particle tracks have to be (anti)parallel in the azimuthal plane. In contrast, events where  $S_O \approx 1$  require all particles to be uniformly distributed in the azimuthal plane. This is also reflected in Eq. 7.1; assuming the  $p_T$  is equal for each particle track, and distributed isotropically, such that the sum approximates an integral. Integrating over  $d\phi$  yields  $2/\pi$ , and thereby  $S_O = 1$ .

The azimuthal event topology, and thereby  $S_O$ , will reflect the dominant mode of particle production in a given event. Events with  $S_O \rightarrow 0$  are likely to be dominated by a single hard scattering, producing a back-to-back jet<sup>1</sup>. Contrarily, events where  $S_O \rightarrow 1$  implies the absence of a preferred direction w.r.t. particle production, suggesting that particles are produced through several softer interactions. An illustration of the two limits in the azimuthal plane is presented in Fig. 7.1

Throughout this chapter,  $S_O$  is measured for high-multiplicity events, which is then used to categorize the topology of a given event. The categories are labeled as follows:

- *Jetty* events, where  $S_O \rightarrow 0$ .
- *Isotropic* events, where  $S_O \rightarrow 1$ .

---

<sup>1</sup>At this point, I am describing  $S_O$  as it was described in earlier publications, c.f., Ref. [105]. However, throughout this chapter it will become apparent that this description is not necessarily accurate; a single, large  $p_T$  track can have an enormous weight, which can completely skew the measurement of  $S_O$



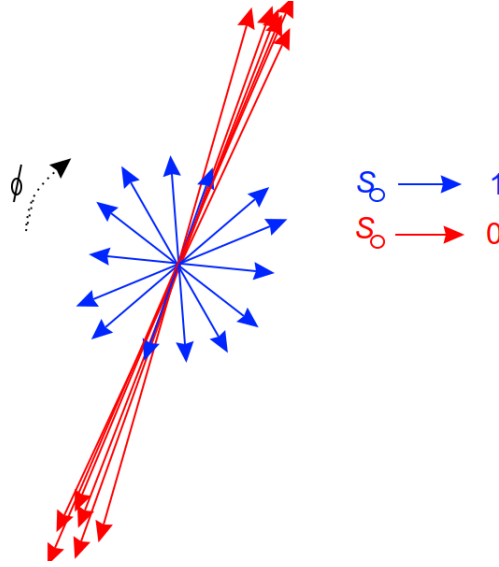


**Figure 7.1:** Illustration of the characteristic topologies in the azimuthal plane, for the two  $S_O$  limits.

The selection occurs in percentiles of the total  $S_O$  distribution. The selected percentiles range from [0-20%]- [80-100%], to, [0-1%]-[99-100%] for jetty<sup>2</sup> and isotropic selections, respectively. One should keep in mind that "jetty" in this case is simply a label. Even though jetty events are dominated by physics associated with hard scatterings (which will be discussed in the following), no rigorous jet-finding algorithm is implemented. Therefore, jetty events will not necessarily satisfy the standard ALICE definition of a jet [107].

### 7.1.2 Track Selection

As the Transverse Sphericity is sensitive to the azimuthal distribution of particles, it is important to have a consistent, global azimuthal acceptance. Losses in global azimuthal reconstruction efficiency would introduce a large experimental bias, and particle production measured as a function of  $S_O$  would require unfolding. Particles produced in azimuthal regions where there is high reconstruction efficiency would give a precise estimate of the event shape, whereas particles produced in regions with poor reconstruction efficiency would result in a poor description of the event topology.

The SPD contains inactive regions, which creates "holes" in the azimuth. The

---

<sup>2</sup>Jetty events are also ubiquitously referred to as "jet-like", or "pencil-shaped" throughout this thesis.

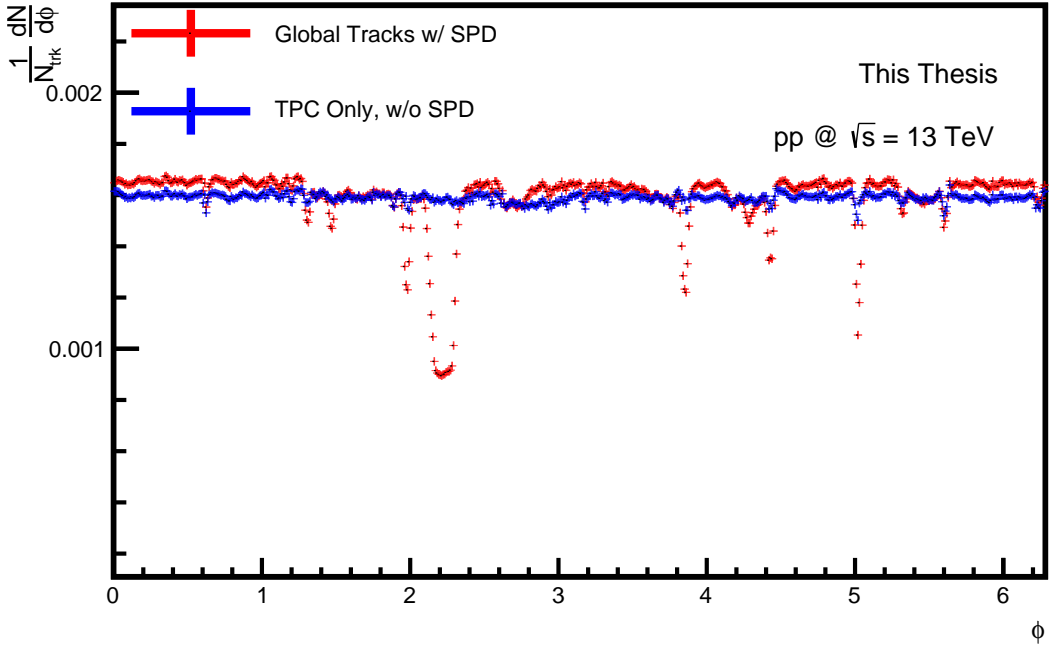


**Figure 7.2:** The azimuthal probability distribution of reconstructed tracks, utilizing global track cuts, as well as only information from the TPC (without the SPD). See text for details.

reconstruction efficiency around the holes is poor, as can be seen in the azimuthal distribution of global tracks<sup>3</sup>, presented in Fig. 7.2. To avoid a potential bias, no track information is required from the SPD when measuring  $S_O$ . However, the SPD is only used to locate the initial primary vertex. To obtain an overall large reconstruction efficiency, the TPC requirements are also loosened, retaining a good spatial performance, but resulting in a poorer momentum resolution. The loss in momentum resolution will not have a large impact on the presented results, for reasons discussed in Sec. 7.2. Tracks that are considered in the calculation for  $S_O$  have to pass the following criteria:

1. A minimum of 50 clusters in the TPC require a hit.
2. The track trajectory fit cannot exceed  $\chi^2 > 4$  for each cluster in the TPC.
3. Kink daughters are rejected (defined in Sec. 6.2.1)
4. Selection criteria to identify and reconstruct the primary vertex are implemented. The impact parameters, relative to the primary vertex, are

---

<sup>3</sup>Refer to Sec. 6.2.1 for definition

constrained both in the  $z$ -plane ( $\text{DCA}_z \leq 3.2$  cm) and the  $xy$ -plane ( $\text{DCA}_{xy} \leq 2.4$  cm).

5. Both valid ITS and TPC refits are required, which improves OOB pile-up and improves the spatial resolution of each reconstructed trajectory.

### 7.1.3 Neutral-to-Charged Bias

The ALICE reconstruction efficiency for charged tracks is not perfect, and losses of a large number of tracks, or loss of a single high- $p_T$  track, can distort the experimental estimation of  $S_O$ . This effect is commonly referred to as *folding*, where the "real" value of  $S_O$  is smeared due to limited detector

ALICE has previously reported results on unidentified, primary charged particle production  $N_{\text{ch}}$ , as a function of  $S_O$  [106]. It was observed that the discrepancy between the "real" and "reconstructed"  $S_O$  was limited. This was extensively tested, by generating PYTHIA 8 events (in this sense, the generated, "real" particle distribution), and propagating them through a GEANT 3 simulation of ALICE, following standard reconstruction procedure. It was found that biases due to tracking efficiency were only relevant for low-multiplicity events, retaining an overall good  $S_O$  resolution for reconstructed events. Likewise, preliminary ALICE results on  $\pi, K, p$ , as a function of  $S_O$ , demonstrated that the reconstructed and generated yield of  $\pi^+ + \pi^-$ , measured for reconstructed and generated selections of  $S_O$ , were found to be consistent [108].

One could naively expect that the same would apply to the particles measured in the work presented here. However, one should keep in mind that primary  $\pi, K$  and  $p$ , *themselves* enter directly into calculation for  $S_O$ . The same does not apply to weakly decaying particles. Decay-daughters from  $\Xi, \Lambda$ , and  $K_S^0$  are reconstructed as secondary particles, and therefore will only rarely<sup>4</sup> enter the  $S_O$  calculation. Furthermore, strongly decaying resonances, such as  $\phi$ , will enter *twice*, since both kaons are experimentally indistinguishable from primary kaons produced in the collision. We will evaluate the experimental bias for the  $S_O$  event selection, relative to extracting the yield of weakly decaying particles,

---

<sup>4</sup>This can occur if secondary decay daughters from weakly-decaying particles are misidentified as primary particles.

as well as the  $\phi$  meson, by constructing the closure test  $C(\text{PID}, p_T)^{S_O}$ :

$$C(\text{PID}, p_T)^{S_O} = \frac{\frac{1}{\epsilon} \left( \frac{d^2 N_{\text{Rec}}}{d\eta dp_T} \right)_{S_O, \text{Rec}}^{\text{PID}}}{\left( \frac{d^2 N_{\text{Gen}}}{d\eta dp_T} \right)_{S_O, \text{Gen}}^{\text{PID}}} \quad (7.2)$$

- PID is the particle specie on which the closure test is performed for.
- $\epsilon$  is the minimum bias reconstruction efficiency. Unless there is additional smearing introduced by the  $S_O$  selection, the generated spectra should be recovered by correcting the reconstructed spectra with the minimum bias efficiency.
- $\left( \frac{d^2 N_{\text{Rec}}}{d\eta dp_T} \right)_{S_O, \text{Rec}}^{\text{PID}}$  is the reconstructed particle yield, where the topological selection has been done using the *reconstructed*  $S_O$ .
- $\left( \frac{d^2 N_{\text{Gen}}}{d\eta dp_T} \right)_{S_O, \text{Gen}}^{\text{PID}}$  is the generated particle yield produced in the simulation, where the topological selection has been done using the *generated*  $S_O$ .

Figure 7.3 presents the estimate for the experimental biases,  $C(\text{PID}, p_T)^{S_O}$ , for primary  $\pi, K, p$ . The results are in agreement with previous findings from Ref. [108], demonstrating a negligible experimental bias for primary  $\pi, K, p$  when selecting events based on  $S_O$ . However, a significant bias is present when selecting  $\phi$ , and neutral, weakly-decaying particles, shown in Fig. 7.4, where  $C(\text{PID}, p_T)^{S_O}$  are presented as functions of  $p_T$  (alongside a new estimator, described shortly in the following). Consequently, measured spectra of weakly-decaying particles as functions of  $S_O$  will contain a large bias. In Sec. 7.2, the case will be made that this bias would remain after unfolding, as the bias does not rely on the experimental setup, but instead on the underlying definition of  $S_O$ . Therefore, measurements of  $S_O$  will always be biased when estimating the topology between charged and neutral particles. However, changes could be made to the definition of  $S_O$ , to construct a more robust observable. This was done for the work presented in this thesis, which is described in the following.

## 7.2 Unweighted Transverse Spherocity $S_O^{p_T=1}$

The hypothesis for why the experimental bias is particularly large for weakly decaying particles is that neither secondary nor neutral particles are considered

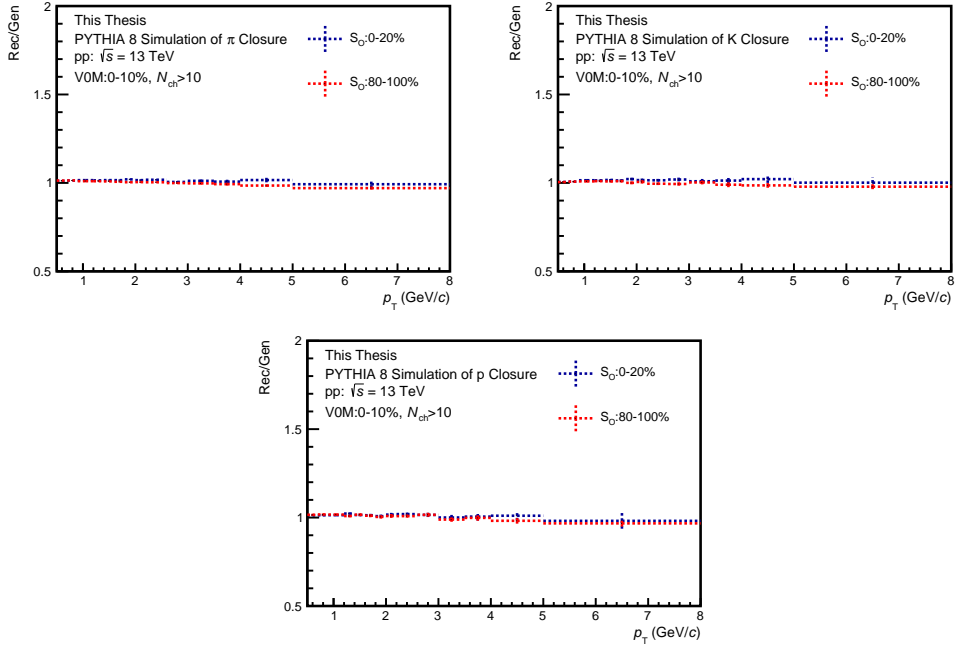


**Figure 7.3:** Results of experimental bias using  $S_O$ , for  $\pi$ , K, p. Experimental bias is evaluated by measuring  $C(\text{PID}, p_T)^{S_O}$ , as a function of  $p_T$ . Uncertainties are purely statistical. Refer to the text for details.

for the generator measurement of  $S_O$ . To illustrate this effect, Fig. 7.5 presents a set of two boosted jets, consisting of two charged  $\pi$  mesons, and two neutral  $\pi^0$  mesons. The two jets are identical, except that the position of the charged and neutral  $\pi$  mesons are swapped. Even though the overall topology is identical between the pair of jets, a measurement of  $S_O$  would describe two completely different topologies. In an event with several low- $p_T$  particles that are isotropically distributed, a single high- $p_T$  track can drive the entire  $S_O$  calculation towards 0. Such a single high  $p_T$  track will have an enormous weight in the sphericity calculation, which can occur for a charged pion, but never for a neutral pion. This applies to all neutral particles, which are not able to carry a large- $p_T$  weight, as long as  $S_O$  is defined solely by charged particles.

To mitigate this bias, one could instead re-normalize the weights in Eq. 7.1. By setting the magnitude of each track to  $|\vec{p}_T| = 1.0 \text{ GeV}/c$ , the same weight is assigned to each track. In this sense, the measurement becomes more robust against individual tracks with large  $p_T$ , which can skew the description of the azimuthal event topology. With equal  $p_T$  weights, and assuming that neutral and charged particles are similarly distributed, we can use the charged particles as a proxy of the event topology for neutral particles:

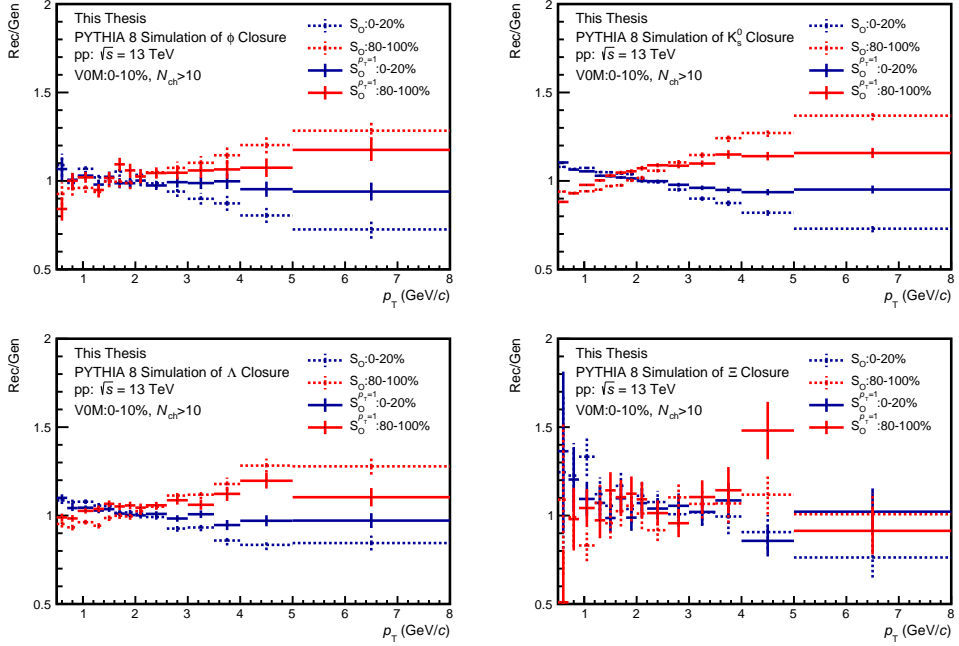


**Figure 7.4:** Results of experimental bias, using both  $S_O$  and  $S_O^{p_T=1}$ , for particles that are reconstructed as long-lived particles. Experimental bias is evaluated by measuring  $C(\text{PID}, p_T)^{S_O}$ , as a function of  $p_T$ . Uncertainties are purely statistical. Refer to the text for details.

- A jet will contain both charged and neutral particles in the shower.
- An isotropic event will have an isotropic distribution of both charged and neutral particles.

Therefore, I introduce the *Unweighted Transverse Spherocity*  $S_O^{p_T=1}$ , defined as:

$$S_O^{p_T=1} = \frac{\pi^2}{4} \min_{\hat{n}} \left( \frac{\sum_i |p_{T,i} \times \hat{n}|}{N_{\text{trks}}} \right)^2. \quad (7.3)$$

As illustrated in Fig. 7.5,  $S_O^{p_T=1}$  describes very similar topologies regardless of whether the leading particle is neutral or charged. In this sense,  $S_O^{p_T=1}$  is more robust and reduces the possible charged-vs-neutral biases. Figure 7.4 includes closure tests as a function of  $S_O^{p_T=1}$ , where one can note that there is a significant improvement when estimating the topology with  $S_O^{p_T=1}$ , drastically reducing the charged-to-neutral bias.

A substantial effort has been made to ensure that  $S_O^{p_T=1}$  is sensitive to the same associated modes of particle production as  $S_O$ . The distribution of the azimuthal

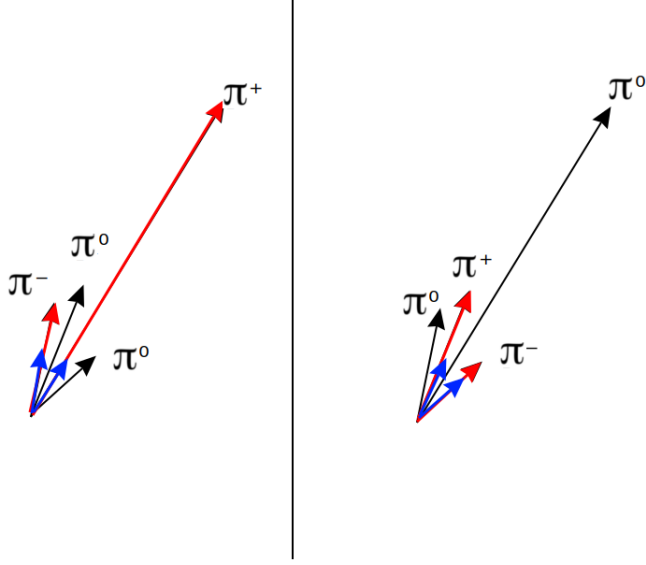


Figure 7.5: Illustration of the charged-to-neutral bias between two jets. Red arrows represent the weights utilized when measuring  $S_O$ , whereas blue arrows represent the weights utilized when measuring  $S_O^{pT=1}$ .

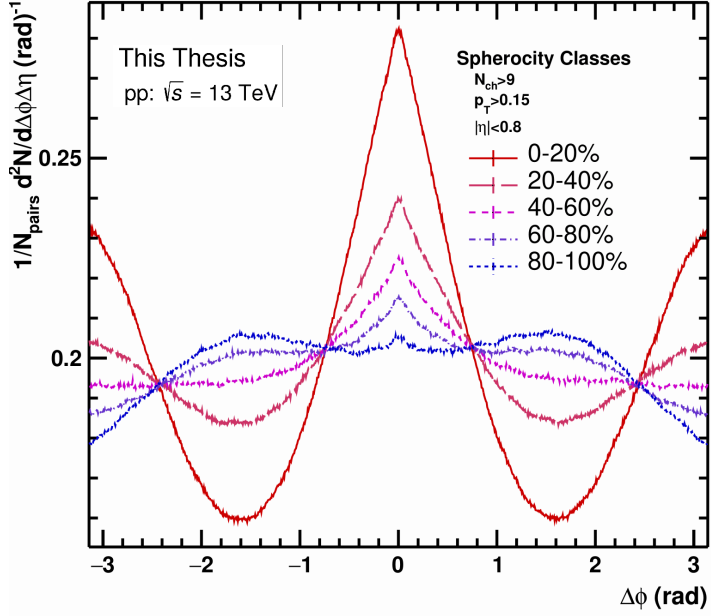
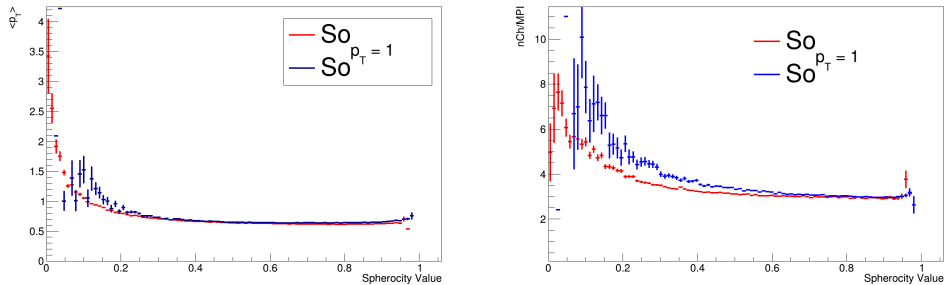


Figure 7.6: The distribution of azimuthal difference between charged particle tracks,  $\Delta\phi$ , presented in five different  $S_O^{pT=1}$  intervals. Errors are purely statistical.



**Figure 7.7:** (Left panel): PYTHIA 8 simulations of the  $\langle p_T \rangle$  of charged primary particles, presented as functions of both  $S_O$  and  $S_O^{p_T=1}$ . (Right Panel): PYTHIA 8 simulations of the number of primary charged particles, relative to the number of MPIs, presented as functions of both  $S_O$  and  $S_O^{p_T=1}$ . See text for details.

difference between particle tracks,  $\Delta\phi$  is presented in Fig. 7.6, confirming that lower values of  $S_O^{p_T=1}$  retain a distinct di-jet topology, which is smeared out for higher values of  $S_O^{p_T=1}$ . Furthermore, the  $\langle p_T \rangle$  of charged, primary particles are presented as a function of  $S_O^{p_T=1}$  in the upper panel of Fig. 7.7, demonstrating that  $S_O^{p_T=1}$  can select events based on their hardness. Lastly, the lower panel of Fig. 7.7 presents PYTHIA 8 simulations of primary charged particles, relative to the number of MPIs (c.f., Sec. 4.1.1), suggesting that  $S_O^{p_T=1}$  is sensitive to the magnitude of the underlying event.

However, one should consider that  $S_O^{p_T=1}$  is a fundamentally different observable than  $S_O$ . This means that prior results obtained using the traditional definition of  $S_O$  can only be qualitatively compared with new results obtained using  $S_O^{p_T=1}$ . Furthermore,  $S_O^{p_T=1}$  requires a substantial amount of particles to construct a well-defined measure of the event topology, as the observable is independent of  $\vec{p}_T$ . For this reason, results presented in this thesis will require that events have at least 10 charged tracks, to ensure that one can study and contrast event topologies in a meaningful way.

### 7.2.1 Further Caveats

A very important aspect of the  $S_O^{p_T=1}$  analysis has been to ensure that MC generator predictions and experimentally measured results are directly comparable. While more robust against the charged-vs-neutral bias,  $S_O^{p_T=1}$  selection still features a significant experimental bias. Moreover, the experimental bias grows larger with narrower selections in  $S_O^{p_T=1}$ . For the work presented here, extensive studies have been performed to understand and mitigate the remaining experimental bias that arises due to the  $S_O^{p_T=1}$  selection. Similar to  $S_O$ , the



experimental bias of  $S_{\text{O}}^{p_{\text{T}}=1}$  is estimated by the closure of PYTHIA generated events, propagated through an ALICE simulation,  $\text{C}(\text{PID}, p_{\text{T}})^{S_{\text{O}}^{p_{\text{T}}=1}}$ , defined in Eq. 7.2. The experimental uncertainty is minimized by adopting the following criteria, allowing for direct comparisons between data and model predictions, ensuring that  $S_{\text{O}}^{p_{\text{T}}=1}$  is a robust and model-independent observable:

### $S_{\text{O}}^{p_{\text{T}}=1}$ selection in quantiles

The first major source of experimental bias is the smearing of the measured  $S_{\text{O}}^{p_{\text{T}}=1}$  distribution by detector effects. This bias is exacerbated when selecting extreme values of  $S_{\text{O}}^{p_{\text{T}}=1}$ , even for measured yields of  $\pi, \text{K}, \text{p}$ . The measured  $\text{C}([\pi, \text{K}, \text{p}], p_{\text{T}})^{S_{\text{O}}^{p_{\text{T}}=1}}$  are presented in Fig 7.8, as functions of  $p_{\text{T}}$ , with events selected by  $S_{\text{O}}^{p_{\text{T}}=1}$  in different percentiles. A significant experimental bias is introduced when selecting events with extremely small values of  $S_{\text{O}}^{p_{\text{T}}=1}$ . It is important to stress that the  $S_{\text{O}}^{p_{\text{T}}=1}$  percentiles are calibrated to the reconstructed distribution, and the cutoff value is then used for both the reconstructed and generated yields, i.e., for the jetty events in Fig. 7.8, both reconstructed and generated particles are selected for  $S_{\text{O}}^{p_{\text{T}}=1}_{\text{Rec,Gen}} < 0.487$ . This corresponds to the bottom-1% percentile of the reconstructed  $S_{\text{O}}^{p_{\text{T}}=1}$  distribution, *but not* the bottom-1% percentile of the generated distribution, as the mean of the generated and reconstructed  $S_{\text{O}}^{p_{\text{T}}=1}$  distributions are not equal.

However, it is possible to minimize the effects of the smearing by measuring  $S_{\text{O}}^{p_{\text{T}}=1}$  percentiles, *both* for reconstructed and generated events, similar to how multiplicity classes are defined (c.f., Sec. 5.2.1[109]). This is demonstrated in Fig. 7.9, where  $\text{C}([\pi, \text{K}, \text{p}], p_{\text{T}})^{S_{\text{O}}^{p_{\text{T}}=1}}$  is presented as a function of  $p_{\text{T}}$ , in  $S_{\text{O}}^{p_{\text{T}}=1}$  percentiles, where the percentile cut-off now applies for both reconstructed and generated  $S_{\text{O}}^{p_{\text{T}}=1}$  distributions. The tail toward lower values of  $S_{\text{O}}^{p_{\text{T}}=1}$  is broad, and consequently, the particle production will be softer for the generated  $S_{\text{O}}^{p_{\text{T}}=1}$  distribution. The closure tests suggest that a loss of a track during the reconstruction will shift, rather than smear, the  $S_{\text{O}}^{p_{\text{T}}=1}$  distribution. Furthermore, the closure tests indicate that this “shift” can be recovered when measuring the  $S_{\text{O}}^{p_{\text{T}}=1}$  distribution in percentiles.

Consequently, making model predictions based on quantiles, rather than on the reported experimental  $S_{\text{O}}^{p_{\text{T}}=1}$  ranges, allow for precise model-to-data comparisons. Since the quantile measurement is robust and can be directly compared to MC generator predictions, one can unfold the  $S_{\text{O}}^{p_{\text{T}}=1}$  distribution to obtain direct comparisons for generated  $S_{\text{O}}^{p_{\text{T}}=1}$  values.

## Only the charged decay modes are included for resonance yields

Since the decay daughters of  $\phi$  meet the standard ALICE definition of primary particles [67], each  $\phi$  meson will produce two kaons, which, if reconstructed, will both enter into the  $S_{\text{O}}^{p_{\text{T}}=1}$  distribution. These daughters will also contribute to the multiplicity estimate at mid-rapidity, making events with a  $\phi$  that decays to two charged kaons more likely to pass the requirement of having 10 charged tracks. As  $\phi$  mesons have both charged and neutral decay modes, the branching ratio for the charged decay mode will therefore be enhanced in high-multiplicity events. This bias can be completely avoided by only including (and correcting for) the charged decay mode in the resulting spectra:  $\phi \rightarrow K^+ K^-$ . This effect is illustrated in Fig. 7.10. For this reason, the correction for the branching ratio, described in Sec. 6.2.4, is *not* applied to the fully corrected  $\phi$  yield, when measured as a function of  $S_{\text{O}}^{p_{\text{T}}=1}$ . This correction is not directly attributed to the  $S_{\text{O}}^{p_{\text{T}}=1}$  selection but is rather a consequence of a high-multiplicity selection at midrapidity.

## Contamination of secondary particles

The loose DCA cuts described in Sec. 7.1.2, which are primarily utilized to maintain a full azimuthal acceptance, consequently lead to some decay daughters from  $V^0$ s and cascades to be incorrectly reconstructed as primary particles. To minimize the experimental bias from this effect, we include  $\Lambda$  and  $K_{\text{S}}^0$  in the calculation of  $S_{\text{O}}^{p_{\text{T}}=1}$  for the generated MC predictions. This improves the experimental closure for weakly-decaying particles and is demonstrated for  $\Lambda + \bar{\Lambda}$  in Fig. 7.11. The inclusion of these particles on the generator level makes the results directly comparable to MC generator predictions.

However, there is still a significant bias at  $p_{\text{T}} < 1.0\text{GeV}/c$ , even with the inclusion of secondary particles in the calculation for the MC predictions. The current hypothesis is that, for these very low  $p_{\text{T}}$  tracks, the azimuthal angles of the decay daughters that enter the  $S_{\text{O}}^{p_{\text{T}}=1}$  measurement are too different from their mother to give a precise result. Therefore,  $\Lambda$  ( $\bar{\Lambda}$ ) and  $K_{\text{S}}^0$  results will only be presented for  $p_{\text{T}} \geq 1.0\text{GeV}/c$ .

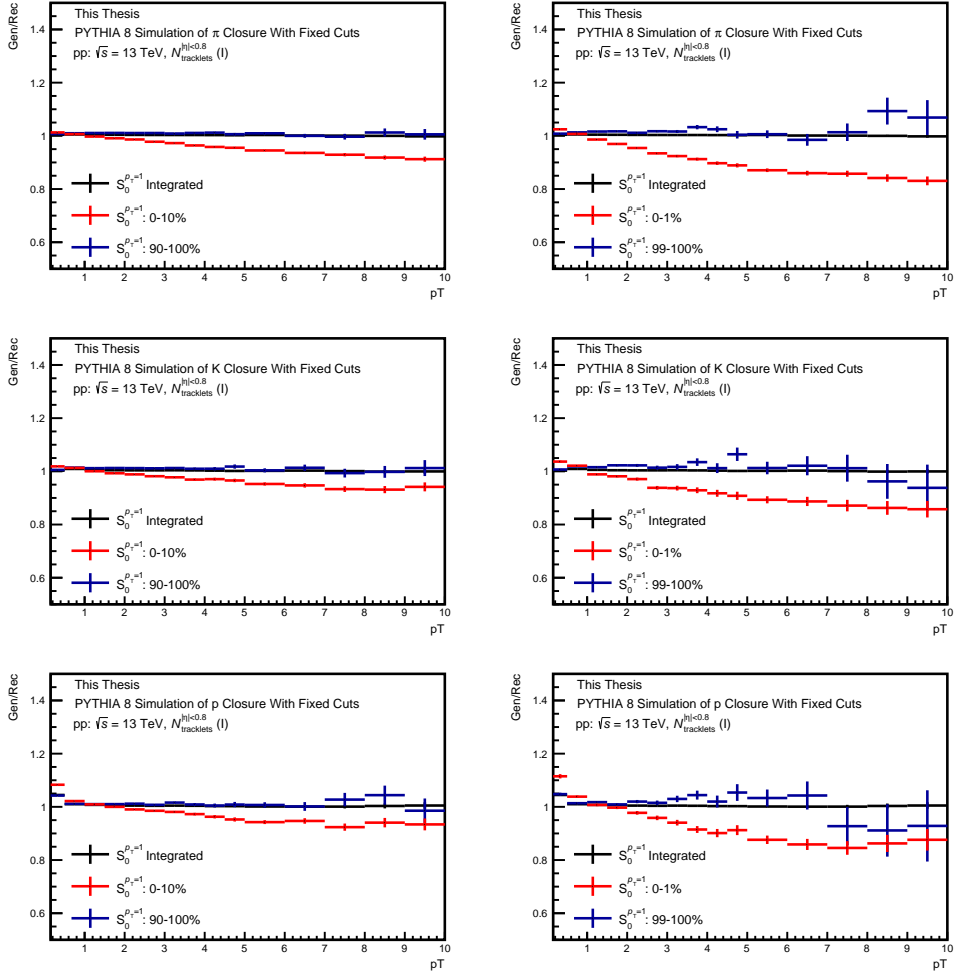


**Figure 7.8:**  $C(\text{PID}, p_T)^{S_O}$  for  $\pi$ , K, p using fixed 10% and 1% percentile  $S_O^{p_{T=1}}$  event selection. Fixed cuts are applied for the  $S_O^{p_{T=1}}$  calculation, meaning that percentiles shown in the legend apply to ONLY the reconstructed  $S_O^{p_{T=1}}$  distributions, and do not map to the generated  $S_O^{p_{T=1}}$  distribution (due to smearing by the detector). Blue and Red lines represent isotropic and jetty events, respectively.

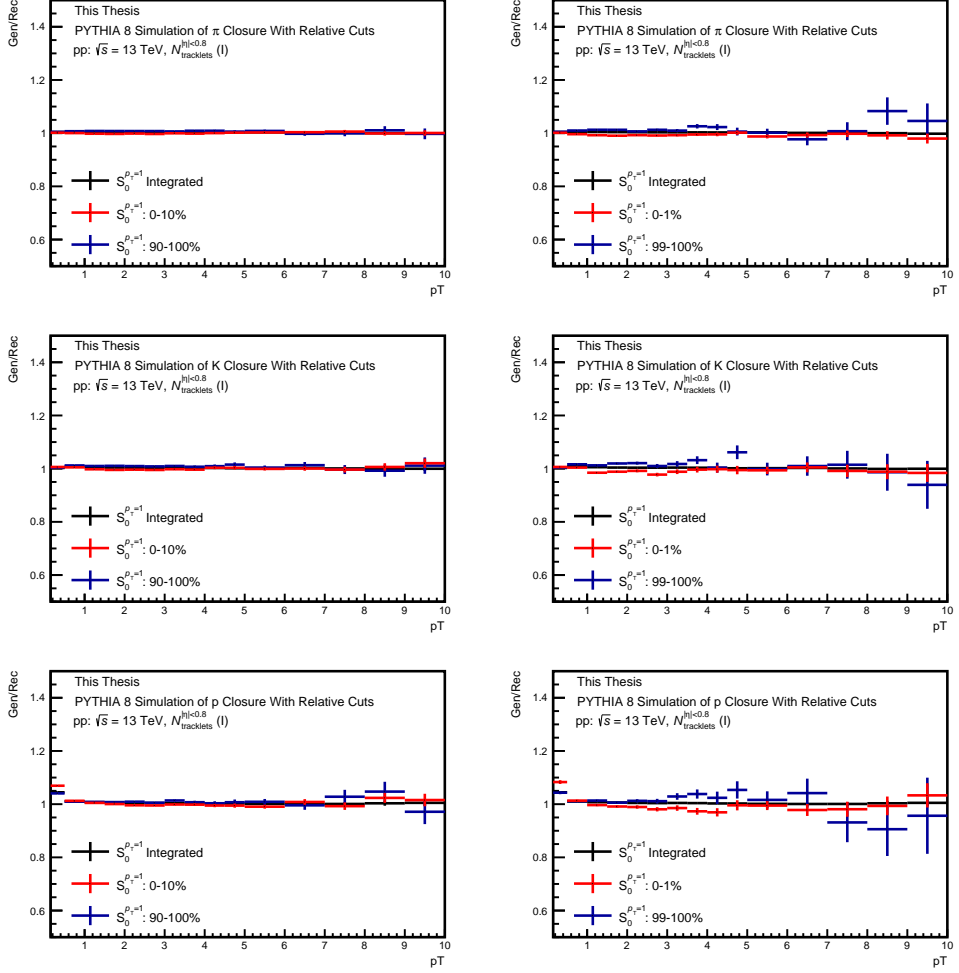


**Figure 7.9:**  $C(\text{PID}, p_T)^{S_0}$  for  $\pi$ , K, p using relative 10% and 1% percentile  $S_0^{pT=1}$  event selection. Relative cuts are applied for the  $S_0^{pT=1}$  calculation, meaning that percentiles in the legend apply to BOTH generated and reconstructed  $S_0^{pT=1}$  distributions. Blue and Red lines represent isotropic and jetty events, respectively

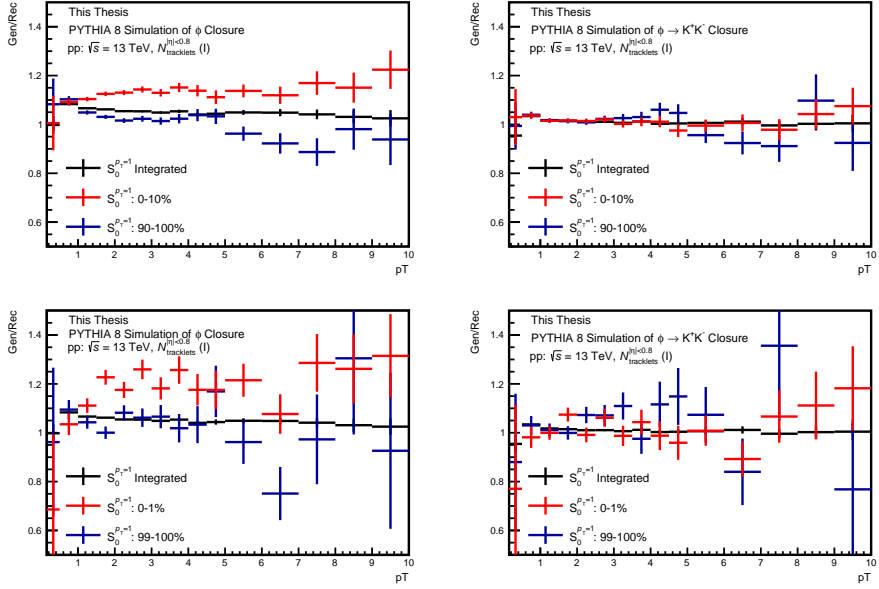


**Figure 7.10:**  $C(\phi, p_T)^{S_0}$ , using relative (quantiles are independently measured in both Rec and Gen) event selection, for 10% and 1%  $S_0^{p_T=1}$  percentiles. The left panels showcase full  $\phi$  production, whereas the right panels only contain  $\phi \rightarrow K^+K^-$  decay mode. Blue and Red lines represent isotropic and jetty events, respectively.

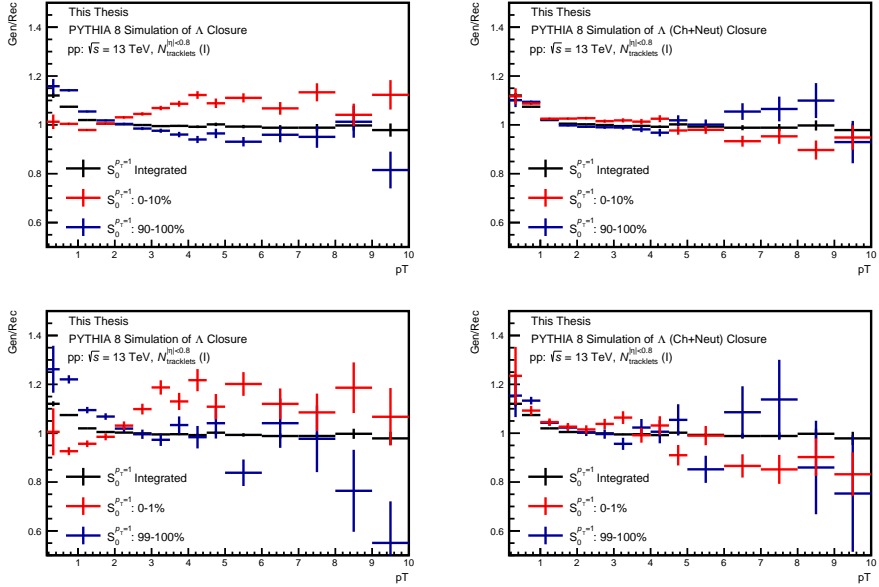


**Figure 7.11:**  $C(\Lambda, p_T)^{S_O^{p_T=1}}$ , using a Relative (quantiles are independently measured in both Rec and Gen) event selection, for 0-10% (top), and 0-1% (bottom)  $S_O^{p_T=1}$  quantiles. The left panels only include charged primary particles for the determination of the generated  $S_O^{p_T=1}$  distribution, whereas the right panels include primary  $\Lambda$  and  $K_S^0$ . Blue and Red lines represent isotropic and jetty events, respectively.

## 7.3 Definition of “High-Multiplicity”

The main goal of this analysis is to study particle dynamics in high-multiplicity events, in the regime where QGP-like phenomena are most visible in pp collisions (c.f., Sec. 3.4). Therefore, a multiplicity selection is required, in addition to the  $S_{\text{O}}^{p_{\text{T}}=1}$  event selection. Two different multiplicity estimators are used for this analysis; The total signal deposited in the V0 detectors, denoted V0M<sup>5</sup>, and the number of SPD tracklets<sup>6</sup> with  $|\eta| < 0.8$ , denoted  $N_{\text{tracklets}}^{|\eta| < 0.8}$ . The multiplicity is classified as a percentile for each estimator, where 0 % corresponds to the highest and 100 % to the lowest multiplicities. The high-multiplicity events presented in this thesis are selected from the top-1%(10%) multiplicity percentiles from both multiplicity estimators. The  $S_{\text{O}}^{p_{\text{T}}=1}$  distributions<sup>7</sup> for the top-1% V0M and  $N_{\text{tracklets}}^{|\eta| < 0.8}$  high-multiplicity events, are presented in Fig. 7.12.

### 7.3.1 Multiplicity Estimation at Forward Vs Midrapidity.

Previous measurements of QGP signatures in small system collisions, such as strangeness enhancement [45] and long-range correlations [16], have indicated that there is a strong correlation between the onset of QGP-like effects and multiplicity. However, if one considers pp collisions to be built up from several, incoherent sub-collisions (which is the case for PYTHIA, through multiple parton-parton interactions), there could be a trivial isotropization with increasing multiplicities. It is therefore important to disentangle this potential trivial bias, to study the underlying physical properties we are interested in. One can explore this bias by utilizing two different multiplicity estimators, covering different  $\eta$  intervals. The  $\langle p_{\text{T}} \rangle$  and the average pion yield  $\langle dN_{\pi}/dy \rangle$ , with different multiplicity and sphericity selection criteria, are reported in Fig. 7.13. Results are shown for both the forward (V0M) and mid-rapidity ( $N_{\text{tracklets}}^{|\eta| < 0.8}$ ) multiplicity estimators. A clear distinction is observed between how the different multiplicity estimators relate to the hardness of  $S_{\text{O}}^{p_{\text{T}}=1}$  selected events. One should keep in mind that this effect is *solely* driven by the rapidity region where the multiplicity is estimated, and not by properties or inefficiencies of the ALICE apparatus.

<sup>5</sup>The mean amplitude measured in V0A and V0C

<sup>6</sup>Tracklets are not “fully” reconstructed tracks. Refer to Sec. 5.2.2 for details.

<sup>7</sup>A 1D unfolding technique has been applied to the  $S_{\text{O}}^{p_{\text{T}}=1}$  distributions presented in Fig. 7.12, according to the procedure described in Ref. [19]. This ensures that the distribution is directly comparable with data. However, one should keep in mind that no unfolding is applied to the extracted particle yield relative to  $S_{\text{O}}^{p_{\text{T}}=1}$  since there already is good closure, demonstrated in Sec. 7.2.1.

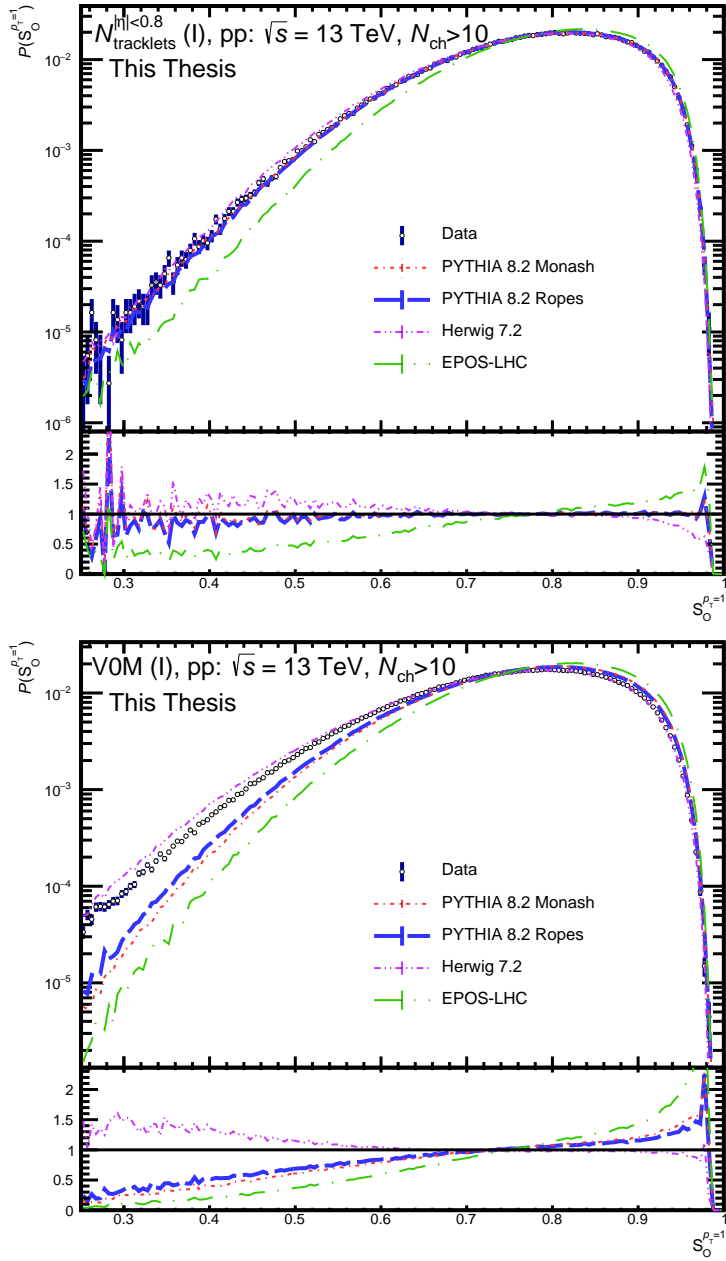


**Figure 7.12:**  $S_O^{pT=1}$  probability distributions for pp collisions at  $\sqrt{s} = 13$  TeV, for high-multiplicity events, measured by ALICE. The multiplicity is estimated both by the number of  $N_{\text{tracklets}}^{|\eta|<0.8}$  (top panel), and the activity in V0M (bottom panel). The obtained data is compared to different model predictions. Errors are purely statistical. See text for more details.



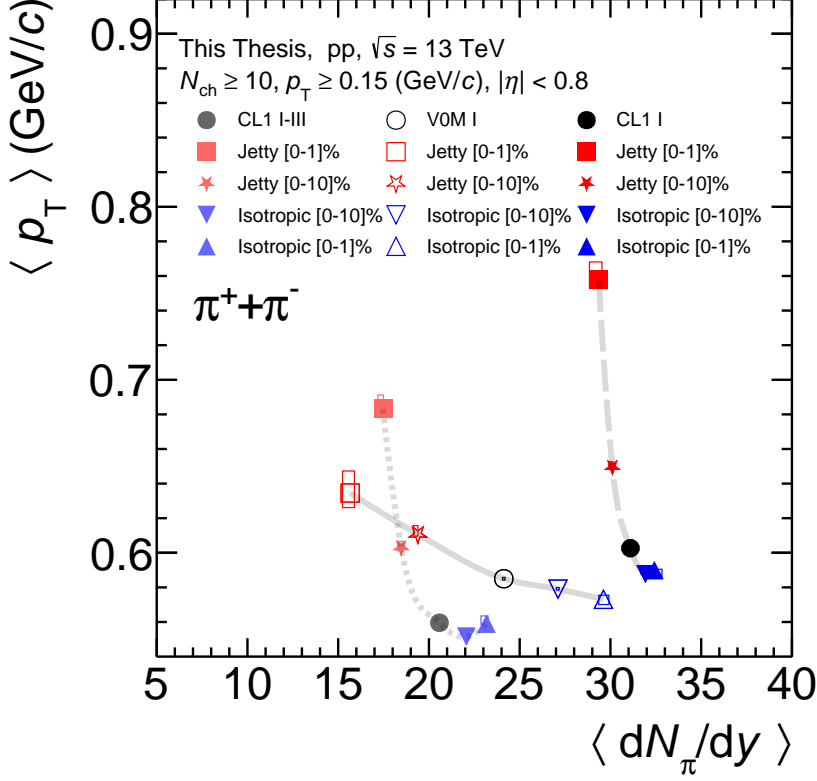


**Figure 7.13:** Correlation between  $\langle p_T \rangle$  and  $\langle dN_\pi/dy \rangle$  as a function of  $S_O^{p_T=1}$ , in the 0 – 10% and 0 – 1% V0M and  $N_{\text{tracklets}}^{|\eta| < 0.8}$  multiplicity classes. The statistical and total systematic uncertainties are represented with crosses and empty boxes, respectively. “CL1” is used in this plot to refer to  $N_{\text{tracklets}}^{|\eta| < 0.8}$ . This (incorrectly) assumes that the  $N_{\text{tracklets}}^{|\eta| < 0.8}$  only uses the “1st” layer in the SPD. However, both SPD layers are used to reconstruct  $N_{\text{tracklets}}^{|\eta| < 0.8}$ .

It is apparent that the  $S_O^{p_T=1}$  analysis of the V0M multiplicity selected events maintains a similar  $\langle p_T \rangle$ , but covers large variations in  $\langle dN_\pi/dy \rangle$ , for the different  $S_O^{p_T=1}$  selections. Since V0M multiplicity is estimated outside the central region, each multiplicity interval (e.g., 0-10%) will have a broad distribution of particles produced at midrapidity. This can easily be understood like this: consider two jets, boosted along forward rapidities, with no underlying event produced at midrapidity. Conversely, two jets at midrapidity with no UE would produce very low multiplicity at forward rapidities. Such an event would create large multiplicities at forward rapidities, while essentially no particles are produced at midrapidity. The results suggest that, if multiplicities are estimated at forward rapidities, a  $S_O^{p_T=1}$  selection at midrapidity is largely driven by a

trivial multiplicity dependence, as opposed to sensitivity to different particle production processes<sup>8</sup>.

In contrast, the  $N_{\text{tracklets}}^{|\eta| < 0.8}$  selected events are characterized by large differences in  $\langle p_T \rangle$  between the event classes, indicating that we are indeed selecting events according to their hardness. The implicit multiplicity dependence of  $S_O^{p_T=1}$  is minimized by using a mid-rapidity multiplicity estimator so that the multiplicity and  $S_O^{p_T=1}$  are measured in the same region. This implies that the  $N_{\text{tracklets}}^{|\eta| < 0.8}$  multiplicity estimator, in tandem with a  $S_O^{p_T=1}$  selection, is best at separating events based on their hardness. The spread in  $\langle dN_\pi/d\eta \rangle$  for the various  $S_O^{p_T=1}$  selections is the smallest for  $N_{\text{tracklets}}^{|\eta| < 0.8}$  0 – 1%, which makes this the preferred multiplicity estimation. To summarize, the event classes featured in this analysis are:

- $N_{\text{tracklets}}^{|\eta| < 0.8}$  0-1%, with  $S_O^{p_T=1}$  selections of [0-10%] and [0-1%]. As is shown in Fig. 7.13,  $N_{\text{tracklets}}^{|\eta| < 0.8}$  0-1% can minimize the trivial multiplicity dependence of  $S_O^{p_T=1}$ , whereas the most extreme topologies,  $S_O^{p_T=1}$  [0-1%], highlight the impact on the QCD dynamics of the extreme event-topologies. Unfortunately, limited statistics for  $S_O^{p_T=1}$  [0-1%]. (0.01% of the total amount of available events) does not allow for  $\phi$  production to be measured accurately. Consequently, the  $S_O^{p_T=1}$  selection is extended to [0-10%] (0.1% of the events) to allow for a direct comparison between  $\phi$  and  $\Xi$ .
- $N_{\text{tracklets}}^{|\eta| < 0.8}$  0-10% with  $S_O^{p_T=1}$  [0-1%]. This broader multiplicity range retains sufficient statistics (0.1% of the events) to study  $\phi$  meson production in the most extreme event topologies.
- V0M 0-1%,  $S_O^{p_T=1}$  [0-10%]. This is to study the impact of a broader  $\langle dN_\pi/dy \rangle$  selection, as well as being able to compare midrapidity to forward-rapidity multiplicity estimation between approximately similar  $dN_{\text{ch}}/d\eta$ , as is seen in Fig. 7.13.

Furthermore, the ratio between charged and neutral kaons are presented for both multiplicity estimators, with a 0-10% multiplicity selection, in Fig. 7.14. The charged-to-neutral ratios are consistent with unity, hinting at an overall suppression of neutral kaons when estimating multiplicity at midrapidity, which is in agreement with earlier findings [89] (discussed in Sec. 5.2.2). The most important feature is that there is no significant charged-to-neutral bias between

---

<sup>8</sup>The main modes of particle production, which are associated with characteristic azimuthal topologies described in Sec. 7.1.1.

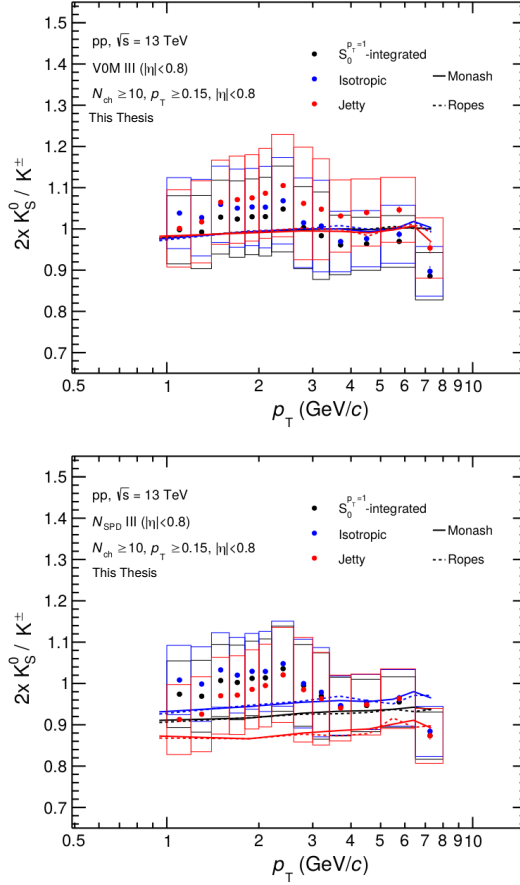


**Figure 7.14:** The ratio between charged and neutral kaons, obtained for pp collisions at  $\sqrt{s}=13$  TeV, for high-multiplicity events estimated by V0M activity (top panel), and the number of  $N_{\text{tracklets}}^{|\eta| < 0.8}$  (bottom panel). The data is compared to equivalent PYTHIA predictions, with the standard Monash tune, and with rope hadronization. Statistical and Systematic errors are represented by lines and boxes, respectively.

the different  $S_O^{p_T=1}$  selections, with either multiplicity estimator. This gives data-driven support to the claim that  $S_O^{p_T=1}$  is a robust estimator of the azimuthal topology, where charged particles can be utilized as a proxy to describe the event topology of neutral particles.

## 7.4 Systematic uncertainties for the $S_O^{p_T=1}$ analysis

Systematic uncertainties are evaluated by slightly adjusting the yield extraction parameters. The variations used to perform this evaluation are described in

detail in Sec. 7.4.1 and Sec. 7.4.2, for  $\phi$  mesons and  $\Xi$  baryons, respectively.

#### 7.4.1 Systematic uncertainties for $\phi$ meson production as a function of $S_{\text{O}}^{p_{\text{T}}=1}$ .

Several of the parameters in the  $\phi$  extraction yield are correlated, to the extent that it is impossible to evaluate the individual systematic uncertainty of each parameter variation. The variations are therefore grouped, and the systematic uncertainties are evaluated for variations in the entire group. The variations are defined in Sec. 6.2.5. The systematic uncertainties are grouped as follows:

- Signal Extraction:
  - Fitting Range: Variations of the fitting range for the combined peak fit.
  - Normalization Range: Variations of the normalization range for the estimate of the combinatorial background
  - Residual Background Function: The function used to evaluate the residual background, after subtraction of combinatorial background.
- Combinatorial Background Estimation: The uncertainties associated with the combinatorial background reduction.
- Tracking Uncertainty:
  - Variations in PID technique
  - Variation in track quality cuts
  - Variations in the maximum allowed displacement of the vertex along the  $z$ -plane.
- Material Budget: The uncertainty associated with the material budget of the ALICE detector.
- Hadronic Interaction: The uncertainties attributed to account for  $\phi$  production between hadronic interactions.
- Tracking Efficiency: Uncertainty associated with overall ALICE tracking efficiency

The systematic uncertainty procedure starts by first assigning a "default" yield  $D$ , defined as the  $\phi$  yield obtained when all the parameters are set to the nominal

configuration (c.f., Sec. 6.2.5). The yield  $A$  is then defined as the  $\phi$  yield obtained when changing the value of a single parameter. For each parameter and  $p_T$  interval, the variation average of  $(D - A)/D$  is assumed to be a measure of the deviation caused by varying this parameter.

However, not all variations described in Sec. 6.2.4 are considered for the final systematic uncertainty. To ensure that assigned uncertainties are of systematic origin, which cannot be accounted for statistical fluctuations, it is required that discrepancies between variations are significant *in quadrature*. As argued in Ref. [110], it is not sufficient for deviations between  $D$  and  $A$  to be within statistical uncertainties, since  $D$  and  $A$  use (for the vast majority) overlapping datasets. If variations are consistent within quadratures of statistical uncertainties, the variations *are not* considered as sources of systematic uncertainty. The variations are tested within each topological event selection (high-multiplicity, jetty, isotropic), where differences in quadrature are measured across the entire  $p_T$ -range, and aggregated into distributions of  $(D - A)/\sqrt{|\sigma_D^2 - \sigma_A^2|}$ , where  $\sigma_D$  and  $\sigma_A$  are statistical uncertainties for the default and alternate variation, respectively. If the distribution of  $(D - A)/\sqrt{|\sigma_D^2 - \sigma_A^2|}$  for a given parameter variation can be described by a Gaussian, with a mean of approximately 0, and a standard deviation near 1, the variation is deemed to be consistent within statistical uncertainties. A full set of  $(D - A)/\sqrt{|\sigma_D^2 - \sigma_A^2|}$  distributions, for each variation and event type, is found in Appendix C. To summarize, the following variations are excluded from the calculation of systematic uncertainties:

- High-Multiplicity Events
  - Looser TPC variation for Kaon PID,  $|n\sigma_K^{\text{TPC}}| < 2 + |n\sigma_K^{\text{TOF}}| < 3$ .
- Isotropic Events
  - Looser TPC variation for Kaon PID,  $|n\sigma_K^{\text{TPC}}| < 2 + |n\sigma_K^{\text{TOF}}| < 3$ .
  - Looser requirement for track quality cuts (c.f., Sec. 6.2.4)
  - Upper and lower variations of vertex displacement in  $z$ -plane,  $v_z$ .
- Jetty Events
  - Upper variation of vertex displacement in  $z$ -plane,  $v_z$ .

Moreover, while the parameters in each uncertainty group are correlated, they are not so strongly correlated that they could also be averaged over. In each  $p_T$ -interval, the *largest* deviation for a single parameter (averaged across individual

parameter variations), is therefore assigned as the systematic uncertainty *for the entire group*. This gives a conservative estimate of the total systematic uncertainty, with numerical values that are similar to previous ALICE publications. The systematic uncertainties are evaluated independently for  $S_O^{p_T=1}$ -integrated, high-multiplicity events, as well as for  $S_O^{p_T=1}$  selections in [0–10%] and [90–100%], for jetty and isotropic events, respectively. An example of the mean-variation in the PID technique, and the total systematic uncertainty for the "tracking uncertainty" group, are presented in Fig. 7.15.

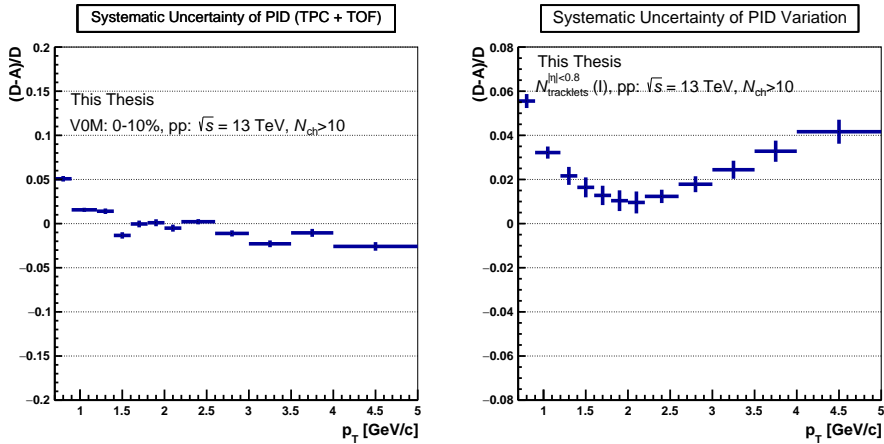


**Figure 7.15:** (left-panel) The mean-difference in yields from variations in the PID selection scheme for high-multiplicity events. (right-panel) The maximum uncertainties in each  $p_T$ -bin, among variations in PID technique, track quality cuts, and variations in the vertex along the z-plane.

The fractional uncertainties are presented in Fig. 7.16, high-multiplicity events, as well as the topological jetty and isotropic  $S_O^{p_T=1}$  selections. Keep in mind that Material Budget, Hadronic Interaction, and Tracking Efficiency are fully correlated across the different event selections, and therefore are canceled in the ratios (lower panels of spectra, and  $\phi$ -to- $\pi$  plots in Sec. 7.5.1).

#### 7.4.2 Systematic uncertainties for $\Xi$ baryon production as a function of $S_O^{p_T=1}$

In this section, we will describe how the systematic uncertainties were obtained for the  $\Xi$  yield extraction. One should keep in mind that I was not the primary analyzer for the  $\Xi$  studies. Therefore, there are differences in how the systematic uncertainties are evaluated between the  $\phi$  and  $\Xi$  analysis.

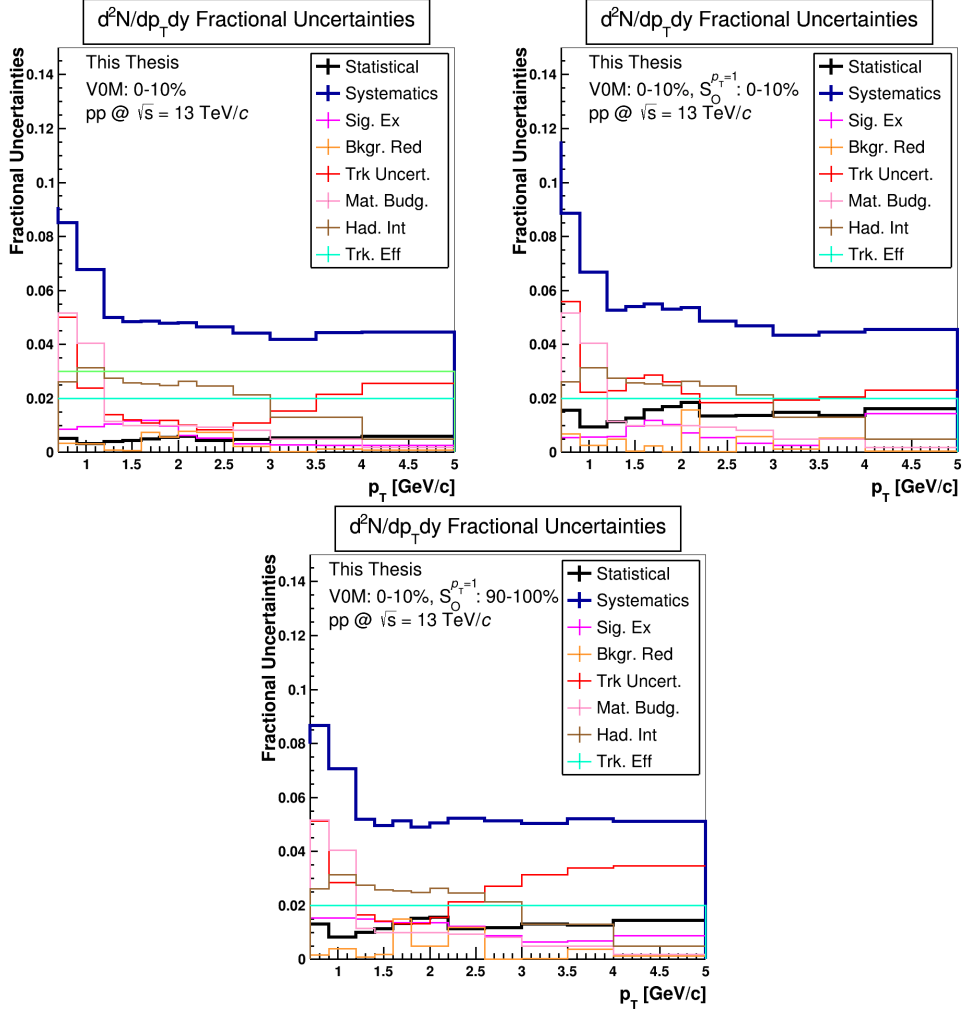


**Figure 7.16:** Fractional Systematic Uncertainties for  $\phi$  extraction, in High-Multiplicity (top-left panel), jetty (top-right panel), and isotropic (lower panel) events.

Since the yield extraction for the  $\Xi$  analysis contains less background<sup>9</sup> compared to the  $\phi$  analysis, the procedure of estimating systematic uncertainties is different. First, the focus will be on determining the systematic uncertainties for the 0-10% high-multiplicity selection, both for V0M and  $N_{\text{tracklets}}^{|\eta| < 0.8}$ . Subsequently, the uncertainties are evaluated for the jetty and isotropic ratios, to see what systematic uncertainties are either correlated or uncorrelated w.r.t., the high-multiplicity reference. With a larger amount of statistics, one can more precisely

<sup>9</sup>Due to characteristic cascade topologies, which are easily identifiable, thus reducing combinatorial background.

disentangle systematic effects from statistical uncertainties. For this reason, a 0-10% multiplicity interval is used for the evaluation of systematic uncertainties, with a 0-1% multiplicity interval utilized to validate that the uncertainties are stable, and do not strongly depend on multiplicity. Likewise, 20% intervals are used for high-precision studies of uncertainties in jetty and isotropic events, with 5% intervals for stability checks.

For the  $\Xi$  analysis, all variations are performed by looking at a double-ratio between default ("def") and alternate ("var") variations, in both real data, and Monte-Carlo generated events (which are supposed to correct for the same variation in data):

$$R(p_T) = \frac{\left(\frac{\text{Data}_{\text{var}}}{\text{Data}_{\text{def}}}\right)}{\left(\frac{\text{MC}_{\text{var}}}{\text{MC}_{\text{def}}}\right)}. \quad (7.4)$$

Similar to the  $\phi$  analysis, default and alternate variations will have overlapping datasets in the central peak region. However, variations are not rejected if they are consistent within statistical uncertainties in quadrature. Instead, the statistical fluctuations are assumed to be binomially distributed  $(N_{\text{def}}, p, N_{\text{var}})$ . 1000 variations are generated, using both real data, and MC simulations, resulting in 1000 random estimates for  $N_{\text{var}}$ , and then calculate 1000 estimates for  $R(p_T)$ , where the statistical uncertainty is:

$$\sigma_{R(p_T)} = \sqrt{\langle R(p_T)^2 \rangle - \langle R(p_T) \rangle^2}. \quad (7.5)$$

The systematic uncertainties are then evaluated by measuring the deviation between  $R(p_T)$  to unity. If  $R(p_T)$  is consistent within statistical uncertainties, estimated by  $\sigma_{R(p_T)}$ , the variation is rejected, and not considered for the measurement of systematic uncertainties. There are partial correlations between the systematic uncertainties between the high-multiplicity events, to the  $S_{\text{O}}^{p_T=1}$ -selected events. The correlation is larger than for the  $\phi$  analysis. Due to the cascade identification, there is very little combinatorial background, and therefore the correlation between event topology and the side-band background estimation is not as strong.  $R(p_T)$  is evaluated for  $S_{\text{O}}^{p_T=1}$ -differential variations, and the uncorrelated systematic uncertainty is then assigned as:

$$R_{\text{Unc.}S_{\text{O}}^{p_T=1}}(p_T) = \frac{R(p_T)_{S_{\text{O}}^{p_T=1}}}{R(p_T)_{\text{HM}}}, \quad (7.6)$$



Where "HM" denotes the  $R(p_T)$  measured from high-multiplicity events. This allows one to test which systematic uncertainties cancel in the ratio between  $S_O^{p_T=1}$ -differential, and  $S_O^{p_T=1}$ -independent high-multiplicity selection. Similar to  $\sigma_{R(p_T)}$ ,  $\sigma_{R_{\text{Unc}, S_O^{p_T=1}}(p_T)}$  is then measured as:

$$\sigma_{R_{\text{Unc}, S_O^{p_T=1}}(p_T)} = \frac{\sqrt{\sigma_{R(p_T)_{S_O^{p_T=1}}}^2 - \sigma_{R(p_T)_{\text{HM}}}^2}}{R(p_T)_{\text{HM}}}, \quad (7.7)$$

The fractional uncertainties for the  $\Xi$  analysis in Fig. 7.17, for high-multiplicity events, as well as the topological jetty and isotropic  $S_O^{p_T=1}$  selections.

## 7.5 Results

### 7.5.1 Results of $S_O^{p_T=1}$ -differential $p_T$ spectra at $N_{\text{tracklets}}^{|\eta| < 0.8}$ 0-1%

Figure 7.18 presents  $p_T$ -differential particle spectra of  $\phi$  and  $\Xi$  yields in  $S_O^{p_T=1}$  intervals of 10% percentiles. The  $S_O^{p_T=1}$  modification of the spectral shape, both for  $\Xi$  and  $\phi$  hadrons, are similar, demonstrating a significant hardening of the  $p_T$  in the lower, jetty  $S_O^{p_T=1}$  selection, and a softening of the  $p_T$  for larger, isotropic  $S_O^{p_T=1}$  selections. These trends are also well reflected in the model predictions. The PYTHIA 8 default Monash tune can describe the high- $p_T$  trends seen for  $\phi$ , but cannot accurately describe  $\Xi$  production, while the PYTHIA 8 rope tune is able to give qualitatively accurate predictions of both  $\Xi$  and  $\phi$  production as functions of  $S_O^{p_T=1}$ . EPOS-LHC overestimates the  $p_T$  dependence, while Herwig 7 can give an accurate prediction of the  $\Xi$  production, but severely underestimates the overall production of  $\phi$  mesons.

The  $S_O^{p_T=1}$ -differential average  $p_T$  ( $\langle p_T \rangle$ ) and yield ( $dN/dy$ ) are reported in Fig 7.19 as a function of the extracted particle masses,  $\Xi$  and  $\phi$ , alongside additional light-flavor particles;  $\pi$ , K, p (contributed from O. Vázquez Rueda [19]),  $K^{*0}$  (contributed from R. Rath [111]),  $K_S^0$  and  $\Lambda$  ( $\bar{\Lambda}$ ) (contributed from upcoming thesis of O. Matonoha).  $\langle dN_{\text{ch}}/d\eta \rangle$  and  $\langle p_T \rangle$  are obtained from the measured kinematic range, and the results are then extrapolated to the unmeasured  $p_T$  regions using Levy-Tsallis fits to the spectra [112]. To account for the additional systematic uncertainties arising from this procedure, the fit ranges are varied, and alternative parameterizations of the spectral shape are utilized, such as Boltzmann distributions,  $m_T$ -exponential,  $p_T$ -exponential, Fermi-Dirac (only for fermions) and Bose-Einstein statistics (only for bosons), and Boltzmann-Gibbs

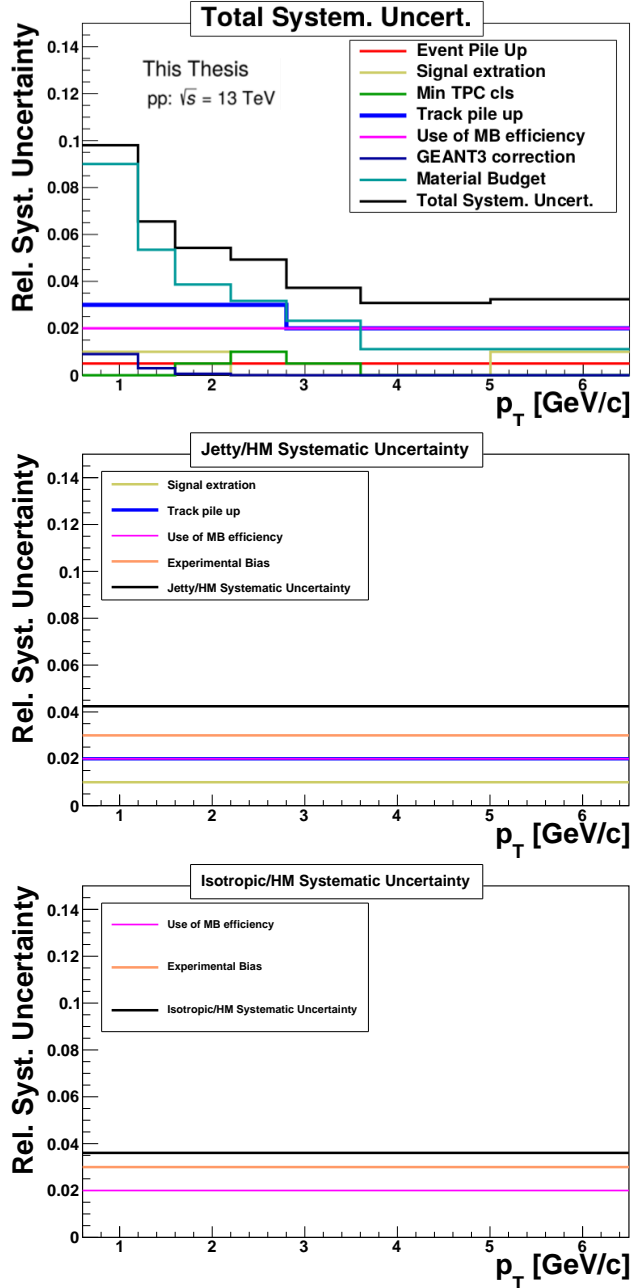


**Figure 7.17:** Fractional Systematic Uncertainties for  $\Xi$  extraction, in High-Multiplicity (top panel), jetty (middle panel), and isotropic (lower panel) events.

blast-wave functions. The differences in integrated yield from the extrapolated functions are added in quadrature to the total systematic uncertainties. More

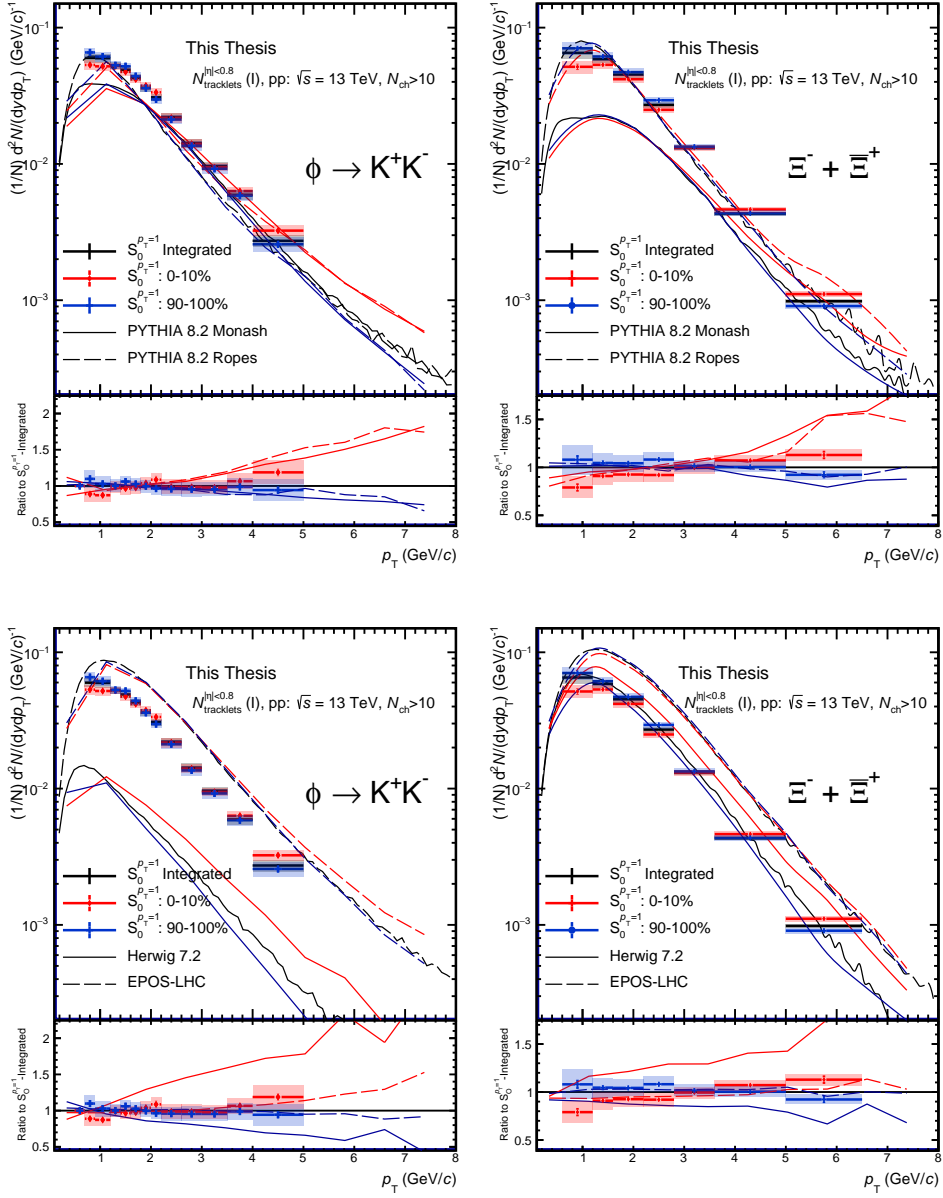


**Figure 7.18:** Transverse momentum spectra of  $\phi$  and  $\Xi$ , for  $S_0^{p_T=1}$  selected events at high-multiplicity, determined for events with a  $0-1\% N_{\text{tracklets}}^{|\eta|<0.8}$  multiplicity estimation, in  $0-1\% S_0^{p_T=1}$  percentiles. The upper and lower panels contain the same data points but are compared to different predictions of the same measurement, from PYTHIA (upper panels) and Herwig 7.2 + EPOS-LHC (lower panels), represented by different curves. Statistical and total systematic uncertainties are shown by error bars and boxes, respectively.

details about this procedure can be found in Ref [15].

The  $\langle p_T \rangle$  values extracted from the full range of light-flavor particles quantify the observations seen for the  $p_T$ -differential  $\Xi$  and  $\phi$  spectra; a significant  $p_T$  hardening in jetty events, consistent across all measured light-flavor particle species. Moreover, the  $\langle p_T \rangle$  of the high-multiplicity reference is consistent with the  $\langle p_T \rangle$  of the isotropic sample, for all particle species. This observation indicates that average properties of extreme, high-multiplicity events (top-1%), are well-described by isotropic event shapes, dominated by similar underlying physics processes. This suggests that the  $S_O^{p_T=1}$ -integrated event class cannot be described as an average between jetty and isotropic subsamples. Instead, the high-multiplicity reference seems to consist of a much more homogenous group of isotropic topologies, where jetty events are rare outliers. This observation is of particular interest, as it implies that events dominated by hard, jet-like physics are outliers, where QGP-like effects, such as radial flow and strangeness enhancement, are suppressed.

The lower panels of Fig. 7.19 demonstrate that the variance in particle density  $dN/dy$  is constrained between different  $S_O^{p_T=1}$  selections, for all measured particle species, when utilizing a 0-1%  $N_{\text{tracklets}}^{|\eta| < 0.8}$  multiplicity estimation. This is in agreement with what was previously observed for the pion yields in Fig.7.13. Hence, it is unlikely that any observed deviations between isotropic and jetty events are driven by a trivial multiplicity bias.

The presented models give reasonable descriptions of the integrated quantities relative to the dynamics to pions, but overestimate the overall  $\langle p_T \rangle$  for all particle species (except for  $K^{*0}$ ). One can note that PYTHIA, in particular for the Ropes, overestimates the production of protons and pions, but qualitatively describes the production of most strange hadrons. Moreover, Rope hadronization seems to primarily affect the baryons, as the resonance particles show only a small difference in the integrated yield between Ropes and Monash, in particular for the  $K^{*0}$ . In contrast, EPOS-LHC describes the production rates of most particles within the uncertainties of the data but is unable to capture the trend observed for charged kaons. Herwig 7 can qualitatively capture the behavior of  $\pi$  mesons but severely underestimates the integrated  $\phi$  properties.

Finally, the  $\Xi$  particle spectra are presented for the most extreme  $N_{\text{tracklets}}^{|\eta| < 0.8}$  0–1%,  $S_O^{p_T=1}$  0–1% event selection in Fig. 7.20. Notably, the  $\Xi$  production in the most extreme topologies supports the hypothesis that average high-multiplicity events are well-described by isotropic topologies, whereas jetty events demonstrate very different particle dynamics compared to the integrated  $S_O^{p_T=1}$  reference.

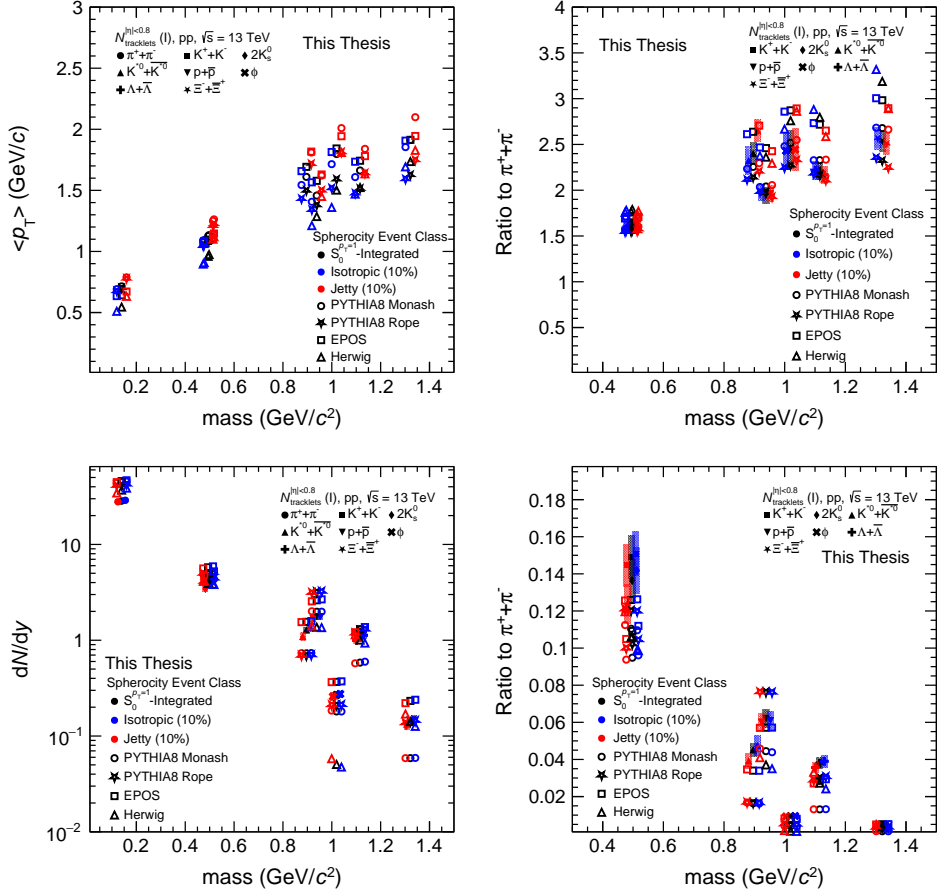


**Figure 7.19:** The  $\langle p_T \rangle$  and  $dN/dy$  as a function of particle masses obtained for  $S_0^{pT=1}$  classes selected for high-multiplicity events, determined by the events in the 0 – 1% of  $N_{\text{tracklets}}^{|\eta| < 0.8}$ . The upper (lower) panel shows the  $\langle p_T \rangle$  ( $dN/dy$ ). The left panels contain the absolute quantities for each particle, while the right panels show the ratios relative to pions. Systematic errors are depicted by the shaded bands, statistical errors are smaller than the presented marker sizes.

### 7.5.2 Particle ratios for $N_{\text{tracklets}}^{|\eta| < 0.8}$ 0-1%

The impact of QGP-like effects, such as strangeness enhancement, varies between different particle species. In previous measurements by the ALICE Collaboration [45], the enhancement of strange hadrons has been found to scale with the number of strange quarks. The  $\pi$  meson constitutes a good reference to study this scaling, as it is produced abundantly, and has no strange valance quarks. Therefore, by studying the  $p_T$ -differential particle-to-pion ratios, we can potentially identify QGP-like features in the data. "Double-ratios" (DR) are utilized to study the quantitative modifications of the particle dynamics in

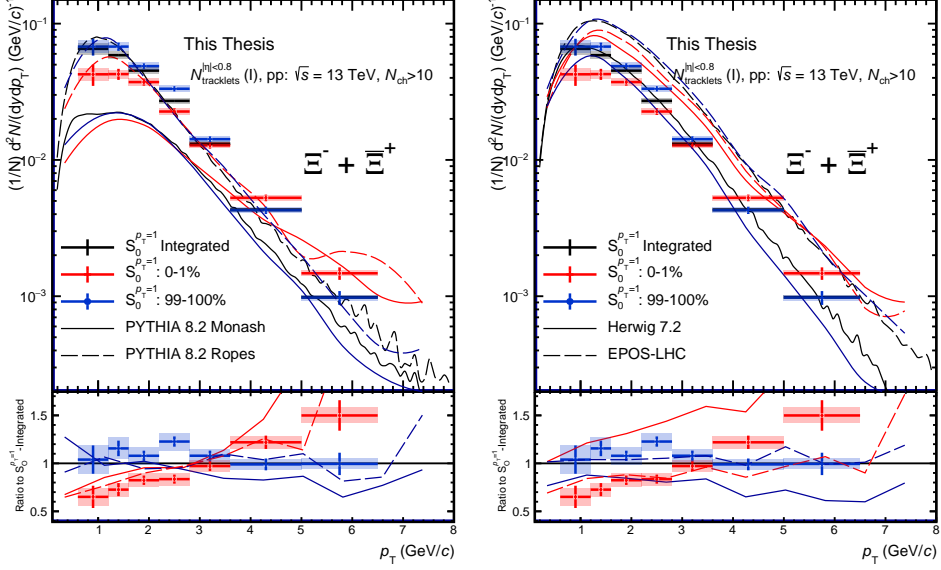


**Figure 7.20:** Transverse momentum spectra of  $\Xi$ , for  $S_O^{p_T=1}$  selected events at high-multiplicity, determined for events with a 0–1%  $N_{\text{tracklets}}^{|\eta| < 0.8}$  multiplicity estimation, in 0–1%  $S_O^{p_T=1}$  percentiles. The left and right panels contain the same data points but are compared to different predictions of the same measurement, from PYTHIA (left panel) and Herwig 7.2 + EPOS-LHC (right panel), represented by different curves. Statistical and total systematic uncertainties are shown by error bars and boxes, respectively.

different  $S_O^{p_T=1}$  topologies, of  $\Xi$  and  $\phi$  w.r.t.  $\pi$  mesons, as defined in Eq. 7.8:

$$\left( \frac{d^2N/d\eta dp_T}{d^2N_\pi/d\eta dp_T} \right)_{S_O^{p_T=1}} \bigg/ \left( \frac{d^2N/d\eta dp_T}{d^2N_\pi/d\eta dp_T} \right)_{HM} \quad (7.8)$$

where  $HM$  represents the  $S_O^{p_T=1}$ -integrated, high-multiplicity reference. From an experimental standpoint, there is a significant advantage of studying particle production through the DR. A large fraction of systematic uncertainty will cancel in the ratio between the  $S_O^{p_T=1}$ -differential and  $S_O^{p_T=1}$ -integrated spectra, for the same species. Consequently, the DR has the best systematic precision out of all measurements presented in this thesis. There are also significant advantages with the DR for MC model predictions; The DR means that focus can be shifted away from the large discrepancies between data and model in terms of absolute particle production, to instead test if the *relative* particle dynamics between event topologies are the same as in measured data.

Figure 7.21 presents the  $\Xi$ -to- $\pi$  and  $\phi$ -to- $\pi$  ratios in intervals of  $S_O^{p_T=1}$ , as functions of  $p_T$  for 0–1%  $N_{\text{tracklets}}^{|\eta| < 0.8}$  multiplicities, with corresponding DR, presented in the lower panels. Remarkably, the DR for both  $\Xi$  and  $\phi$  decrease significantly

for jetty events. While the effect is not as clear as for  $\phi$ , due to large uncertainties,  $\Xi$  production is suppressed for events with jet-like topologies. Furthermore,  $\Xi$  production in isotropic events is enhanced w.r.t. the high-multiplicity reference, suggesting that strangeness enhancement in high-multiplicity pp collisions originate from events softer events, with an isotropic distribution of particles. Both single-ratios (upper panels) converge down to zero, as  $p_T \rightarrow 0$ , suggesting that pion production will always be dominant at low- $p_T$ .

In contrast to MC model predictions, neither of the PYTHIA 8 tunes can describe the trends seen in the absolute  $\phi$  ( $\Xi$ )-to- $\pi$  ratios. However, both PYTHIA tunes are able to qualitatively predict the interplay between the  $S_O^{p_T=1}$ -integrated high-multiplicity reference, and the  $S_O^{p_T=1}$ -differential event classes. Remarkably, there is no difference between the PYTHIA8 Monash to the PYTHIA8 Rope curves. Even though the production rates of light-flavor hadrons are different, both variations can capture the trends presented for the  $S_O^{p_T=1}$ -selected events. This can also be seen for EPOS-LHC and Herwig 7; while the generators give very different predictions of the single ratio, they both give qualitatively good descriptions of the DR.

The  $p_T$ -differential  $\Xi$ -to- $\pi$  ratio for the most extreme event selection is presented in Fig. 7.22, for 0–1% multiplicity and 0–1%  $S_O^{p_T=1}$  percentiles. The effects observed in  $\Xi$ -to- $\pi$  ratios for the broader  $S_O^{p_T=1}$ -intervals are now enhanced; there is a clear effect of an enhancement/suppression of  $\Xi$  production, relative to pions, in isotropic and jetty events, respectively. This is demonstrated both through the single particle-to- $\pi$  ratio, and in the DR. In particular, one can note a large suppression of strange hadrons across the entire measured  $p_T$  range for events with jetty topologies. This novel feature suggests that the abundance of strange hadrons in high-multiplicity events is driven by events associated with soft physics, in terms of the azimuthal topology. This observation also implies that there is a significant amount of high-multiplicity events that reflect the same rates of reduced strangeness production found in low-multiplicity events. ALICE has previously published studies of the  $\Lambda/K_S^0$  in the UE and the UE-subtracted jet, where it was found that the ratio in the jet was far below that of the ratio in the UE [113]. This is qualitatively similar to what we observe for the most extreme jetty events in this study. One could therefore understand the results obtained here as a generalization to jet-dominated events.

Similar to Fig. 7.21, the two PYTHIA tunes are qualitatively able to predict the interplay between the high-multiplicity reference, and the  $S_O^{p_T=1}$  selected events. However, both tunes dramatically underestimate the total amount of  $\Xi$  production. This is remarkable since Rope hadronization has previously been able to predict observations of strangeness enhancement [114].

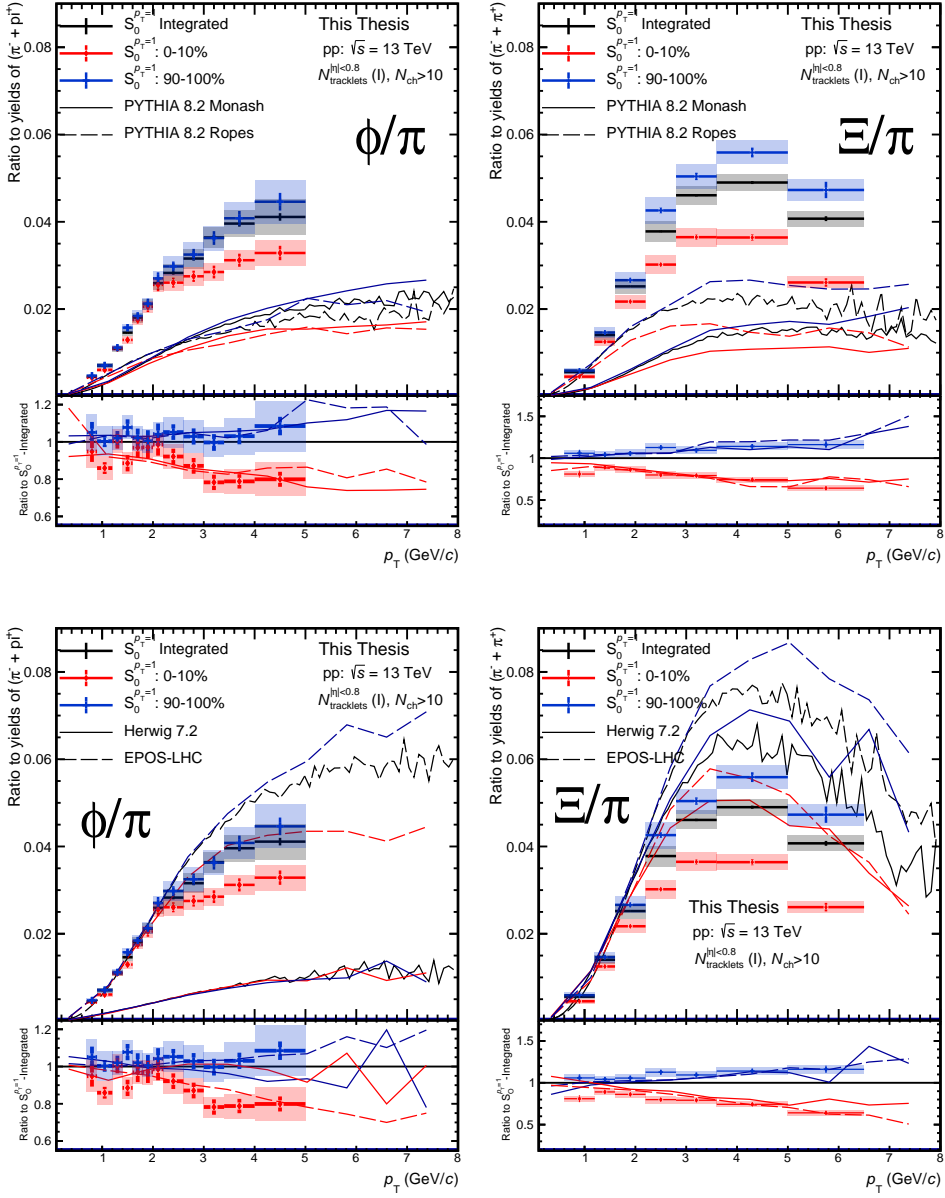


**Figure 7.21:** Transverse momentum distribution of  $\phi$  and  $\Xi$  production, relative to  $\pi$  production for  $S_0^{pT=1}$  selected events at high-multiplicity, determined by events in the top-1% distribution of  $N_{\text{tracklets}}^{|\eta| < 0.8}$ . Statistical and total systematic uncertainties are shown by error bars and boxes, respectively. The upper and lower panels contain the same data points but are compared to different predictions of the same measurement, from PYTHIA (upper panels) and Herwig 7.2 + EPOS-LHC (lower panels), represented by different curves.



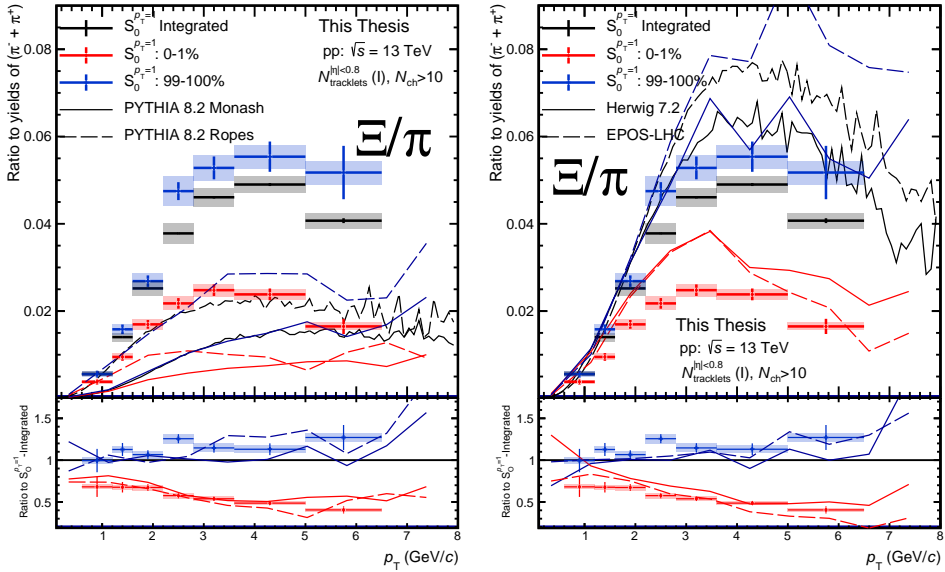


**Figure 7.22:** Transverse momentum distribution of  $\phi$  and  $\Xi$  production, relative to  $\pi$  production for the most extreme  $S_0^{p_T=1}$  selected events at high-multiplicity, determined by events in the top-1% distribution of  $N_{\text{tracklets}}^{|\eta|<0.8}$ . Statistical and total systematic uncertainties are shown by error bars and boxes, respectively. The left and right panels contain the same data points but are compared to different predictions of the same measurement, from PYTHIA (left panel) and Herwig 7.2 + EPOS-LHC (right panel), represented by different curves.

The  $\phi$ -to- $\Xi$   $p_T$ -differential ratio is presented in Fig. 7.23. Even though  $\phi$  has a net strangeness of zero, there are clear similarities in the production dynamics between  $\Xi$  and  $\phi$ , suggesting that it is effectively double strange. The rope hadronization framework in PYTHIA predicts both the single and double ratio reasonably well. It is remarkable that even though Monash fails to predict the single ratio, Monash and the Rope predictions show no significant deviations for the double ratios.

### 7.5.3 Integrated yields as a function of $S_0^{p_T=1}$

The integrated double ratios of  $\Xi$ ,  $\Lambda$ , and protons, relative to  $\pi$  mesons, are presented as functions of  $S_0^{p_T=1}$  in Fig. 7.24 and Fig. 7.25. The two plots contain the same data points, but use different ordinate ranges in the ratio to accommodate the MC-generator predictions. The  $\phi$  meson could not be included in this measurement due to insufficient statistics<sup>10</sup>.

<sup>10</sup>The current statistical limitations of the  $\phi$  analysis would only allow for the three most central bins (0-10%) to be covered.

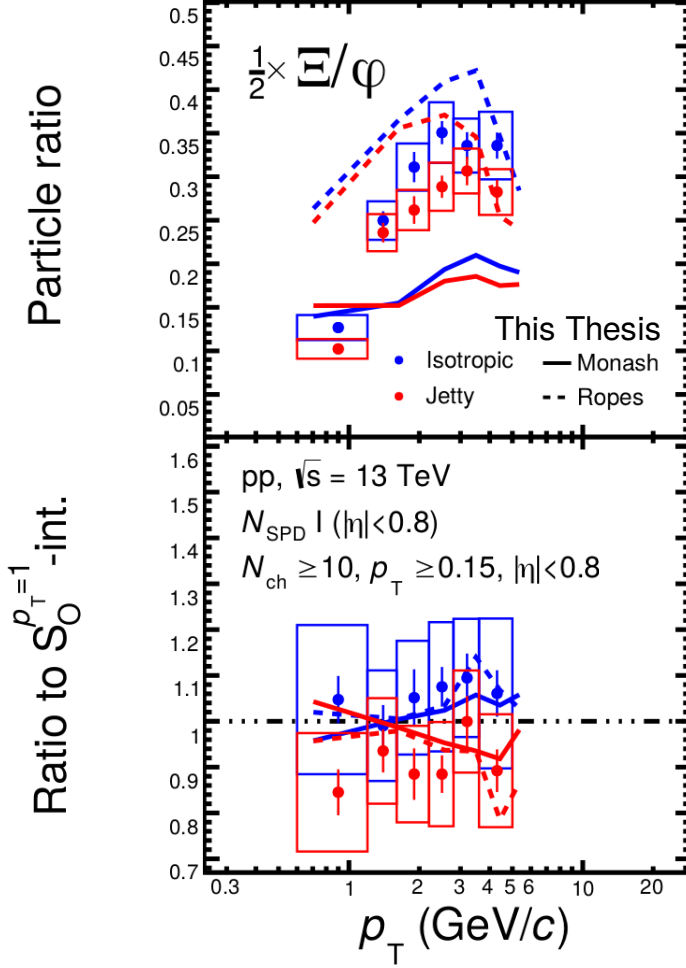


**Figure 7.23:**  $\Xi$ -to- $\phi$  ratio for different  $S_O^{p_T=1}$  classes are obtained for 0 – 1% events measured by the  $N_{\text{tracklets}}^{|\eta| < 0.8}$ . Lower panels show the ratio to  $S_O^{p_T=1}$ -integrated event selection. Statistical and total systematic uncertainties are shown by bars and boxes, respectively. The curves represent different model predictions of the same measurement.

The results demonstrate that the strange-hadron yield increases as a function of  $S_O^{p_T=1}$ , with indications of a significant mass ordering. We find that the strange-ness production is suppressed in events with jet-like topologies, and slightly enhanced in softer, isotropic event topologies. One should keep in mind that the charged particle density for the 0–1%  $N_{\text{tracklets}}^{|\eta| < 0.8}$  is practically fixed between the different  $S_O^{p_T=1}$ -selections, as one can see in Fig. 7.13. This is remarkable, as earlier ALICE publications of measurements in pp collisions at  $\sqrt{s} = 13$  have strongly suggested that the charged particle density,  $dN_{\text{ch}}/d\eta$ , is the driving

factor for strangeness enhancement [1].

While the multiplicity is constrained, the charged particle densities are not identical between the different  $S_{\text{O}}^{p_{\text{T}}=1}$  event selections. As can be seen in Fig. 7.13, there is approximately a 10% difference in pion densities between the most jetty and isotropic  $S_{\text{O}}^{p_{\text{T}}=1}$  event classes. However, the results presented in Fig. 7.24 demonstrate that the relative  $\Xi$  production decreases in the order of 20%, for the most jetty events. Based on estimates from Ref. [1], to obtain a 20% effect in relative  $\Xi$  production solely based on multiplicity, one would require a multiplicity difference of an order of approximately 60–70%. This indicates that the strangeness suppression presented in this analysis is less likely to be driven by a trivial difference in multiplicity, and more so driven by the physics processes associated with the event topology.

This novel feature can give further insight into the underlying mechanism(s) that drives both strangeness enhancement, and overall charged particle production. Remarkably, these findings suggest that charged particle production is not driven by a single source, given that one can obtain high-multiplicity events, with relative strangeness production rates observed in average low-multiplicity events. This indicates that particle production is driven by parallel sources, with varying strangeness-to- $\pi$  production rates. One can characterize jetty events as exhibiting less QGP-like effects, with a large amount of strangeness suppression, whereas isotropic events are characterized as the complete opposite, with enhanced strangeness production and more QGP-like effects. This suggests that one can control the degree of QGP-like effects in small systems, by categorizing events based on their event topology. Furthermore, it demonstrates that average high-multiplicity collisions are well-described by azimuthal topologies dominated by soft processes, where harder, jet-like processes are clear outliers.

The PYTHIA8 Rope hadronization framework and EPOS-LHC, models incorporating two-component phenomenologies, can predict the qualitative trend of enhancement/suppression of strange particle production as a function of  $S_{\text{O}}^{p_{\text{T}}=1}$ , albeit with a different mass-ordering for  $\Lambda$  and  $\Xi$ . In contrast, both the PYTHIA8 Monash and Herwig 7 predictions are unable to describe the reported experimental observation. Surprisingly, Herwig 7 predicts the opposite trend; enhancement of all three baryons in jetty events, and suppression of all three baryons in isotropic events. If this is a generic feature of the new strangeness-enhancement process introduced in Herwig 7.2 [115], then the results presented in this thesis seem to rule out this mechanism.

### 7.5.4 $S_O^{p_T=1}$ results with a broadened multiplicity range

In Sec. 7.5.1, it was shown that the 0-1% topology selection produced the largest effects w.r.t. strange particle production. However, the  $\phi$  meson had to be excluded from those measurements due to statistical limitations related to signal extraction. Therefore, in this Section, we report on  $S_O^{p_T=1}$  measurements with the broader multiplicity selection described in Sec. 7.5.1; first by expanding to 0–10%  $N_{\text{tracklets}}^{|\eta| < 0.8}$ , and then by estimating the multiplicities at forward rapidities with the V0M. The  $p_T$ -differential  $\Xi$  and  $\phi$  particle spectra are shown for both 0–10%  $N_{\text{tracklets}}^{|\eta| < 0.8}$  and 0–1% V0M percentiles in Fig. 7.26, and Fig. 7.27, respectively, for events in different  $S_O^{p_T=1}$  intervals.

$\phi$  meson production exhibits similar features to  $\Xi$  production when narrowing the  $S_O^{p_T=1}$  interval, highlighting a large suppression of the  $p_T$ -differential yield of strange hadrons relative to pions in events with extreme jet-like topologies, presented in Fig. 7.28 for a 0–10%  $N_{\text{tracklets}}^{|\eta| < 0.8}$  multiplicity estimation. The large modification of the jetty  $p_T$ -spectra, relative to the high-multiplicity reference, further indicates the jet-like topologies are not well-described by the average high-multiplicity events. The results suggest that  $\phi$  meson production is favored in softer events containing QGP-like features. While the origin of the

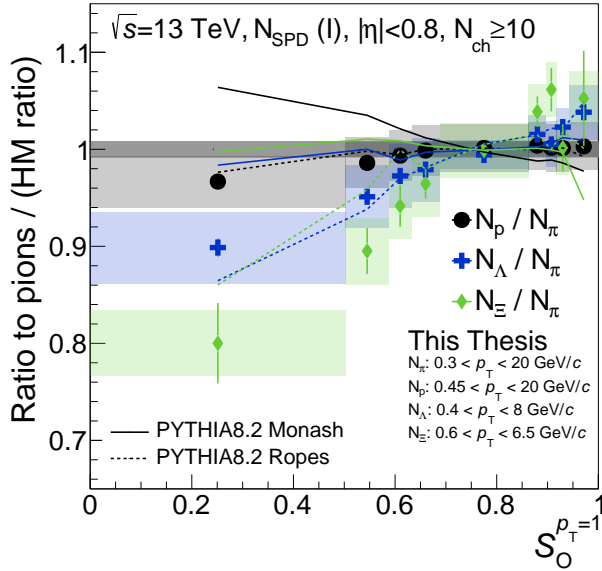


**Figure 7.24:** The Double-Ratios of integrated yield as a function of  $S_O^{p_T=1}$  are represented in the top-1% of  $N_{\text{tracklets}}^{|\eta| < 0.8}$ . Statistical and total systematic uncertainties are shown by bars and boxes, respectively. The curves represent different model predictions of the same measurement.

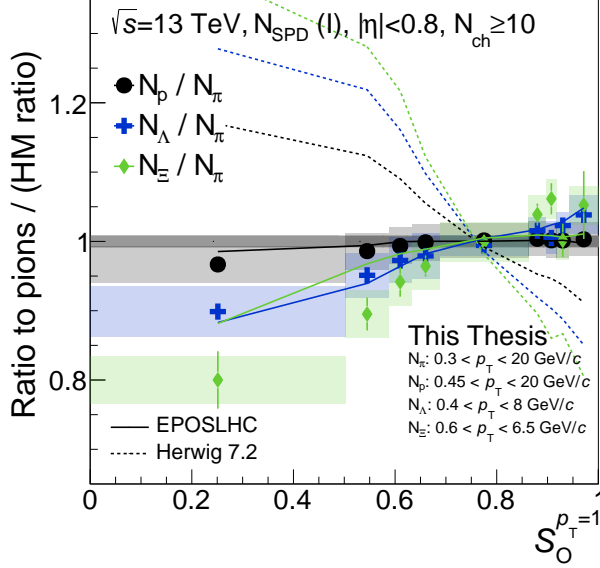


**Figure 7.25:** The Double-Ratios of integrated yield as a function of  $S_O^{p_T=1}$  are represented in the top-1% of  $N_{\text{tracklets}}^{|\eta| < 0.8}$ . Statistical and total systematic uncertainties are shown by bars and boxes, respectively. The curves represent different model predictions of the same measurement.

suppression of  $\phi$  production is not fully understood, the behavior is consistent with other strange particles as functions of  $S_O^{p_T=1}$ .

In contrast, spectra and particle ratios utilizing a forward-rapidity estimation of multiplicity showcase very different behavior, presented in Fig. 7.27 and Fig. 7.29. The  $p_T$ -differential particle spectra, for both  $\phi$  and  $\Xi$ , report a weak modification of the  $S_O^{p_T=1}$  selection, compared to either percentile of  $N_{\text{tracklets}}^{|\eta| < 0.8}$  multiplicities/ $S_O^{p_T=1}$  intervals presented in this thesis. The particle spectra exhibit a flat difference in the ratio to the high-multiplicity reference, suggesting that  $S_O^{p_T=1}$  event selection is not sensitive w.r.t. the forward multiplicity, and the difference in yield is largely driven by a multiplicity bias. This interpretation is strengthened by the observations seen in the  $\phi$  ( $\Xi$ )-to- $\pi$  ratios, highlighting a very small modification (and is consistent with unity for  $\phi$ ).

The  $p_T$ -integrated,  $S_O^{p_T=1}$ -differential yields are presented in Fig. 7.30, for the two expanded multiplicity estimations. Remarkably, the  $S_O^{p_T=1}$ -dependent enhancement of strange hadrons seems to vanish once the multiplicity estimation is measured at forward rapidities. Similarly to Fig. 7.24 and Fig. 7.25, the effect of strangeness enhancement is consistent between different ranges of the mid-rapidity multiplicity estimation, and the effect is suggested to be slightly stronger in the more extreme multiplicity case.

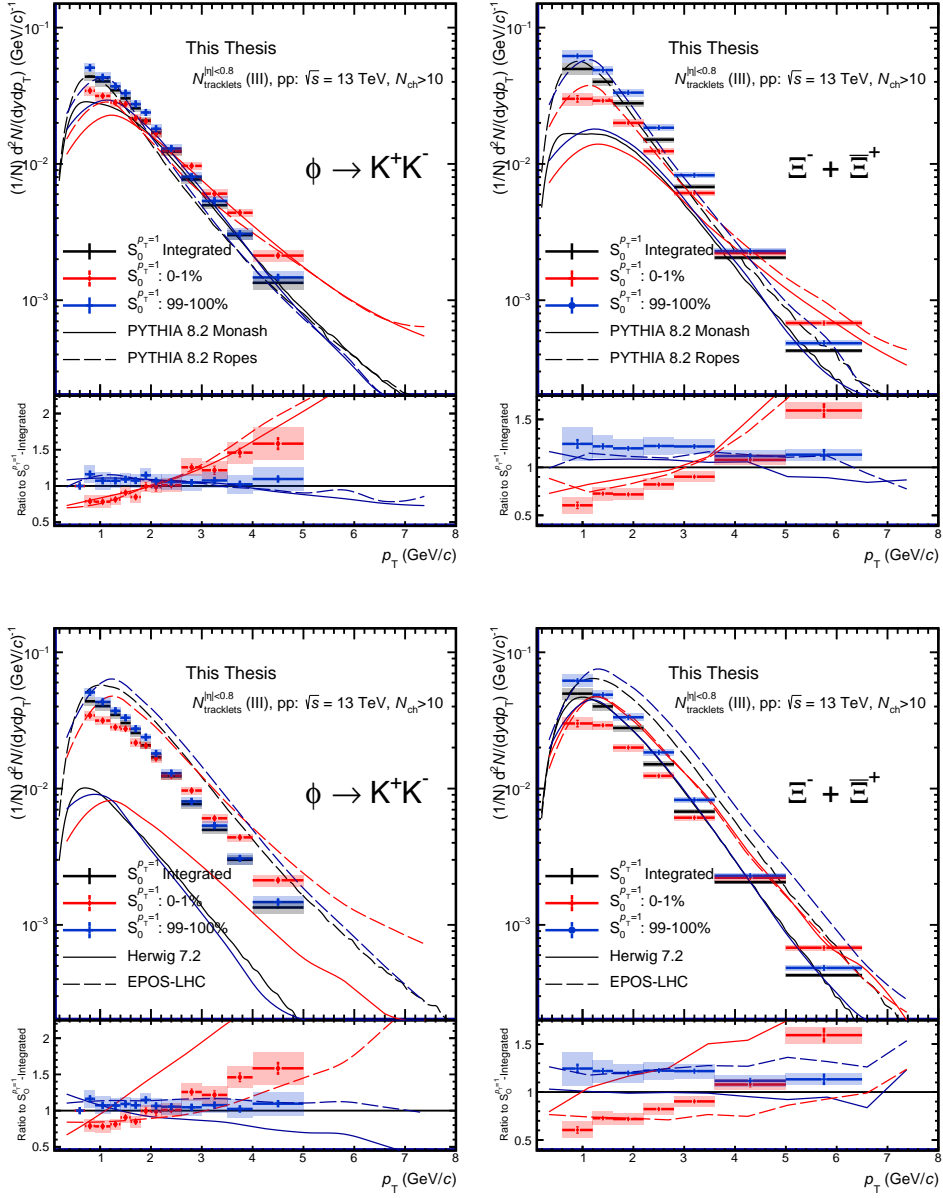


**Figure 7.26:** Transverse momentum spectra of  $\phi$  and  $\Xi$ , for  $S_0^{p_T=1}$  selected events at high-multiplicity, determined for events with a 0–10%  $N_{\text{tracklets}}^{|\eta| < 0.8}$  multiplicity estimation, in 0–1%  $S_0^{p_T=1}$  percentiles. The upper and lower panels contain the same data points but are compared to different predictions of the same measurement, from PYTHIA (top panels) and Herwig 7.2 + EPOS-LHC (bottom panels), represented by different curves. Statistical and total systematic uncertainties are shown by error bars and boxes, respectively.

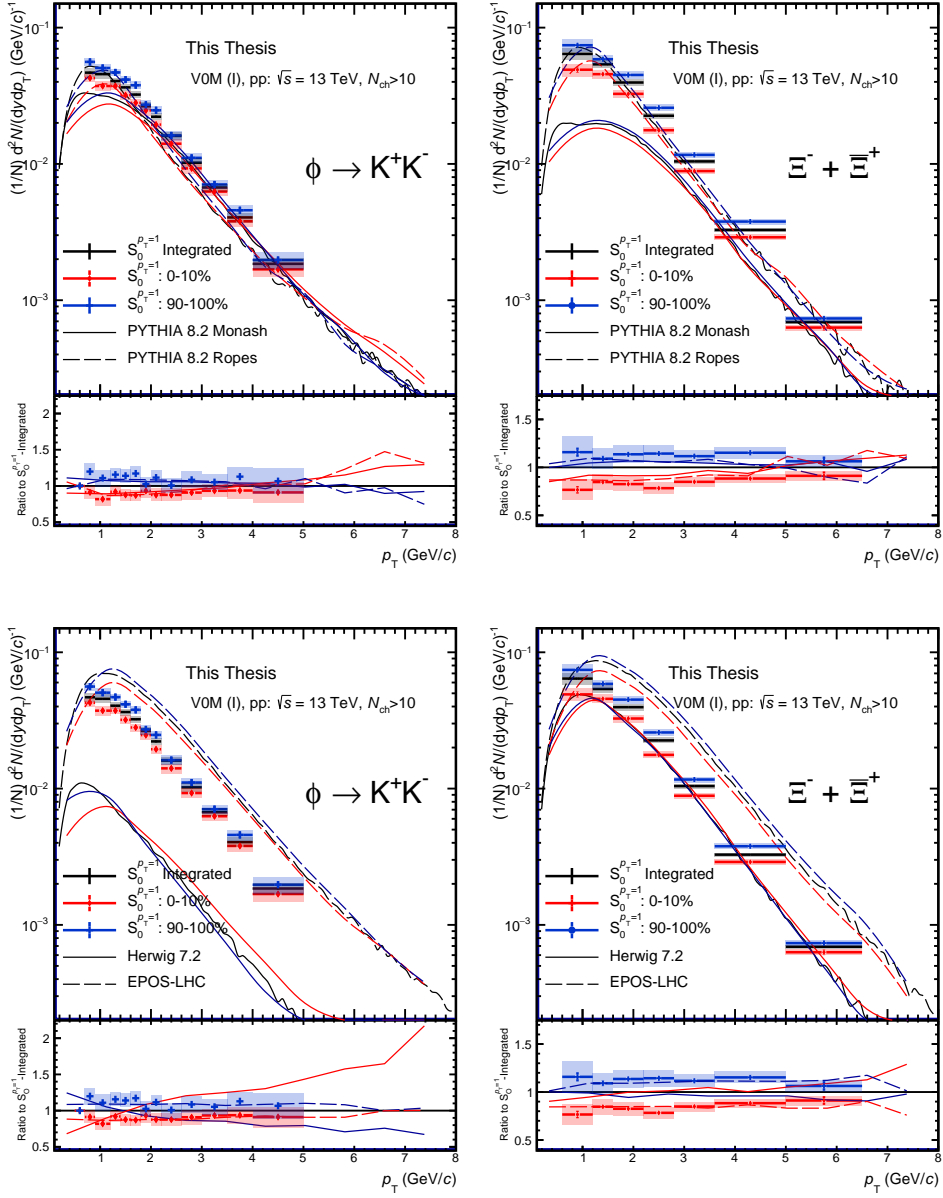


**Figure 7.27:** Transverse momentum spectra of  $\phi$  and  $\Xi$ , for  $S_0^{p_T=1}$  selected events at high-multiplicity, determined for events with a 0–1% V0M multiplicity estimation, in 0–10%  $S_0^{p_T=1}$  percentiles. The upper and lower panels contain the same data points but are compared to different predictions of the same measurement, from PYTHIA (top panels) and Herwig 7.2 + EPOS-LHC (bottom panels), represented by different curves. Statistical and total systematic uncertainties are shown by error bars and boxes, respectively.

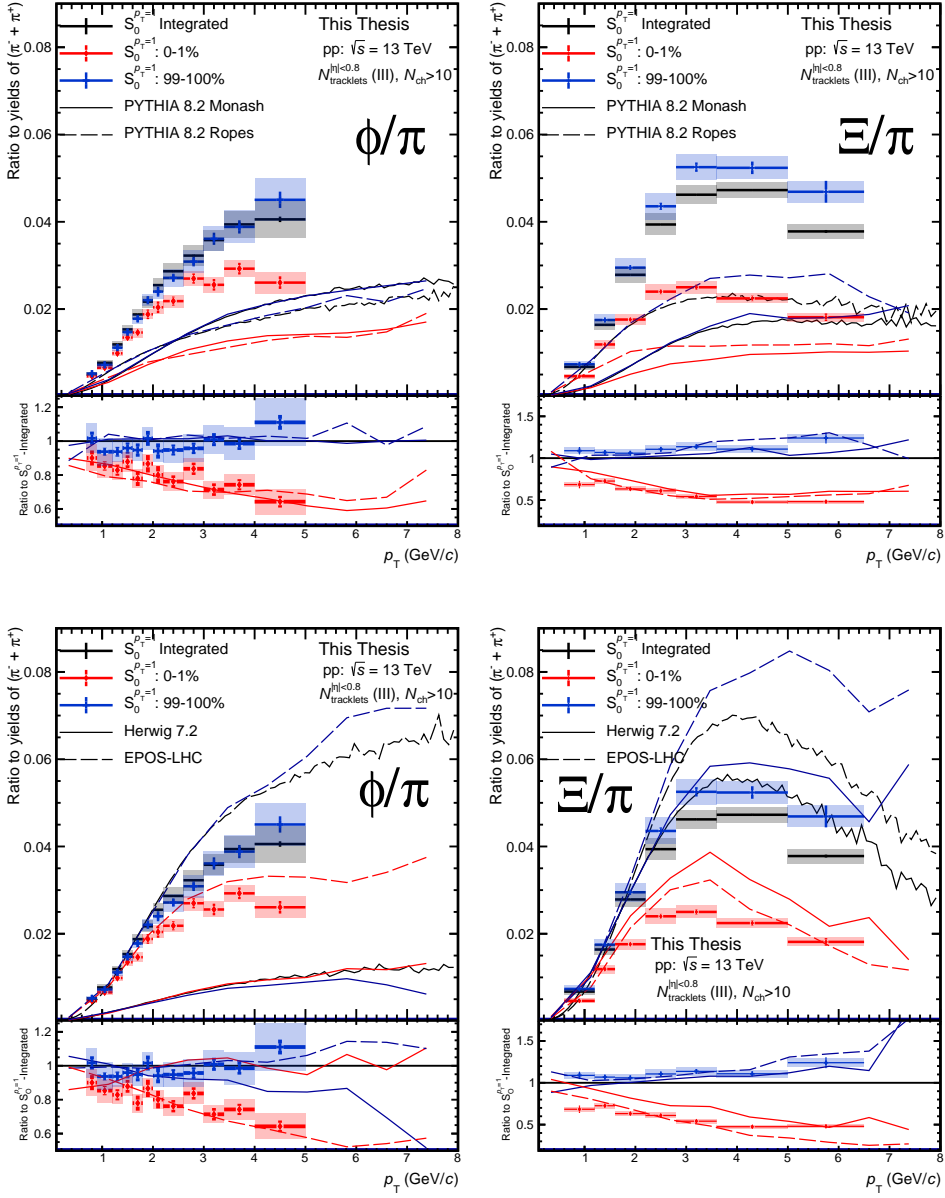


**Figure 7.28:**  $p_T$ -differential production of  $\phi$  and  $\Xi$  relative to  $\pi$ , for  $S_0^{pT=1}$  selected events at high-multiplicity, determined for events with a 0–10%  $N_{\text{tracklets}}^{|\eta|<0.8}$  multiplicity estimation, in 0–1%  $S_0^{pT=1}$  percentiles. The upper and lower panels contain the same data points but are compared to different predictions of the same measurement, from PYTHIA (top panels) and Herwig 7.2 + EPOS-LHC (bottom panels), represented by different curves. Statistical and total systematic uncertainties are shown by error bars and boxes, respectively.



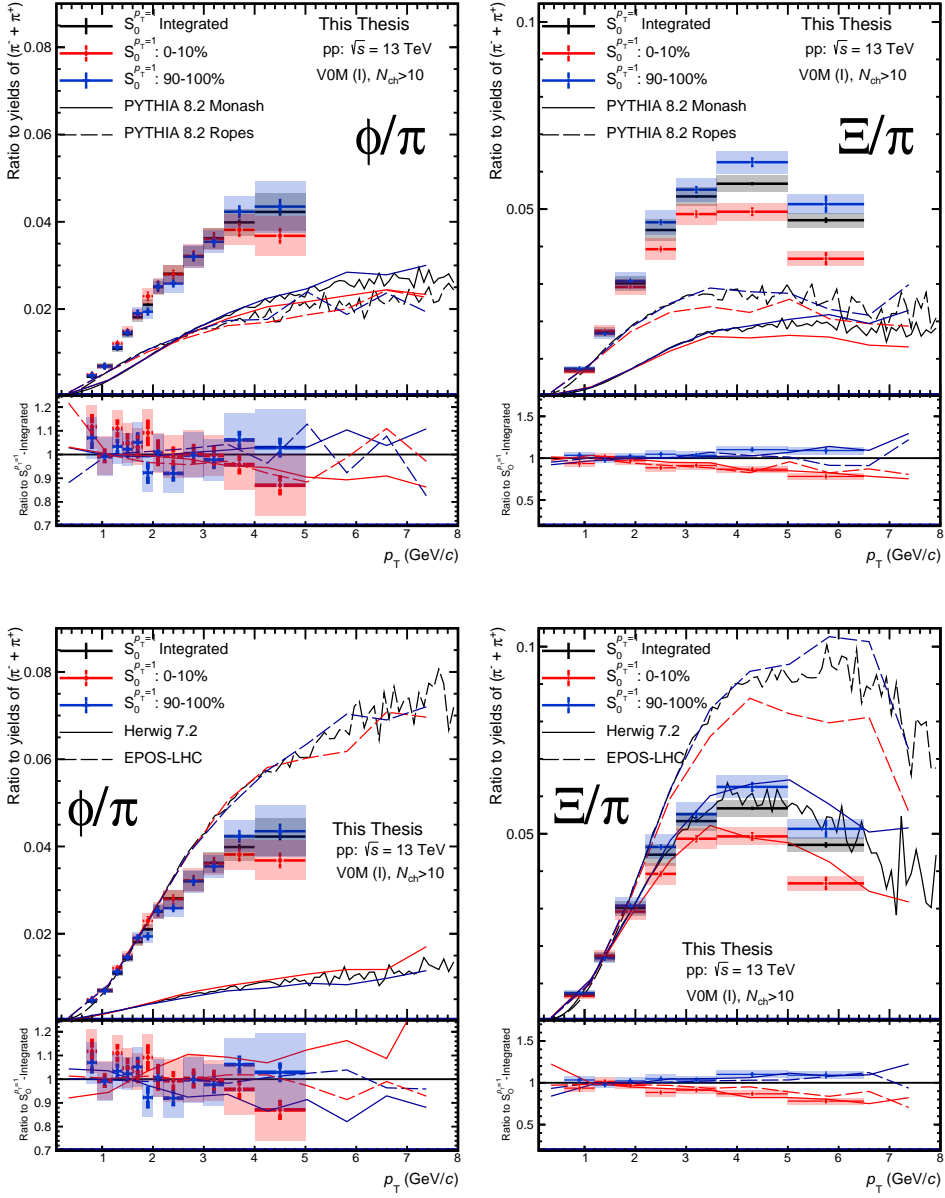


**Figure 7.29:**  $p_T$ -differential production of  $\phi$  and  $\Xi$  relative to  $\pi$ , for  $S_0^{p_T=1}$  selected events at high-multiplicity, determined for events with a 0–1% VOM multiplicity estimation, in 0–10%  $S_0^{p_T=1}$  percentiles. The upper and lower panels contain the same data points but are compared to different predictions of the same measurement, from PYTHIA (top panels) and Herwig 7.2 + EPOS-LHC (bottom panels), represented by different curves. Statistical and total systematic uncertainties are shown by error bars and boxes, respectively.

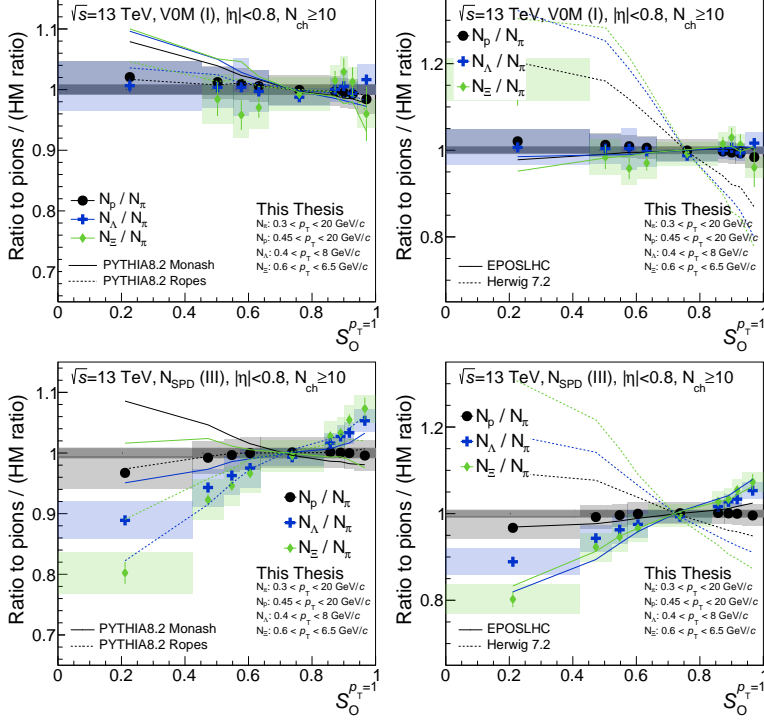


**Figure 7.30:** The Double-Ratios of integrated yield as a function of  $S_O^{p_T=1}$  are presented for V0M 0 – 1% (upper) and  $N_{\text{tracklets}}^{|\eta| < 0.8}$  0 – 10% (lower). Left and right-hand plots contain the same data points, but with different model predictions. Statistical and total systematic uncertainties are shown by bars and boxes, respectively. The curves represent different model predictions of the same measurement.

Both EPOS-LHC and the PYTHIA8 rope hadronization framework can qualitatively describe the enhancement of  $\Lambda$  and  $\Xi$  with increasing  $S_O^{p_T=1}$ , while simultaneously predicting the insensitivity of strange particle production as a function of  $S_O^{p_T=1}$  when estimating multiplicity at forward-rapidity.

Finally, one should keep in mind that the fractional  $\langle dN_\pi/dy \rangle$  difference between V0M 0–10%, and  $N_{\text{tracklets}}^{|\eta| < 0.8}$  0–1% are similar. This observation suggests that the effects of the relative enhancement (suppression) of light-flavor hadron production to  $\pi$  mesons, in isotropic (jet-like) topologies, are smaller while estimating multiplicity with V0M. This implies that one can study different physical properties relative to the rapidity ranges in which the multiplicity is estimated. The underlying reason for the non-sensitivity to  $S_O^{p_T=1}$  when estimating multiplicity in forward rapidities is not yet understood.

## 7.6 Summary And conclusions

In this chapter, I have presented the production of  $\Xi$  and  $\phi$ <sup>11</sup> at  $|\eta| < 0.8$  in high-multiplicity pp collisions at  $\sqrt{s} = 13$  TeV, as a function of the unweighted transverse sphericity  $S_O^{p_T=1}$ . A large bulk of my Ph.D. work has been dedicated to understanding the biases between weakly decaying, resonances, and charged primary hadrons w.r.t., the traditional transverse sphericity  $S_O$ . To reduce the bias, I have elaborated on how the observable was updated to the current definition of  $S_O^{p_T=1}$ .

During this project, I have experimented with estimating multiplicities in two kinematic regions; at mid-rapidity ( $|\eta| < 0.8$ ) by measuring the activity in the SPD ( $N_{\text{tracklets}}^{|\eta| < 0.8}$ ), and at forward-rapidity ( $2.8 < \eta < 5.1$  and  $-3.7 < \eta < -1.7$ ) by measuring the activity in the V0 forward detector. I have found that, in conjunction with  $S_O^{p_T=1}$ , it is possible to extract different physics depending on the kinematic region in which the multiplicity is estimated. By estimating the multiplicity with the V0 detector, one obtains a large variance in midrapidity charged-particle density for different  $S_O^{p_T=1}$  event selections. In contrast,  $S_O^{p_T=1}$  selected events have similar  $dN_{\text{ch}}/d\eta$  when estimating multiplicity at midrapidity. Moreover, by estimating multiplicity at midrapidity, one obtains a large difference in  $\langle p_T \rangle$  between the different  $S_O^{p_T=1}$  classes, whereas the equivalent measurement obtained from the V0 activity is roughly equal in terms of  $\langle p_T \rangle$ . From observations presented in this thesis, estimating multiplicity at midrapidity allows one to isolate and study the dynamics of particle productions that are driven by either soft or hard QCD physics.

The main features of this analysis are reported in the particle-to-pion ratios, highlighting an enhancement of both  $\phi$  and  $\Xi$  production in events with an isotropic topology, and a strong suppression in events with a jet-like topology. Furthermore, events with isotropic topologies give good descriptions of the average,  $S_O^{p_T=1}$ -unbiased high-multiplicity event selection, while high-multiplicity events heavily influenced by jet-like physics are clear outliers. The  $\phi$ -to- $\Xi$  ratio also indicates that, in the context of  $S_O^{p_T=1}$ ,  $\phi$  exhibits dynamics similar to a double-strange particle.

Most presented model predictions can describe the qualitative trends in the  $\phi$  and  $\Xi$  particle  $p_T$ -spectra, especially the PYTHIA 8 rope hadronization. The model comparisons are not able to describe the quantitative observations found in the data for the single particle ratios. However, the presented models are mostly able to describe the overall interplay between  $S_O^{p_T=1}$  selected events, to

---

<sup>11</sup>Including guest appearances of  $\pi$ , K, p,  $\Lambda$ ,  $K_S^0$  and  $K^{*0}$

the high-multiplicity reference. Remarkably, even though the production mechanisms for the PYTHIA8 Monash and PYTHIA8 Ropes tunes (ropes formed by layers of overlapping strings) are qualitatively different, they both predict the interplay with only minor differences between them.

Finally, the relative integrated strange particle yield to pions, as functions of  $S_O^{p_T=1}$ , are presented. The results indicate that it is possible to obtain similar strangeness enhancement found in multiplicity differential analysis, by instead fixing the variance in local charge particle density, and instead varying the azimuthal topology through  $S_O^{p_T=1}$ . This observation suggests that multiplicity production at high multiplicities is driven by more than a single source, with different strangeness-to-pion production rates. Remarkably, this goes contrary to expectations based on prior ALICE publications seen in Ref. [1]. While the origin of this effect is currently not well understood, both PYTHIA 8 Ropes and EPOS-LHC can qualitatively capture the (in)sensitivity of  $S_O^{p_T=1}$  w.r.t estimating multiplicity in (forward)mid-rapidity. Furthermore, PYTHIA 8 Ropes and EPOS-LHC can capture the large suppression of strangeness production in jet-like events, although with a different mass ordering that is incompatible with the measured data.

In conclusion, this Chapter has demonstrated that  $S_O^{p_T=1}$  can be utilized to categorize events in classes based on characteristic azimuthal topologies, from jet-like events associated with hard QCD physics, to isotropic events associated with soft-QCD physics. One of the strongest findings from this analysis is that average high-multiplicity events, even in the most extreme cases, appear to be dominated by soft processes, whereas rare hard processes play little or no role in bulk observables.

## Chapter 8

# $\phi$ and $\Xi$ yields as Functions of Relative Transverse Activity $R_T$

The 2nd analysis presented in this thesis will focus on particle production relative to the magnitude of the Underlying Event (UE). The size of the UE is estimated through the Relative Transverse Activity,  $R_T$ . I will report preliminary results obtained from ALICE, presenting  $p_T$ -differential particle ratios for both  $\Xi$  and  $\phi$  as functions of  $R_T$ . Individual particle spectra are not presented, due to a large experimental bias, which is discussed in the following.

### 8.1 Definition of Relative Transverse Activity $R_T$ .

The Relative Transverse Activity  $R_T$  was first proposed as an event classifier by the theoretical community, in a paper by T.Martin *et al.* [116], where  $R_T$  could be measured to estimate the size of the *underlying event* (UE). In general terms, hadronic particle collisions consist of an initial hard parton-parton scattering(s) (which can be estimated perturbatively through QCD), followed by processes with softer  $p_T$ . The details of the soft processes are model-specific, and implementation varies from model to model. Produced particles *not* associated with the initial hard scattering, nor associated with any of the parton showers originating from the hard scattering, are referred to as the UE. These components cannot be described perturbatively, and phenomenological implementations are required to accurately model the UE. Assuming that  $R_T$  can be

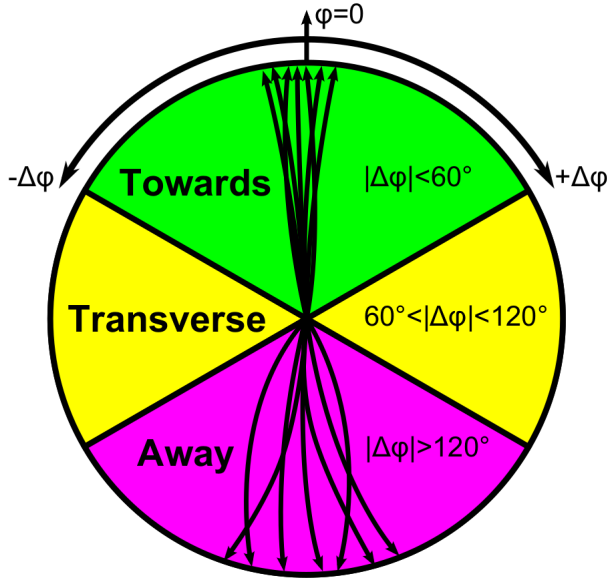


**Figure 8.1:** A sketch of the azimuthal regions defined relative to the leading particle track, used for the  $R_T$  analysis.  $R_T$  is estimated by measuring the number of charged particle tracks in the transverse region. Figure is obtained from Ref. [116].

used to estimate the size of the UE, measurements of  $R_T$  can therefore validate or reject phenomenological descriptions of the UE, giving  $R_T$  measurements a strong discriminatory power, which can further improve the development of MC generators.

For the work presented here,  $R_T$  will be used as an event classifier to measure the production of  $\phi$  and  $\Xi$  hadrons, relative to the size of the UE. The event classifier is defined by rotating the azimuthal frame with respect to the leading particle track. The event is then divided into three different regions, as illustrated in Fig. 8.1. Assumptions are made regarding the properties of particle production in each azimuthal region:

- The *Toward Region* will contribute to the overall particle production from different sources, both from the hard scattering, and the UE.
- The *Transverse Region* will mainly consist of particles produced in the UE. By construction, this region is the least affected by the hard scattering [116], since it is perpendicular to the leading particle track. Therefore, due to momentum conservation, the transverse region is also expected to be separated far in azimuthal angle w.r.t. the recoil jet.

- The *Away Region* will, similar to the Toward region, also contain contributions to particle production from the hard scattering and the UE. This region is not directly biased by the event selection, as neither the leading particle track nor the  $R_T$  is measured in this region.

One can test the above assumptions by comparing the charged particle production, as a function of the transverse momentum of the leading particle track,  $p_T^{\text{Leading}}$ , separately in each region. This is presented in Fig. 8.2, for pp collisions at  $\sqrt{s} = 13$  TeV [117]. One can note that the number of produced particles in the Toward region grows as a function of  $p_T^{\text{Leading}}$ . This is to be expected if the products of the initial hard scattering are captured in the Toward region, given that the total jet particle production<sup>1</sup> increases with  $p_T^{\text{Leading}}$ .

In contrast, the particle production plateaus in the Transverse region, suggesting that at  $p_T^{\text{Leading}} \geq 5\text{GeV}/c$ , particle production in the UE becomes practically independent of increases in  $p_T^{\text{Leading}}$ , and can be decoupled from the hard scattering processes. This suggests that the collision geometry of events with a  $p_T^{\text{Leading}}$  above this threshold are “equally biased”, ensuring a homogenous event sample of collisions. Therefore, the work presented in this thesis will **require a leading particle track with at least  $p_T^{\text{Leading}} \geq 5.0$  GeV/c**, also referred to as the  $R_T$  “trigger”, to constrain the average hard scattering and isolate it in the Toward region, while being able to vary the UE by measuring the Transverse region.

If a leading particle has a momentum of  $p_T^{\text{Leading}} \geq 5\text{GeV}/c$ , within  $|\eta| \leq 0.8$ ,  $R_T$  is defined by measuring the *number of charged particle tracks in the Transverse region*,  $N_T$  (also referred to as “transverse multiplicity”), on an event-by-event basis, normalized to the average amount of charged particles produced in the same region:

$$R_T = \frac{N_T}{\langle N_T \rangle}. \quad (8.1)$$

By construction, an event with  $R_T \approx 1$  has an average-sized UE. Values of  $R_T \rightarrow 0$  describe events with small, or no UE, where collisions are almost entirely dominated by the hard scatterings process. Low- $R_T$  events produce pronounced di-jet topologies in the azimuthal plane and are expected to have particle-production dynamics similar to  $e^+e^-$  collisions. In contrast,  $R_T \rightarrow \infty$

---

<sup>1</sup>The size of partonic showers, in most models, expands with the momentum transfer from the initial hard process.

<sup>2</sup>This is in reference to the particle dynamics produced through hard scatterings in an  $e^+e^- \rightarrow q\bar{q}$  event.

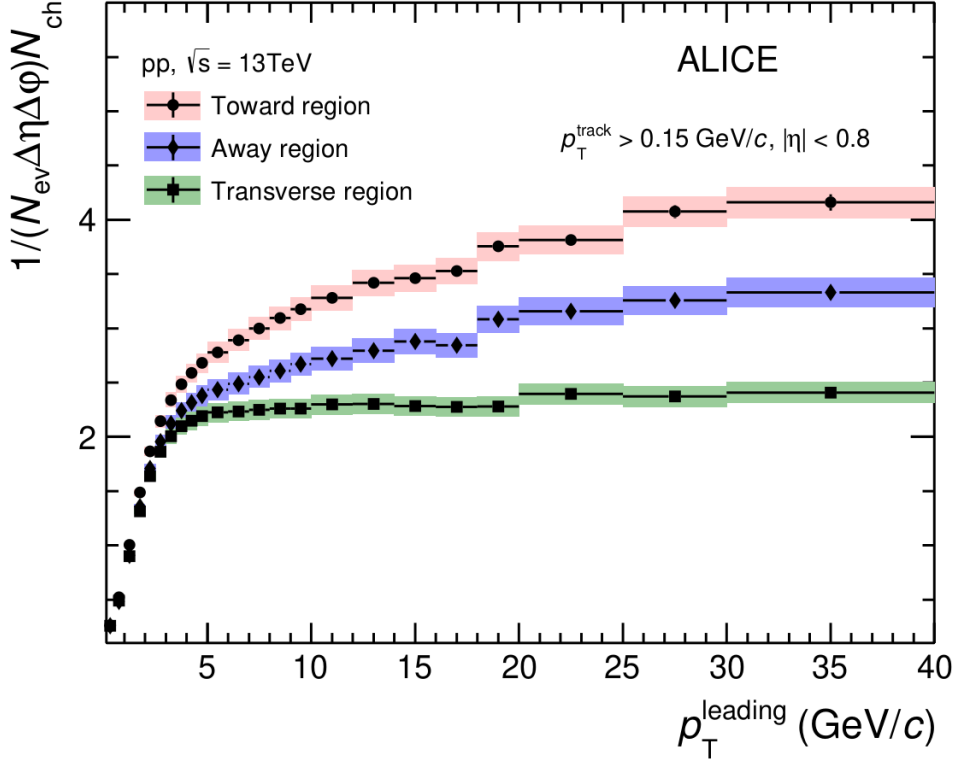


**Figure 8.2:** Number density of charged particles as a function of  $p_T^{\text{Leading}}$ , in the corresponding Toward, Transverse, and Away azimuthal regions. The data is measured by ALICE for pp collisions at  $\sqrt{s} = 13$  TeV. [117]

describes events that are almost completely dominated by the UE, where we expect that particle-production dynamics are more similar to heavy-ion collisions. By varying  $R_T$ , one can expect, within reason, to control the QGP-like effects associated with particle production.

For the work presented in this thesis, measurements of particle ratios, between  $\phi$  and  $\Xi$  relative to the number of  $\pi$  mesons, are compared to predictions from both PYTHIA 8 and EPOS-LHC as functions of  $R_T$ . For QCD-inspired event generators, such as PYTHIA 8, the size of the UE is related to the number of Multiple-Parton Interactions (MPIs)<sup>3</sup>. A collision between two protons will often contain multiple MPIs, resulting in a more or less isotropic UE.<sup>4</sup>

<sup>3</sup>Refer to Sec. 4.1.1 for details

<sup>4</sup>The UE will also contain contributions from initial-state and final-state radiation (ISR and FSR, respectively). Particles produced via ISR and FSR are still associated with the magnitude of the momentum transfer in the initial hard scattering.



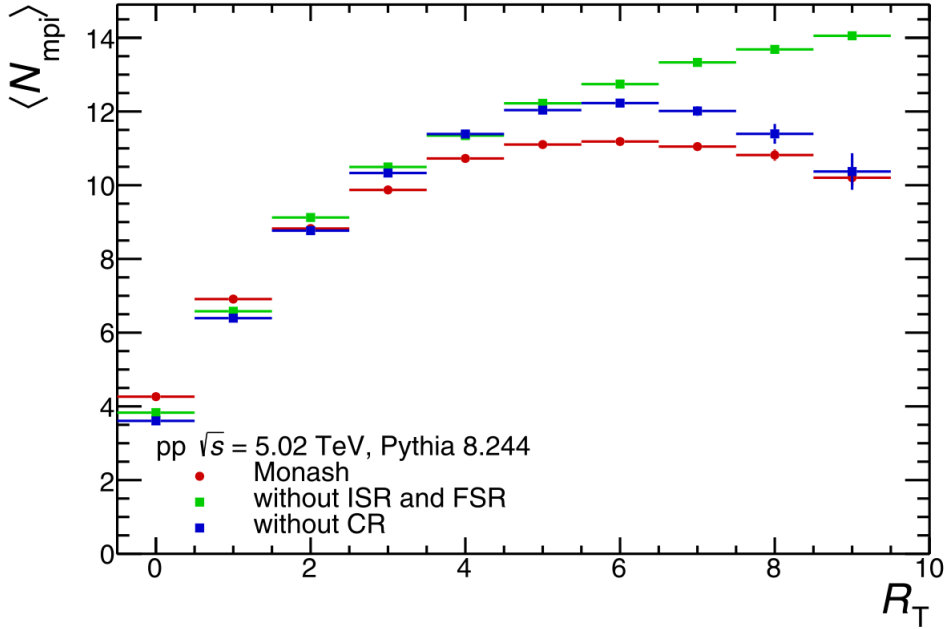


**Figure 8.3:** ALICE simulation using different PYTHIA 8 variations, where the number of average MPIs are measured with respect to the Relative Transverse Activity  $R_T$ . ISR, FSR, and CR refer to initial-state radiation, Final-state radiation, and color reconnection, respectively. Results are obtained from Ref. [118].

Fig. 8.3 presents the correlation between the average number of MPIs in PYTHIA 8 and  $R_T$ , with and without ISR and FSR enabled (as well as PYTHIA color reconnection, details discussed in Sec. 4.1.1). One can note that, for all three PYTHIA configurations,  $R_T$  is strongly correlated to the number of  $\langle N_{\text{mpi}} \rangle$ , up to approximately  $R_T \approx 5$ . This simulation supports the hypothesis that  $R_T$  can give an estimate of the size of the UE. However, the correlation flattens at large  $R_T$  for more realistic configurations, where ISR and FSR (“Monash”) are enabled. This implies that at large values of  $R_T$ , the Transverse region is contaminated by wide-angle FSR, originating from the hard scattering. Consequently, the sensitivity to the soft, MPI-driven UE, is lost at large  $R_T$ , which is expected to be most relevant for QGP-like effects. Therefore, results in this thesis are presented in  $R_T$  intervals up to  $R_T = 5$ , to mainly retain and probe the MPI dependence.

In contrast to PYTHIA 8, EPOS-LHC models the size of the UE by adjusting the relative fraction of core and corona produced in each event<sup>5</sup>. Both processes from the core and the corona will contribute to the UE, although the relative fraction of particles produced from the core grows with the charged particle

<sup>5</sup>Refer to Sec. 4.3.1 for details.

density. Given that the corona describes the hard,  $e^+e^-$ -like component, the  $R_T$  trigger is likely to be produced in the corona, while events with large values of  $R_T$  are likely to have a large contribution from the core. Furthermore, in EPOS-LHC, strangeness enhancement is also driven by a larger relative size of the core. One would therefore expect larger UE to also contain a larger fraction of strange particles produced. This interpretation is contrary to what one would expect from a traditional Lund string model, where the size of the UE is not directly tied to the relative fraction of produced strange particles.

## 8.2 Track Selection and Bias Estimation

### Track Selection for Leading Particle Track

The work presented in this thesis use two different sets of track selection criteria; one for leading particle tracks, and one for tracks that contribute to the estimation of  $N_T$ . The leading particle track functions as  $R_T$  event triggers, in addition to defining the geometry of the Transverse region. Therefore, good precision is required for the leading particle, both in terms of spatial and momentum resolution. For this reason, the reconstructed leading particle track is required to satisfy the "global track" criteria, defined in Sec. 6.2.1, with  $p_T^{\text{Leading}} \geq 5\text{GeV}/c$ .

Furthermore, the reconstructed track is also required to satisfy a "Geometrical Cut", due to gaps in the azimuthal acceptance between the different sectors of the TPC. This is illustrated in Fig. 8.4. For low-momentum particles, this is not an issue, since the curved particle trajectory will cross the required number of TPC pad rows, and cross the sector gaps at large angles.

However, for particles at intermediate and high  $p_T$ , there is a possibility, due to the smaller curvature, that large parts of the particle trajectory align with the sector gap (demonstrated in Fig. 8.4). These tracks can satisfy the total required amount of crossed pad rows but have poor momentum resolution due to large gaps in tracking. This can potentially misidentify  $R_T$  triggers, where a particle with  $p_T \ll 5.0\text{GeV}/c$  is reconstructed as if it had  $p_T \geq 5.0\text{GeV}/c$ .

Preliminary studies on simulated PYTHIA 8 events found that 3.7% of the total amount of  $R_T$  triggers were incorrectly reconstructed with a large broad momentum resolution. After implementing the geometric cut, simulation studies indicated that the selection is robust, with a good momentum resolution for all considered  $R_T$  triggers. The full details of the development and implementation of this cut are discussed in Appendix B.

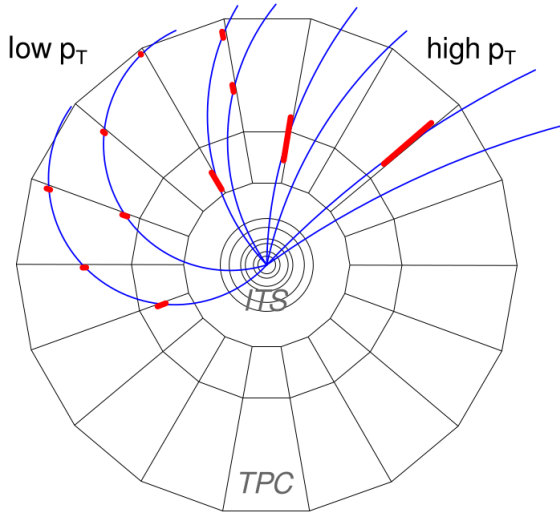


**Figure 8.4:** Illustration of charged particle tracks aligning with the sectors gaps in the ALICE TPC. At the right  $p_T$ , a track can line up such that it aligns perfectly with the sector gap. Figure is taken from Ref. [119]

### 8.2.1 Track Selection for $N_T$ Estimate

The  $R_T$  analysis uses a set of loose selection criteria for tracks used to estimate the  $N_T$ . Similar to the discussion in Sec. 7.1.2, this is due to the dead regions in the SPD, creating gaps in the azimuthal angle with low reconstruction efficiency, demonstrated in Fig. 7.2. This could create large fluctuations in the estimate of  $N_T$ , if the Transverse region is pointing toward the dead regions of the SPD, illustrated in Fig. 8.5, which would consequently result in each  $R_T$  interval containing an inhomogeneous event distribution.

Therefore, the reconstruction criteria for  $N_T$  only utilizes information from TPC, except for a refit down to the primary vertex. The momentum resolution is not critical to this measurement, as  $N_T$  only considers the *amount* of tracks in the Transverse region. For this reason, the reconstruction criteria are optimized for high efficiency to get a measurement of  $N_T$  with high precision. The track selection is identical to the criteria also used for tracks to measure  $S_O^{p_T=1}$ , detailed in Sec. 7.1.2.

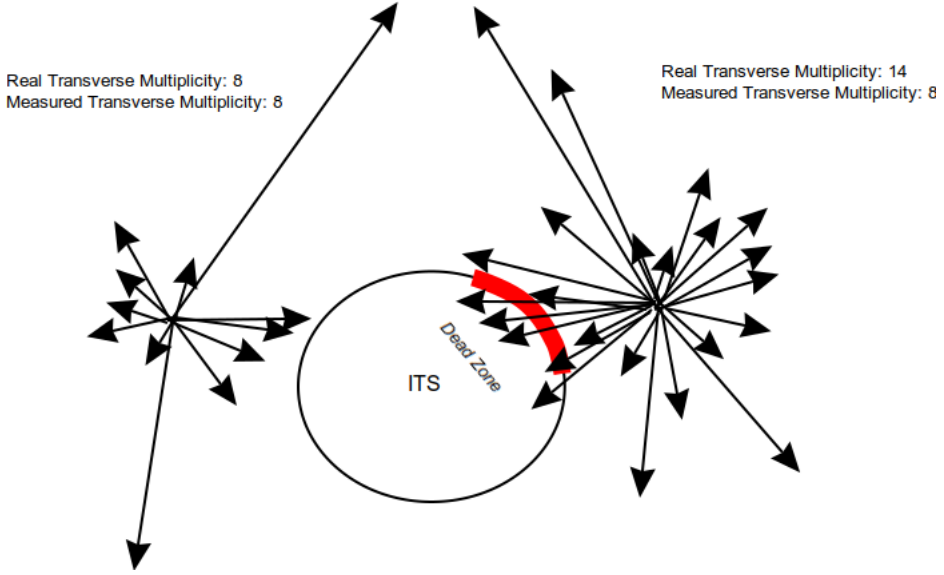


**Figure 8.5:** Illustration of how holes in the ITS can induce large fluctuations in the measured value for  $N_T$ . These would render the definition of  $R_T$  to not be well-defined.

### 8.3 Investigation of Experimental Bias

The underlying principle illustrated in Fig. 8.5 remains an issue, even for a flat azimuthal acceptance. Due to tracking performance, ALICE is not able to consistently reconstruct ALL particles produced in each collision, and will sometimes wrongly identify a secondary track as a primary track. The ALICE tracking efficiency is approximately 80–90%, depending on particle mass. A study of particle efficiencies for primary  $\pi$ , K, p is presented in Fig. 8.6. The efficiencies are estimated according to the procedure described in Sec. 6.2.4. Figure 8.7 shows the  $R_T$  distribution from measured  $R_T$ , and the "real"<sup>6</sup>  $R_T$ , generated from PYTHIA 8 events. One can observe that the reconstructed  $R_T$  distribution is smeared w.r.t. the generated distribution, attributed to the folding effect described in Sec. 7.1.3<sup>7</sup>.

However, one should note that Fig. 8.7 suggests that the shapes between the two distributions are similar, even after smearing. This implies that the probability of an event being shifted in/out from a single  $R_T$  interval is similar. If the particle-production dynamics are relatively homogenous in each  $R_T$  interval, bi-

<sup>6</sup>In the case of simulation studies, this is the "generated"  $R_T$  before it is reconstructed by the detector.

<sup>7</sup>This refers to the experimental folding, *not* the neutral-to-charged bias discussed in the same section.

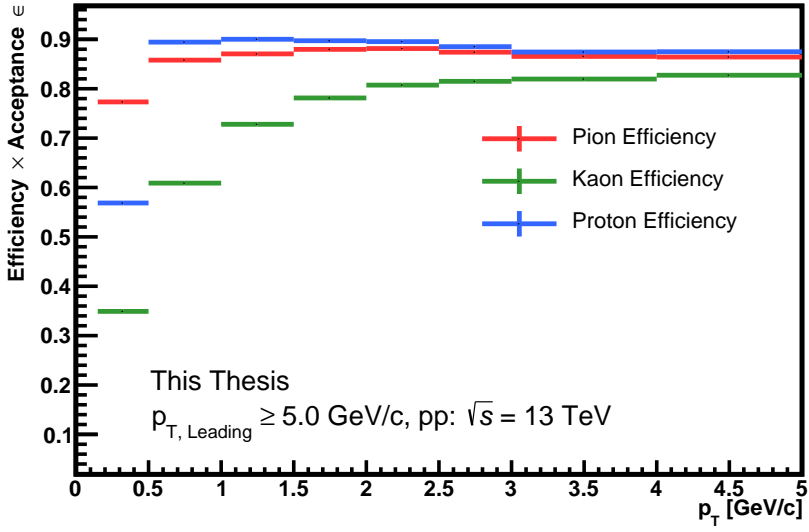


Figure 8.6: Reconstruction efficiencies for primary pions, kaons, and protons, utilizing the looser track configuration, which is used to measure  $R_T$ . Statistical errors are smaller than the line width presented in the figure.

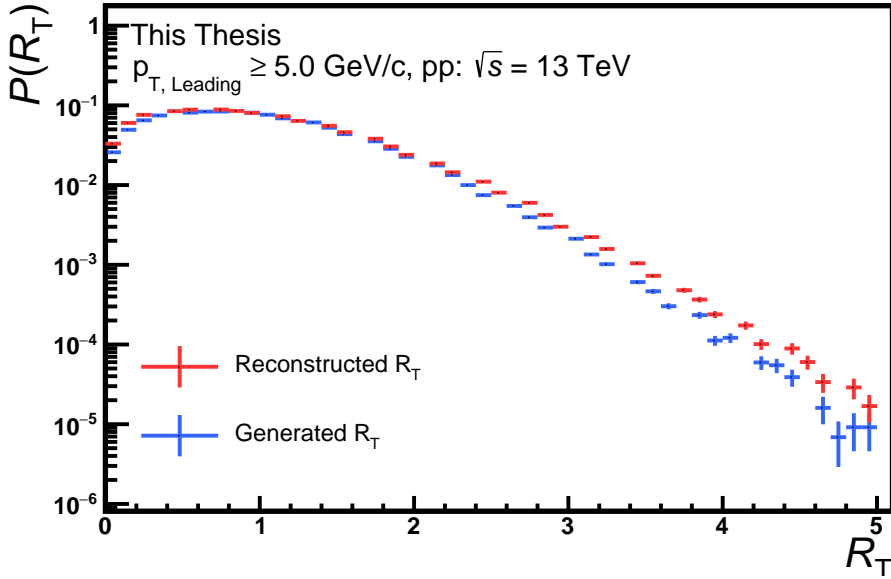


Figure 8.7:  $R_T$  distributions of generated PYTHIA 8 events, measured before (generated), and after (reconstructed), the events are propagated through a simulation of the ALICE detector. The simulation is performed with GEANT3. The uncertainties are purely statistical.

ases due to folding should have a relatively minor impact. This can be evaluated by performing closure tests, in the same manner as described in Chapter 7.1.3, where the closure  $C(\text{PID}, p_T)^{R_T}$  is defined as:

$$C(\text{PID}, p_T)^{R_T} = \frac{\frac{1}{\epsilon} \left( \frac{d^2 N_{\text{Rec}}}{d\eta dp_T} \right)_{R_T, \text{Rec}}^{\text{PID}}}{\left( \frac{d^2 N_{\text{Gen}}}{d\eta dp_T} \right)_{R_T, \text{Gen}}^{\text{PID}}} \quad (8.2)$$

The quantities in Eq. 8.2 are defined like the equivalent  $C(\text{PID}, p_T)^{S_O^{\text{PT}=1}}$  described in Sec. 7.1.3, substituting  $S_O^{\text{PT}=1}$  for  $R_T$ . Furthermore,  $C(\text{PID}, p_T)^{R_T}$  is an intricate quantity, and one should clarify two important points. First, the reconstructed particle yields are extracted using *global tracks*, while the reconstructed  $R_T$  is estimated utilizing the looser track cuts described in Sec. 7.1.2, which only rely on information from the TPC. Any potential non-closure does therefore not reflect a change in particle yield extraction, as the standard procedure is applied. Secondly,  $R_{T, \text{Rec}}$  and  $R_{T, \text{Gen}}$  are *different* quantities, demonstrated in Fig. 8.4, where the former is estimated through reconstructed tracks, the latter estimated by counting generated tracks.

The spectra and  $C(\text{PID}, p_T)^{R_T}$  of simulated  $\pi^- + \pi^+$  as a function of  $p_T$  are presented in Fig. 8.8, in different  $R_T$  intervals, for each azimuthal region. Pions are utilized due to their abundance. A systemic,  $R_T$ -dependent folding bias is present in all three azimuthal regions. Consequently, measured particle spectra as functions of  $R_T$  cannot be directly compared with MC event generator predictions. Therefore, spectra of the  $\phi$  and  $\Xi$  yields as functions of  $R_T$  were not made public in the preliminary stage of this analysis, and will not be presented in this thesis, since they could not be fully corrected. A solution to correct the experimental bias, and "unfold" the spectra, has since been found and is currently being implemented for future iterations of this analysis.

However, it was found that the experimental bias is heavily reduced when taking  $p_T$ -differential ratios between different particle species. Closure tests for  $C(\text{PID}, p_T)^{R_T}$  are reported for  $\phi$ -to- $\pi$  and  $\Xi$ -to- $\pi$  ratios as a function  $p_T$ , in different  $R_T$  intervals for different azimuthal regions, in Fig. 8.9 and Fig. 8.10, respectively. One can note that the systematic biases seen in Fig. 8.8 are no longer present. The fluctuations that remain are mostly driven by insufficient statistics. These findings suggest that the folding distorts different particle species similarly. Therefore, the relative particle-production dynamics stay consistent with respect to  $R_T$ , meaning that measured "particle"-to- $\pi$  ratios are directly comparable to predictions from MC generators. The fluctuations are quantified and applied as a 4% systematic uncertainty to all h-to- $\pi$  ratios.

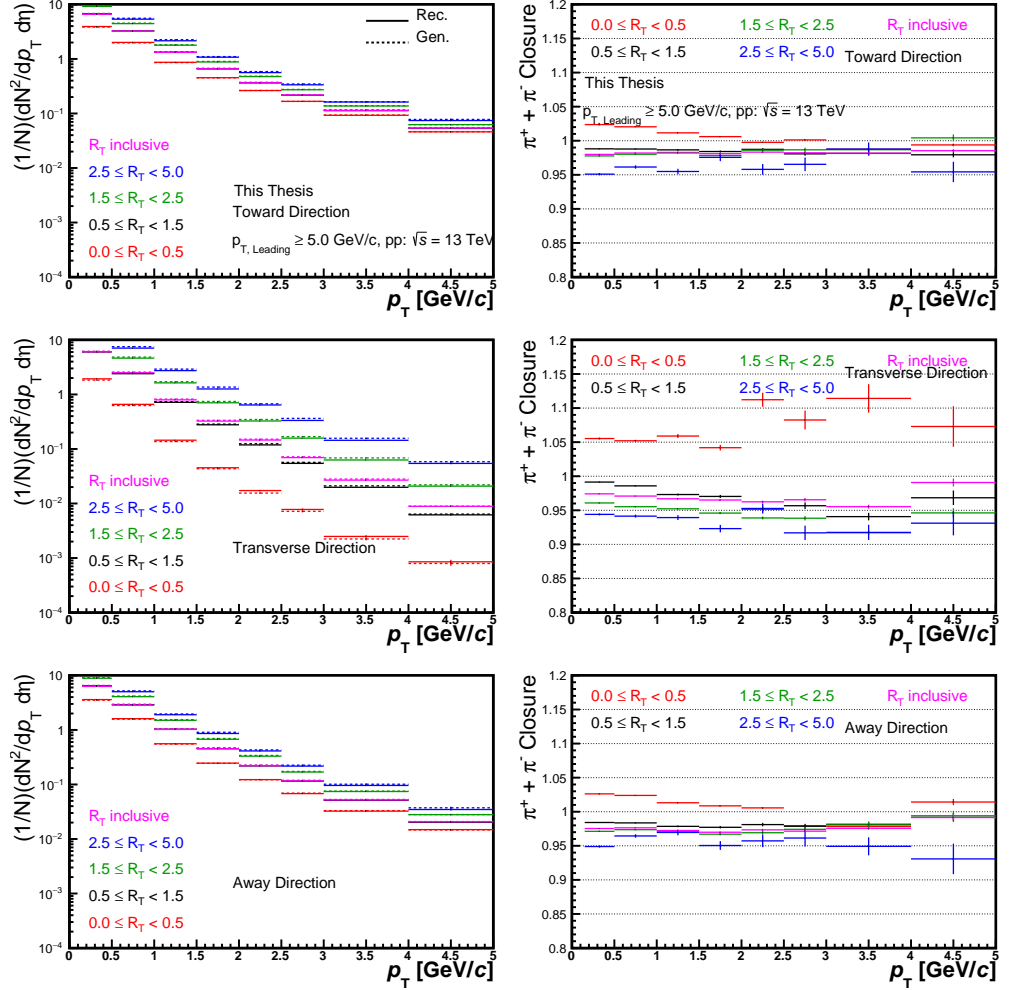


**Figure 8.8:** (Left panels): Monte-Carlo (MC) simulations of  $\pi^- + \pi^+$  spectra as a function of  $p_T$ , in different azimuthal regions, within different  $R_T$  intervals. Solid lines are reconstructed pions, while dashed lines are generated pions. Errors are purely statistical. (Right panels): Ratio between corrected Reconstructed/Generated ratio,  $C(R_T)$ , to evaluate biases that arise due to detector folding effects.

## 8.4 Systematic Uncertainties

The systematic uncertainties are evaluated according to the procedure described in Chapter 7, Sec. 7.4, both for the  $\phi$  meson and  $\Xi$  baryon analysis. In addition to the analysis-specific uncertainties, a flat 4%-uncertainty is added for both analyses, in each  $R_T$  interval, to account for the experimental biases discussed in Sec. 8.3.

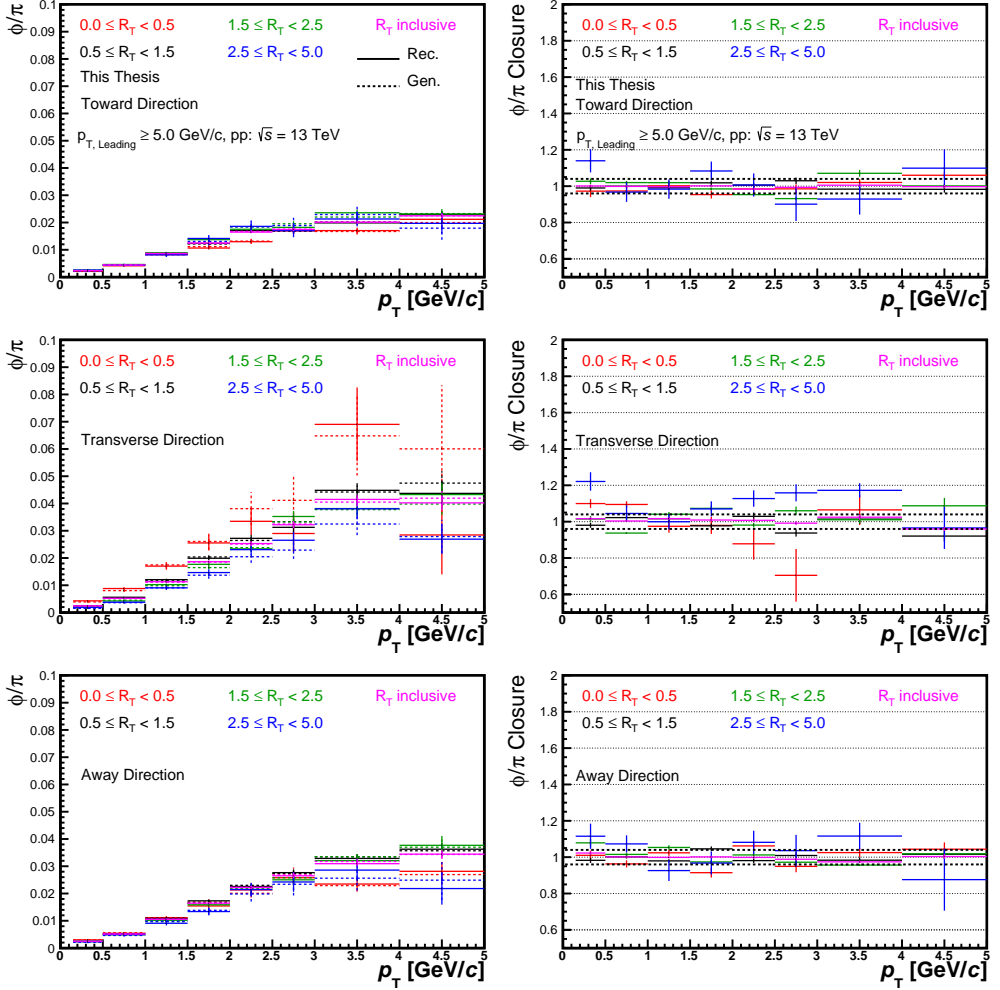


**Figure 8.9:** (Left panels): Monte-Carlo (MC) simulations of  $\phi$ -to- $\pi$  ratios as a function of  $p_T$ , in different azimuthal regions, within different  $R_T$  intervals. Solid lines are reconstructed pions, while dashed lines are generated pions. Errors are purely statistical. (Right panels): Ratio between corrected Reconstructed/Generated particle ratios,  $C(R_T)$ , to evaluate biases that arise due to detector folding effects. The black, dashed lines represent the systematic error assigned due to the estimated bias.

### 8.4.1 Systematic Uncertainties & Caveats for $\phi$ analysis

The limited amount of statistics available ( $\approx 1\%$  of available events, due to requiring a  $p_{T, \text{Leading}} \geq 5 \text{ GeV/c}$  leading particle), imposes a difficulty when evaluating the systematic uncertainties. For individual  $R_T$  intervals, the statistics were not sufficient to distinguish systematic effects from statistical fluctuations. In an attempt to disentangle the systematic and statistical uncertainties, it was assumed that the shape of the combinatorial background would remain



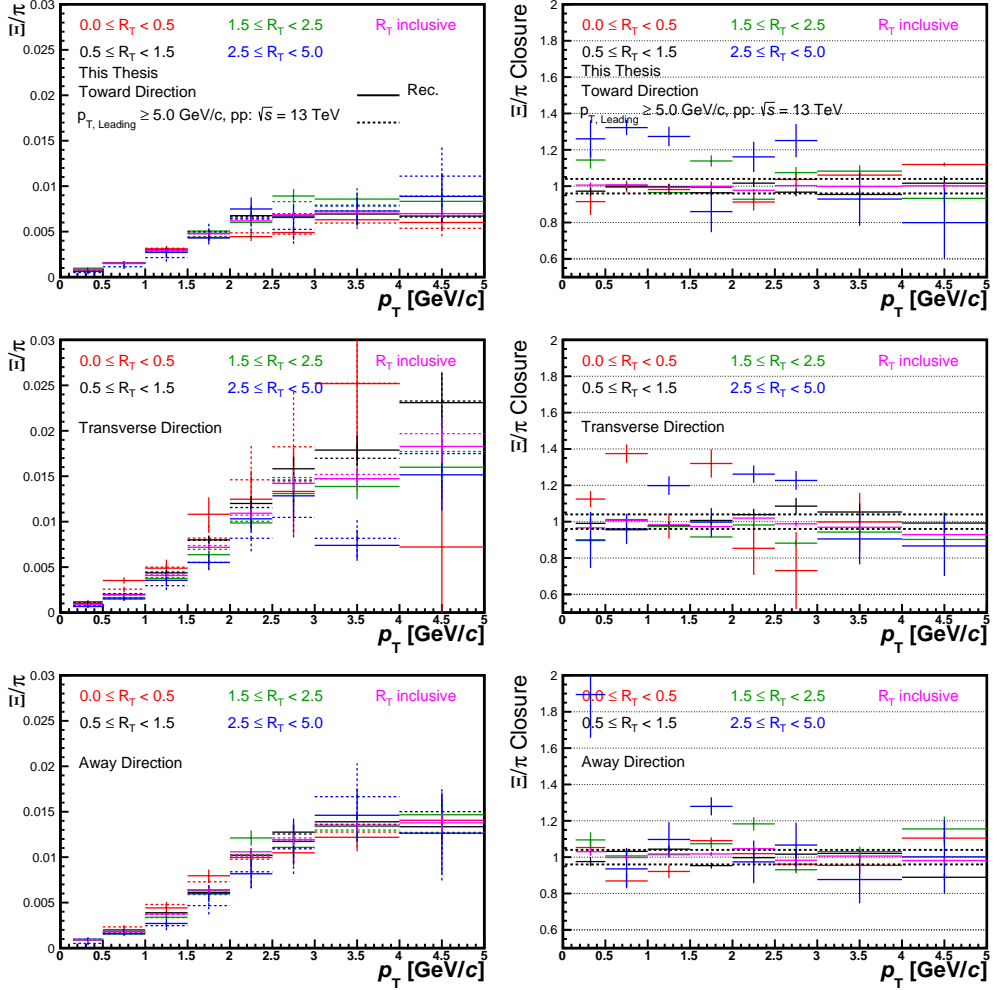


**Figure 8.10:** (Left panels): Monte-Carlo (MC) simulations of  $\Xi$ -to- $\pi$  ratios as a function of  $p_T$ , in different azimuthal regions, within different  $R_T$  intervals. Solid lines are reconstructed pions, while dashed lines are generated pions. Errors are purely statistical. (Right panels): Ratio between corrected Reconstructed/Generated particle ratios,  $C(R_T)$ , to evaluate biases that arise due to detector folding effects. The black, dashed lines represent the systematic error assigned due to the estimated bias.

relatively consistent within the different azimuthal regions. The uncertainties are evaluated using the  $R_T$  integrated yield, within the Toward, Transverse, and Away regions, thereby making it easier to evaluate the "true" systematic uncertainty of the  $\phi$  meson signal extraction.

For the  $R_T$  analysis, the signal extraction was performed without any reduction of the combinatorial background. The combined Voigtian peak fit (defined in Sec. 6.2.4) is applied directly to the raw  $M_{\text{inv}}$  spectra. This choice was made for

two reasons; First, neither the like-sign nor the event-mixed backgrounds were able to accurately describe the combinatorial background. Secondly, the selected events have large S/B ratios, due to the requirement of  $p_{T}^{\text{Leading}} \geq 5\text{GeV}/c$ . Therefore, a 2nd-degree polynomial function can give an adequate description of the combinatorial background in the raw  $M_{\text{inv}}$  spectra. Consequently, the error groups associated with the background reduction have been removed entirely. Refer to Sec. 7.4.1 for the definitions of the error groups. Furthermore, since the dynamics in the Toward and Away region are similar, the same systematic uncertainty is assigned for both regions.

The systematic uncertainties in the  $\phi$  signal extraction, for the Toward/Away and Transverse regions, are presented in Fig. 8.11. The uncertainties are qualitatively similar to the uncertainties estimated for the  $S_{O^T=1}^{p_T=1}$  analysis. The largest contribution comes from the track uncertainty, which includes the PID selection scheme, as the shape of the combinatorial background is sensitive to the selected PID scheme. Since background reduction is not implemented, the uncertainty of how well the combinatorial background is described is directly attributed to the combined peak fit. Small changes in PID precision will therefore result in large variances in yield estimation.

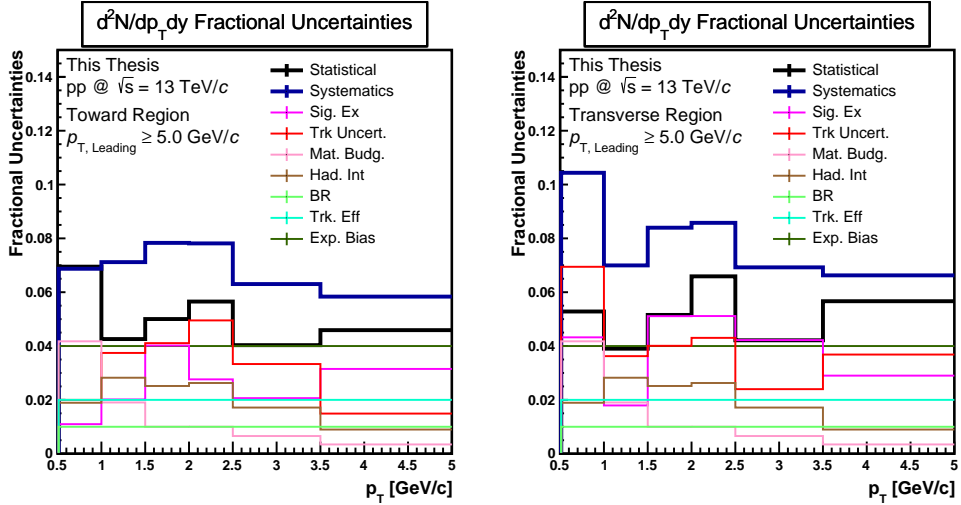


**Figure 8.11:** Fractional Uncertainties of the  $\phi$  yield in the Toward (left panel) and Transverse (right panel) region, requiring a  $p_{T}^{\text{Leading}}$  of  $> 5.0\text{ GeV}$ . The uncertainties for the Toward region are also utilized to estimate the uncertainty for the results in the Away region.

### 8.4.2 Systematic Uncertainties for the $\Xi$ analysis

Similar to the  $\phi$  analysis, the statistical uncertainties make it difficult to properly assign systematic uncertainties, as it is difficult to disentangle the two. Initial studies revealed that trends for different parameter variations in the  $R_T$  analysis were similar to trends observed for the  $S_O^{p_T=1}$  analysis. It was therefore decided that the  $R_T$  analysis would inherit the systematic uncertainties from the  $S_O^{p_T=1}$  analysis. Conservative estimates of the  $S_O^{p_T=1}$  uncertainties are applied directly to the  $R_T$  analysis. This was considered an ad-hoc solution at the time, and the systematic uncertainties will be updated for future iterations (with increased statistics) of this analysis.

## 8.5 Results & Discussion

The results presented in this section are obtained only utilizing the data sets measured in 2016 and 2018. The fraction of events with  $p_T^{\text{Leading}} \geq 5.0\text{GeV}/c$  corresponds to approximately 1.01% of the amount of total accepted (passing the event criteria listed in Sec. 6.1) minimum bias events. The number of events within each  $R_T$  interval are detailed in Tab.8.1

**Table 8.1:** The number of accepted events in each  $R_T$  interval. The events are required to satisfy the default reconstruction requirements, in addition to containing a  $p_T^{\text{Leading}} \geq 5.0\text{GeV}/c$ .

Event Category	# of Events
Minimum-Bias	823820000
$0.0 \leq R_T \leq 5.0$	8345403
$0.0 \leq R_T < 0.5$	1855945
$0.5 \leq R_T < 1.5$	4619694
$1.5 \leq R_T < 2.5$	1634454
$2.5 \leq R_T \leq 5.0$	235310

The measured, uncorrected  $N_T$  and  $R_T$  probability distributions are presented in Fig. 8.12. The raw measurement of  $\langle N_T \rangle$  was found to equal approximately 7,29 tracks. One should note that there are gaps in the binning for the  $R_T$  distribution. While  $N_T$  is measured in integers of 1,  $R_T$  is measured in units of  $1/7,29$ . This can create irrational numbers, which are rounded up to the closest bin edge, creating gaps in the binning.

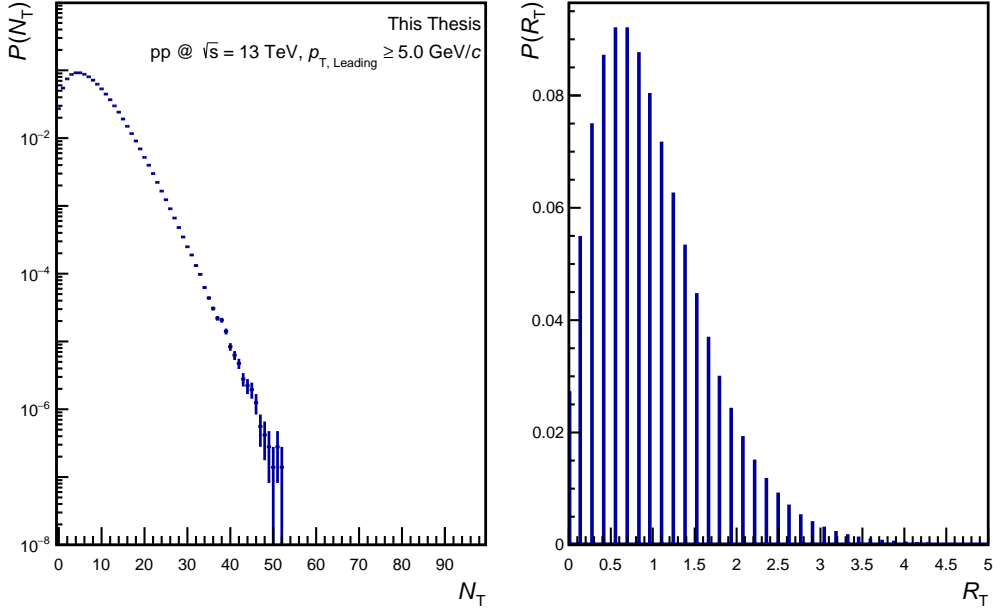


**Figure 8.12:** Measured, uncorrected probability distributions for  $N_T$  (left panel) and  $R_T$  (right panel), in pp collisions at  $\sqrt{s}=13\text{GeV}/c$ , for data measured in 2016 and 2018.

### 8.5.1 Results on $\phi$ and $\Xi$ -to- $\pi$ ratios as a function of $R_T$

The  $\Xi$ -to- $\pi$  ratios are presented as a function of  $p_T$  in Fig. 8.13, in  $R_T$  intervals of  $[0-0.5)$ ,  $[0.5-1.5)$ ,  $[1.5-2.5)$  and  $[2.5-5.0]$ , for each azimuthal region. The relative  $\Xi$  yields in the Towards region show a significant dependence on  $R_T$ . The  $p_T$ -dependent  $\Xi$ -production rate increases by approximately a factor of 4, going from low-to-high  $R_T$ . The Toward region contains contributions from the hard-scattering/jet fragmentation but also from the UE, which scales with  $R_T$ . The results suggest that the  $\Xi$  production rate is fundamentally different in events where hadronization is primarily driven by jet fragmentation ( $0 \leq R_T < 0.5$ ), to events where hadronization is driven by the UE ( $2.5 \leq R_T < 5.0$ ). The intermediate  $R_T$  intervals demonstrate an evolution of this effect, where ( $0.5 \leq R_T < 1.5$ ) represents the "average" event<sup>8</sup>, where  $\langle R_T \rangle \approx 1$ .

In contrast, the  $\Xi$ -to- $\pi$  ratio measured in the Transverse region suggests that there is no significant  $R_T$  dependence for  $\Xi$ . Naively, one could find these results incongruent with the observations seen in the Toward region, where there is

<sup>8</sup>Not average minimum bias events, but events which satisfy  $p_T^{\text{Leading}} \geq 5.0\text{GeV}/c$ .

a clear  $R_T$  dependence. The comparison between these two measurements is crucial to understand the interplay between the UE and the hard scattering; one has to keep in mind that hadrons in the Toward region are produced from either a hard scattering or the UE, whereas the Transverse region consists of hadrons almost entirely produced by UE. The Transverse region isolates the UE, selecting essentially a single  $\Xi$  production mechanism. In the context of MPIs, one would expect the production rate to scale linearly with the size of the UE, so that the ratios between different particles are constant. This is exactly what is observed in the Transverse region, reinforcing this interpretation.

Furthermore, the Transverse and Toward regions converge, quantitatively, to the same  $\Xi$ -to- $\pi$  values at large  $R_T$ . This implies that the relative contribution from the hard-scattering to overall  $\Xi$  production is relatively small, compared to the contribution from the UE. For events with approximately half the average UE volume (the lowest  $R_T$  interval is weighted toward the upper limit, c.f., Fig. 8.12), the hard process dominates, with a notably low  $\Xi$ -to- $\pi$  production rate. However, for UE that are approximately 2.5 times the nominal size, the contributions from the UE appear to be completely dominant, seeing as the high  $R_T$  values saturate toward the same limit for both the Toward and Transverse regions, diluting the contribution from the hard processes. These findings are in agreement with ALICE results that measure  $\Lambda$  production inside and outside jets. It was found that the density of  $\Lambda$  baryons is larger outside-of-jets (the UE), compared to production within the jet-cone, and the inclusive case [109].

Neither EPOS-LHC nor PYTHIA 8 can qualitatively describe the trends seen in all regions. PYTHIA 8 is able to predict the low- $R_T$  measurement in the Toward region. This is to be expected, given that PYTHIA should be able to accurately describe the  $e^+e^-$ -like hard scattering. EPOS-LHC performs well in the Toward region, qualitatively describing the interplay between the hard scattering and the UE. However, EPOS-LHC predicts an  $R_T$ -dependence in the Transverse region and overestimates the production rate for high- $R_T$  events. This trend is fundamentally connected to the core-corona modeling for EPOS-LHC, where the core drives both the UE and strangeness enhancement simultaneously. Therefore, a larger UE will contain a larger fraction of core, and therefore a larger amount of  $\Xi$  production. While PYTHIA 8 is not quantitatively able to predict the ratios in the Transverse region, it can qualitatively predict the observed independence of  $R_T$ .

The  $\phi$ -to- $\pi$  ratios are presented as a function of  $p_T$  in Fig. 8.14, in  $R_T$  intervals of  $[0-0.5)$ ,  $[0.5-1.5)$ ,  $[1.5-2.5)$  and  $[2.5-5.0]$ , for the Toward region. Due to statistical limitations, the particle extraction could not be performed in the lowest (largest)  $R_T$  interval for the Toward (Away) region. The  $\phi$ -to- $\pi$  ratios

show similar behavior to the  $\Xi$ -to- $\pi$  ratios, with a strong  $R_T$ -dependence in the Toward region, and no significant  $R_T$ -dependence in the Transverse region. Notably, EPOS-LHC predicts the trends in the Transverse and Away regions, but not the enhancement observed in the Toward region. Similar to the case of  $\Xi$ ,  $\phi$  production is dominated by contributions attributed to the UE, where the Toward and Transverse regions approach the same limit at high- $R_T$ . In the context of  $R_T$ , the results suggest that  $\phi$  has similar dynamics to multi-strange particles. This is in contrast to the behavior which is observed for the  $S_O^{p_T=1}$  analysis. The discrepancy between the two measurements is discussed more in detail in Chapter 9.

The  $\Xi$ -to- $\pi$  region shows a significant suppression of relative  $\Xi$  production, at low- $p_T$  for high- $R_T$ . Notably, this trend is also reinforced by both model predictions. Enhancement of  $\phi$  production is also observed in the Away region for low- $p_T$ , at lower  $R_T$ . A possible interpretation of this effect could be due to the broadening of the Away jet, leading to particle tracks entering the Transverse region. This is also supported by the reduced statistics for  $\phi$  signal extraction in the Away side for large  $R_T$ .

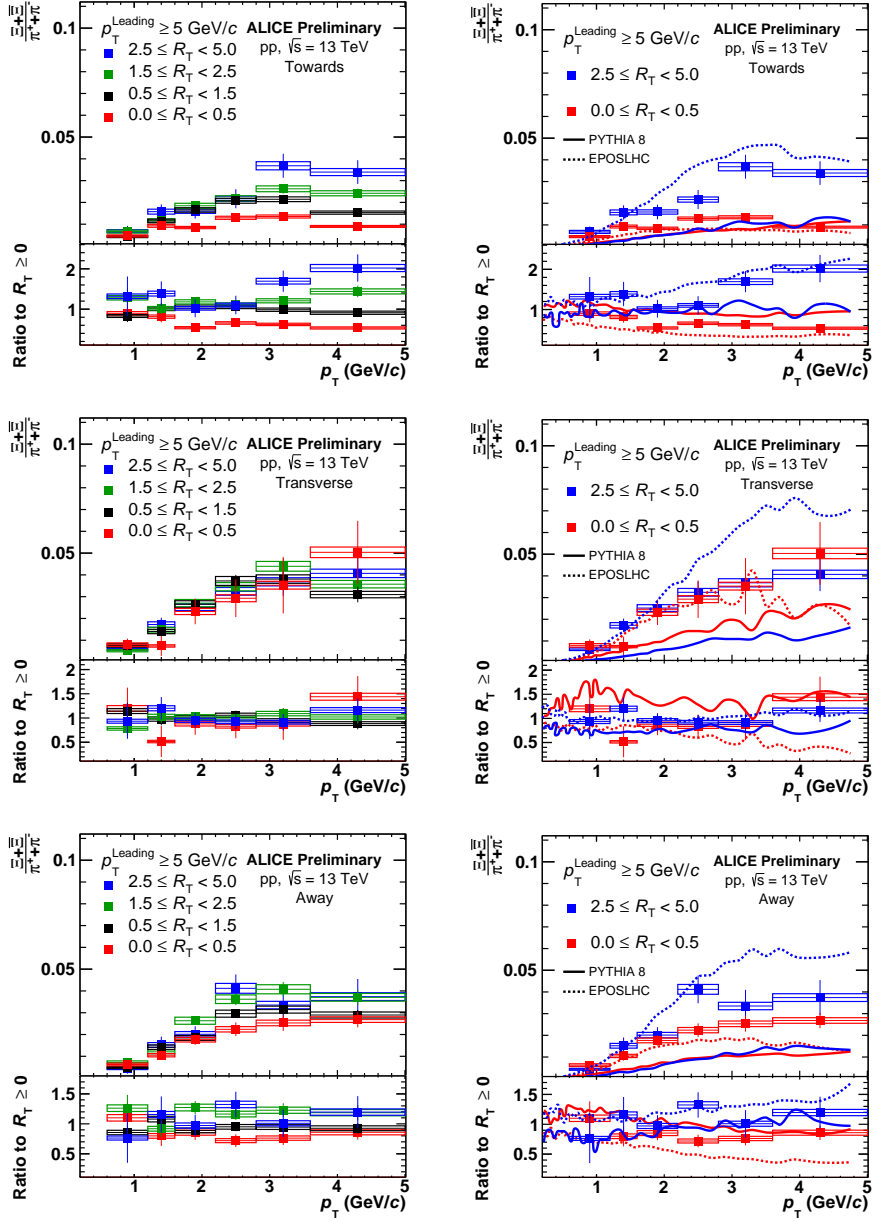


Figure 8.13: The corrected ratio of  $\Xi$ -to- $\pi$  as a function of  $p_T$  for different  $R_T$  selections, measured in the Towards (top row), Transverse (center row), and Away (bottom row) regions. (Left column): The  $\Xi$ -to- $\pi$  ratios are presented over the fully measured  $R_T$  range, in four different intervals. (Right column): The  $\Xi$ -to- $\pi$  are presented in the two most extreme  $R_T$  intervals and are compared to predictions from PYTHIA 8 and EPOS-LHC. Systematic uncertainties are represented by boxes and statistical uncertainties by vertical lines.

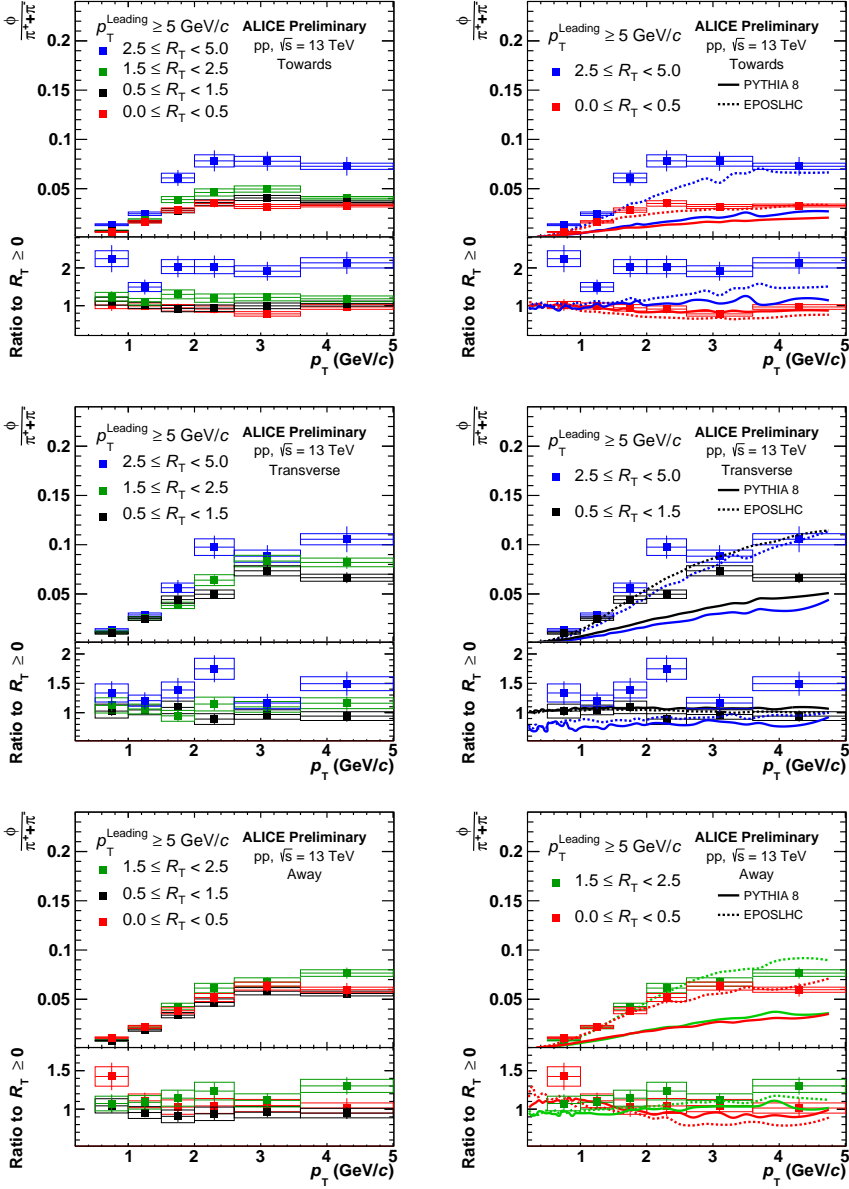


Figure 8.14: The corrected ratio of  $\phi$ -to- $\pi$  as a function of  $p_T$  for different  $R_T$  selections, measured in the Towards (top row), Transverse (center row), and Away (bottom row) regions. (Left column): The  $\phi$ -to- $\pi$  ratios are presented over the fully measured  $R_T$  range, in four different intervals. Due to statistical constraints, yield extraction could not be performed for the lowest (highest)  $R_T$  interval in the Transverse (Away) region. (Right column): The  $\phi$ -to- $\pi$  are presented in the two most extreme  $R_T$  intervals and are compared to predictions from PYTHIA 8 and EPOS-LHC. Systematic uncertainties are represented by boxes and statistical uncertainties by vertical lines.



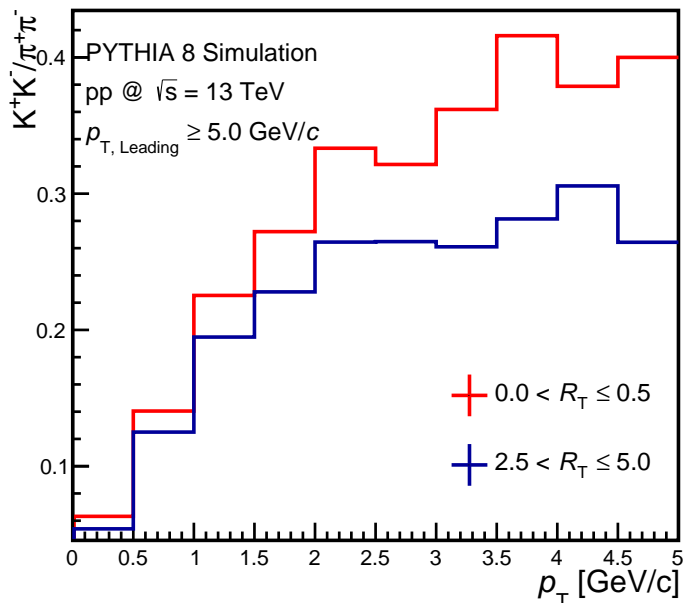


Figure 8.15: PYTHIA 8 simulation of K-to- $\pi$  ratios for the two most extreme  $R_T$  intervals.

## 8.6 Interpretation of Ratios, and Outlook

The results for both  $\phi$  and  $\Xi$  presented in Fig. 8.13 could potentially be misleading, if one extrapolates the trends for the integrated  $\Xi$  baryon yield. The spectra are currently not fully corrected. Therefore, accurate, integrated particle yields for each  $R_T$  interval cannot yet be measured. It is important to keep in mind that the  $p_T$ -differential  $\Xi$ -to- $\pi$  ratios are not ratios of yields, but rather *ratios of  $p_T$ -spectra*. Naively, one would expect that a constant enhancement of  $\Xi$ -to- $\pi$ , across the entire  $p_T$  range, naturally implies an enhancement of the total yield. However, this is not necessarily the case, as most of the yield for each particle is extracted from the  $p_T$ -spectra at  $\langle p_T \rangle$ . The  $\langle p_T \rangle$  is different for different particle species, where the  $R_T$ -dependence of  $\langle p_T \rangle$  might also vary across particle species.

This can be exemplified using generated PYTHIA 8 events. The Kaon(K)-to- $\pi$  ratio at  $0.0 \leq R_T < 0.5$ , presented in Fig. 8.15, is consistently enhanced, relative to the equivalent ratio at  $2.5 \leq R_T \leq 5.0$ , across the entire  $p_T$  range. However, the  $p_T$ -integrated yield is in fact larger for high- $R_T$  events: by integrating the yield of Kaons and Pions, for both  $R_T$  intervals presented in Fig. 8.15, the integrated  $\sum K / \sum \pi$  for the low  $R_T$  interval equals 0.106057, while the integral integrated yield for the higher  $R_T$  interval equals 0.116937.

Therefore, one should take caution when extrapolating the  $p_T$ -differential interpretation to the  $p_T$ -integrated yield. This also implies that fully corrected spectra are required to fully exploit and understand the particle-production dynamics relative to  $R_T$ . The next steps for this analysis will incorporate a Bayesian unfolding, based on the technique described in Ref. [120]. This has already been proven to work for  $R_T$  studies on the production of primary  $\pi$ , K, p, reported in Ref. [19]. At the time of writing this thesis, the hope is that a similar technique could be utilized to correct the  $R_T$ -differential  $p_T$  spectra for both  $\phi$  mesons and  $\Xi$  baryons. The interplay between strange hadron production and  $R_T$  might be re-evaluated once the corrected, integrated quantities are obtained.

## Chapter 9

# Conclusions

This thesis presented  $\phi$  and  $\Xi$  production as functions of two new differential observables, measured in pp collisions at  $\sqrt{s}=13$  TeV, recorded by ALICE. The main aim has been to provide new insights into the mechanisms of the production and enhancement of strange hadrons. It has been demonstrated that the Unweighted Transverse Spherocity  $S_{\text{O}}^{p_{\text{T}}=1}$  and the Relative Transverse Activity  $R_{\text{T}}$  can be utilized as tools to vary the dominant mode of particle production, via the even topology and the size of the UE, respectively.

This allows one to contrast events that are primarily dominated by hard, pQCD-like processes, with events that are driven by softer (QGP-like), non-perturbative QCD processes. Understanding the interplay between  $\phi$  and  $\Xi$  production relative to the aforementioned observables can shed light on the underlying production mechanism of  $\phi$  mesons: whether the  $\phi$  mimics other strange particles, or behaves like a non-strange particle. This can be used to discriminate between thermal models (where the probability to produce  $\phi$  is related to its total mass) and QCD-inspired, string-like models (where the probability to produce  $\phi$  is related to the mass of the valance quarks).

One of the most important aspects of my work has been to ensure that the measured results for both  $S_{\text{O}}^{p_{\text{T}}=1}$  and  $R_{\text{T}}$  can be directly compared to model predictions. I developed the  $S_{\text{O}}^{p_{\text{T}}=1}$  observable, where a large amount of time was invested in understanding the origin of the biases for weakly decaying/resonances when measured as a function of the traditional  $S_{\text{O}}$ . Naively, the change from  $S_{\text{O}} \rightarrow S_{\text{O}}^{p_{\text{T}}=1}$  can come across as a rather rough, ad-hoc solution. However, thorough checks were made to guarantee that  $S_{\text{O}}^{p_{\text{T}}=1}$  would remain qualitatively sensitive to the physics probed by  $S_{\text{O}}$ , and the solution turned out to be a robust

alternative. This can be observed both in the closure tests in Fig. 7.9 - 7.11, but also through the data-driven charged-to-neutral kaon ratio, reported in Fig. 7.14.

Furthermore, the  $S_O^{p_T=1}$  analysis revealed that the observable has a varying degree of sensitivity w.r.t the pseudorapidity region where the multiplicity is evaluated. The  $dN_{\text{ch}}/d\eta$  range between different  $S_O^{p_T=1}$  classes is broad when estimating multiplicity at forward rapidities while maintaining a relatively homogenous  $\langle p_T \rangle$ . In this sense, a  $S_O^{p_T=1}$  selection at forward multiplicities is primarily driven by a trivial multiplicity bias. Moreover, it was found that a midrapidity estimate of the multiplicity gave a much more narrow separation in  $dN_{\text{ch}}/d\eta$  between  $S_O^{p_T=1}$  classes, as well as large separations of  $\langle p_T \rangle$ . A midrapidity estimate of the multiplicity, in tandem with a  $S_O^{p_T=1}$  selection, is optimal for separating events based on their hardness. This conclusion is supported by the dynamics demonstrated in Fig. 7.13, as well as in the double-ratios presented in Sec. 7.5.4.

A more traditional view of a pp collision could suggest that high-multiplicity events are dominated by multi-jet final states, where particle production is primarily driven by hard processes. Moreover, QGP-like effects were originally assumed to be very rare features of high-multiplicity events, and the idea was to isolate and study these effects in events with an extreme isotropic distribution of particles. However, the results presented in this thesis seem to indicate that these underlying assumptions are not correct. Isotropic events seem to give an almost perfect description of average, high-multiplicity events, suggesting that high-multiplicity events are quite homogenous and QGP-like effects are the norm, whereas the jetty event class can isolate the seemingly rare, non-QGP-like effects. Furthermore, the presented results suggest that  $\Xi$  and  $\phi$  are primarily produced in events characterized by soft physics, and heavily suppressed in events driven by hard, pQCD physics. This claim is strongly supported by the double-ratios, both in Sec. 7.5.2 and Sec. 7.5.4, but also by the integrated  $\Xi$  yield as a function of  $S_O^{p_T=1}$ , presented in Fig. 7.24. While the  $\phi$  meson does not show a significant modification in the isotropic event class, there is a clear,  $p_T$ -differential suppression of  $\phi$  mesons in the jetty events, w.r.t to a midrapidity multiplicity estimation, highlighted in both Fig. 7.21 and Fig. 7.28.

The results from the  $R_T$  analysis suggest the particle-production dynamics of strange particles are very different, based on the underlying physics processes. The preliminary study indicates that strangeness production is a property of the underlying event, and the relative contributions from hard, pQCD physics seem to be small. This can be seen by comparing the  $R_T$ -dependence in the Toward region, highlighted in both Fig. 8.13 and Fig. 8.14, for  $\Xi$  and  $\phi$  production, respectively. Furthermore, the production of strange hadrons does not scale

exponentially with the UE, demonstrated by the non-sensitivity of  $R_T$  in the Transverse region.

	$S_0^{p_T=1}$	$R_T$
$\Xi$ -to- $\pi$	Enhancement in Isotropic Suppression in Jetty	Significant $R_T$ dependence in Towards
$\phi$ -to- $\pi$	No Significant Suppression/ Enhancement	Significant $R_T$ dependence in Towards

**Figure 9.1:** Summary of the  $\phi$  and  $\Xi$  results between the unweighted transverse sphericity  $S_0^{p_T=1}$  and the relative transverse activity  $R_T$ .

The role of the  $\phi$  meson is puzzling. when comparing the  $R_T$  and  $S_0^{p_T=1}$  analyses w.r.t to the  $\Xi$  meson. One should note that the two observables develop in tandem, even though they are defined by different means<sup>1</sup>. A larger  $R_T$  will produce a larger UE, which on average will make the azimuthal topology more isotropic. Likewise, an event with zero  $N_T$  will have all particles produced in the Toward/Away regions, which will have a di-jet topology in the azimuth. The production of  $\Xi$  baryons between the two observables is self-consistent; One can see a suppression of  $\Xi$  production for both low- $R_T$  events in the Toward region, and for jetty events, while also enhancing the production in high- $R_T$  and isotropic events (demonstrated in Fig. 8.13 and Fig. 7.24). The same does not apply for  $\phi$ , summarized in Fig. 9.1: One can observe a  $R_T$ -dependence similar to that of  $\Xi$  (c.f., Fig. 8.14), but there is no apparent modification of  $\phi$  production in isotropic events (c.f., Fig. 7.21), with a slight  $p_T$ -differential suppression in the 0-1% most jetty events (highlighted in Fig. 7.28). This discrepancy is currently not well understood and requires further studies. This analysis would greatly benefit from increased statistics, allowing the integrated yield of  $\phi$  mesons to be measured in a 0-1% high-multiplicity and  $S_0^{p_T=1}$  event selection.

<sup>1</sup>Although caveats still apply. While correlated (events with  $p_T^{\text{Leading}} \geq 5.0\text{GeV}/c$  are weighted towards higher multiplicities), the underlying reference samples are different, and therefore one is not able to perform a direct, quantitative comparison.

Overall, the results presented in this thesis indicate that soft, non-perturbative QCD physics is not a rare phenomenon in high-multiplicity pp collisions, but rather the norm. Both  $R_T$  and  $S_O^{p_T=1}$  indicate that strangeness production is favored in events dominated by soft processes. The EPOS-LHC model seems to qualitatively describe the relative production of  $\phi$  in most  $R_T$  measurements but overpredicts the strangeness enhancement in the core. The PYTHIA Rope model can qualitatively predict the particle dynamics for the  $S_O^{p_T=1}$  measurements, while the "cluster hadronization" model in Herwig 7.2 seems to be incompatible with the measurements presented in this thesis.

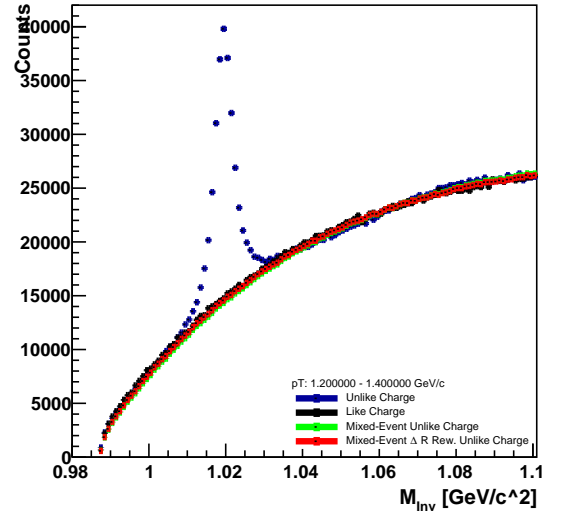
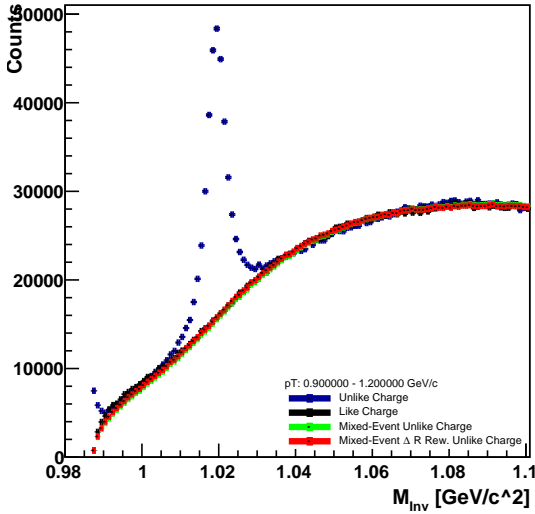
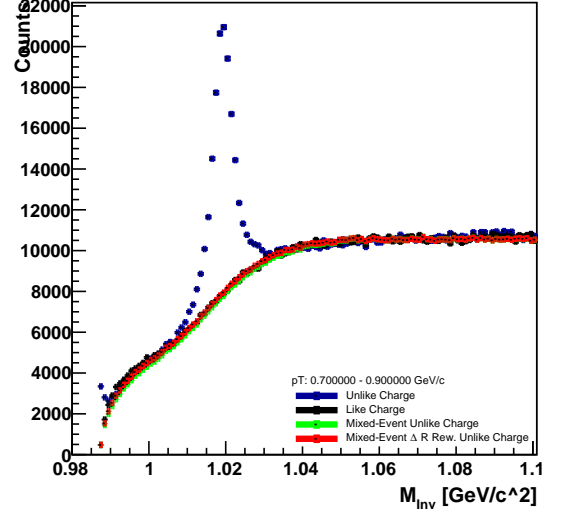
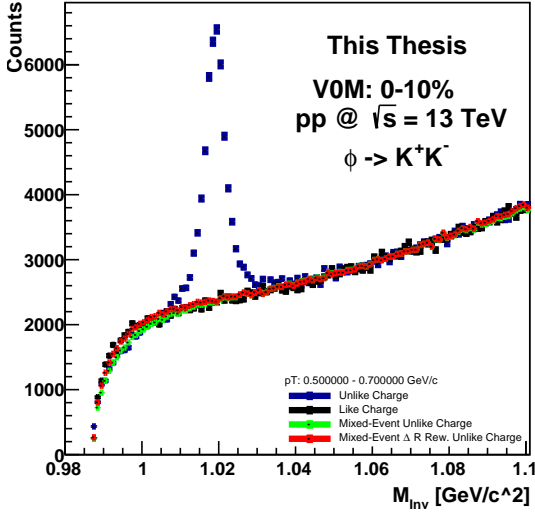
## Chapter 10

# Appendix A: Invariant Mass Distributions and Fits for the $S_{\text{O}}^{p_{\text{T}}=1}$ Analysis.

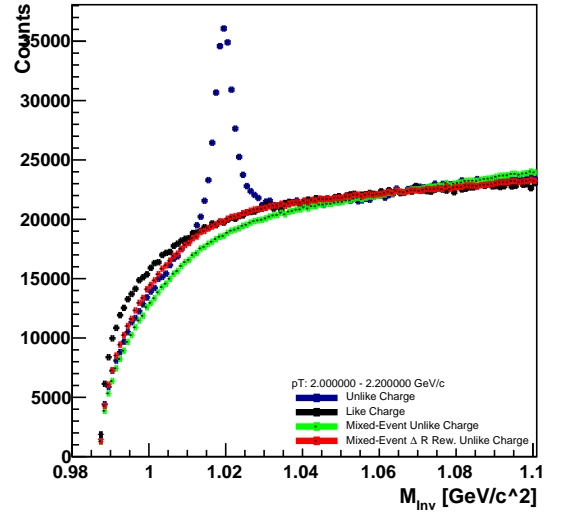
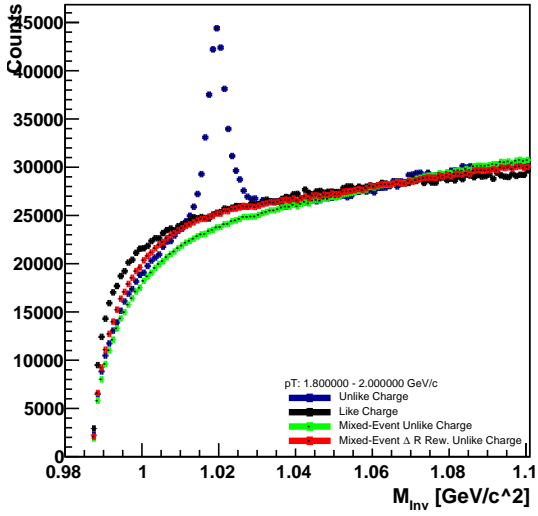
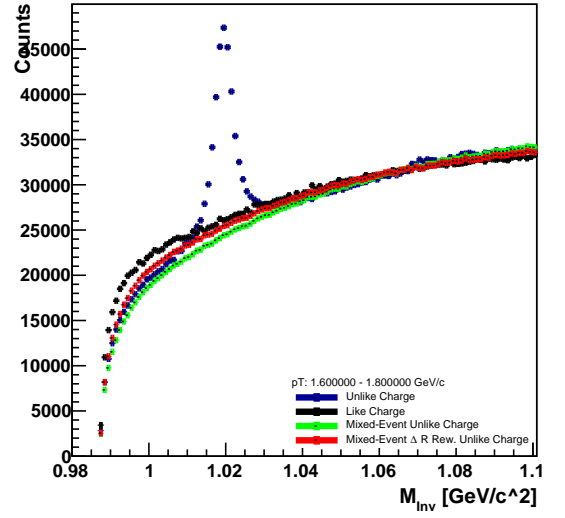
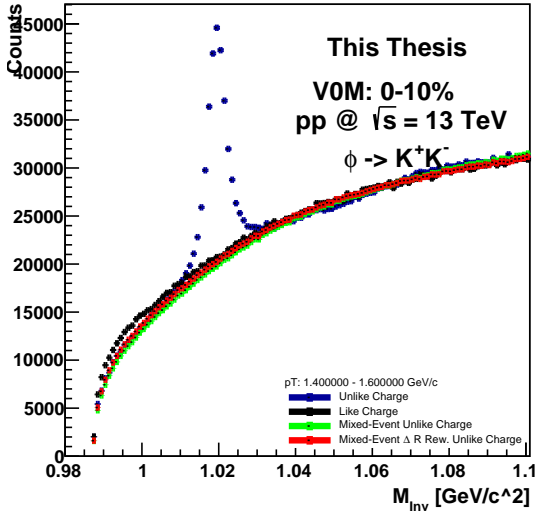
This chapter contains all the invariant mass distributions of peak fits for the  $S_{\text{O}}^{p_{\text{T}}=1}$  analysis, presented in Ch. 7. The distributions are presented for V0M:0-1%, in  $S_{\text{O}}^{p_{\text{T}}=1}$  percentiles of 10%. This selection gives a good representation of the different peak shapes. All configurations and variations that are presented in the Thesis are not included, to ensure a reasonable size of this Appendix.

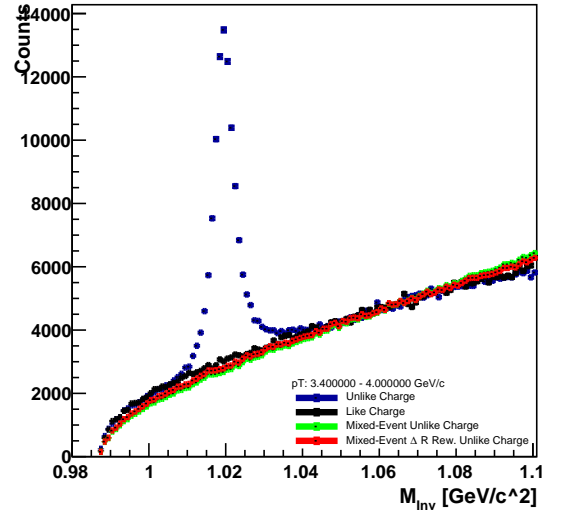
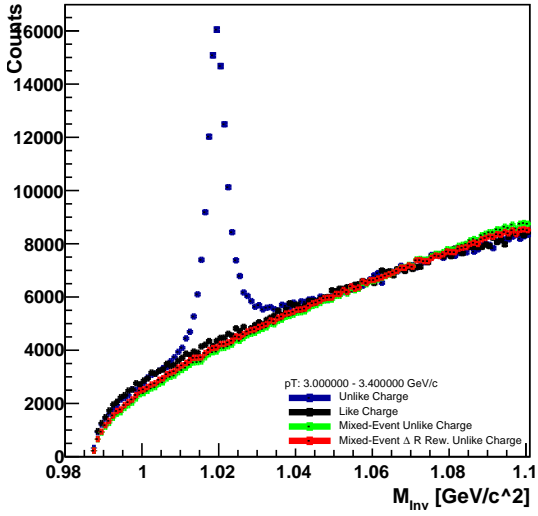
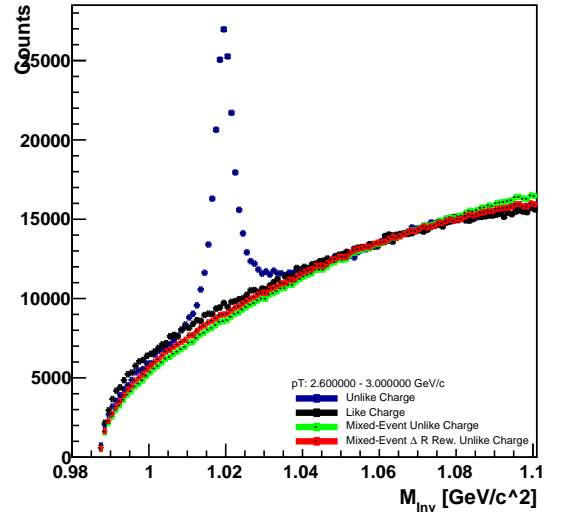
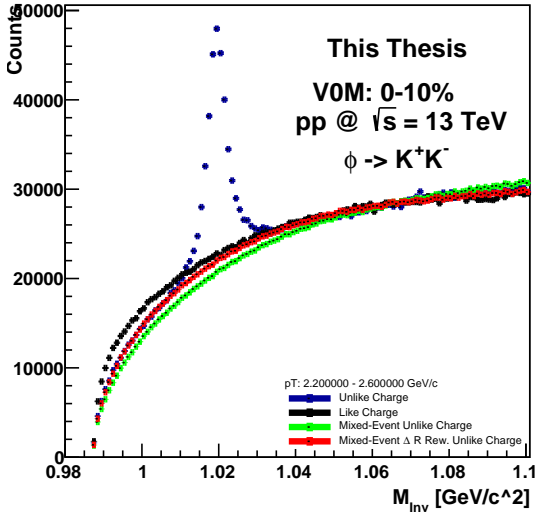
## 10.1 Invariant Mass Distributions

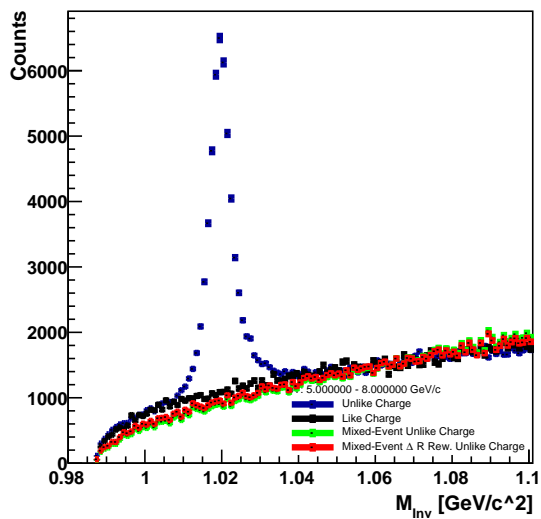
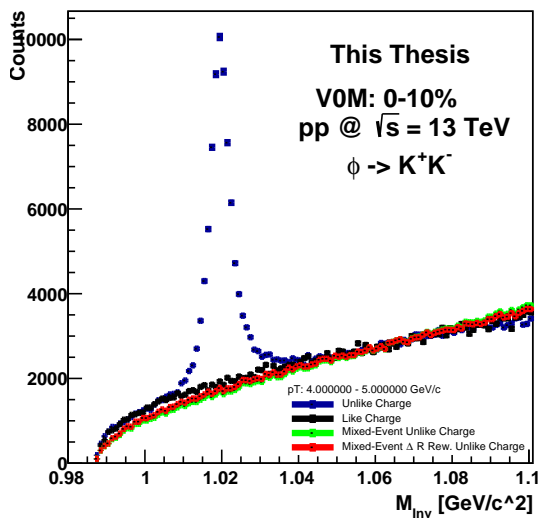
### 10.1.1 V0M: 0-10%



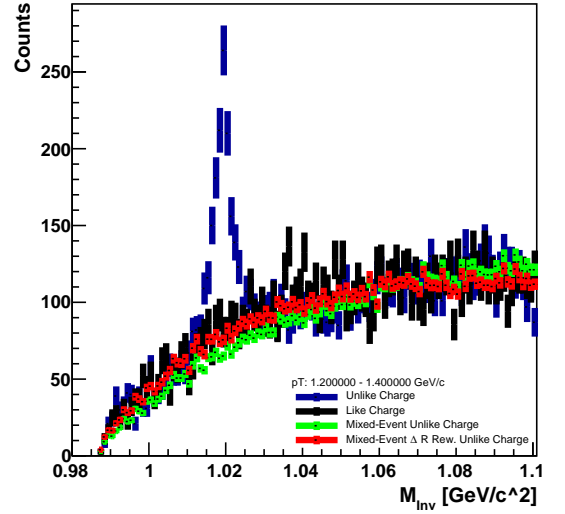
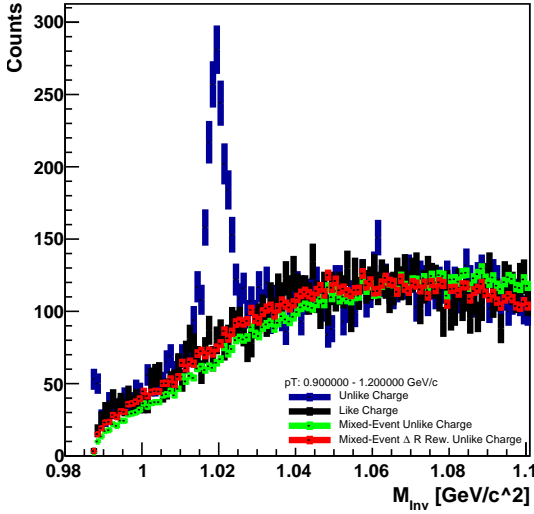
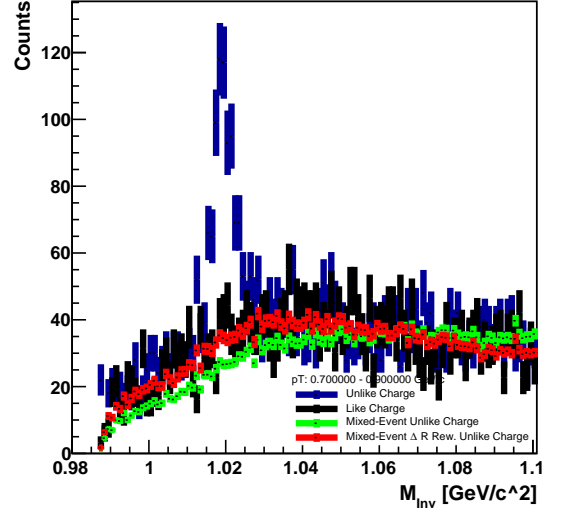
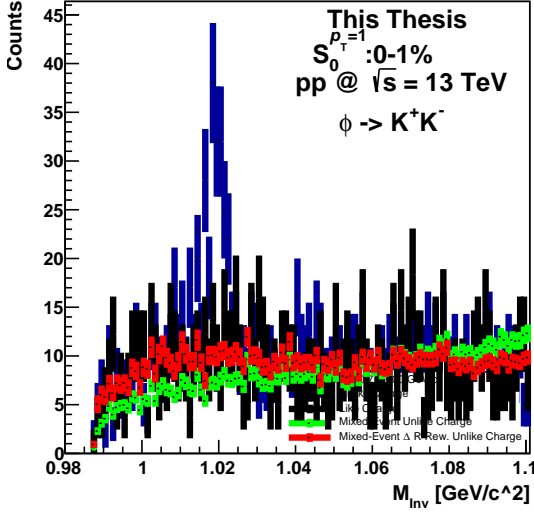


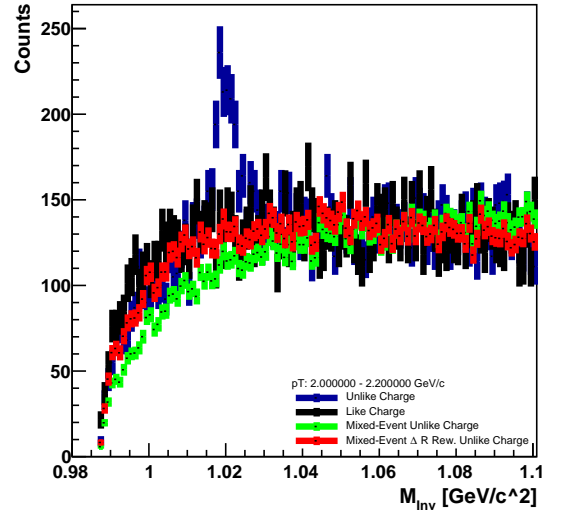
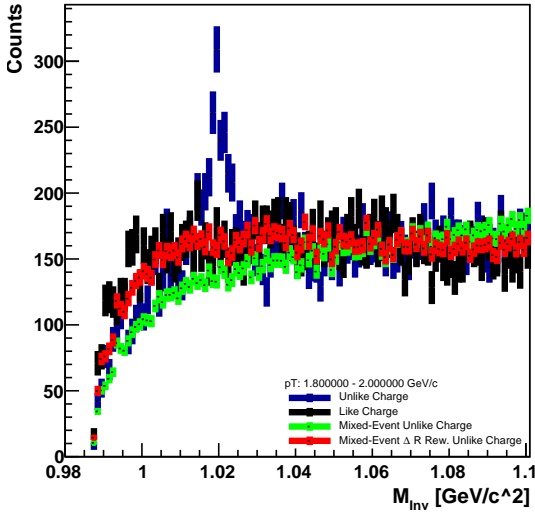
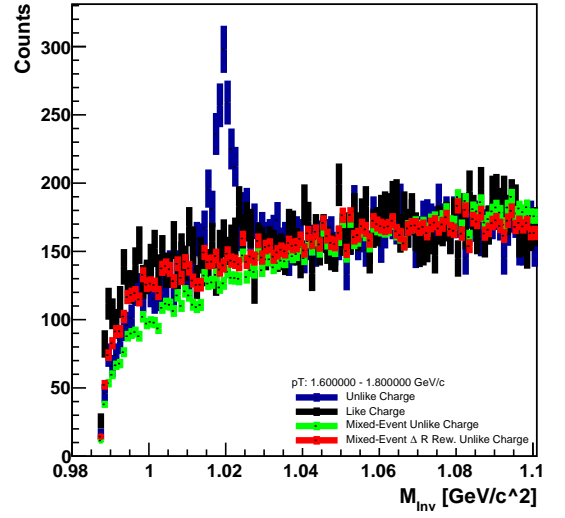
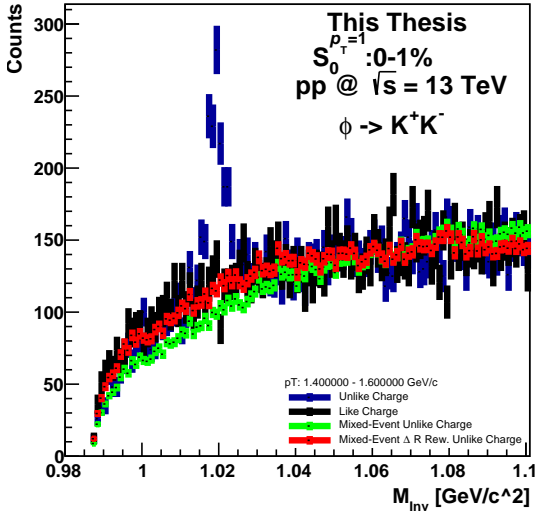


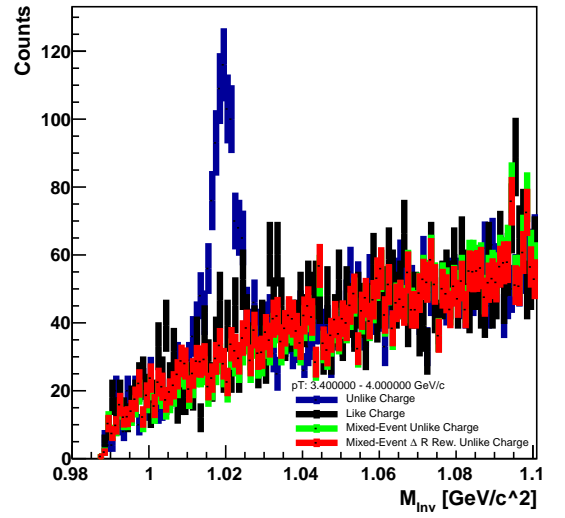
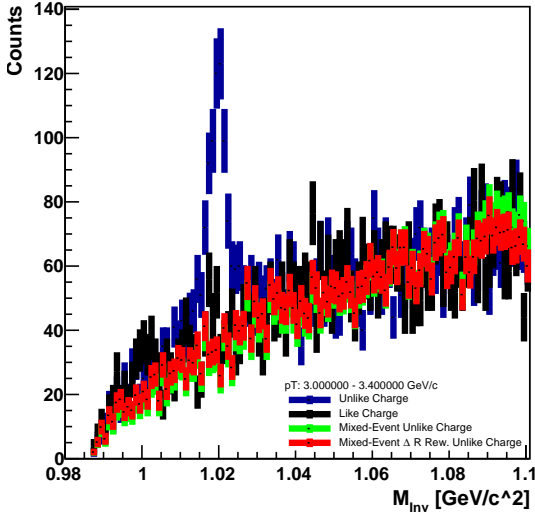
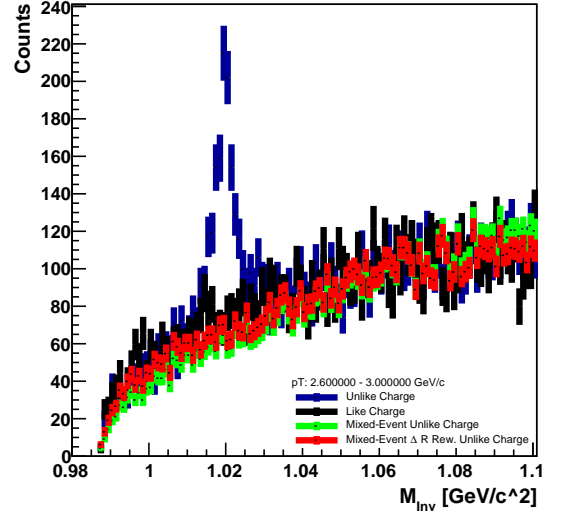
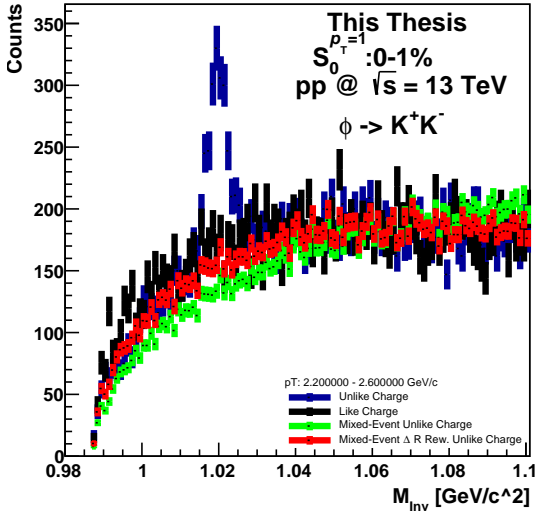


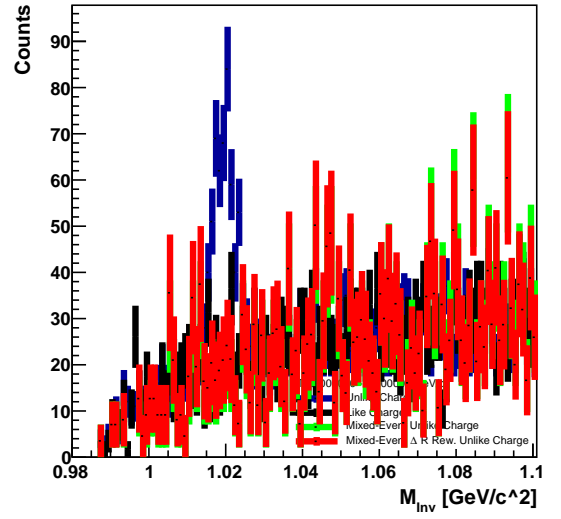
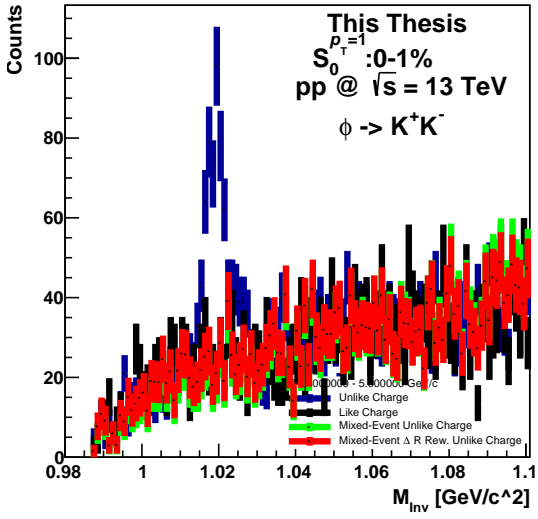


### 10.1.2 Jetty Events, VOM: 0-10% + $S_O^{p_T=1}$ 0-1%

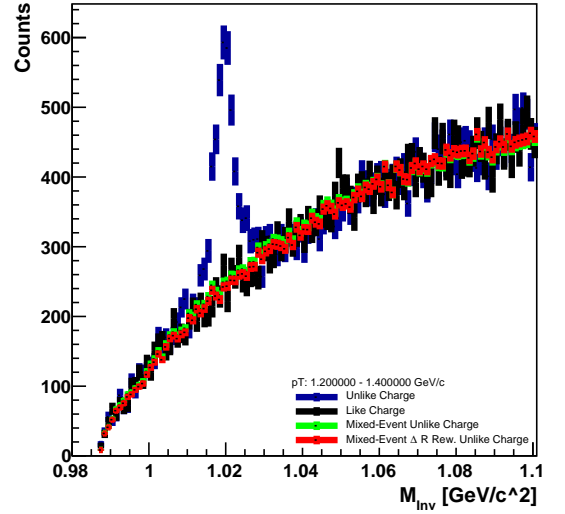
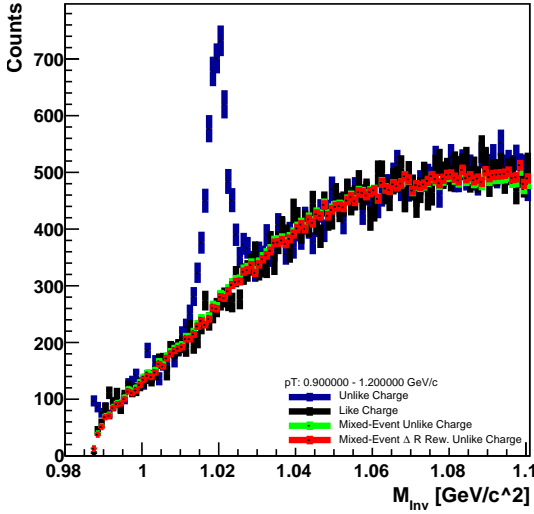
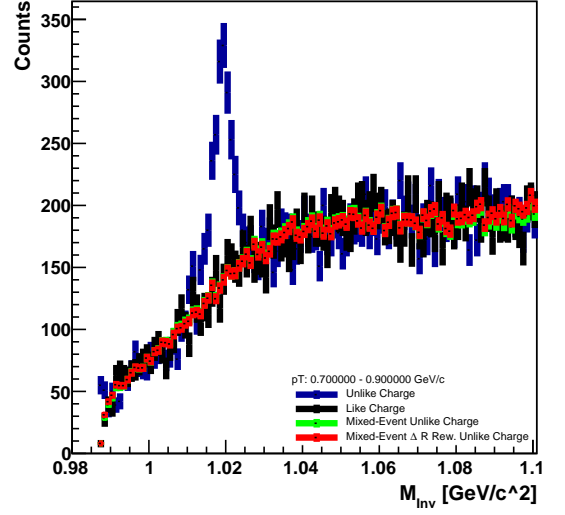
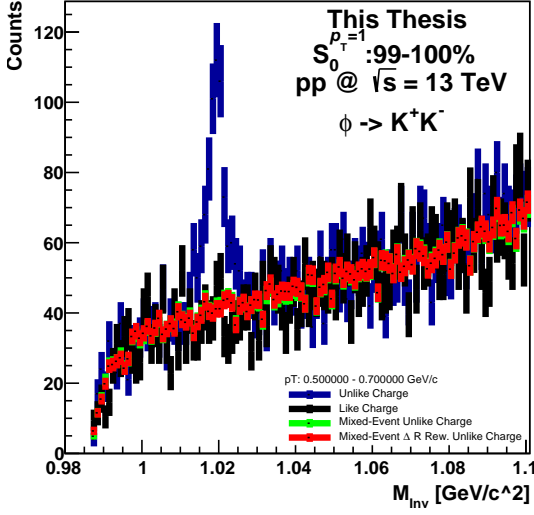




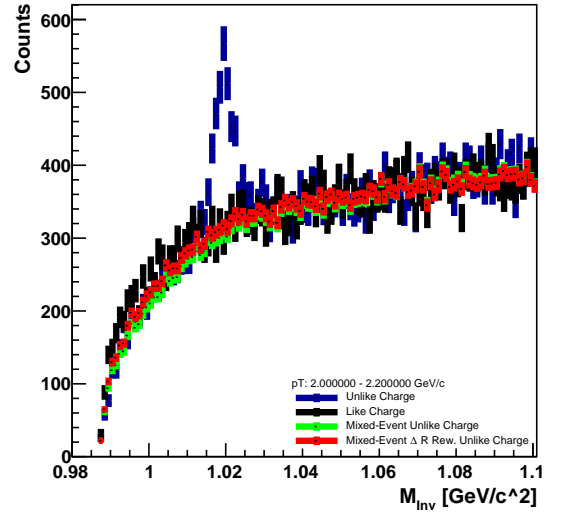
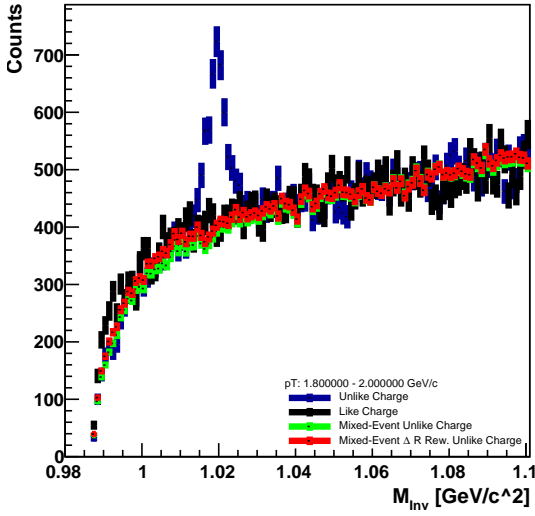
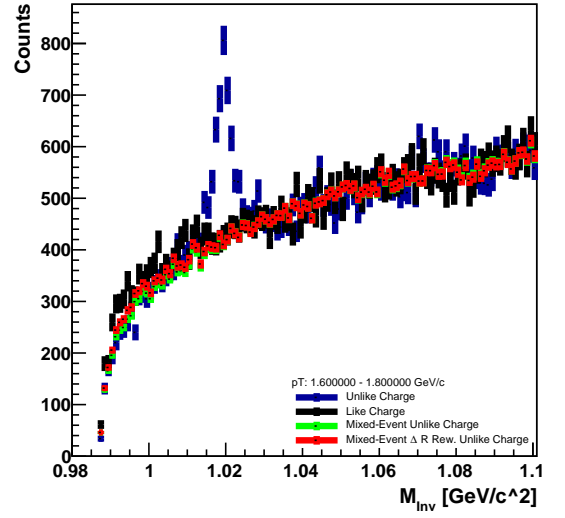
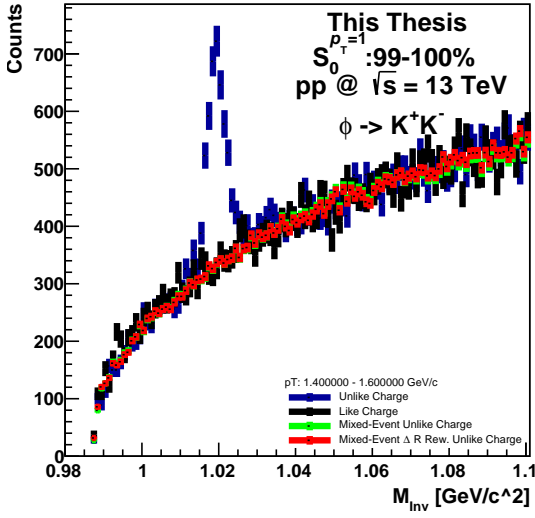


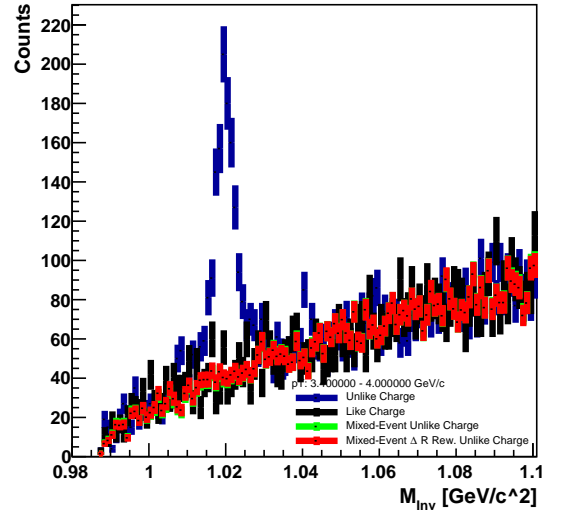
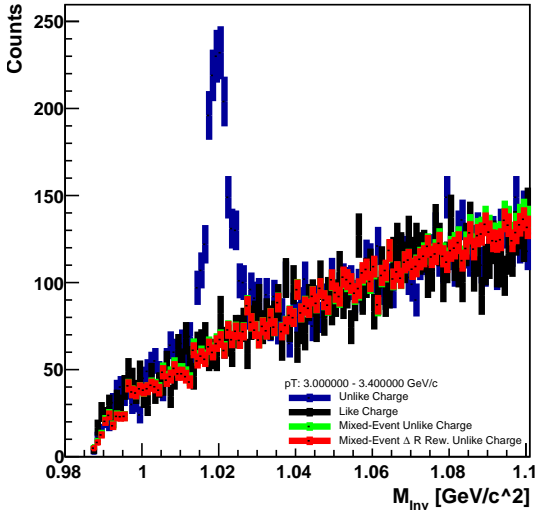
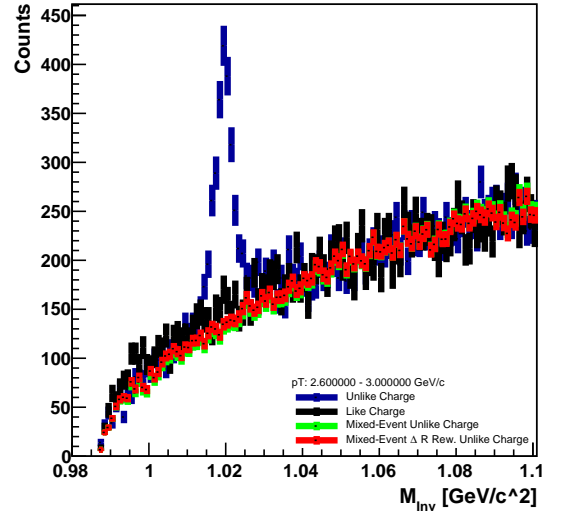
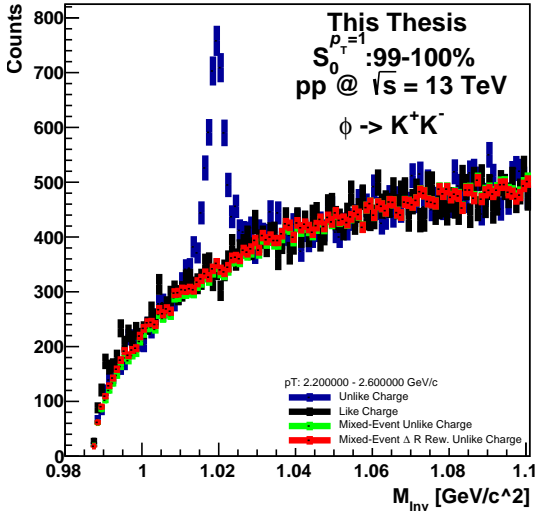


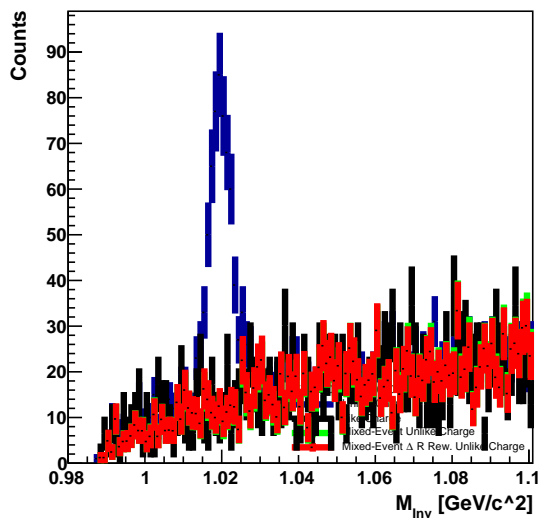
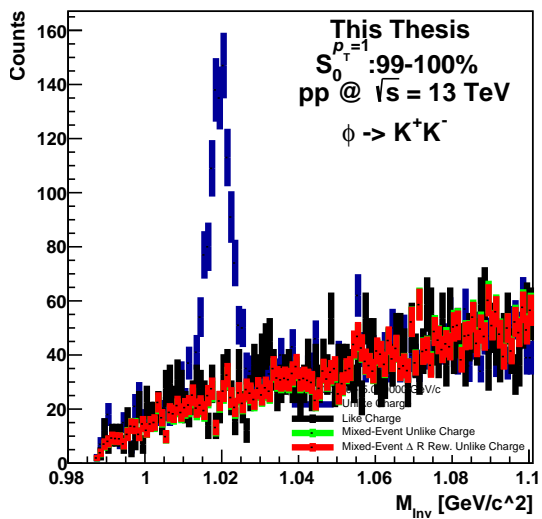
### 10.1.3 Isotropic Events, V0M: 0-1% + $S_O^{p_T=1}$ 99-100%





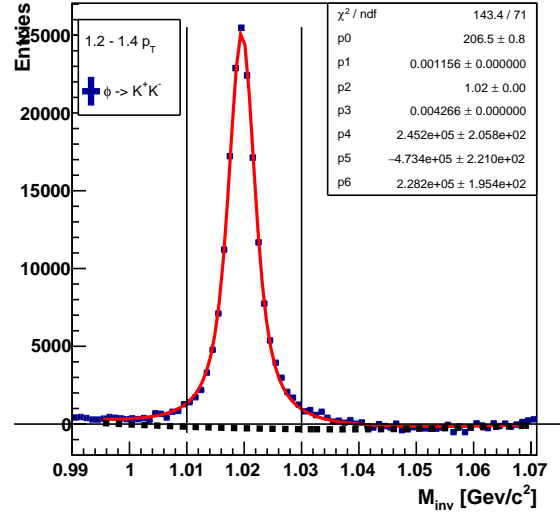
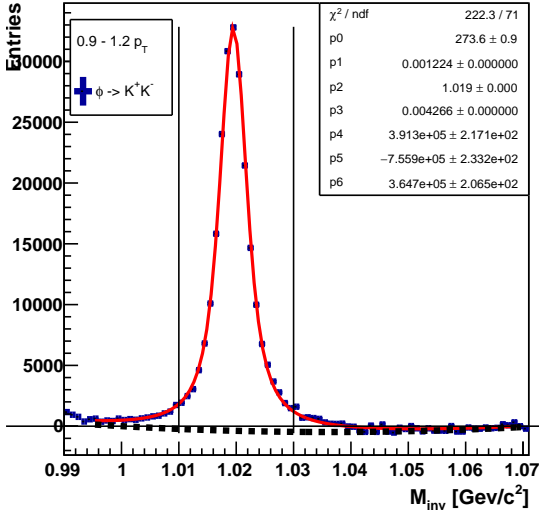
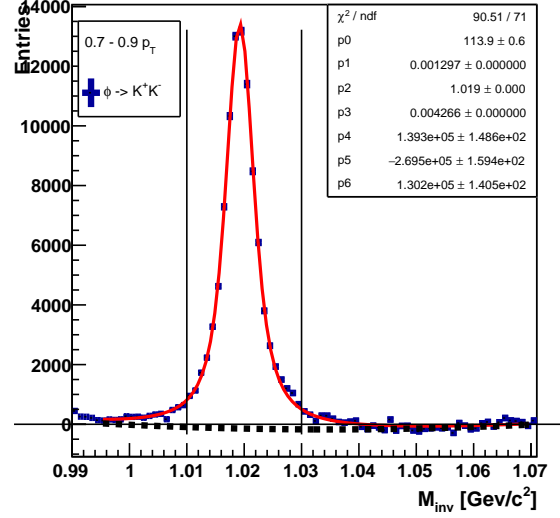
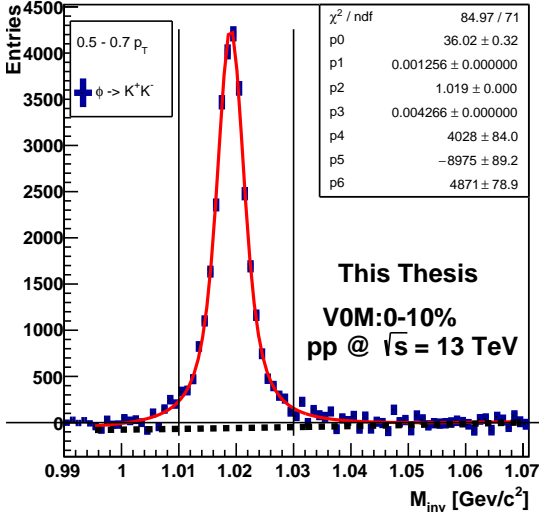


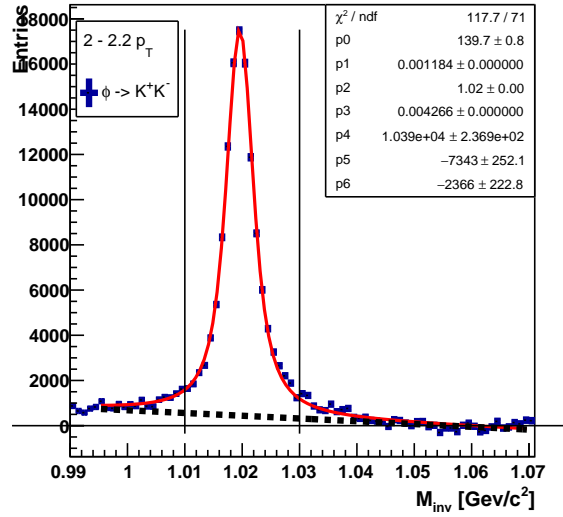
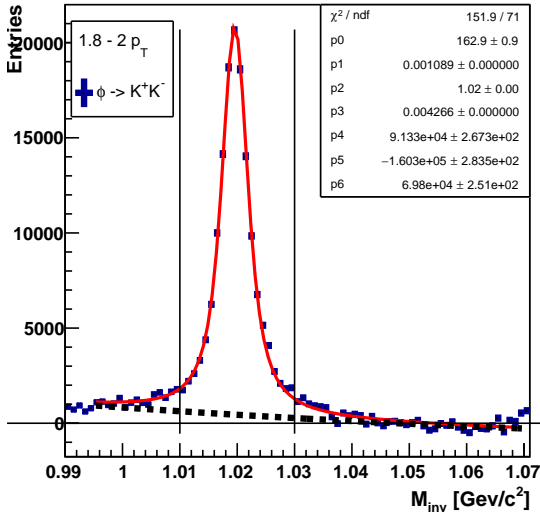
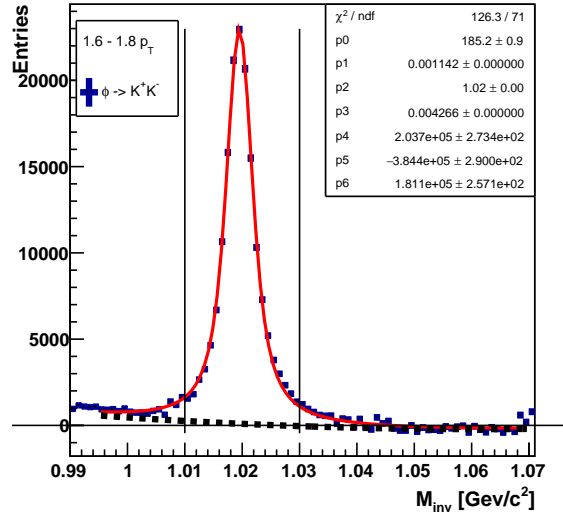
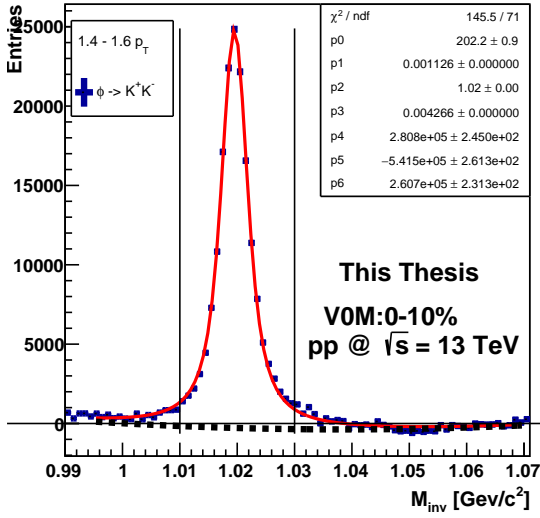


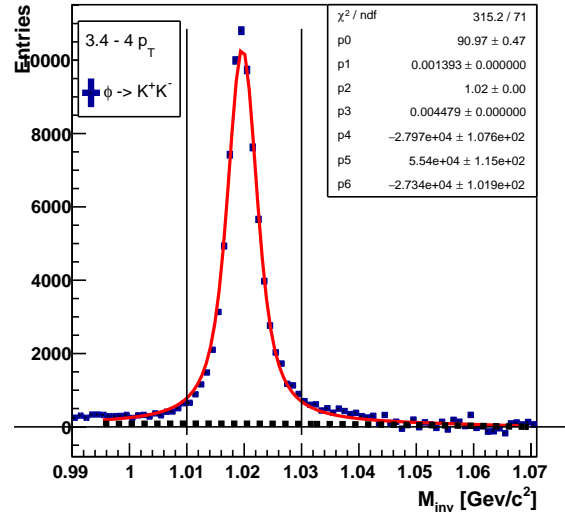
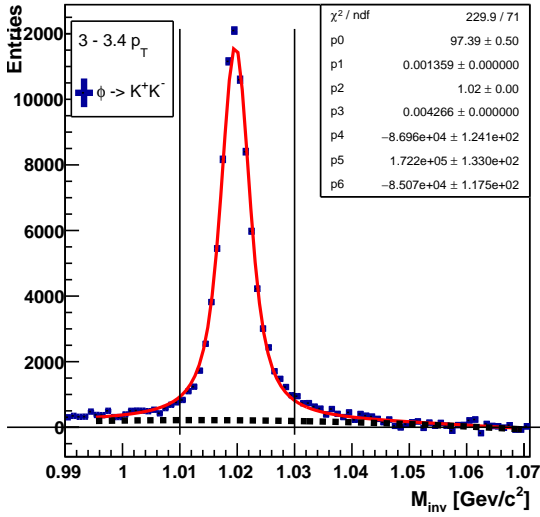
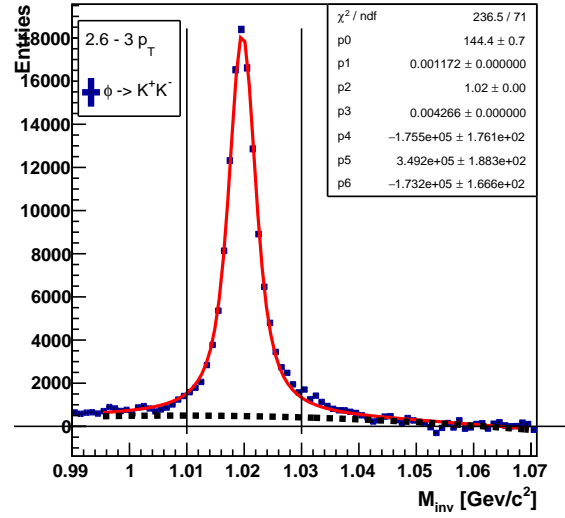
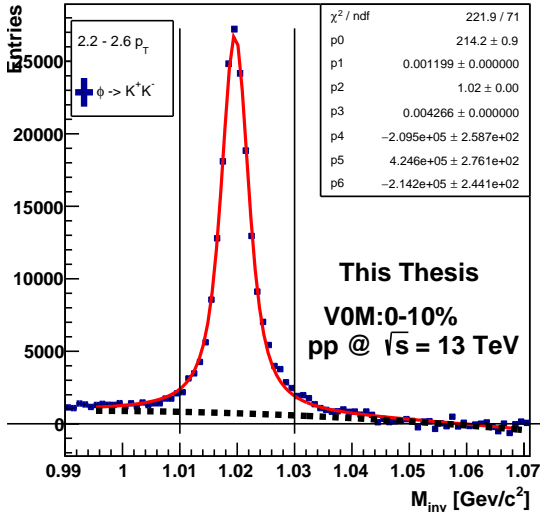


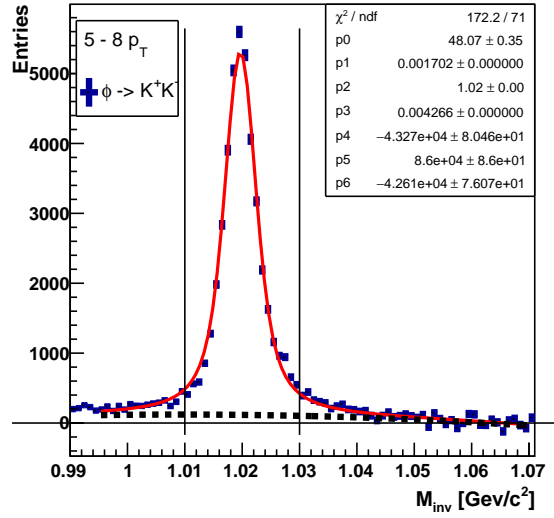
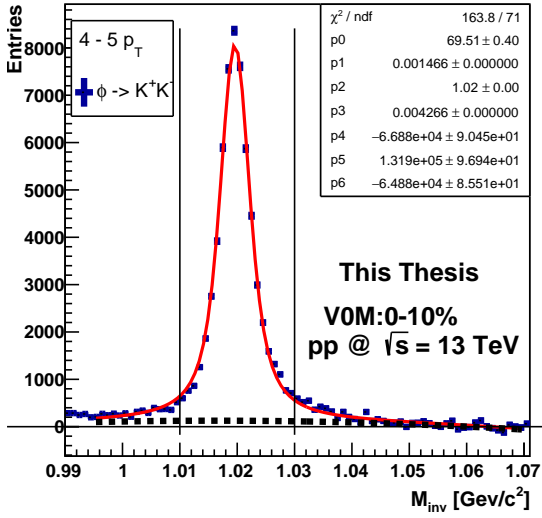
## 10.2 Invariant Mass Peak Fits

### 10.2.1 V0M: 0-10%

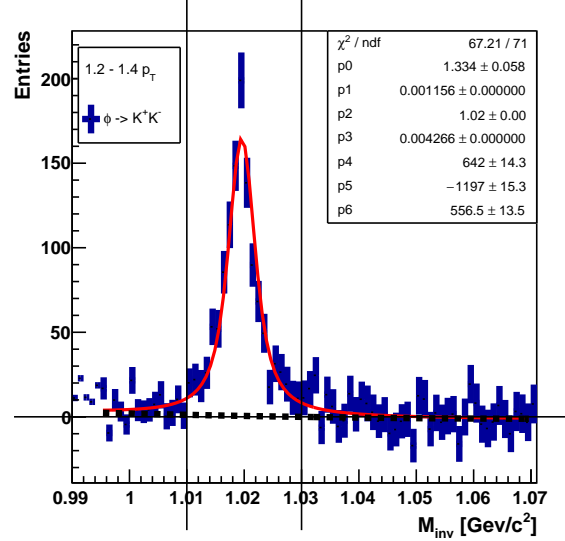
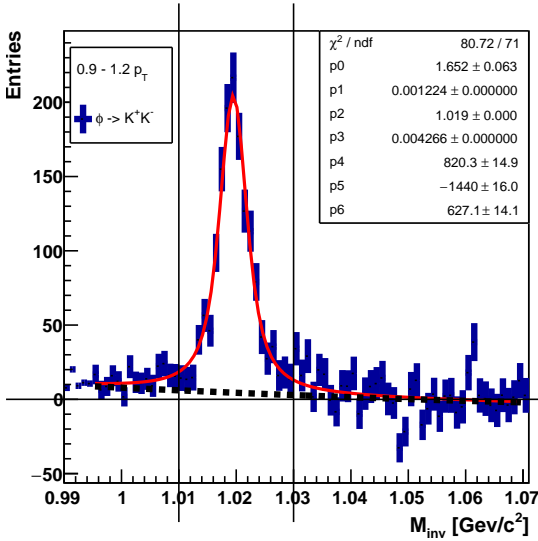
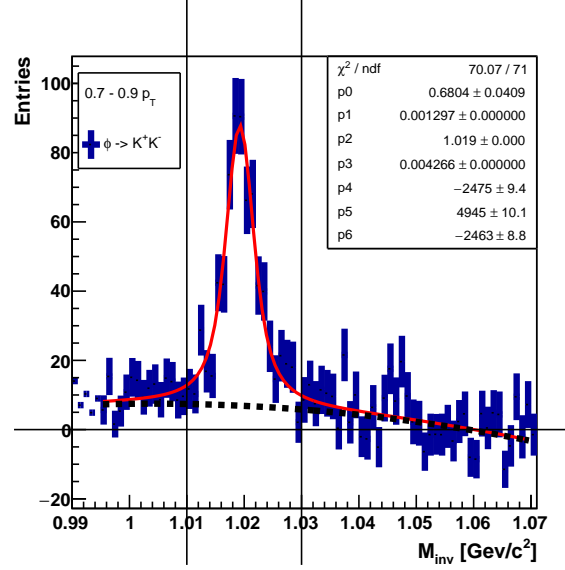
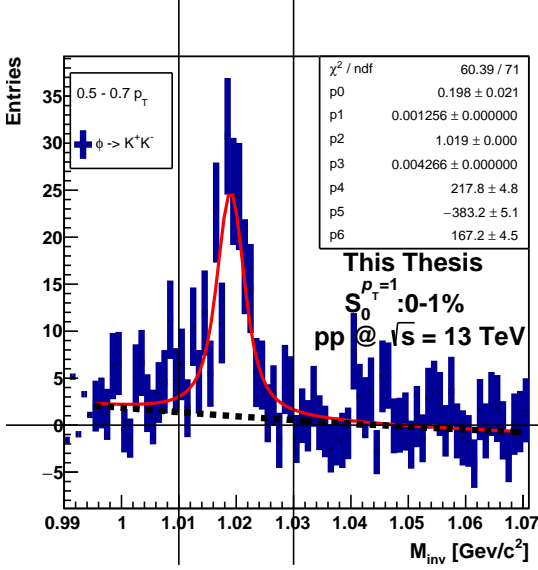




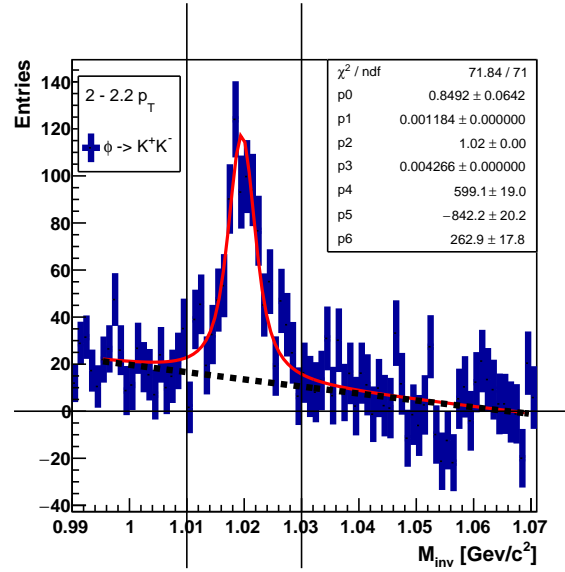
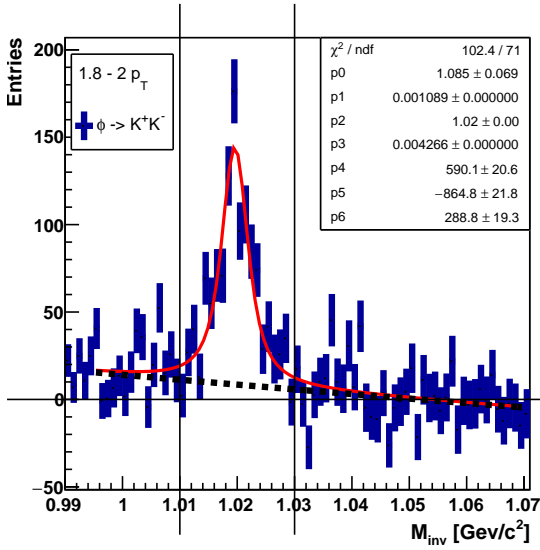
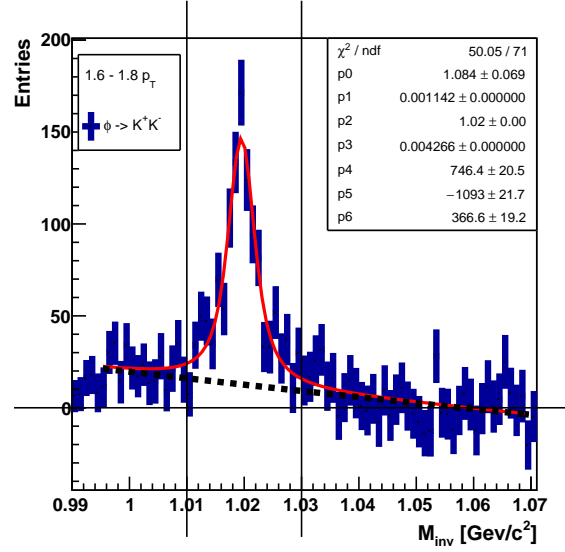
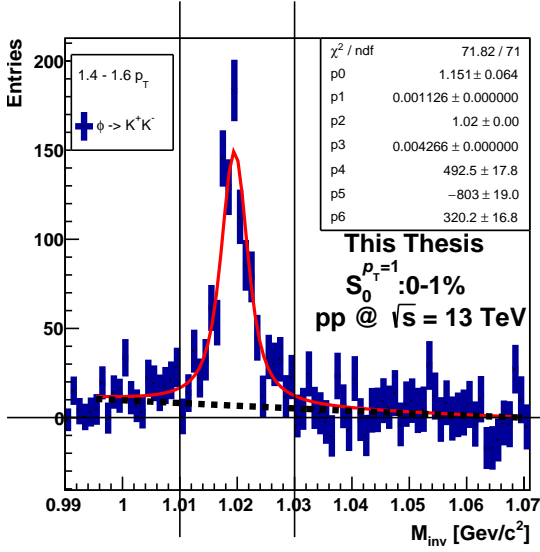


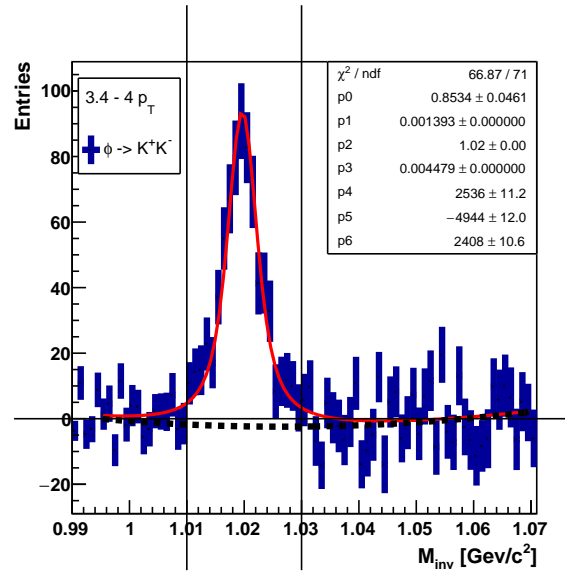
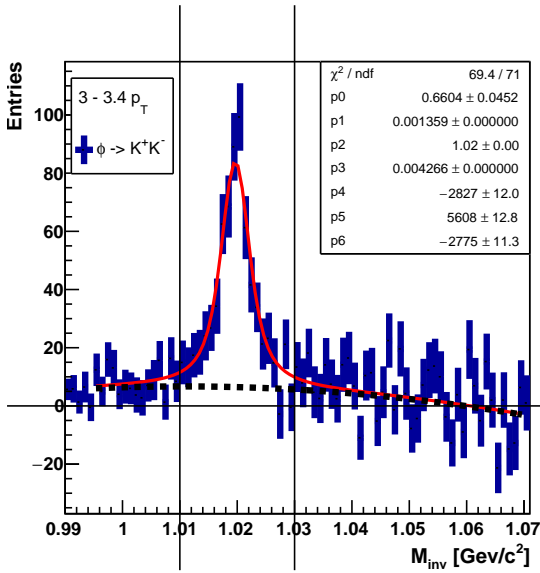
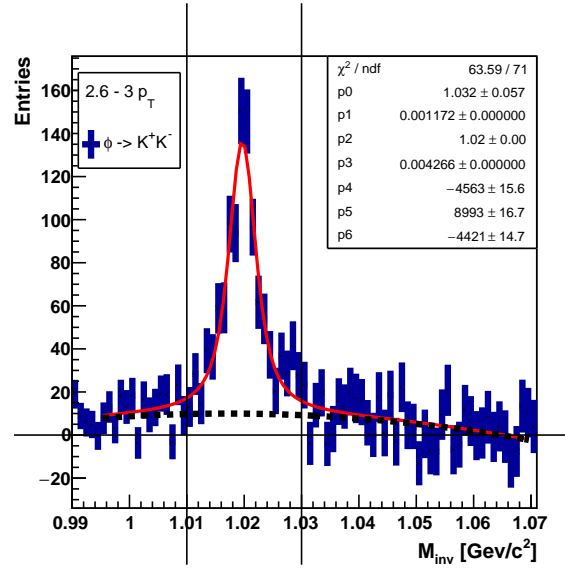
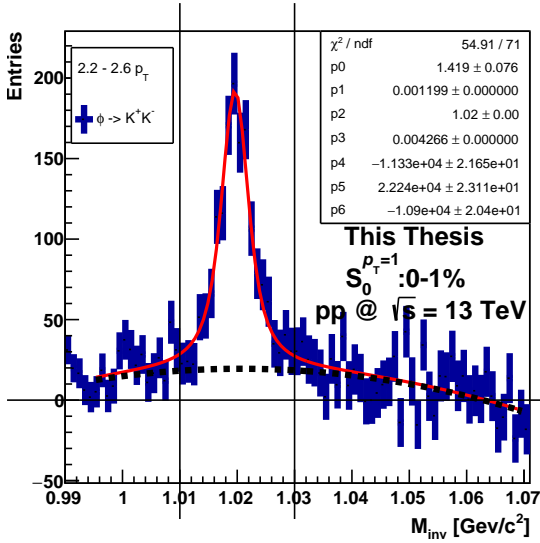


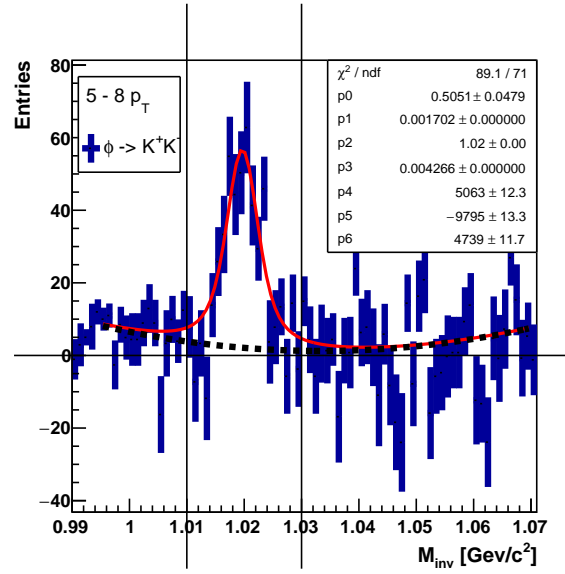
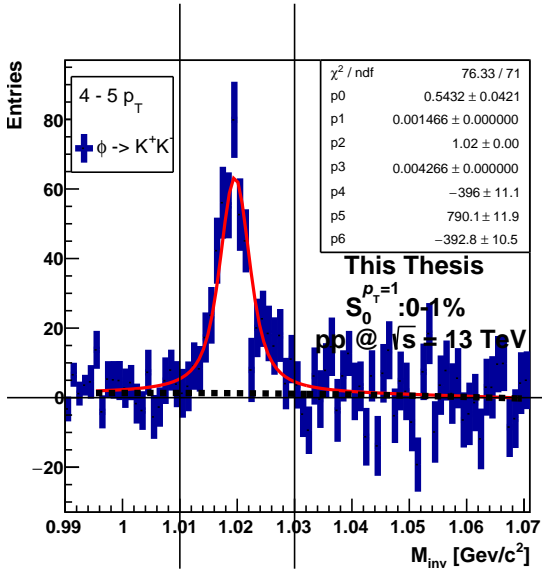
## 10.2.2 Jetty Events, VOM: 0-10% + $S_0^{p_T=1}$ 0-1%



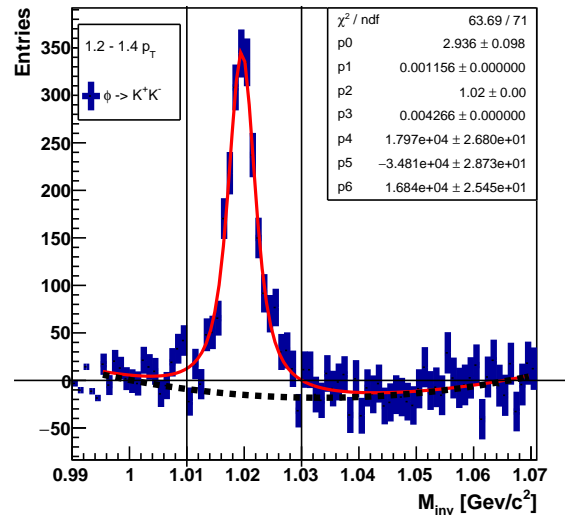
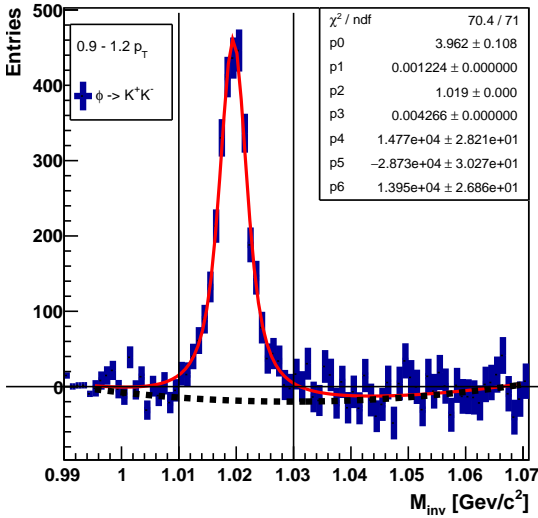
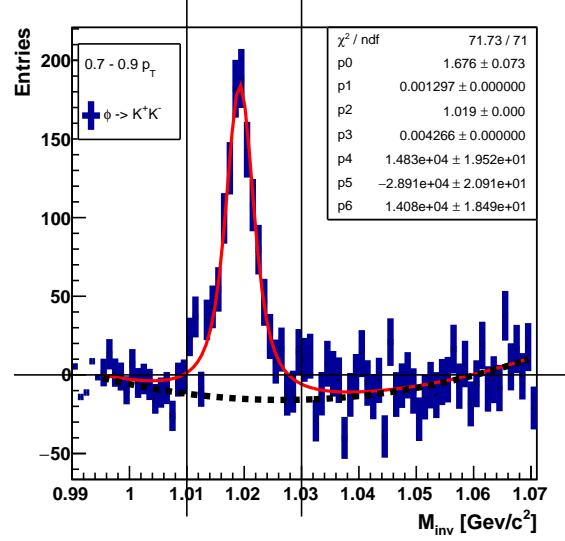
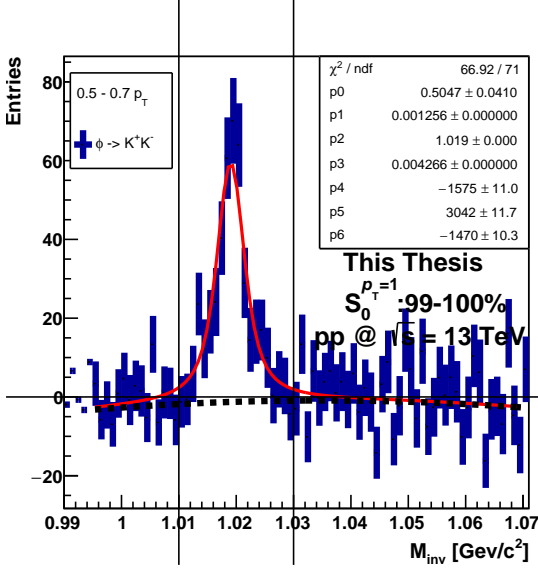


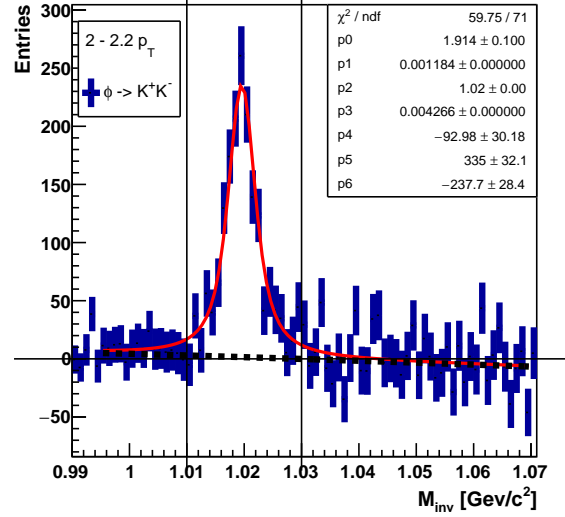
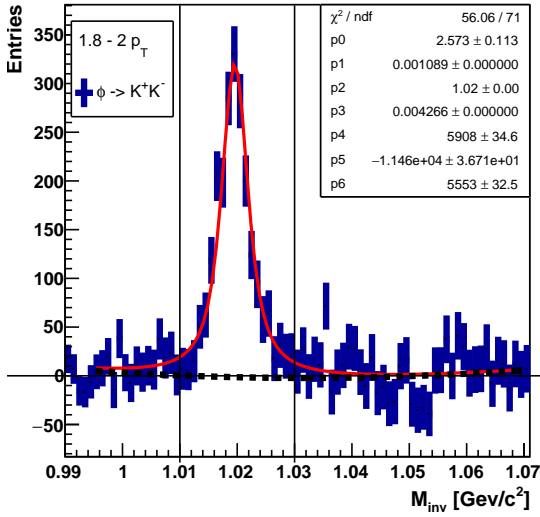
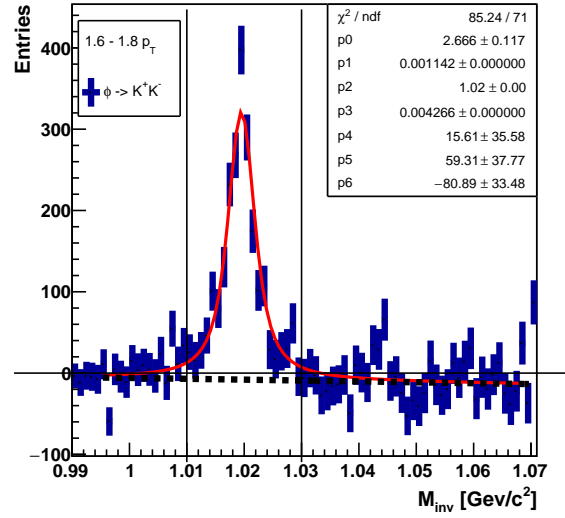
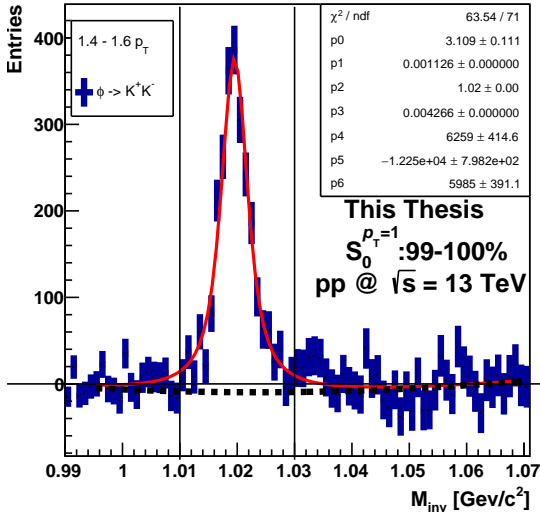


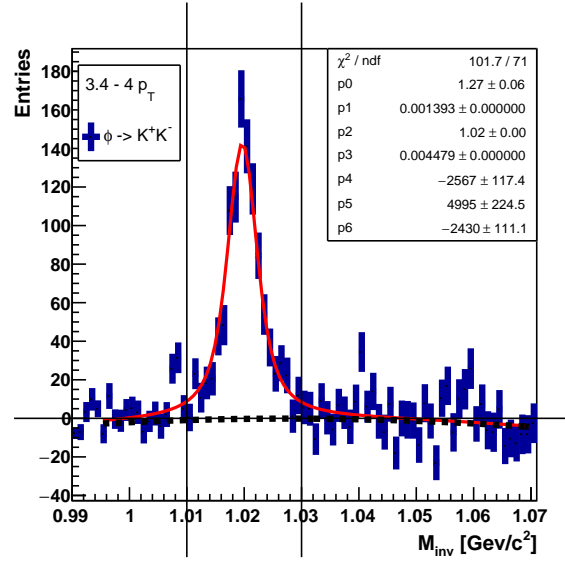
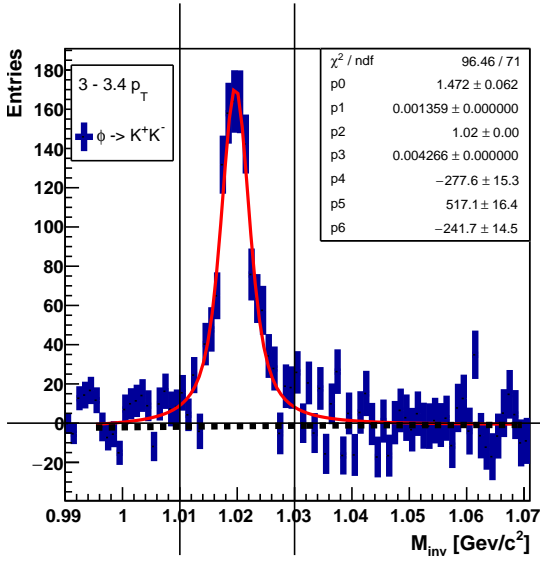
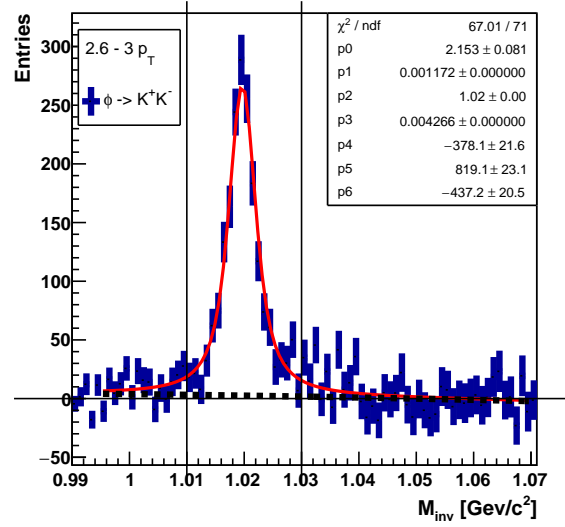
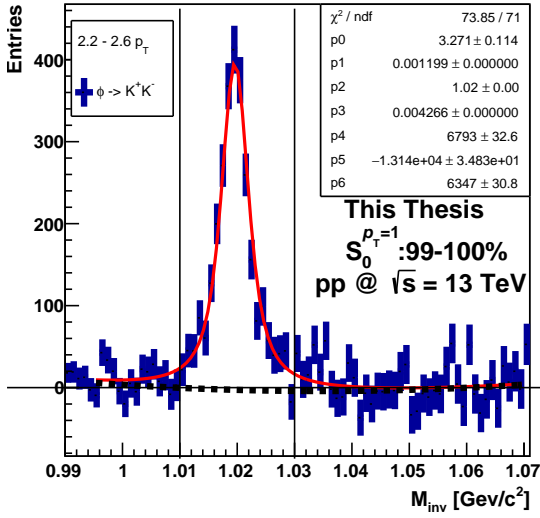


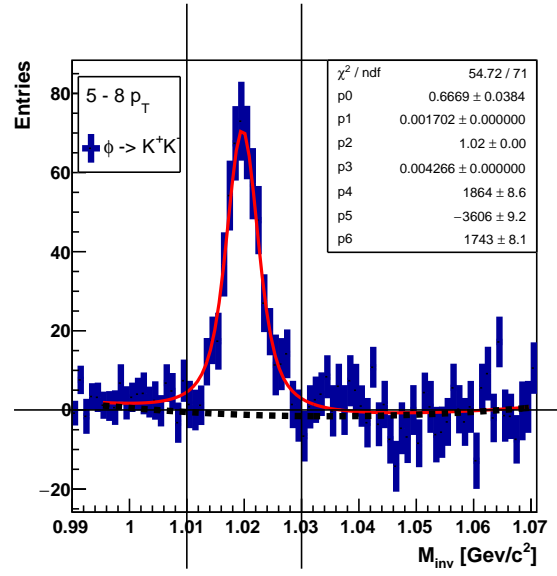
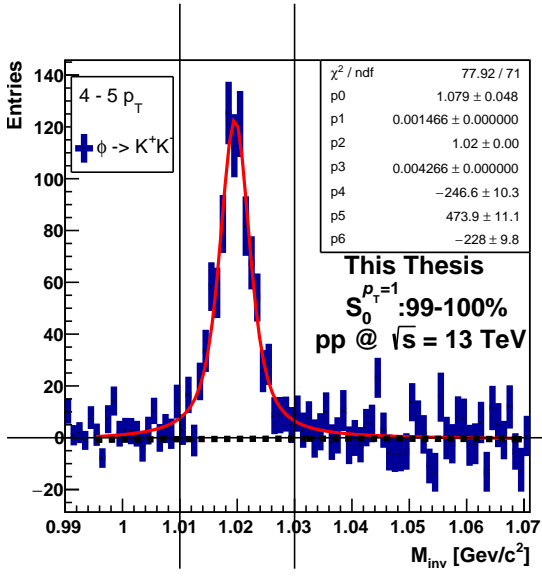


### 10.2.3 Isotropic Events, V0M: 0-10% + $S_0^{p_T=1}$ 99-100%













# Chapter 11

## Appendix B: Geometrical Cut for the $R_T$ Analysis

The  $R_T$  utilizes a "Geometrical Cut", for identifying the leading particle. This selection is required to reject reconstructed tracks, with a sufficient amount of crossed-rows, but large gaps in tracking, due to the sector gaps. The reconstructed tracks that align with the sector gaps will have bad momentum resolution, and can potentially create a "fake"  $R_T$  trigger, where a low- $p_T$  leading particle is reconstructed as if it had  $p_T^{\text{Leading}} \geq 5\text{GeV}/c$ . The underlying motivation for this cut is discussed in detail in Sec. 8.2, and the technical details of the implementation of this cut are discussed in the following.

During simulation studies, it was found that there was a significant,  $p_T$ -dependent discrepancy, between the reconstructed  $p_T$  and generated  $p_T$  for a large amount of reconstructed  $p_T^{\text{Leading}}$ . Figure 11.1 highlights the difference in  $p_T$  between reconstructed and generated tracks, as a function of  $p_T^{\text{Leading}}$ . Here, one can note that there is a large portion of reconstructed  $R_T$  triggers with  $p_T^{\text{Leading}} \geq 5\text{GeV}/c$ , with no associated generated particles  $\geq 5\text{GeV}/c$ .

The particle tracks at the very edge of the sector gaps are removed by imposing a  $p_T$ -differential cut, where we use the azimuthal angle  $\phi$  of each track to require:

- If the magnetic field  $B < 0$ , or the charge  $Q < 0$ , rotate the azimuthal frame such that  $\phi = 2\pi - \phi$ .
- Align the azimuthal angle with the sector gap, such that  $\phi = \phi + \pi/18$ .

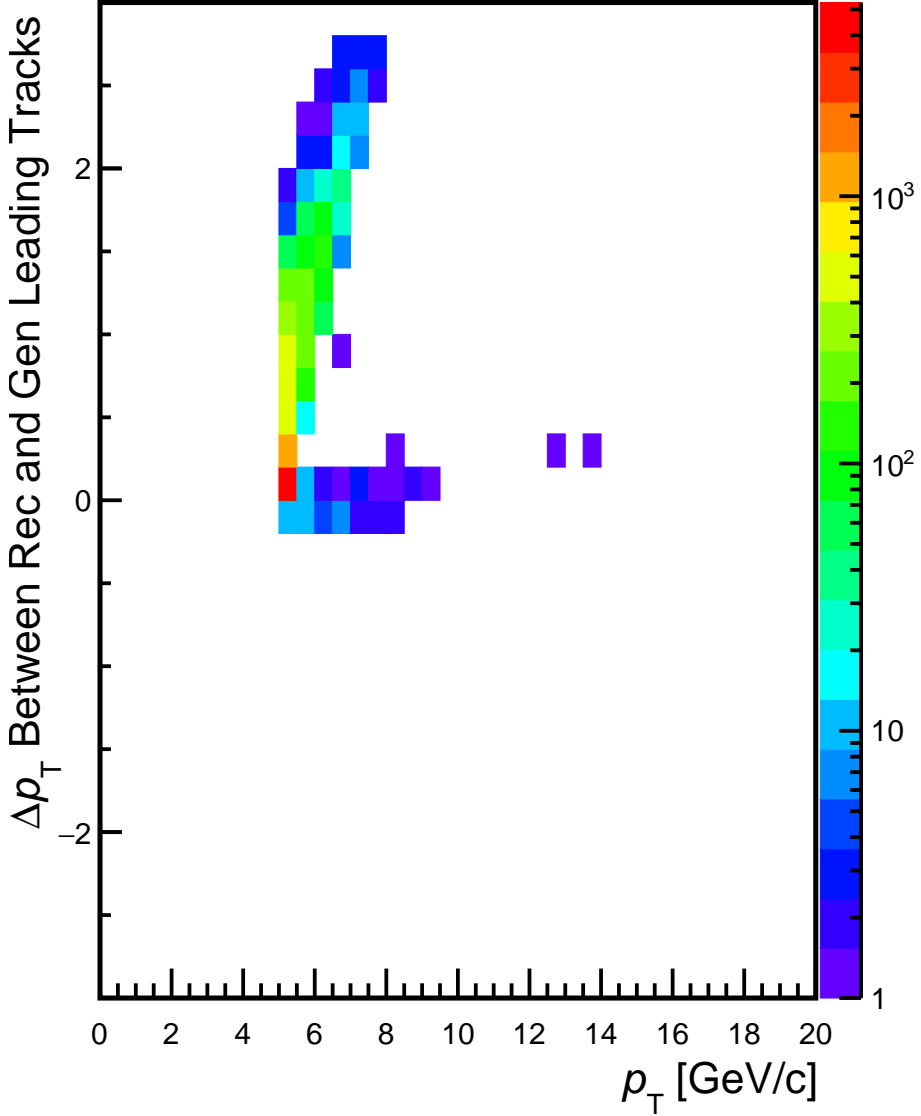


**Figure 11.1:** Demonstration of the large number of leading particle triggers that are reconstructed with an incorrect momentum. The leading particle tracks are generated in PYTHIA and reconstructed after propagation through a GEANT3 simulation of ALICE. The  $y$ -axis shows the difference between the "real" (generated) and reconstructed momentum, plotted against the true  $p_T^{\text{Leading}}$  value on the  $x$ -axis.

- Then, tracks are rejected inside the boundary of:  
 $(0.10/p_T + \pi/18 - 0.025) < \phi < (0.12/p_T + \pi/18 + 0.035)$

An implementation of the geometrical cut is presented in Fig. 11.2, presenting the azimuthal  $\phi$  angle, rotated to align with the sector gap, before and after the geometrical cut is applied.

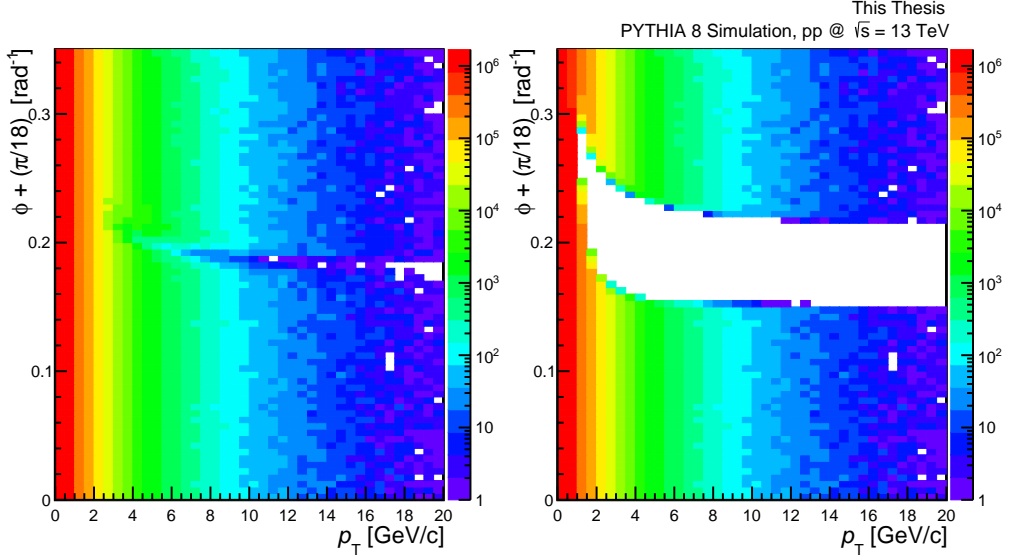


**Figure 11.2:** The  $\phi$  distribution, rotated to align with the sector gap, before (left panel) and after (right panel) the geometrical cut is applied.

The lower panel of Fig. 11.3 presents the reconstructed momentum resolution of the leading track as a function of azimuthal angle  $\phi$ . The figure clearly illustrates that there is a significant loss of momentum resolution near the TPC sector gaps. These badly reconstructed tracks constitute approximately 3.5% of all accepted  $p_T^{\text{Leading}} \geq 5\text{GeV}/c$ . After applying the geometrical cut, the number of incorrectly reconstructed triggers is drastically reduced. This is demonstrated in the upper panel of Fig. 11.3, which presents the same difference in reconstructed and generated momentum resolution as a function of azimuthal angle  $\phi$  after a geometrical cut is applied. The tracks with poor momentum resolution previously present along the sector gaps are now removed, and there is no systemic pattern in loss of resolution. The contamination from the poorly reconstructed  $p_T^{\text{Leading}} \geq 5\text{GeV}/c$  is thereby reduced from 3.5% to 1.2%, after implementing the geometrical cut.

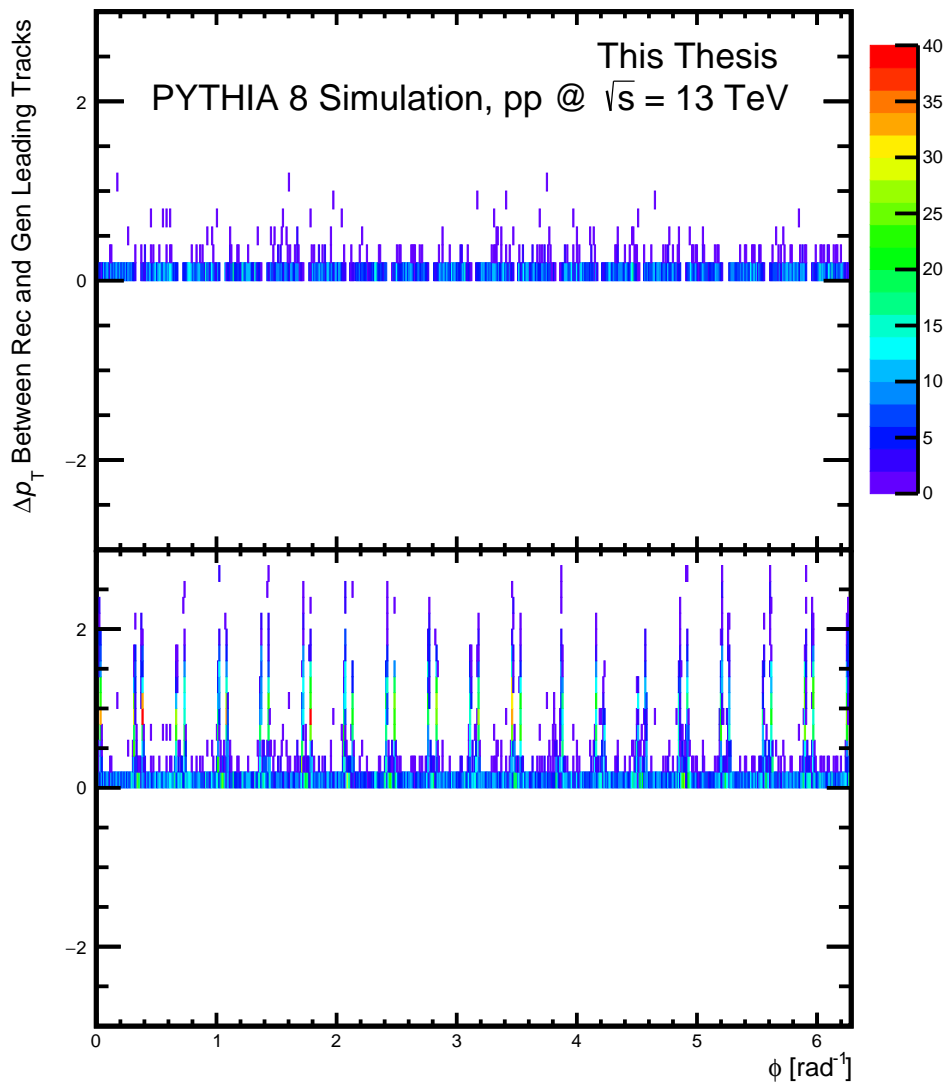


**Figure 11.3:** The difference in momentum between generated and reconstructed leading charged particle tracks, presented as a function of the azimuthal angle, before (lower panel) and after (upper panel) a geometrical cut is implemented

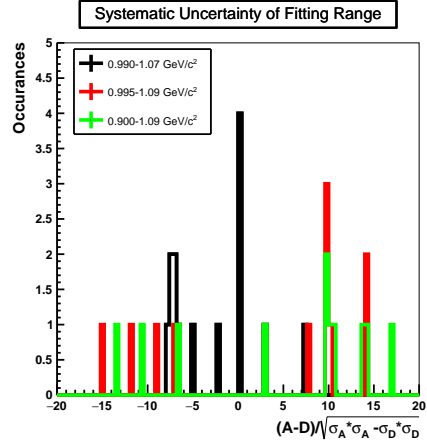
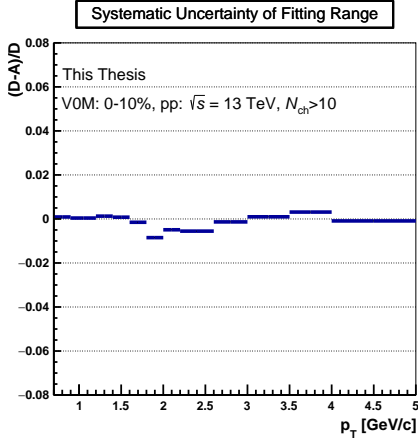
## Chapter 12

# Appendix C: Systematic Uncertainties and Roger-Barlow Checks for $\phi$ Meson Analysis

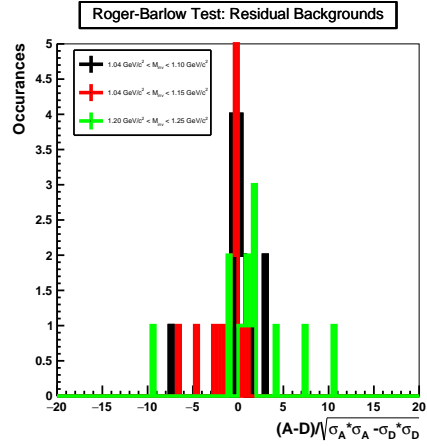
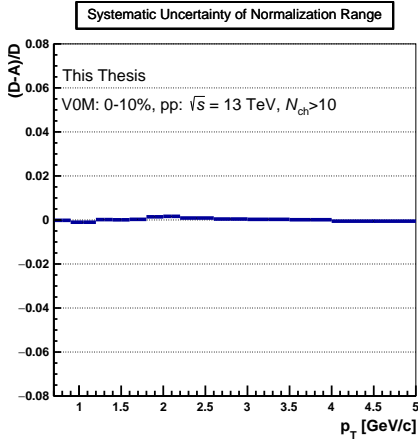
This chapter contains all the checks that ensure that each source of systematic uncertainty for the estimation of  $\phi$  meson yield is significant (referred to here as “Roger-Barlow Tests”). Furthermore, this chapter also reports the systematic uncertainty for the subgroups, described in Sec. 7.4.1. One should note that, unless it is a clear fluctuation, the absolute number is taken as systematic uncertainty in each  $p_T$  bin.

## 12.1 VOM: 0-10%

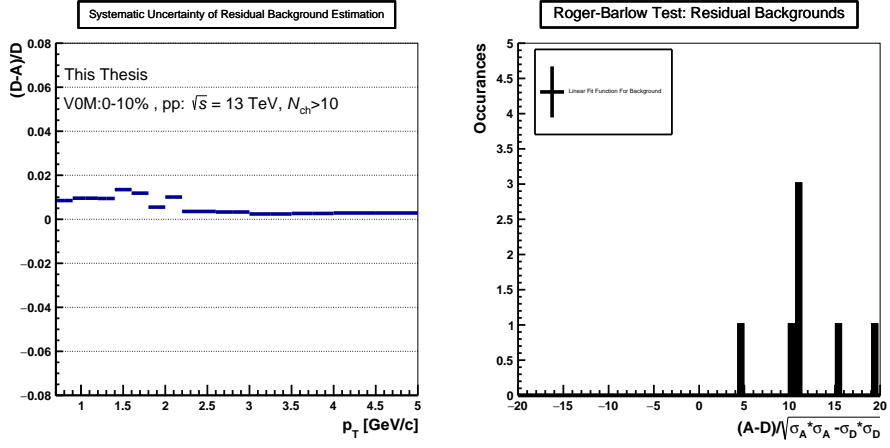
### Uncertainty Due to Fitting Range



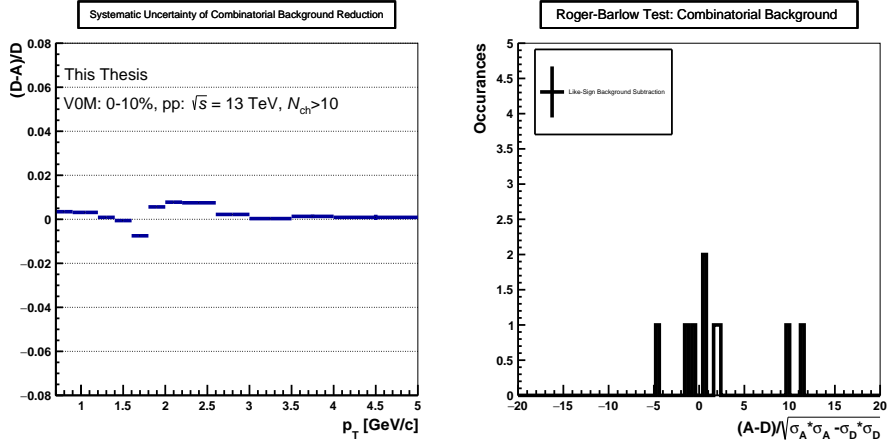
### Uncertainty for Normalization of Combinatorial Background



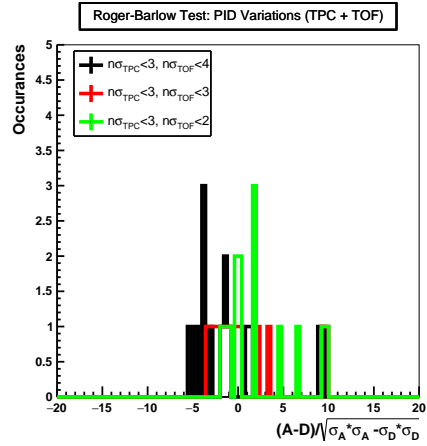
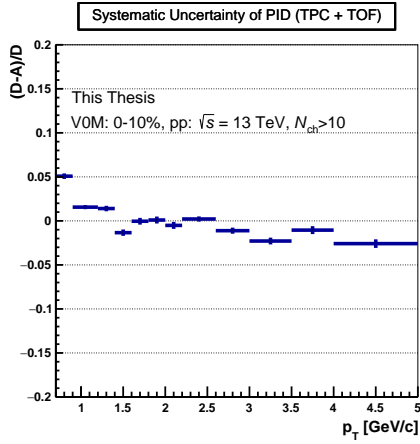
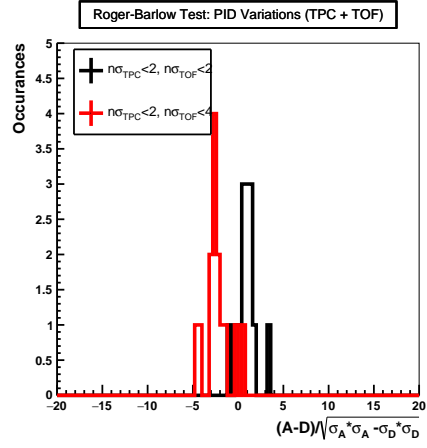
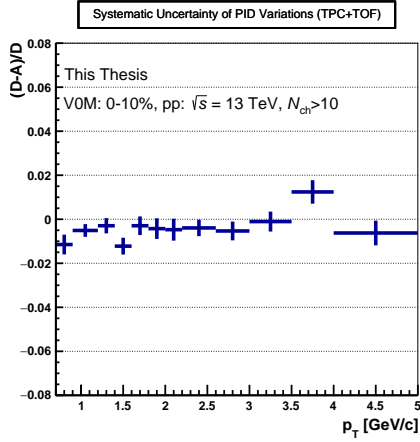
## Uncertainty Due to Residual Background Function



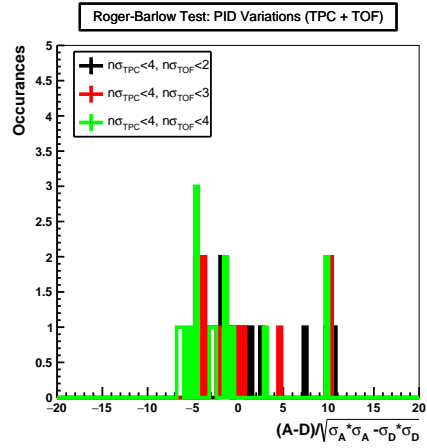
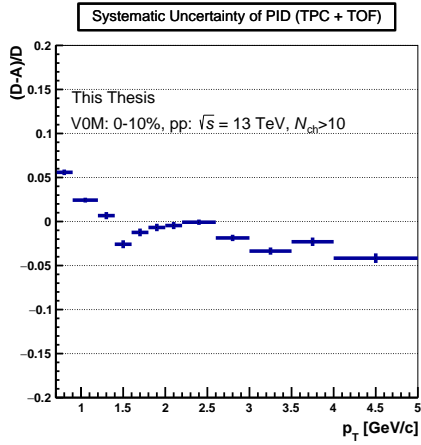
## Uncertainty Combinatorial Background Reduction



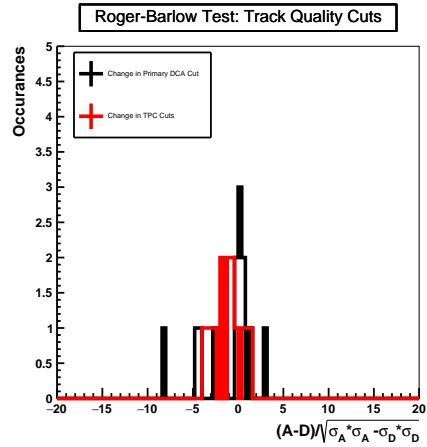
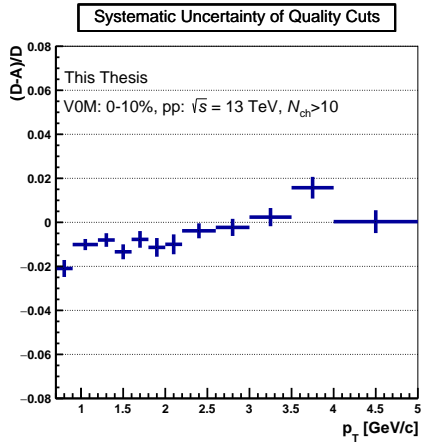
## Uncertainty Due to Residual for PID variations



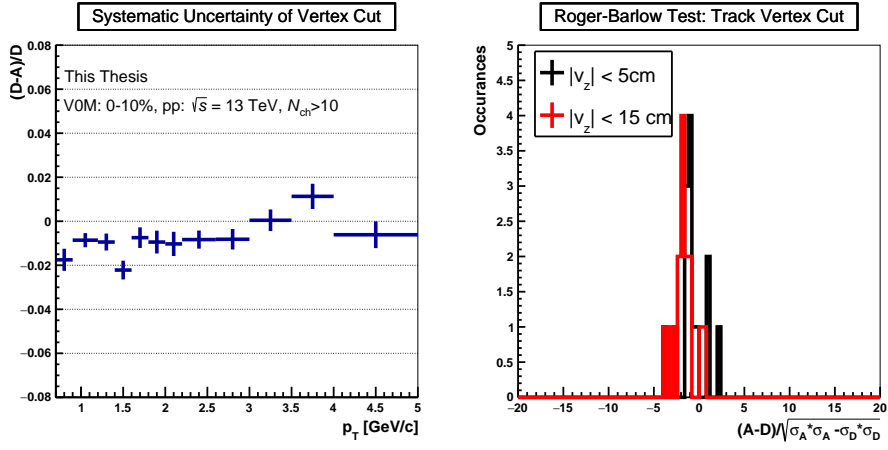




## Uncertainty Due to Residual for Quality Cuts

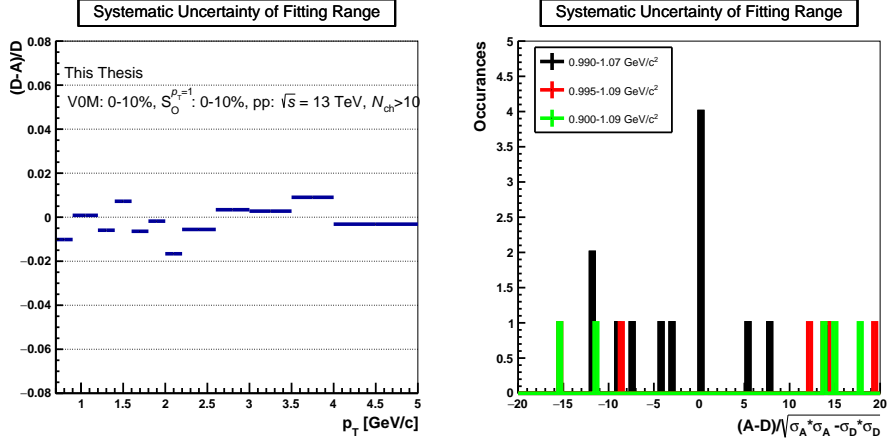


## Uncertainty Due to Vertex Variation

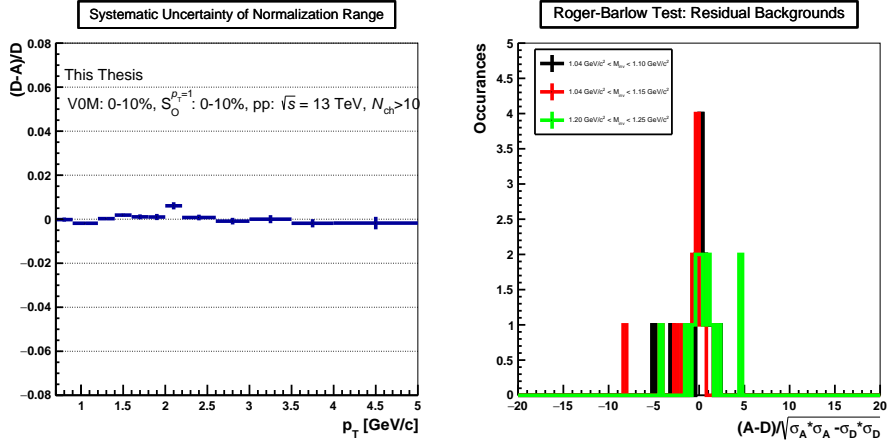


## 12.2 Jetty Events (V0M:0-10%, $S_O^{p_T=1}$ 0-10%)

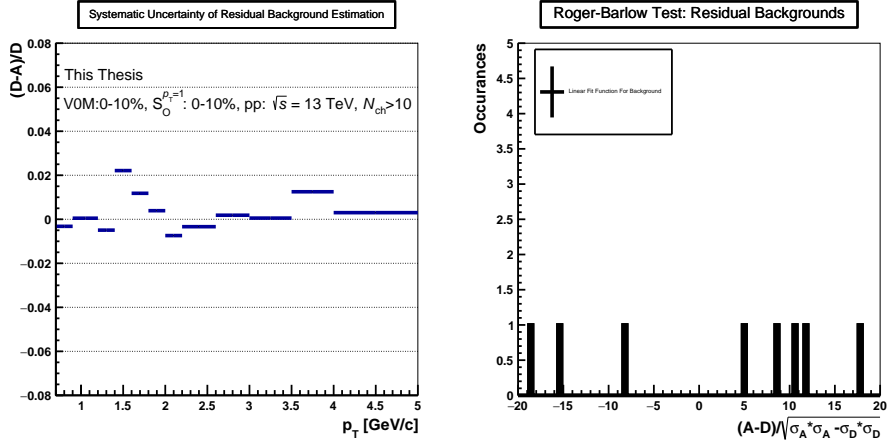
### Uncertainty Due to Fitting Range



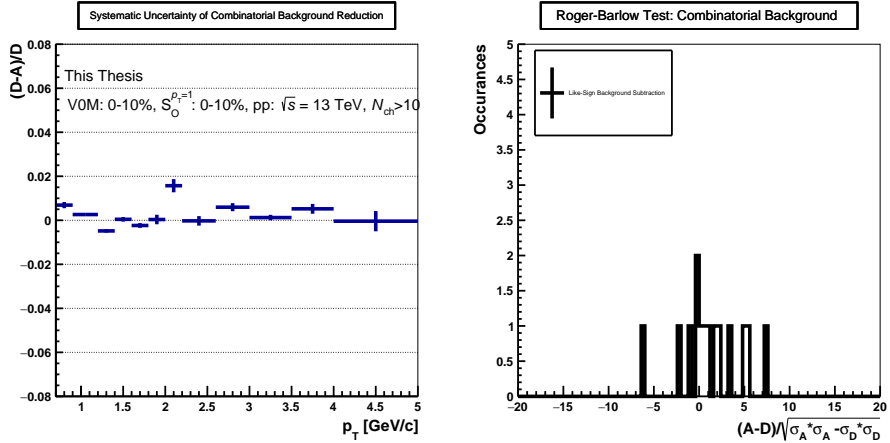
### Uncertainty for Normalization of Combinatorial Background



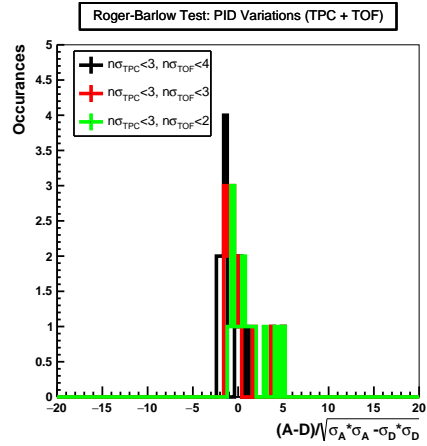
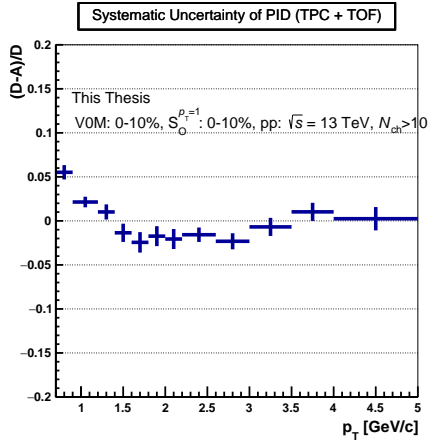
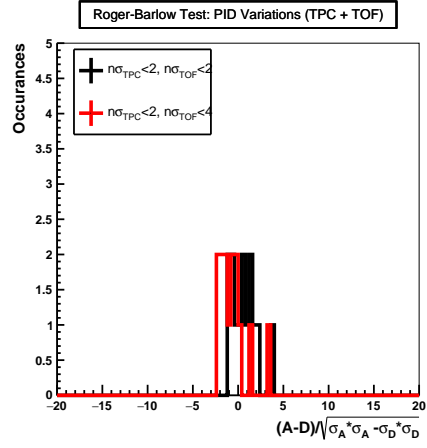
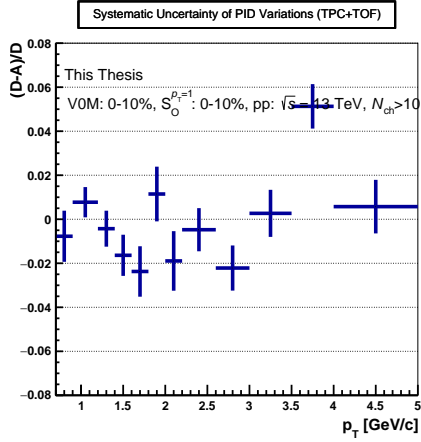
## Uncertainty Due to Residual Background Function

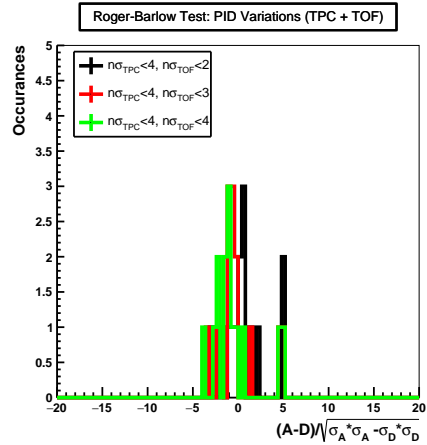
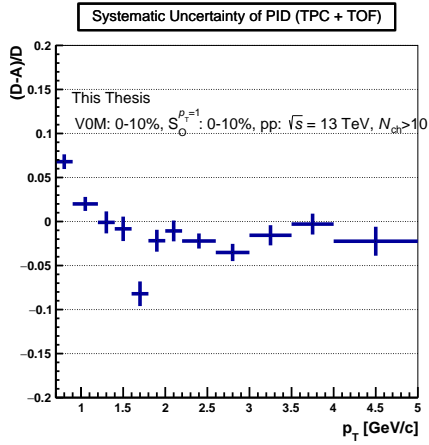


## Uncertainty Combinatorial Background Reduction

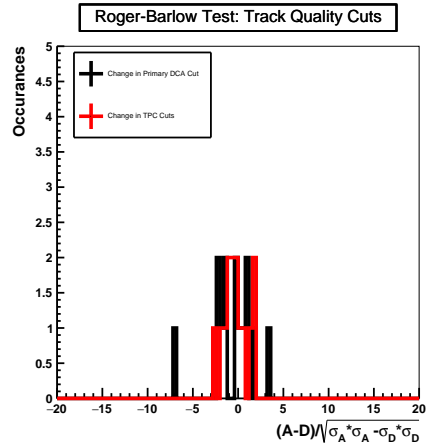
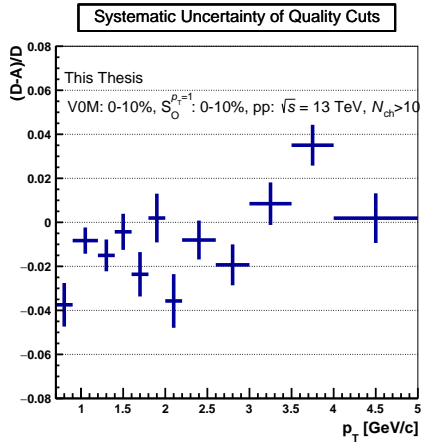


## Uncertainty Due to Residual for PID variations

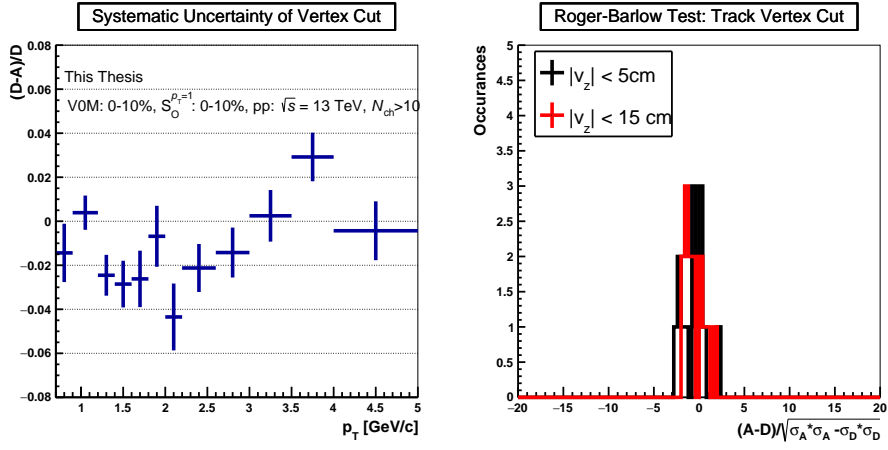




## Uncertainty Due to Residual for Quality Cuts

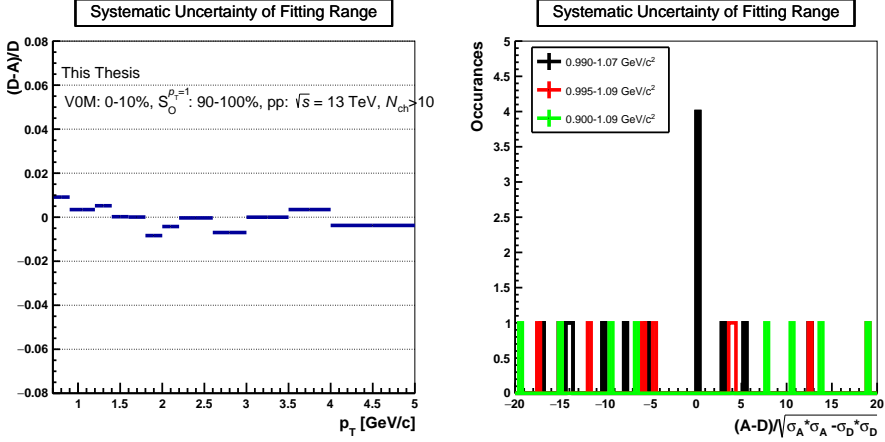


## Uncertainty Due to Vertex Variation

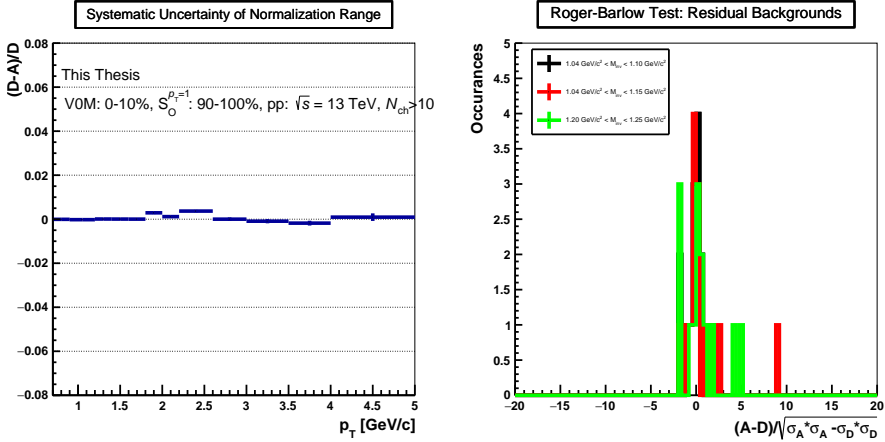


## 12.3 Isotropic Events (V0M:0-10%, $S_O^{p_T=1}$ 90-100%)

### Uncertainty Due to Fitting Range

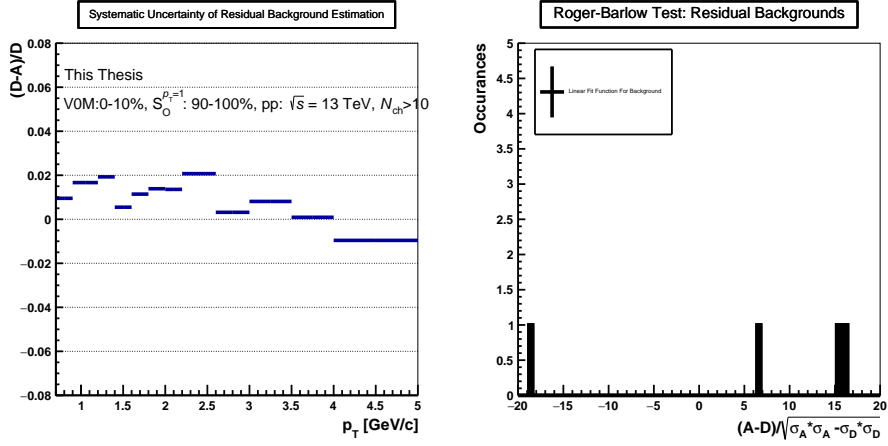


### Uncertainty for Normalization of Combinatorial Background

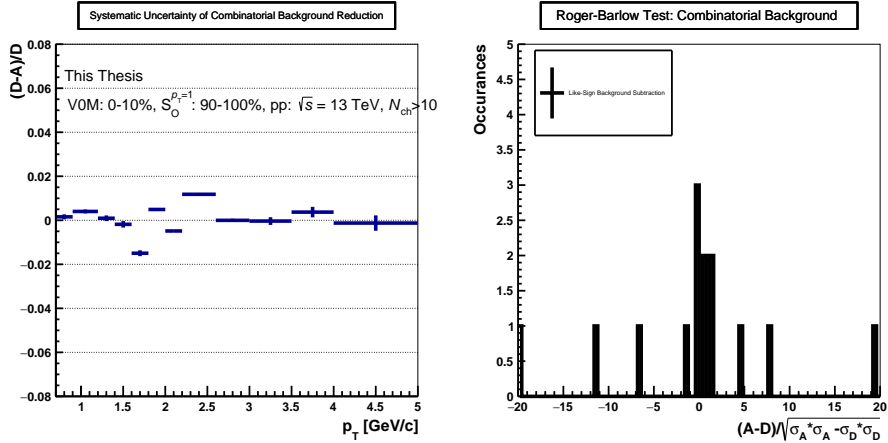




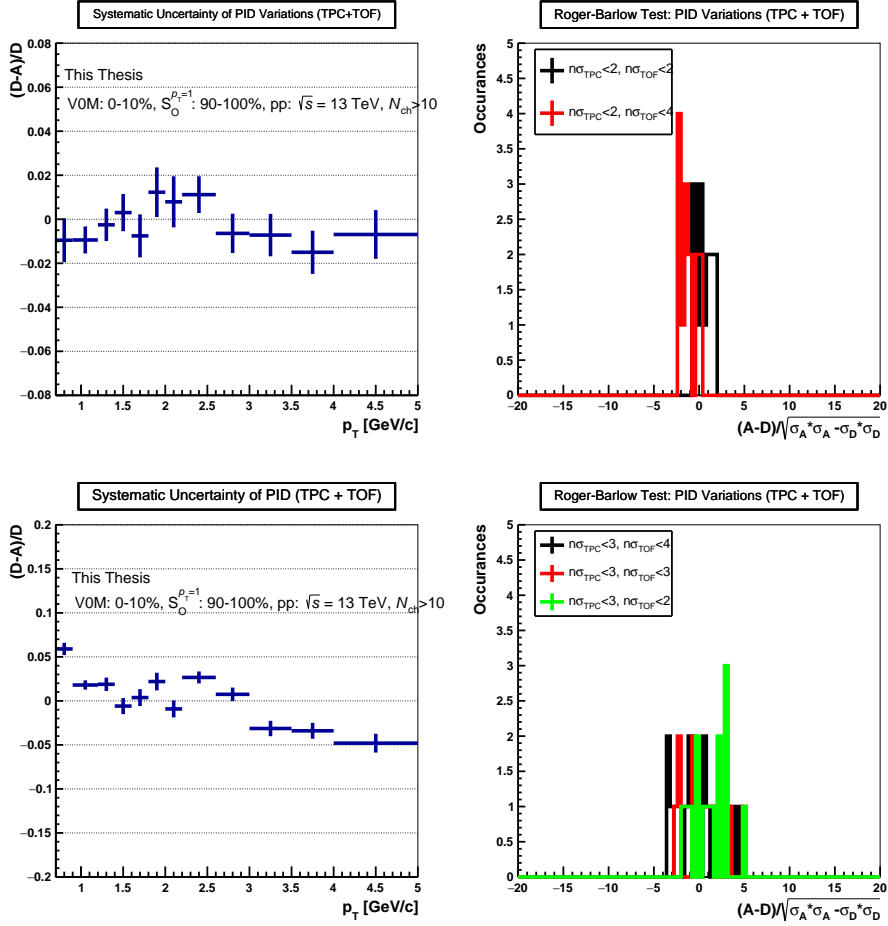
## Uncertainty Due to Residual Background Function

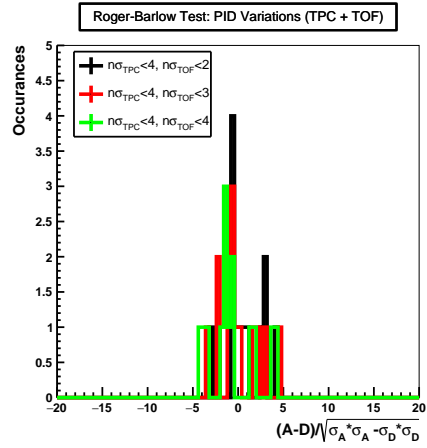
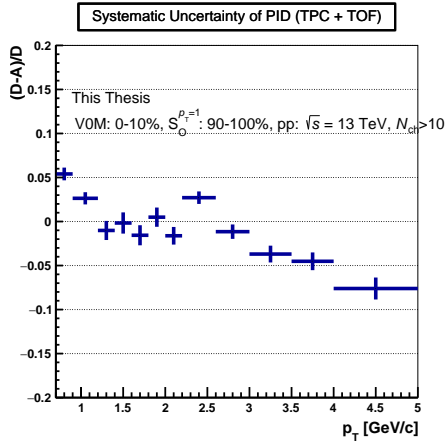


## Uncertainty Combinatorial Background Reduction

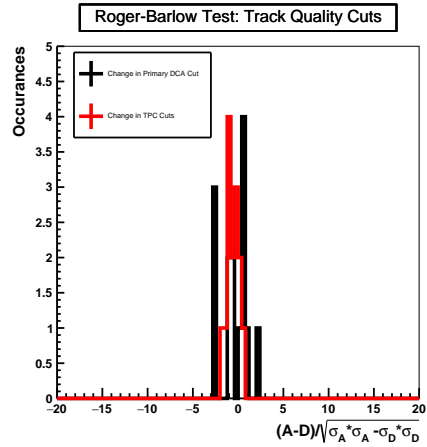
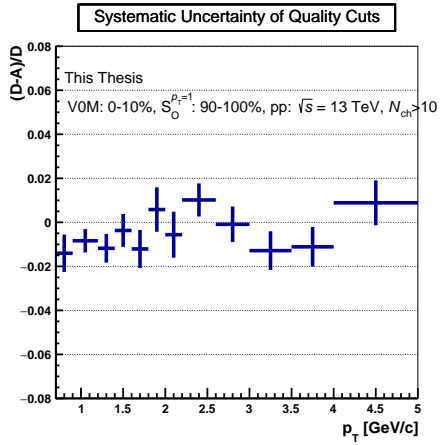


## Uncertainty Due to Residual for PID variations

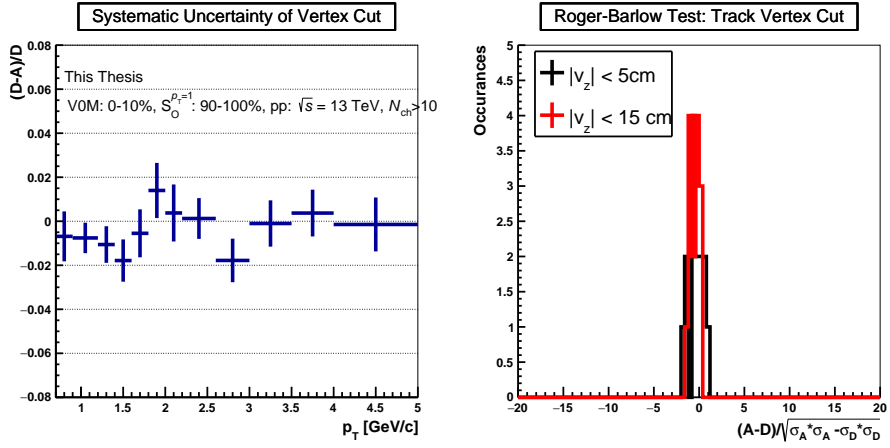




## Uncertainty Due to Residual for Quality Cuts



## Uncertainty Due to Vertex Variation



# Chapter 13

## References

### 13.1 References

- [1] J. Adam et al. (ALICE), Nature Phys. **13**, 535 (2017), 1606.07424.
- [2] J. C. Collins and M. J. Perry, Phys. Rev. Lett. **34**, 1353 (1975).
- [3] J. R. Ellis, J. Phys. Conf. Ser. **50**, 8 (2006), astro-ph/0504501.
- [4] E. Annala, T. Gorda, A. Kurkela, J. Nättilä, and A. Vuorinen, Nature Physics **16**, 907 (2020), ISSN 1745-2481, URL <https://doi.org/10.1038/s41567-020-0914-9>.
- [5] T. D. Lee and G. C. Wick, Phys. Rev. D **9**, 2291 (1974), URL <https://link.aps.org/doi/10.1103/PhysRevD.9.2291>.
- [6] W. Busza, K. Rajagopal, and W. van der Schee, Ann. Rev. Nucl. Part. Sci. **68**, 339 (2018), 1802.04801.
- [7] T. S. H. C. of Theoretical Cosmology, *The Origins of the Universe: The Big Bang.*, [https://www.ctc.cam.ac.uk/outreach/origins/big\\_bang\\_three.php](https://www.ctc.cam.ac.uk/outreach/origins/big_bang_three.php), last visited 2022-10-31.
- [8] U. W. Heinz and M. Jacob (2000), nucl-th/0002042.
- [9] CERN Press Release, February 10, 2022. <https://home.cern/news/press-release/cern/new-state-matter-created-cern>, last visited 2022-10-31.

- [10] B. B. Back et al. (PHOBOS), Nucl. Phys. A **757**, 28 (2005), [nucl-ex/0410022](#).
- [11] I. Arsene et al. (BRAHMS), Nucl. Phys. A **757**, 1 (2005), [nucl-ex/0410020](#).
- [12] J. Adams et al. (STAR), Nucl. Phys. A **757**, 102 (2005), [nucl-ex/0501009](#).
- [13] K. Adcox et al. (PHENIX), Nucl. Phys. A **757**, 184 (2005), [nucl-ex/0410003](#).
- [14] M. Wilde (ALICE), Nucl. Phys. A **904-905**, 573c (2013), [1210.5958](#).
- [15] S. Acharya et al. (ALICE), Eur. Phys. J. C **80**, 167 (2020), [1908.01861](#).
- [16] S. Chatrchyan et al. (CMS), Phys. Lett. B **718**, 795 (2013), [1210.5482](#).
- [17] S. G. Weber and A. Andronic (2016), general Photo, URL <https://cds.cern.ch/record/2202730>.
- [18] J. Rafelski and R. Hagedorn, p. 22 p (1981), URL <https://cds.cern.ch/record/126179>.
- [19] Vazquez Rueda, Omar, Ph.D. thesis, Lund University (2022), URL [https://lup.lub.lu.se/search/files/118013005/Doctoral\\_Thesis\\_OmarVazquezRueda.pdf](https://lup.lub.lu.se/search/files/118013005/Doctoral_Thesis_OmarVazquezRueda.pdf).
- [20] MissMJ, *Cush. Standard Model of Elementary Particles.*, [https://commons.wikimedia.org/wiki/File:Standard\\_Model\\_of\\_Elementary\\_Particles.svg](https://commons.wikimedia.org/wiki/File:Standard_Model_of_Elementary_Particles.svg), last visited 2022-10-31.
- [21] G. Kane, *Modern Elementary Particle Physics: The Fundamental Particles and Forces?* (1993), ISBN 0-201-62460-5.
- [22] R. Aaij et al. (LHCb), Phys. Rev. Lett. **122**, 222001 (2019), [1904.03947](#).
- [23] B. R. Martin and G. Shaw, *Particle physics.*, The Manchester physics series (John Wiley Sons, 2017), ISBN 9781118911907.
- [24] M. Tanabashi et al. (Particle Data Group), Phys. Rev. D **98**, 030001 (2018).
- [25] Istituto Nazionale di Fisica Nucleare (INFN), *The “Variable” Constant*, <https://w3.lnf.infn.it/the-variable-constant/?lang=en>, last visited 2022-10-31.

- [26] P. A. Zyla et al. (Particle Data Group), PTEP **2020**, 083C01 (2020).
- [27] W. Florkowski, *Phenomenology of Ultra-Relativistic Heavy-Ion Collisions* (2010), ISBN 978-981-4280-66-2.
- [28] Mets501, *Different values of pseudorapidity shown against a polar grid.*, [https://commons.wikimedia.org/wiki/File:Pseudorapidity\\_plot.svg](https://commons.wikimedia.org/wiki/File:Pseudorapidity_plot.svg), last visited 2022-10-31.
- [29] M. L. J. Miller, K. Reygers, S. J. Sanders, and P. Steinberg, Annual Review of Nuclear and Particle Science **57**, 205 (2007).
- [30] D. d’Enterria and C. Loizides, Ann. Rev. Nucl. Part. Sci. **71**, 315 (2021), 2011.14909.
- [31] A. Bialas, M. Bleszynski, and W. Czyz, Acta Phys. Polon. B **8**, 389 (1977).
- [32] (2018), URL <https://cds.cern.ch/record/2636623>.
- [33] C. Loizides, J. Kamin, and D. d’Enterria, Phys. Rev. C **97**, 054910 (2018), [Erratum: Phys.Rev.C 99, 019901 (2019)], 1710.07098.
- [34] E. Shuryak, Physics Letters B **78**, 150 (1978), ISSN 0370-2693, URL <https://www.sciencedirect.com/science/article/pii/0370269378903702>.
- [35] M. A. Stephanov, International Journal of Modern Physics A **20**, 4387 (2005), URL <https://doi.org/10.1142/2Fs0217751x05027965>.
- [36] I. G. Bearden et al. (BRAHMS), Phys. Rev. Lett. **93**, 102301 (2004), nucl-ex/0312023.
- [37] R. Pasechnik and M. Šumbera, Universe **3**, 7 (2017), 1611.01533.
- [38] A. Bazavov et al. (HotQCD), Phys. Rev. D **90**, 094503 (2014), 1407.6387.
- [39] N. Brambilla, S. Eidelman, B. K. Heltsley, R. Vogt, G. T. Bodwin, E. Eichten, A. D. Frawley, A. B. Meyer, R. E. Mitchell, V. Papadimitriou, et al., The European Physical Journal C **71**, 1534 (2011), ISSN 1434-6052, URL <https://doi.org/10.1140/epjc/s10052-010-1534-9>.
- [40] P. B. Arnold, G. D. Moore, and L. G. Yaffe, JHEP **01**, 030 (2003), hep-ph/0209353.
- [41] H. Nastase (2007), 0712.0689.

- [42] P. K. Kovtun, D. T. Son, and A. O. Starinets, Physical Review Letters **94** (2005), URL <https://doi.org/10.1103/PhysRevLett.94.111601>.
- [43] U. W. Heinz, *"rhic serves the perfect fluid" – hydrodynamic flow of the qgp* (2005), URL <https://arxiv.org/abs/nuc1-th/0512051>.
- [44] J. Rafelski and B. Müller, Phys. Rev. Lett. **48**, 1066 (1982), URL <https://link.aps.org/doi/10.1103/PhysRevLett.48.1066>.
- [45] B. Abelev, J. Adam, D. Adamová, A. Adare, M. Aggarwal, G. A. Rinella, M. Agnello, A. Agocs, A. Agostinelli, Z. Ahammed, et al., Physics Letters B **728**, 216 (2014), URL <https://doi.org/10.1016/PhysLetb.2013.11.048>.
- [46] V. Khachatryan et al. (CMS), Phys. Lett. B **770**, 357 (2017), 1611.01510.
- [47] A. M. Sirunyan et al. (CMS), Phys. Rev. Lett. **120**, 142301 (2018), 1706.05984.
- [48] B. Hippolyte, private Correspondence, based on a previous iteration of this figure, created by Masashi Kaneta.
- [49] T. Snellman, obtained from lecture notes by Dong-Jo Kim, Jyväskylä University.
- [50] J. Adam et al. (ALICE), Phys. Rev. Lett. **116**, 132302 (2016), 1602.01119.
- [51] B. I. Abelev et al. (STAR), Phys. Rev. C **80**, 064912 (2009), 0909.0191.
- [52] L. P. Csernai, J. I. Kapusta, and L. D. McLerran, Phys. Rev. Lett. **97**, 152303 (2006), URL <https://link.aps.org/doi/10.1103/PhysRevLett.97.152303>.
- [53] J. Adams et al. (STAR), Phys. Rev. Lett. **91**, 072304 (2003), nuc1-ex/0306024.
- [54] M. Aaboud et al. (ATLAS), Phys. Lett. B **790**, 108 (2019), 1805.05635.
- [55] M. Connors, C. Nattrass, R. Reed, and S. Salur, Rev. Mod. Phys. **90**, 025005 (2018), 1705.01974.
- [56] V. Khachatryan et al. (CMS), Phys. Rev. Lett. **116**, 172302 (2016), 1510.03068.
- [57] S. Acharya et al. (ALICE), Phys. Rev. C **99**, 024906 (2019), 1807.11321.



- [58] S. Acharya et al. (ALICE), Phys. Rev. Lett. **123**, 142301 (2019), 1903.01790.
- [59] T. Pierog, I. Karpenko, J. M. Katzy, E. Yatsenko, and K. Werner, Phys. Rev. C **92**, 034906 (2015), 1306.0121.
- [60] B. Andersson, *Introduction* (Cambridge University Press, 1998), p. 1–5, Cambridge Monographs on Particle Physics, Nuclear Physics and Cosmology.
- [61] S. Ferreres-Solé and T. Sjöstrand, Eur. Phys. J. C **78**, 983 (2018), 1808.04619.
- [62] H. Suganuma, K. Amemiya, H. Ichie, H. Matsufuru, Y. Nemoto, and T. T. Takahashi, in *International Symposium on Quantum Chromodynamics (QCD) and Color Confinement (Confinement 2000)* (2004), pp. 103–119, hep-lat/0407020.
- [63] C. Bierlich, G. Gustafson, L. Lönnblad, and A. Tarasov, JHEP **03**, 148 (2015), 1412.6259.
- [64] C. Bierlich et al. (2022), 2203.11601.
- [65] T. Sjöstrand, *Old Ideas in Hadronization: The Lund string*, [https://conference.ippp.dur.ac.uk/event/265/?view=standard\\_numbered](https://conference.ippp.dur.ac.uk/event/265/?view=standard_numbered), last visited 2022-10-31.
- [66] J. Adolfsson et al., Eur. Phys. J. A **56**, 288 (2020), 2003.10997.
- [67] (2017), URL <https://cds.cern.ch/record/2270008>.
- [68] C. Bierlich, private Correspondence.
- [69] C. Bierlich, S. Chakraborty, G. Gustafson, and L. Lönnblad, SciPost Phys. **13**, 023 (2022), 2202.12783.
- [70] S. Acharya, D. Adamova, A. Adler, J. Adolfsson, M. Aggarwal, G. Aglieri Rinella, M. Agnello, N. Agrawal, Z. Ahammed, S. Ahmad, et al., The European Physical Journal C **80** (2020).
- [71] J. Bellm et al., Eur. Phys. J. C **80**, 452 (2020), 1912.06509.
- [72] J. Bellm et al., Eur. Phys. J. C **76**, 196 (2016), 1512.01178.

- [73] R. K. Ellis, W. J. Stirling, and B. R. Webber, *QCD and collider physics*, Cambridge monographs on particle physics, nuclear physics, and cosmology (Cambridge University Press, Cambridge, 2003), photography by S. Vascotto, URL <https://cds.cern.ch/record/318585>.
- [74] K. Adcox et al. (PHENIX), Nucl. Phys. A **757**, 184 (2005), [nucl-ex/0410003](#).
- [75] H. Petersen, J. Steinheimer, G. Burau, M. Bleicher, and H. Stöcker, Phys. Rev. C **78**, 044901 (2008), [0806.1695](#).
- [76] A. Andronic, P. Braun-Munzinger, K. Redlich, and J. Stachel, Nature **561**, 321 (2018), [1710.09425](#).
- [77] K. Werner, *Resonance production (from small to big systems)*, <https://indico.cern.ch/event/576735/contributions/2566940/attachments/1493037/2321590/sqm.20.pdf>, last visited 2022-10-31.
- [78] S. Tripathy (ALICE), Springer Proc. Phys. **261**, 683 (2021), [1907.00842](#).
- [79] J. Adam et al. (ALICE), Eur. Phys. J. C **76**, 245 (2016), [1601.07868](#).
- [80] S. Acharya et al. (ALICE), JHEP **09**, 006 (2018), [1805.04390](#).
- [81] K. Aamodt et al. (ALICE), JINST **3**, S08002 (2008).
- [82] Description of the LHC accelerator complex, <https://home.cern/science/accelerators/accelerator-complex>, visited 2022-10-31.
- [83] A. Collaboration, *Real-time data processing in the alice high level trigger at the lhc* (2018).
- [84] S. Acharya et al. (ALICE), Eur. Phys. J. C **81**, 630 (2021), [2009.09434](#).
- [85] J. Adam et al. (ALICE), Phys. Rev. Lett. **116**, 222302 (2016), [1512.06104](#).
- [86] Saint-Gobain Crystals, "BC-400,BC-404,BC-408,BC-412,BC-416 Premium Plastic Scintillators", <https://www.crystals.saint-gobain.com/radiation-detection-scintillators/plastic-scintillators/bc400-bc404-bc408-bc412-bc416#>, visited 2022-10-31.
- [87] E. Abbas et al. (ALICE), JINST **8**, P10016 (2013), [1306.3130](#).
- [88] S. Acharya et al. (ALICE), Eur. Phys. J. C **81**, 630 (2021), [2009.09434](#).
- [89] S. Acharya et al. (ALICE), Phys. Rev. C **99**, 024906 (2019), [1807.11321](#).

- [90] K. S. Krane, *Introductory nuclear physics* (Wiley, New York, NY, 1988), URL <https://cds.cern.ch/record/359790>.
- [91] G. Dellacasa et al. (ALICE) (2000).
- [92] A. N. Akindinov et al., Nucl. Instrum. Meth. A **533**, 74 (2004).
- [93] Y. Belikov, K. Safarík, and B. Batyunya (ALICE) (1997).
- [94] A. Maire (2011), general Photo, URL <https://cds.cern.ch/record/1984041>.
- [95] S. Acharya et al. (ALICE), Eur. Phys. J. C **81**, 256 (2021), 2005.11120.
- [96] R. Brun, F. Bruyant, M. Maire, A. C. McPherson, and P. Zancarini, *GEANT 3: user's guide Geant 3.10, Geant 3.11; rev. version* (CERN, Geneva, 1987), URL <https://cds.cern.ch/record/1119728>.
- [97] J. B. et al. (Particle Data Group), PR **D86**, 010001 (2012), URL <http://pdg.lbl.gov>.
- [98] A. F. Nassirpour, Proceedings **10** (2019), ISSN 2504-3900, URL <https://www.mdpi.com/2504-3900/10/1/26>.
- [99] S. Acharya et al. (ALICE), Phys. Lett. B **807**, 135501 (2020), 1910.14397.
- [100] M. T. et al. (Particle Data Group), Phys. Rev. D **98**, 030001 (2018).
- [101] P. Z. et al. (Particle Data Group), Prog. Theor. Exp. Phys. **083C01** (2020).
- [102] D. D. Chinellato, private Correspondence.
- [103] Angelsmark, Martin, *Xi Production in pp Collisions at Different Multiplicity and Sphericity* (2019), Student Paper.
- [104] A. Banfi, G. P. Salam, and G. Zanderighi, Journal of High Energy Physics **2010**, 38 (2010), ISSN 1029-8479, URL [https://doi.org/10.1007/JHEP06\(2010\)038](https://doi.org/10.1007/JHEP06(2010)038).
- [105] A. Ortiz, G. Paicé, and E. Cuautle, Nucl. Phys. A **941**, 78 (2015), 1503.03129.
- [106] S. Acharya et al. (ALICE), Eur. Phys. J. C **79**, 857 (2019), 1905.07208.
- [107] S. K. Prasad (ALICE), J. Phys. Conf. Ser. **389**, 012005 (2012), 1208.5080.

- [108] V. Vislavicius, *Identified Hadron Production as a Function of Event Multiplicity and Transverse Sphericity in pp Collisions at  $\sqrt{s} = 7$  and 13 TeV with the ALICE Detector* (2018), presented 23 Mar 2018, URL <https://cds.cern.ch/record/2310568>.
- [109] S. Acharya et al. (ALICE), Phys. Lett. B **827**, 136984 (2022), 2105.04890.
- [110] R. Barlow, in *Conference on Advanced Statistical Techniques in Particle Physics* (2002), pp. 134–144, [hep-ex/0207026](#).
- [111] R. Rath, *Event topology and multiplicity dependence of  $K(892)^0$  production in proton+proton collisions with ALICE at the LHC and probing TeV collisions through particle production and transport properties* (2021), presented 10 Dec 2021, URL <https://cds.cern.ch/record/2798406>.
- [112] B. B. Abelev et al. (ALICE), Phys. Lett. B **728**, 25 (2014), 1307.6796.
- [113] S. Acharya et al. (ALICE), Phys. Lett. B **827**, 136984 (2022), 2105.04890.
- [114] C. Bierlich, EPJ Web Conf. **171**, 14003 (2018), 1710.04464.
- [115] J. Bellm et al., Eur. Phys. J. C **80**, 452 (2020), 1912.06509.
- [116] T. Martin, P. Skands, and S. Farrington, The European Physical Journal C **76** (2016).
- [117] S. Acharya et al. (ALICE), JHEP **04**, 192 (2020), 1910.14400.
- [118] G. Bencédi, A. Ortiz, and S. Tripathy, Journal of Physics G: Nuclear and Particle Physics **48**, 015007 (2020), URL <https://doi.org/10.1088/1361-6471/abc5fb>.
- [119] J. Gronefeld, internal ALICE Analysis Note.
- [120] M. Krüger (ALICE), PoS **Confinement2018**, 236 (2018), 1909.06109.



